The Formation and Evolution of Cataclysmic Variables

Thesis

Faculty of Science, The Open University

The Formation and Evolution of Cataclysmic Variables

Philip Davis MPhys.

Submitted for the degree of Doctor of Philosophy

June 2009

DATE OF SUBMISSION : 19 JUNE 2009
DATE OF AWARD : 24 NOV 2009

ProQuest LLC.
789 East Eisenhower Parkway
P.O. Box 1346
Ann Arbor, MI 48106 – 1346

CONTENTS

LIST OF FIGURES

LIST OF TABLES

The Formation and Evolution of Cataclysmic Variables

Philip Davis MPhys.
June 2009

Faculty of Science, The Open University
Submitted for the degree of Doctor of Philosophy

White dwarf-main sequence star (WD+MS) binaries allows us to investigate two major, poorly understood, paradigms of binary evolution. Firstly, the disrupted magnetic braking (DMB) model; a widely cited explanation for the paucity of observed cataclysmic variables (CVs) with orbital periods of between about 2 and 3 hours (coined the period gap). Secondly, common envelope (CE) evolution, which is thought to be a major formation mechanism of semi-detached, compact binaries. Despite the ubiquity of these models in the literature, they have yet to be comprehensively tested with observations.

To test the former paradigm, we exploit the model's main prediction: the existence of detached WD+MS binaries within the period gap that were CVs but ceased mass transfer as a result of DMB ('detached CVs'; dCVs). For a range of models describing the CE phase and magnetic braking, we employ population synthesis techniques to calculate the present day population of dCVs and detached WD+MS that have formed from a CE phase (post-common envelope binaries; PCEBs).

We find that dCVs outnumber PCEBs with late spectral-type secondary stars within the period gap by a factor of between 4 and 13. This excess manifests as a prominent peak within the period gap of the combined PCEB and dCV orbital period distribution. If this feature is detected in the observed WD+MS orbital period distribution, it would strongly corroborate the DMB model.

Our comprehensive analysis between the theoretical and observed PCEB populations shows that an $\alpha_{\rm CE} > 0.1$ and an initial mass ratio distribution favouring small mass ratios, $q < 1$, best reproduces the observed PCEB distribution, and the observed local space density. Finally, we reconstruct the CE phase for the observed PCEBs and investigate any dependence of $\alpha_{\rm CE}$ on the secondary mass and the orbital period of the PCEB. Indeed, this may shed light into the CE ejection mechanism.

Acknowledgements

I must first extend my sincere thanks to my Ph. D. supervisor, Ulrich Kolb, for the excellent and unstinting support he has given me over the course of my Ph. D. His patient and enthusiastic encouragement and guidance have been an inspiration. I would also like to thank Bart Willems, whose guidance and contributions to both the BiSEPS code and the research contained within this thesis, is very much appreciated. My other collaborators, Boris Gänsicke and John Barker also deserve much thanks.

I'd also like to thank my examiners, Christian Knigge and Simon Clark, for an enjoyable, constructive and productive four-hour viva. Christian's subsequent guidance, specifically with the bootstrapping techniques used in Chapter 8, is also very much appreciated.

I am also very grateful to the Open University Physics and Astronomy Department, particularly Robin Barnard and Jonti Horner who have helped me out. I'd also like to thank my friends, both in the Physics and Astronomy Department, and in the Planetary Science and Space Institute, for the laughs, endless games of Halo and just for a generally fun four years.

Finally, I'd like to thank my family who have offered me tremendous support throughout the past few years, and who have always believed I could do it...

PART I

Background and Context

1

Introduction

Observing our lonesome Sun, one could be forgiven for inferring that this isolated state graces the majority of stars within our Galaxy. On the contrary, the single status of the Sun is an exception, rather than the rule. As a consequence of the fragmentation process which occurs during the isothermal collapse of a star-forming giant molecular cloud, a cluster of stars will be produced, each one under the gravitational influence of its neighbours. Theoretical modelling of star-forming processes indeed estimate that approximately 70 per cent of stars should have a close companion (Bate et al. 2003), which is also supported observationally. Duchêne (1999) finds that approximately 60 per cent of stars are typically found in binary systems.

Such multiple star systems constitute two or more stars orbiting about one common centre of mass. However, systems containing more than two stars tend to be gravitationally unstable, with stars being prone to ejection from the system. Subsequent ejections will eventually leave the most stable configuration: a binary star system.

A graphical illustration of a binary system is shown in Figure 1.1, which shows two stars of masses M_1 and M_2 orbiting about a common centre of mass (shown as the black cross) with an orbital period $P_{\rm orb} = 2\pi/\Omega$, where Ω is the orbital angular frequency. Throughout the thesis, we adopt the convention that the initially more massive star (i.e. on the zero-age main sequence, or ZAMS) is called the primary star, while its less massive companion is

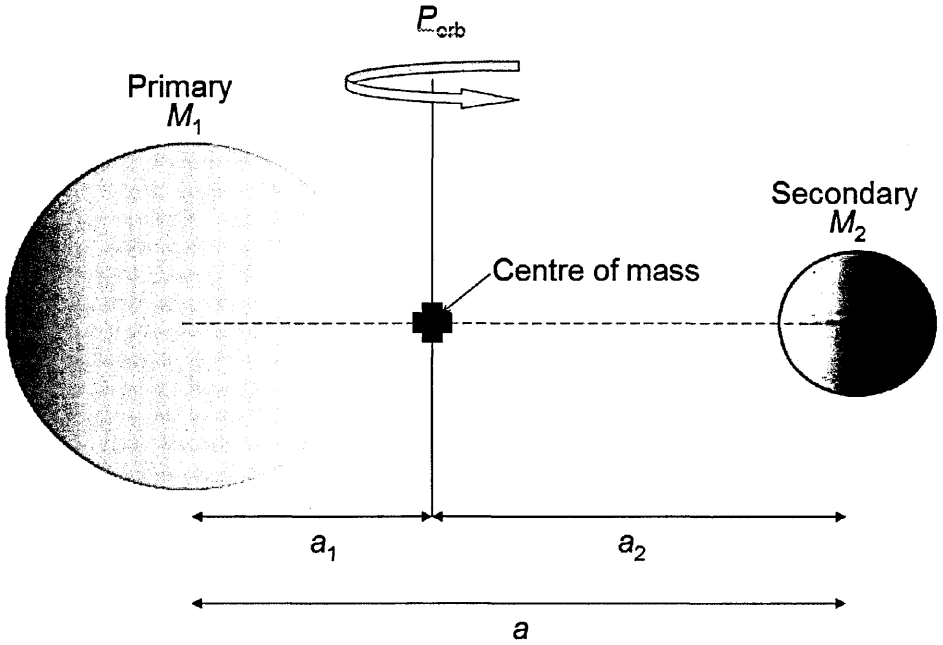

Figure 1.1: An illustration of a binary system (looking into the orbital plane) with a primary star of mass M_1, and a secondary star of mass M_2, orbiting about the common centre of mass with an orbital period $P_{\rm orb}$. The distance from the centres of the primary and secondary stars to the common centre of mass is a_1 and a_2 respectively, with the orbital separation between the centres of the two stellar components given by $a = a_1 + a_2$.

called the secondary star.

The distance from the centre of the primary star to the common centre of mass, a_1, is given by

$$a_1 = a\mu_2, \tag{1.1}$$

where

$$\mu_2 \equiv \frac{M_2}{M_1 + M_2}. \tag{1.2}$$

Similarly, the distance from the centre of the secondary star to the centre of mass is given by

$$a_2 = a\mu_1, \tag{1.3}$$

where

$$\mu_1 \equiv \frac{M_1}{M_1 + M_2}. \tag{1.4}$$

Thus, the total orbital separation between the centres of the primary and secondary is $a = a_1 + a_2$.

If the orbital period of a binary system is sufficiently long, then the two stellar components will evolve as though they were two isolated stars with no interaction between them. Indeed, Willems & Kolb (2004) find non-interacting systems with initial $P_{\rm orb} \gtrsim 10^3$ days.

On the other hand, given sufficient proximity between the two stellar components, interactions beyond the usual gravitational attraction may occur. This may take the form of mass transfer between the two stars, either as a stellar wind, or by the removal of the outer layers of one of the stars due to the gravitational influence of the companion. A well studied example of a binary which undergoes the latter case of mass transfer is the cataclysmic variable (CV). This is a compact binary which contains a white dwarf which accretes material from a main sequence star donor.

In this chapter, we begin by discussing in detail how mass transfer occurs in the context of the Roche model, followed by a discussion of the mechanisms which drive mass transfer. Next, we discuss a quantitative description of mass transfer timescales and stability. Finally, we describe the theoretical framework which describes the evolution of the binary parameters as a result of mass transfer.

The structure of the rest of the thesis is as follows. In Chapter 2 we describe the orbital period distribution of the observed sample of CVs, and discuss the standard evolutionary picture which attempts to explain the different features of this orbital period distribution. For the purpose of this thesis, we concentrate on a feature within the orbital period distribution coined the period gap; a dearth of observed CVs with orbital periods in the range $2 \lesssim P_{\rm orb}/{\rm hours} \lesssim 3$ which is explained via the disrupted magnetic braking hypothesis. We intend to devise a simple and robust test for this hypothesis. In Chapter 3, we then move on to describe how compact binaries, specifically CVs, form via the common envelope phase. In this chapter we discuss in detail our current understanding of how the common envelope phase occurs, how it ultimately terminates, and the different attempts to model it.

In Chapter 4 we describe the technique of population synthesis, and the code that we use, called BiSEPS. For the purpose of our test of the disrupted magnetic braking hypothesis, where we employ our population synthesis technique, we describe the significant modifications made to the BiSEPS code in Chapter 5. The results of this investigation are discussed in Chapter 6. Much of the material presented in Chapters 5 and 6 has been published in

Davis et al. (2008).

The remainder of the thesis is then devoted to the population synthesis study of white dwarf-main sequence star binaries which have formed from a common envelope phase; the precursors to CVs. The method we employ is described in Chapter 7, and the results of this investigation are presented in Chapter 8. The work presented in Chapters 7 and 8 has been accepted for publication in (Davis et al. 2009) (in press).

Finally, we conclude the thesis with a summary of the work, and present possible future directions, in Chapter 9.

1.1 Mass Transfer In Binary Systems

1.1.1 The Roche Model

As stated above, given a sufficiently large orbital separation of the binary system, the stellar components will evolve as though they were isolated, field stars. By sufficiently decreasing the orbital separation, however, a point will be reached where the gravitational attraction of one of the stars upon the outer layers of its companion will become non-negligible and will dominate over the gravitational attraction of the star's own outer layers towards its centre of mass. At this point these outer layers flow from one star to the other. In this section we shall describe such mass transfer in more detail.

Figure 1.2 shows a set of Cartesian axes, with the origin centred upon the centre of mass of the primary star, which is co-rotating with the binary, and so has an orbital period of $P_{\rm orb}$. The secondary star is therefore located at $(a, 0, 0)$ along the x-axis. We now imagine a test particle with infinitesimal mass located at (x, y, z), which is at a distance $\underline{r}_1$ from the centre of the primary, and a distance $\underline{r}_2$ from the centre of the secondary.

Not only will the test particle experience the gravitational attraction due to the two stellar components, but it will also experience a centrifugal force acting away from the axis of rotation. Thus, the test particle will experience a total potential, $\Phi_{\rm R}$, given by

$$\Phi_{\rm R} = -\frac{GM_1}{(x^2+y^2+z^2)^{1/2}} - \frac{GM_2}{[(x-a)^2+y^2+z^2]^{1/2}} - \frac{1}{2}\Omega^2[(x-\mu_2 a)^2+y^2], \qquad (1.5)$$

where we have used $\underline{r}_1 = (x^2+y^2+z^2)^{1/2}$ and $\underline{r}_2 = [(x-a)^2+y^2+z^2]^{1/2}$ [e.g. Warner (1995)] and G is the gravitational constant. Thus, the first two terms on the right hand side

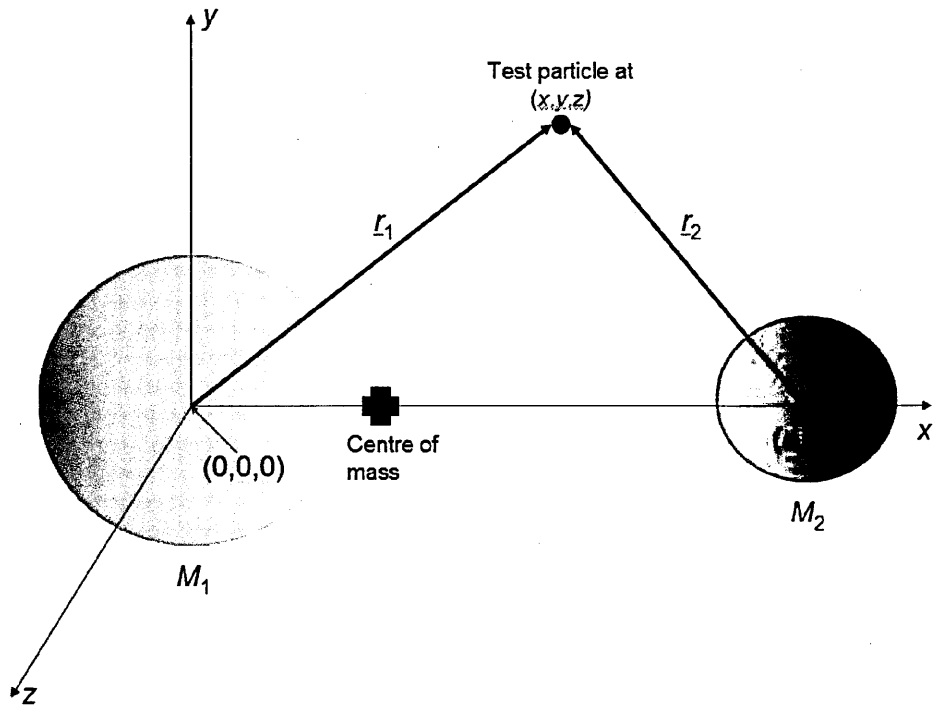

Figure 1.2: A binary system viewed into the orbital plane, with a set of Cartesian axes where the origin is located at the centre of mass of the primary star, and where the secondary star is located at $(a, 0, 0)$. Also shown is the location of a test particle with infinitesimal mass, located at (x, y, z), which is at a distance r_1 from the centre of the primary, and a distance r_2 from the centre of the secondary. The stellar components are orbiting about the common centre of mass indicated by the black cross.

of equation (1.5) give the gravitational potential experienced by the test particle due to the primary and secondary star respectively. The third term on the right hand side of equation (1.5) gives the centrifugal potential experienced by the test particle. The quantity Φ_R is called the Roche potential. The left of Figure 1.3 (Frank et al. 2002) shows the surface representing the potential Φ_R for a binary with a mass ratio $q = M_2/M_1 = 1/4$. The potential wells of each of the stellar components can clearly be seen. The downward slope towards the edges of the surface is due to the centrifugal term in equation (1.5) becoming more dominant as the distance from the stellar components increases.

The derivation of equation (1.5) makes the assumption that the stellar components can be treated like point masses. Pringle & Wade (1985) indeed find that this is an excellent approximation, as most stars for a wide range of evolutionary stages are centrally condensed.

Secondly, is is assumed that the binary orbit is circular, and that the mass losing secondary is rotating synchronously with the binary orbit, i.e. the spin frequency of the donor

is, $\omega = \Omega$ [1]. Again, this is an excellent approximation, which we will now briefly show in the context of CVs.

Consider a white dwarf-main sequence binary before the onset of mass transfer, which has an eccentric orbit, and a secondary star which is rotating asynchronously with the binary orbit. Due to the gravitational attraction of the companion white dwarf, tidal bulges will be raised on the surface of the secondary star. As a result of viscosity in the convective envelopes of secondary stars with masses $M_2 \lesssim 1.2$ $M_\odot$, or within radiative envelopes for those secondaries with $M_2 > 1.2$ $M_\odot$, (Zahn 1966), the tidal bulge does not face the white dwarf companion, but rather the bulge will lead the orbital motion if $\omega > \Omega$ or lag behind if $\omega < \Omega$. There will therefore be a gravitational attraction between the tidal bulges of the secondary star and the white dwarf, producing a torque upon the spin of the secondary star.

If $\omega > \Omega$, then the gravitational torque will act to spin down the secondary's rotation. Conversely, if $\omega < \Omega$, then the gravitational torque will act to spin up the secondary's rotation. Note that this torque is proportional to the term $|\omega - \Omega|$ which will decrease as it spins the star up (or down) until synchronism is reached and $\omega = \Omega$, and no further torque is applied to the secondary star. The time scale by which synchronicity is achieved, $\tau_{\rm sync}$, is given by (Zahn 1977)

$$\tau_{\rm sync} \approx 10^4 \text{ years} \left(\frac{1+q}{2q}\right)^2 \left(\frac{P_{\rm orb}}{\text{days}}\right)^4 . \tag{1.6}$$

Typically, $q < 1$ and $P_{\rm orb} \lesssim 1$ day for CV progenitors. Thus, from equation (1.6) we can expect that $\tau_{\rm sync} \approx 10^4$ years. This is significantly shorter than the lifetime of the binary, and hence we can expect the secondary to be rotating synchronously by the time mass transfer commences.

The turbulent flows within the secondary's convective envelope will dissipate energy. This will act to circularise the orbit, as this is the lowest energy configuration for a given value of the binary's angular momentum. The circularisation timescale, $\tau_{\rm circ}$, (in years) is given by (Zahn 1977)

$$\tau_{\rm circ} \approx \frac{10^6 \text{ years}}{q} \left(\frac{1+q}{2}\right)^{5/3} \left(\frac{P_{\rm orb}}{\text{days}}\right)^{16/3} . \tag{1.7}$$

For typical CV progenitors, we can expect that $\tau_{\rm circ} \approx 10^6$ years. Again, this is much shorter than the lifetime of such binaries. Binary systems in general are indeed found to

[1] In general, the white dwarf is not in synchronous rotation with the binary orbit. However, this has a negligible effect on the Roche potential

have circular orbits, for orbital periods $P_{\rm orb} \lesssim 8$ days (Hilditch 2001). As CVs typically have orbital periods $P_{\rm orb} \lesssim 12$ hours, we can therefore expect CVs to have circular orbits by the time they commence mass transfer. Thus, the Roche model is indeed a valid model for the case of CVs as also demonstrated by Rezzolla et al. (2001).

The right of Figure 1.3 (Frank et al. 2002) shows contours of $\Phi_{\rm R}$ in the orbital plane for a binary system with a mass ratio $q = 1/4$. The labels 1 to 7 indicate the values of $\Phi_{\rm R}$, in order of increasing $\Phi_{\rm R}$. Close to each of the stellar centres the equipotential surfaces are close to circular, as the force of attraction due to the star dominates. Further away from the centres, however, the equipotentials become distorted along the line joining the centres of the two stars, due to the increasing gravitational influence of the second star. Of key significance are the two equipotential surfaces which touch, forming a 'figure of eight' configuration. This is shown in the right of Figure 1.3 as the thick bold line.

These equipotentials are called Roche lobes, and define the maximum volume that a star can inhabit before material falls into the potential well of its companion. For the case of a fluid which has a velocity, $\underline{v}$, relative to the rotating frame, density ρ and pressure P, the Euler equation gives

$$\frac{\partial \underline{v}}{\partial t} + (\underline{v} \cdot \nabla)\underline{v} = -\nabla\Phi_{\rm R} - 2\underline{\Omega} \wedge \underline{v} - \frac{1}{\rho}\nabla P. \tag{1.8}$$

As material in the outer layers of each of the stellar components is rotating synchronously with the binary orbit, we have $\underline{v} = 0$. Thus equation (1.8) reduces to

$$-\nabla\Phi_{\rm R} = \frac{1}{\rho}\nabla P. \tag{1.9}$$

The equipotential surfaces therefore coincide with surfaces of constant pressure. In other words, the shapes of the equipotential surfaces dictate the shapes of the stars. A Roche lobe-filling star becomes elongated along the line joining the centres of the two stars, and compressed perpendicular to this line. The point at which the two Roche lobes of each star touch is a saddle point in $\Phi_{\rm R}$, and is called the inner Lagrangian, or L1, point. This is also shown in the right of Figure 1.3, along with the four other Lagrangian points, labelled L2 to L5. A Roche lobe-filling star can be likened to a punctured container, where the puncture is analogous to the L1 point, through which material is escaping with a speed on the order of the sound speed of the material.

The radius of the secondary's Roche lobe, $R_{\rm L,2}$, is the radius of a sphere which has the same volume as the Roche lobe. Commonly used expressions to evaluate the Roche lobe of

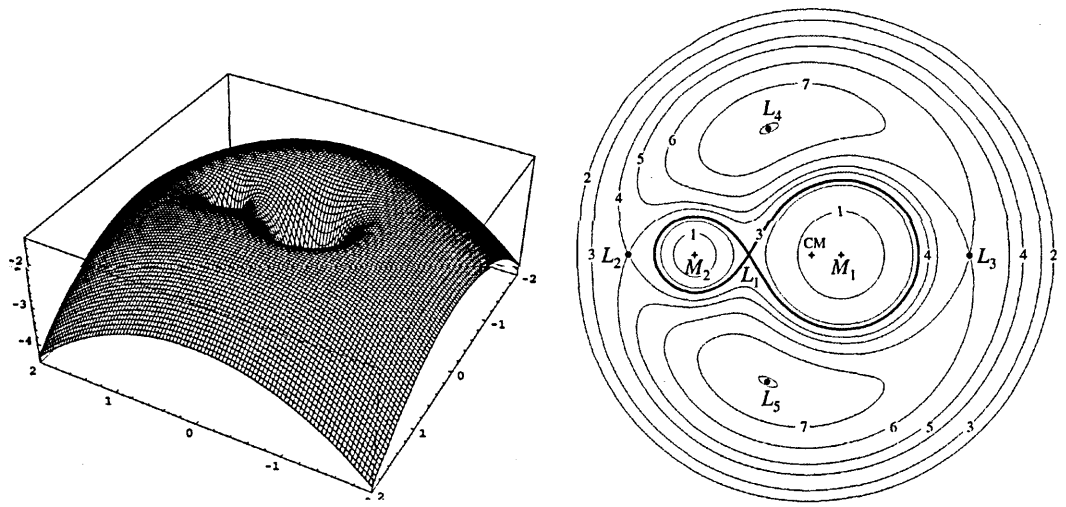

Figure 1.3: Left: surface of the potential Φ_R for a binary with a mass ratio $q = M_2/M_1 = 1/4$. Note the two potential wells of each of the stellar components. The downward slope towards the edges of the surface is due to the centrifugal term in equation (1.5). Right: Roche equipotentials on the plane of the orbit for a binary system with a mass ratio $q = 1/4$. Also shown is the centre of mass of the binary (CM) and the Lagrangian points L1 to L5. The equipotentials shown in bold are the Roche lobes of the stellar components. The numbers 1 to 7 indicate the height of the equipotentials, in order of increasing Φ_R. Both figures are from Frank et al. (2002).

the secondary are given by (Paczyński 1971)

$$R_{L,2} \approx 0.462 \left(\frac{q}{1+q}\right)^{1/3} a, \tag{1.10}$$

which is accurate to 2 per cent for $0.1 < q < 0.8$, and (Eggleton 1983)

$$R_{L,2} = \frac{0.49q^{2/3}}{0.6q^{2/3} + \ln(1+q^{1/3})} a. \tag{1.11}$$

Equation (1.11) is accurate to better than 1 per cent for mass ratios $0 < q < \infty$. Clearly, to find the Roche lobe radius of the primary star, $R_{L,1}$, we replace q with $1/q$ in equation (1.11) [2].

We will now show that, as a good approximation, the orbital period at which mass transfer is occurring in a CV is dictated mainly by the average density of the donor star. Combining equation (1.10) with Kepler's Third Law gives

$$P_{orb} \propto \left(\frac{R_2^3}{M_2}\right)^{1/2}. \tag{1.12}$$

[2]We cannot apply the same scheme using equation (1.10) as $1/q > 1$, and so equation (1.10) is not sufficiently accurate in this regime.

As low-mass main sequence stars follow the approximate mass-radius relation $R_2 \sim M_2$, we can relate the orbital period (in hours) to the mass of the donor star (in solar masses) given by [e.g. King (1988)]

$$\frac{P_{\rm orb}}{\rm hours} \approx 9.1 \frac{M_2}{\rm M_\odot}. \tag{1.13}$$

1.1.2 Driving Mass Transfer

For mass loss to occur, the star must fill its Roche lobe. This can happen either because the radius of the star in question is increasing as a result of evolution, or because the Roche lobe is shrinking around the star.

If we consider the former case, we can distinguish between three phases of mass transfer depending on the evolutionary state of the star. Mass transfer which occurs as a result of the star evolving away from the ZAMS (but still in the core hydrogen burning phase) constitutes case A mass transfer. If mass transfer is occurring as a result of the star's evolution as it approaches or ascends the first giant branch (but before the onset of core helium burning), then this is termed case B mass transfer. Finally, we have case C mass transfer if the star fills its Roche lobe while ascending the asymptotic giant branch after core helium burning has finished.

In the latter scenario, on the other hand, mass transfer can commence if the Roche lobe radius decreases around the star as a result of orbital angular momentum being lost from the binary orbit. This will cause the orbital separation to decrease and hence, from equations (1.10) or (1.11), will cause the radius of the Roche lobe to decrease.

Any of these scenarios which will cause the donor star to over-fill its Roche lobe, i.e. $R_2 \gtrsim R_{\rm L,2}$, will result in mass being instantaneously lost from the donor star at a rate $-\dot{M}_2$, until $R_2 < R_{\rm L,2}$. Mass transfer will only continue by further radial expansion of the donor star due to nuclear evolution, or further shrinking of the binary's orbit. For a main sequence CV donor with an atmospheric scale height of $H_{\rm p} \approx 10^{-4} R_2$, the instantaneous mass transfer rate is given by

$$-\dot{M}_2 = \dot{M}_0 \exp\left(-\frac{R_{\rm L,2} - R_2}{H_{\rm p}}\right), \tag{1.14}$$

(Ritter 1988) where $\dot{M}_0 \approx 10^{-8}$ M$_\odot$ yr^{-1}, i.e. the mass transfer rate when the donor star exactly fills its Roche lobe. Thus, the mass transfer rate is a sensitive function of the amount that the donor star overfills (or just under-fills) its Roche lobe, i.e. the quantity $R_2 - R_{\rm L,2}$.

Any perturbations during the mass transfer process which will cause the donor's Roche lobe to move through the photosphere of the star will cause variations of $\dot{M}_2$ with time. The time derivative of equation (1.14) gives

$$\ddot{M}_2 = \frac{\dot{M}_2}{H_\mathrm{p}}(\dot{R}_2 - \dot{R}_{\mathrm{L},2}) \approx \frac{\dot{M}_2 R_2}{H_\mathrm{p}}\left(\frac{\dot{R}_2}{R_2} - \frac{\dot{R}_{\mathrm{L},2}}{R_{\mathrm{L},2}}\right). \tag{1.15}$$

In the approximation given in equation (1.15), we have made the assumption that $R_2 \approx R_{\mathrm{L},2}$. This is a good approximation because the photospheric scale height is only ≈ 0.01 per cent of the donor's radius. Therefore, for any mass transfer to occur at all we need $R_{\mathrm{L},2} \approx R_2$.

For the same reason, we can expect any variations in the mass transfer rate with time, $\ddot{M}_2$, to be negligible over the evolutionary timescale of the CV, which is on the order of the mass loss timescale, $\tau_{\dot{M}} \equiv M_2/\dot{M}_2 \approx 10^8$ to 10^9 years [e.g. King (1988)]. Indeed, the value of $\dot{M}_2$ will be rapidly adjusted on the timescale $t_{\ddot{M}} = \dot{M}_2/\ddot{M}_2$. Whether any change in $\dot{M}_2$ over time will destabilize or be quenched will depend on the sign of the terms in the parentheses in equation (1.15). Using the approximate form of equation (1.15), and noting that the term in the parenthesis is approximately given by $1/\tau_{\dot{M}}$ (see Section 1.2.2), then we have

$$t_{\ddot{M}} = \frac{H_\mathrm{p}}{R_2}\tau_{\dot{M}}. \tag{1.16}$$

Hence, we find $t_{\ddot{M}} \approx 10^4$ and 10^5 years (King et al. 1996). For CVs, we can therefore make the approximation that mass transfer is stationary, i.e. $\ddot{M}_2 \approx 0$. From equation (1.15), we find that for stationary mass transfer

$$\frac{\dot{R}_2}{R_2} = \frac{\dot{R}_{\mathrm{L},2}}{R_{\mathrm{L},2}}, \tag{1.17}$$

and hence the donor's stellar and Roche lobe radius move in step.

1.1.3 Mass Transfer Stability

The timescale on which the resulting mass transfer will occur depends on the internal structure of the mass-losing star. This in turn dictates how the star will react to mass loss. Firstly, mass loss can perturb the star's hydrostatic equilibrium. If the structure of the star with an average density $\langle\rho\rangle$ is perturbed, then it will re-establish hydrostatic equilibrium on the dynamical timescale, τ_dyn, given by

$$\tau_\mathrm{dyn} \approx (G\langle\rho\rangle)^{-1/2} \approx 40\left(\frac{\langle\rho_\odot\rangle}{\langle\rho\rangle}\right)^{1/2} \text{ minutes}, \tag{1.18}$$

where $\langle \rho_{\odot} \rangle$ is the average density of the Sun. Alternatively, if the thermal structure of the star with mass M, radius R and luminosity L is perturbed, i.e. it is driven out of thermal equilibrium, then thermal equilibrium will be re-established on the Kelvin-Helmholtz timescale, $\tau_{\rm KH}$, according to

$$\tau_{\rm KH} \approx \frac{GM^2}{RL} \approx 3 \times 10^7 \left(\frac{M}{M_{\odot}}\right)^2 \frac{R_{\odot}}{R} \frac{L_{\odot}}{L} \text{ years}, \tag{1.19}$$

where $R_{\odot}$ and $L_{\odot}$ is the radius and the luminosity of the Sun respectively. Finally, if the structure of the star is changing, specifically its radius, as a result of nuclear evolution during its main sequence lifetime, then this change will occur over the star's main sequence lifetime, $\tau_{\rm MS}$, given by

$$\tau_{\rm MS} \approx 10^{10} \left(\frac{M}{\rm M_{\odot}}\right)^{-3} \text{ years}. \tag{1.20}$$

Generally, $\tau_{\rm dyn} << \tau_{\rm KH} << \tau_{\rm MS}$.

We can determine the timescale over which mass loss will occur by examining how the donor's stellar and Roche lobe radius change as a result of mass transfer. As an example, consider a star which initially has a radius R_0 and mass M_0, which fills its Roche lobe radius $R_{\rm L,0}$ and consequently loses an amount of mass δM in a time interval δt. In order to determine whether mass transfer is stable or not, we need to compare the new values of the donor's stellar and Roche lobe radius, $R(M_0 - \delta M)$ and $R_{\rm L}(M_0 - \delta M)$ respectively. If we have $R(M_0 - \delta M) < R_{\rm L}(M_0 - \delta M)$, such that the donor star is within its Roche lobe, then mass loss is stable and will resume either by continual expansion of the donor star's radius as a result of nuclear evolution, or due to the continual shrinkage of the Roche lobe. If, however, $R(M_0 - \delta M) > R_{\rm L}(M_0 - \delta M)$, causing the donor to fill its Roche lobe even further, then the resulting mass transfer is unstable because further mass loss from the star continues to increase its radius beyond the Roche lobe radius.

To describe the reaction of the Roche lobe radius due to mass loss, we follow Webbink (1985) and define the Roche lobe index, $\zeta_{\rm L}$, as

$$\zeta_{\rm L} \equiv \frac{{\rm d}\ln R_{\rm L}}{{\rm d}\ln M}. \tag{1.21}$$

Similarly, we can describe the reaction of the donor's radius to mass loss for the case where the donor reacts adiabatically, such that its entropy profile is constant. For this Webbink (1985) define the adiabatic mass-radius exponent, $\zeta_{\rm ad}$, given by

$$\zeta_{\rm ad} \equiv \left(\frac{{\rm d}\ln R}{{\rm d}\ln M}\right)_S, \tag{1.22}$$

where the subscript S denotes that a constant entropy profile of the star is assumed. Finally, the reaction of the donor's radius to mass loss if it is in thermal equilibrium is given by the equilibrium mass-radius exponent, $\zeta_{\rm eq}$, according to (Webbink 1985)

$$\zeta_{\rm eq} \equiv \left(\frac{{\rm d}\ln R}{{\rm d}\ln M}\right)_{\rm eq}, \tag{1.23}$$

where the subscript 'eq' denotes the donor star is in thermal equilibrium. For example, for the case of a main sequence star in thermal equilibrium, $\zeta_{\rm eq} \approx 1$.

Using the exponents given by equations (1.21) to (1.23), we can give the criteria required for mass transfer to be dynamically or thermally unstable. In dynamically unstable mass transfer, the donor star is expanding relative to its Roche lobe on a dynamical time. Thus, the criterion for dynamically unstable mass transfer is given by

$$\zeta_{\rm L} > \zeta_{\rm ad}. \tag{1.24}$$

If, on the other hand, mass loss occurs on the thermal timescale of the donor star, then because $\tau_{\rm dyn} << \tau_{\rm KH}$, the donor's hydrostatic equilibrium is maintained, and so we have $\zeta_{\rm L} < \zeta_{\rm ad}$. As mass transfer occurs due to the thermal dis-equilibrium of the donor star, which causes the donor star to expand relative to its Roche lobe on a thermal timescale, then $\zeta_{\rm L} > \zeta_{\rm eq}$. The criteria for thermally unstable mass transfer is therefore given by

$$\zeta_{\rm eq} < \zeta_{\rm L} < \zeta_{\rm ad}. \tag{1.25}$$

Finally, we can give a criterion for cases where mass transfer is both dynamically and thermally stable, i.e. mass loss from the donor causes it to shrink within its Roche lobe. Only evolution of the donor, or the shrinking of the Roche lobe, can maintain mass transfer. In this case we have

$$\zeta_{\rm L} < {\rm MIN}(\zeta_{\rm ad}, \zeta_{\rm eq}). \tag{1.26}$$

On what timescale can we expect mass transfer to occur in CVs? Figure 1.4 shows the values of $\zeta_{\rm ad}$ (dashed line) and $\zeta_{\rm th}$ (solid line) as a function of donor mass. The right hand axis gives the critical mass ratio $q(\zeta)$ for which $\zeta_{\rm L} = \zeta_{\rm ad}$ or $\zeta_{\rm L} = \zeta_{\rm eq}$. Thus, $q(\zeta_{\rm ad})$ and $q(\zeta_{\rm eq})$ gives the mass ratios for which mass transfer is just dynamically and thermally stable respectively. The typical mass ratio of CVs is $0.1 \lesssim q \lesssim 1$ with $M_2 \lesssim 1$ M$_\odot$. Hence, $q < q(\zeta_{\rm eq})$ and $q < q(\zeta_{\rm ad})$, and therefore we can expect such CVs to undergo thermally and dynamically stable mass transfer. Clearly, this is somewhat of a selection effect, as systems which undergo dynamically or thermally unstable mass transfer will not appear as CVs, but as another variety of compact binary with different observed characteristics.

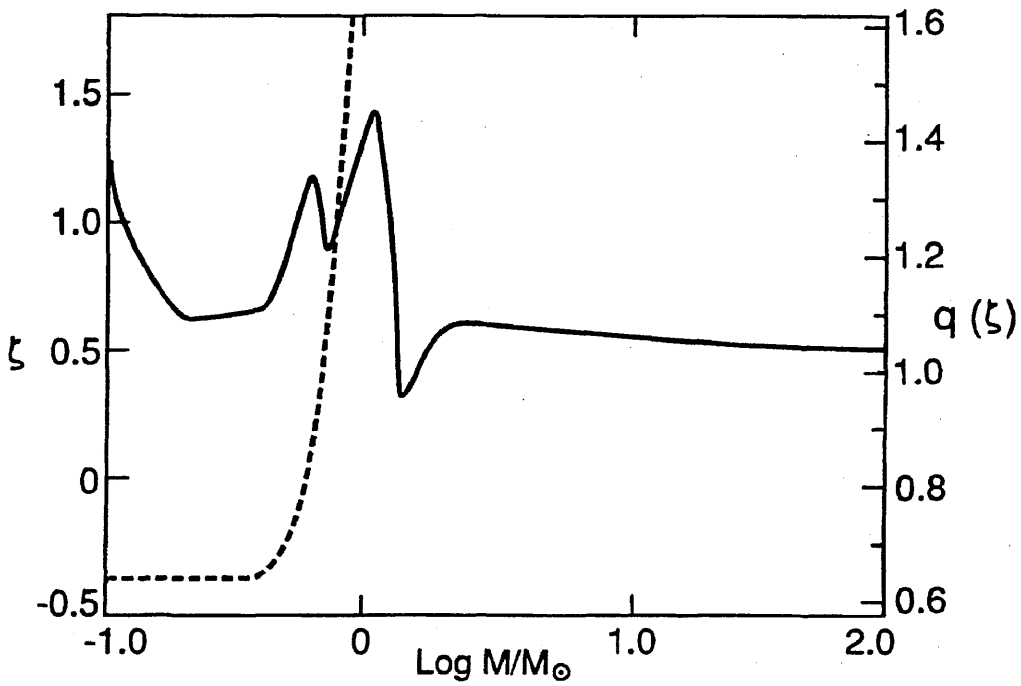

Figure 1.4: The values of the mass-radius exponents $\zeta_{\rm ad}$ (dashed line) and $\zeta_{\rm eq}$ (solid line) as a function of the donor mass, M (Hjellming 1989). The right axis of the plot shows the critical mass ratio, $q(\zeta)$, for which $\zeta_{\rm L} = \zeta$ assuming that mass transfer is conservative [adapted from Politano (1996)].

Indeed, closely related systems which have secondaries with $M_2 \gtrsim 1$ M$_\odot$, and that have significantly evolved away from the main sequence, will undergo thermally unstable mass transfer at rates of approximately 10^{-7} M$_\odot$ yr^{-1}. This mass transfer rate is sufficiently high to induce steady hydrogen burning on the surface of the accreting white dwarf. Such systems are significant sources of supersoft x-rays [see e.g. Schenker et al. (2002)].

Mass transfer in CVs is a result of either nuclear evolution of the secondary star, or because the secondary's Roche lobe is shrinking around it. As donor stars in CVs are observed to be main sequence stars [e.g. Beuermann et al. (1998); Baraffe & Kolb (2000)] mass transfer is unlikely to be a result of nuclear evolution of the donor. Indeed, we can estimate the mass transfer rate in a CV, $\dot{M}_2$, by first assuming that mass transfer is driven as a result of the donor's nuclear evolution, by using $-\dot{M}_2 \sim M_2/\tau_{\rm nuc}$. As donor stars in CVs typically have $M_2 \lesssim 1$ M$_\odot$, then their main sequence lifetimes are $\tau_{\rm nuc} \gtrsim 10^{10}$ years. This gives $-\dot{M}_2 \lesssim 1 \times 10^{-10}$ M$_\odot$ yr^{-1}. However, CVs with $P_{\rm orb} \gtrsim 3$ hours are observed to

have $-\dot{M}_2 \approx 10^{-8}$ to 10^{-9} $M_\odot$ yr^{-1} [e.g. Patterson (1984)].

The most likely explanation for mass transfer in CVs is that the donor's Roche lobe radius is shrinking around it. Indeed, any mass transfer that occurs within a binary system will result in a re-distribution of angular momentum within that binary, further causing the binary's orbital separation to change. As we have seen from equations (1.10) and (1.11), any change in the orbital separation of the binary will result in a change in the radius of the Roche lobes of each of the stellar components. We will therefore describe the evolution of the binary star as a consequence of mass transfer in more detail in the next section.

1.2 Evolution of the Binary Parameters

1.2.1 Orbital Parameters

We begin by considering the total angular momentum of the binary system. This is the sum of the spin angular momenta of the primary, $J_{\rm spin,1}$, and secondary, $J_{\rm spin,2}$, as well as the orbital angular momenta of the primary and secondary about the common centre of mass, given by $J_{\rm orb,1}$ and $J_{\rm orb,2}$ respectively. The total angular momentum of the binary, J is therefore given by

$$\begin{aligned} J &= J_{\rm orb,1} + J_{\rm orb,2} + J_{\rm spin,1} + J_{\rm spin,2} \\ &= M_1 a_1^2 \Omega + M_2 a_2^2 \Omega + I_1 \omega_1 + I_2 \omega_2, \end{aligned} \tag{1.27}$$

[e.g. Tout & Hall (1991)] where I_1 and I_2 are the moments of inertia of the primary and secondary stars respectively, and ω_1 and ω_2 are the respective angular spin frequencies of the primary and secondary stars. Typically, the total spin angular momentum due to both stellar components is between 1 and 2 per cent of the binary's orbital angular momentum (Hilditch 2001), and hence we can neglect the spin angular momentum of the two stars. Even if one of the stellar components is a red giant, its spin angular momentum is ≈ 4 per cent of the binary's orbital angular momentum. We can therefore also neglect the spin angular momentum of such evolved stellar components [e.g. Tout & Hall (1991)]. Using equations (1.1) and (1.3), we get for the total angular momentum of the binary:

$$J = M_1 M_2 \left(\frac{Ga}{M_1 + M_2} \right)^{1/2}. \tag{1.28}$$

Taking the time derivative of equation (1.28) gives

$$\frac{\dot{J}}{J} = \frac{\dot{M}_1}{M_1} + \frac{\dot{M}_2}{M_2} + \frac{\dot{a}}{2a} - \frac{\dot{M}_1 + \dot{M}_2}{M_1 + M_2}, \tag{1.29}$$

which now relates the evolution of the binary's angular momentum to the masses of the stellar components, and the orbital separation between their centres.

We are now in a position to express the evolution of the binary's orbital separation, $\dot{a}/a$, in terms of the re-distribution of mass in the binary system. To illustrate this, we consider a case of binary evolution where the mass transfer, and hence the angular momentum of the binary, is conserved. That is to say, no mass or angular momentum is lost from the system, i.e. $\dot{M}_1 = -\dot{M}_2$ and $\dot{J} = 0$, where mass loss is occurring from the secondary star. Equation (1.29) therefore leads to

$$\frac{\dot{a}}{a} = -\frac{2\dot{M}_2}{M_2}(1 - q). \tag{1.30}$$

Thus, the orbital separation decreases if the mass losing secondary is more massive than the primary ($q > 1$), or expansion of the orbital separation if the mass losing secondary is less massive than the primary ($q < 1$). Note that from equations (1.10) or (1.11), this will give rise to a corresponding expansion or contraction of the Roche lobe radius of the donor star. First, by taking the time derivative of equation (1.10) we get

$$\frac{\dot{R}_{\mathrm{L},2}}{R_{\mathrm{L},2}} = \frac{1}{3}\frac{\dot{M}_2}{M_2} - \frac{1}{3}\frac{\dot{M}_1 + \dot{M}_2}{M_1 + M_2} + \frac{\dot{a}}{a}, \tag{1.31}$$

where we used $q = M_2/M_1$. Combining equations (1.30) and (1.31) gives

$$\frac{\dot{R}_{\mathrm{L},2}}{R_{\mathrm{L},2}} = -\frac{2\dot{M}_2}{M_2}\left(\frac{5}{6} - q\right). \tag{1.32}$$

[e.g. King (1988)]. We argued in the previous section that the most likely reason for mass transfer in CVs is the shrinking of the donor's Roche lobe. However, in the case of compact binaries such as CVs, we have $q < 5/6$, and therefore from equation (1.32) fully conservative mass transfer (with $\dot{J} = 0$ and $\dot{M}_1 + \dot{M}_2 = 0$) in CVs will result in the expansion of the donor's Roche lobe radius. Furthermore, as mass loss from the donor is likely to be dynamically and thermally stable (Section 1.2.3), any removal of matter from the donor star will result in a decrease in the donor's radius appropriate for its new mass. This effect, combined with the expansion of the donor's Roche lobe radius will result in the immediate shut-off of mass transfer [e.g. Patterson (1984)]. Yet CVs with mass ratios as low as $q < 0.1$ have been observed (Littlefair et al. 2008)]. Clearly, some other mechanism must be at work to enforce the shrinkage of the donor's Roche lobe, and ensure long-term mass transfer in CVs. As

noted above, this mechanism is unlikely to be a result of expansion of the donor star due to nuclear evolution.

On the other hand, a shrinking Roche lobe radius can be maintained if angular momentum is being lost from the binary, i.e. $\dot{J}/J < 0$. There are two causes which may give rise to this. The first are systemic losses which remove angular momentum from the binary without (appreciable) mass loss from the binary. The second cause is consequential angular momentum loss, which is the removal of angular momentum from the binary due to mass loss from the system (King & Kolb 1995). However, consequential angular momentum losses only occur when there are systemic angular momentum losses driving mass transfer in the first place. Thus, $\dot{J}/J$ in equation (1.29) is the combination of the angular momentum removed from the binary orbit as a result of systemic and consequential angular momentum losses, i.e.

$$\frac{\dot{J}}{J} = \left(\frac{\dot{J}}{J}\right)_{\rm sys} + \left(\frac{\dot{J}}{J}\right)_{\rm CAML}, \tag{1.33}$$

where the subscripts 'sys' and 'CAML' refer to systemic and consequential angular momentum losses respectively.

We will now discuss the theoretical framework describing mass transfer and mass loss from the system, which will then allows us to obtain an expression giving the mass transfer rate in CVs as a result of systemic and angular momentum losses.

The conservative case previously mentioned is unlikely to be strictly realised for CVs, as material accreted onto the white dwarf may be subsequently lost from the system as a result of nova outbursts (Warner 1995), or alternatively as winds emitted from the accretion disc (Livio & Pringle 1994). This material will then carry away angular momentum from the binary's orbit. We will now follow King & Kolb (1995) and discuss the theoretical treatment for this in more detail.

If a fraction, $\alpha_{\rm CAML}$, of the material lost from the donor star via Roche lobe overflow is subsequently ejected from the binary system, then the rate of change of total mass of the binary, $\dot{M}_1 + \dot{M}_2$, can be parameterized by

$$\dot{M}_1 + \dot{M}_2 = \alpha_{\rm CAML}\dot{M}_2. \tag{1.34}$$

Hence, a fraction $1 - \alpha_{\rm CAML}$ of this material is accreted by the white dwarf, according to

$$\dot{M}_1 = (1 - \alpha_{\rm CAML})(-\dot{M}_2). \tag{1.35}$$

Any material lost from the binary system will consequently remove angular momentum from the binary's orbit. The fractional angular momentum loss rate due to the loss of material

from the system, $(\dot{J}/J)_{\rm CAML}$, can be related to the fractional mass loss rate from the donor star via Roche lobe overflow $\dot{M}_2/M_2$, by

$$\left(\frac{\dot{J}}{J}\right)_{\rm CAML} = \nu_{\rm CAML}\frac{\dot{M}_2}{M_2}, \tag{1.36}$$

where $\nu_{\rm CAML}$ is a dimensionless parameter. We can now express the mass transfer rate (strictly, the mass transfer rate averaged over the orbital evolutionary timescale of the binary of 10^8 to 10^9 years), $\dot{M}_2/M_2$, in terms of the systemic and consequential angular momentum losses. By combining equations (1.29), (1.31), (1.33), (1.35) and (1.36), and assuming that the donor's stellar and Roche lobe radius are in step during mass transfer, then we get

$$\frac{\dot{M}_2}{M_2} = \frac{1}{\mathcal{D}}\left(\frac{\dot{J}}{J}\right)_{\rm sys}, \tag{1.37}$$

where

$$\mathcal{D} \equiv \left(\frac{5}{6}+\frac{\zeta}{2}\right) - q + \alpha_{\rm CAML}\left(q - \frac{1}{3}\frac{q}{1+q}\right) - \nu_{\rm CAML}. \tag{1.38}$$

If we desire to consider the point at which mass transfer is just dynamically or thermally unstable, we can replace ζ in equation (1.38) with either $\zeta_{\rm ad}$ or $\zeta_{\rm eq}$ respectively. In general, however, ζ can take on values between the limits $\zeta_{\rm ad}$ and $\zeta_{\rm eq}$ during the course of CV evolution.

Equation (1.37) shows that it is systemic angular momentum losses which drives mass transfer in the binary, while it is consequential angular momentum losses which further enhances it, as encapsulated by the denominator, $\mathcal{D}$. As a result of consequential angular momentum losses we have $\alpha_{\rm CAML} > 0$ and $\nu_{\rm CAML} > 0$, causing a decrease in the value of $\mathcal{D}$ and an increase in the mass transfer rate. In the case of fully conservative mass transfer where $\alpha_{\rm CAML} = 0$ and $\nu_{\rm CAML} = 0$, we get

$$\mathcal{D} = \left(\frac{5}{6}+\frac{\zeta}{2}\right) - q. \tag{1.39}$$

In this case, any decrease in $\mathcal{D}$ is caused by a decrease in the mass ratio, or in the value of ζ. If $\mathcal{D}$ is decreased sufficiently such that $\mathcal{D} < 0$, then because $(\dot{J}/J)_{\rm sys}$, and therefore $\dot{M}_2/M_2$, are negative, a value $\mathcal{D} < 0$ signals unstable mass transfer.

We will now describe how the angular momentum removed from a CV as a result of nova explosions, parameterized by $\nu_{\rm CAML}$, is determined. Again we follow King & Kolb (1995). Nova explosions can be modeled as an isotropic, spherically symmetric wind emitted from the surface of the white dwarf. The wind leaves the binary system with specific orbital

angular momentum equal to that of the white dwarf, $j_{\rm WD}$, given by

$$j_{\rm WD} = a_1^2 \Omega. \tag{1.40}$$

Thus, from equations (1.1), (1.36) and (1.40) we find that

$$\nu_{\rm CAML} = \frac{M_2^2}{M_1(M_1 + M_2)}. \tag{1.41}$$

Alternatively, the angular momentum removed from a binary due to winds can be parameterized in units of the specific angular momentum of the binary system. Therefore, if material leaves a binary system with angular momentum $\eta_{\rm CAML}$ times the specific angular momentum of the binary, $J/(M_1+M_2)$, then the consequential angular momentum loss rate is given by

$$\left(\frac{\dot{J}}{J}\right)_{\rm CAML} = \eta_{\rm CAML}\frac{\dot{M}_1 + \dot{M}_2}{M_1 + M_2}. \tag{1.42}$$

(Paczyński & Ziółkowski 1967). From this prescription, the angular momentum removed from the system (in units of the specific angular momentum of the binary) due to nova explosions is given by

$$\eta_{\rm CAML} = \frac{M_2}{M_1}. \tag{1.43}$$

1.2.2 Evolution of the Donor's Stellar and Roche Lobe Radius

We will now describe quantitatively how the donor's stellar and Roche lobe radius change as a result of mass transfer, beginning with the Roche lobe radius of the donor star. The evolution of the Roche lobe radius, $\dot{R}_{\rm L,2}/R_{\rm L,2}$, occurs as a result of two factors. The first is a result of mass transfer, $(\dot{R}_{\rm L,2}/R_{\rm L,2})_{\dot{M}\neq 0}$, which will re-distribute mass and angular momentum within the system. This in turn will change both the binary mass ratio, q, and the binary's orbital separation. From equations (1.10) or (1.11), we can see that this will change the Roche lobe radii of both stellar components, although we shall only consider the change of the donor's Roche lobe radius as this ultimately impacts on the stability of the resulting mass transfer.

The second factor which effects the evolution of the donor's Roche lobe radius is due to systemic angular momentum losses, $(\dot{R}_{\rm L,2}/R_{\rm L,2})_{\rm sys}$, which changes the binary's orbital

separation, and hence the donor's Roche lobe radius. As a result of both these factors affecting $\dot{R}_{\mathrm{L},2}/R_{\mathrm{L},2}$, we have

$$\begin{aligned}\frac{\dot{R}_{\mathrm{L},2}}{R_{\mathrm{L},2}} &= \left(\frac{\dot{R}_{\mathrm{L},2}}{R_{\mathrm{L},2}}\right)_{\dot{M}_2\neq 0} + \left(\frac{\dot{R}_{\mathrm{L},2}}{R_{\mathrm{L},2}}\right)_{\mathrm{sys}} \\ &= \zeta_{\mathrm{L}}\frac{\dot{M}_2}{M_2} + 2\left(\frac{\dot{J}}{J}\right)_{\mathrm{sys}}, \end{aligned} \tag{1.44}$$

where we obtained the second term on the right hand side by using equation (1.29) with $\dot{M}_2 = \dot{M}_1 = 0$, and replaced $\dot{a}/a$ using equation (1.31). The first term on the right hand side of equation (1.44) was obtained via

$$\begin{aligned}\left(\frac{\dot{R}_{\mathrm{L},2}}{R_{\mathrm{L},2}}\right)_{\dot{M}\neq 0} &= \frac{1}{R_{\mathrm{L},2}}\left(\frac{\mathrm{d}\,R_{\mathrm{L},2}}{\mathrm{d}\,M_2}\right)\frac{\mathrm{d}\,M_2}{\mathrm{d}\,t} \\ &= \zeta_{\mathrm{L}}\frac{\dot{M}_2}{M_2}. \end{aligned} \tag{1.45}$$

Furthermore, we can derive an expression for ζ_{L}, which can be compared to the values of ζ_{ad} and ζ_{eq} for a given donor star, in order to determine the timescale of the resulting mass transfer. For the case of non-conservative mass transfer [c.f. equations (1.34) and (1.35)], we can combine equations (1.29), (1.32), (1.33) and (1.42) which can then be solved for $\dot{R}_{\mathrm{L},2}/R_{\mathrm{L},2}$, and then compared with the equation (1.44). This finally gives

$$\zeta_{\mathrm{L}} = \alpha_{\mathrm{CAML}}\left(2\eta_{\mathrm{CAML}}\frac{M_2}{M_1+M_2} + \frac{2}{3}\frac{M_2}{M_1+M_2} - 2q\right) + \zeta_{\mathrm{L,c}}, \tag{1.46}$$

(Kolb et al. 2001) where $\zeta_{\mathrm{L,c}} = 2q - 5/3$ is the expression of ζ_{L} for the fully conservative case of mass transfer.

Now the total rate at which the donor's stellar radius evolves, given by $\dot{R}_2/R_2$, is also due to a combination of two factors. The first is a result of the donor's adiabatic reaction to mass loss. If the mass loss rate timescale, $\tau_{\dot{M}}$, is sufficiently short such that $\tau_{\mathrm{KH}} >> \tau_{\dot{M}}$, then the donor star cannot re-establish thermal equilibrium rapidly enough and there is little or no change to the donor's internal energy distribution. The fractional rate of change of the donor's radius due to the donor's adiabatic reaction to mass loss is $(\dot{R}_2/R_2)_{\mathrm{ad}}$.

One example which highlights this first case is when the donor star, initially in thermal equilibrium, establishes contact with its Roche lobe for the first time and mass transfer commences. The turn-on of mass transfer occurs over a timescale given by equation (1.16), which is between approximately 10^4 and 10^5 years (Ritter 1988). Clearly, for the case of lower main sequence donor stars we have a situation where $t_{\ddot{M}} << \tau_{\mathrm{KH}}$, and as a result the donor will react adiabatically.

A pertinent way of determining how the donor star reacts adiabatically to mass loss is by examining the distribution of entropy, S, within the donor star, before and after an amount of mass δM is removed in a time δt. We apply this description to typical donor stars with masses in the range $0.1 \leq M_2/\mathrm{M}_\odot \leq 1.0$, which are on, or close, to the main sequence (Ritter 1996).

If M_r is the mass lying within a radius r, and P_r is the gas pressure at radius r, then the entropy distribution through the star is given by [e.g. Ritter (1996)]

$$\frac{\mathrm{d}S}{\mathrm{d}M_r} = \frac{\mathcal{R}}{\mu}\frac{GM_r}{4\pi r^4 P_r}\left(1 - \frac{\nabla}{\nabla_{\mathrm{ad}}}\right), \tag{1.47}$$

where $\mathcal{R}$ is the ideal gas constant, μ is the mean molecular weight, G is the gravitational constant, while $\nabla \equiv \mathrm{d}\ln T/\mathrm{d}\ln P$ and $\nabla_{\mathrm{ad}} \equiv (\mathrm{d}\ln T/\mathrm{d}\ln P)_{\mathrm{ad}}$ describe the temperature gradient of the star, and the temperature gradient under adiabatic conditions respectively.

The donor stars in CVs have substantial convective envelopes if $M_2 \lesssim 0.8$ $\mathrm{M}_\odot$, while donors with $M_2 > 0.8$ $\mathrm{M}_\odot$ have insignificant or no convective envelopes (Stehle et al. 1996), and instead have appreciable radiative cores. In the former case, the convective envelope has $\nabla \approx \nabla_{\mathrm{ad}}$. From equation (1.47), this means that $S(M_r)$ is constant throughout the convective envelope. For the case where the donor star has an appreciable radiative core, which is stable against convection, then $\nabla < \nabla_{\mathrm{ad}}$. As M_r increases as r increases then, again from equation (1.47), the entropy increases moving outwards within the radiative core.

Figure 1.5 shows the entropy distribution of two stars, which have substantial convective envelopes, with mass M (thick, solid line) and mass $M - \delta M$ (dot-dashed line). Both stars are in thermal equilibrium. We denote the entropy distribution of the two stars as $S_{\mathrm{eq}}(M_r)|_M$ and $S_{\mathrm{eq}}(M_r)|_{M-\delta M}$ respectively, where the subscript 'eq' indicates that the stars are in thermal equilibrium. If the star of mass M undergoes rapid mass transfer such that it cannot maintain thermal equilibrium, then its internal energy, and hence entropy, distribution remain unaltered. The resulting entropy distribution of this star is therefore just the entropy distribution of the original star of mass M at $M_r \leq M - \delta M$, and is indicated in Figure 1.5 as the solid, red line. We denote this as $S_{\mathrm{ad}}(M_r \leq M - \delta M)|_M$, where the subscript 'ad' indicates that mass is lost adiabatically. From Figure 1.5 we can see that in the outer layers of the star

$$S_{\mathrm{ad}}(M_r \leq M - \delta M)|_M > S_{\mathrm{eq}}(M_r)|_{M-\delta M}. \tag{1.48}$$

Thus, the outer layers of a star which has lost δM of mass as a result of rapid mass transfer are hotter than those a star of mass $M - \delta M$, which is in thermal equilibrium. As a result the

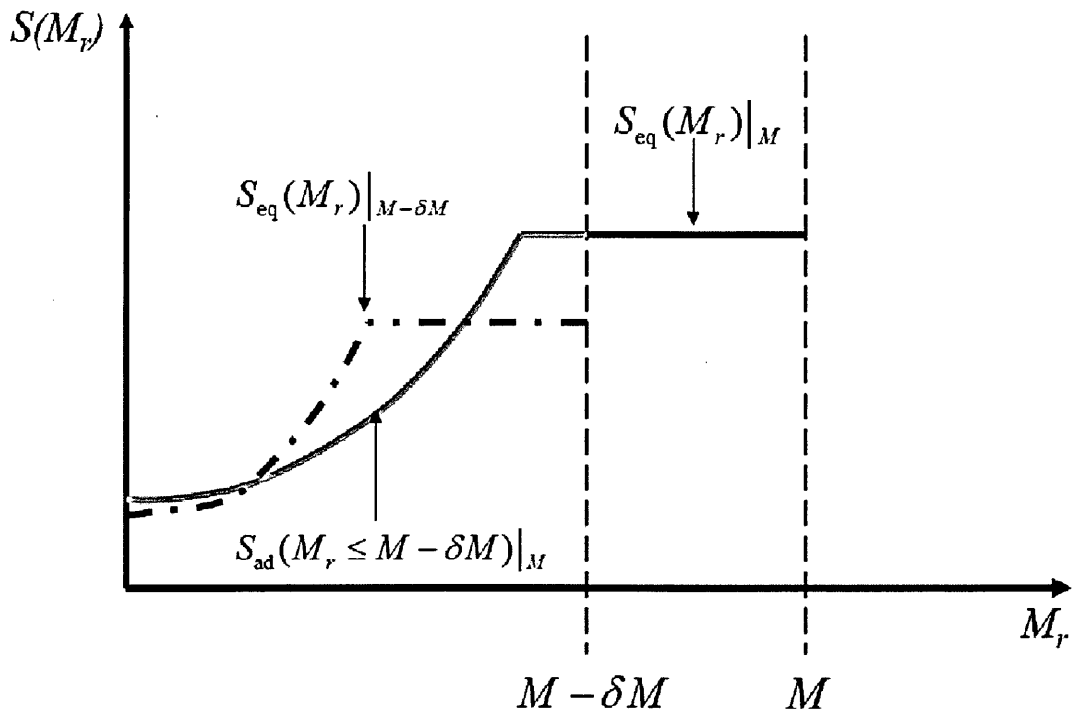

Figure 1.5: Sketch of the entropy distribution for a star of mass M with a substantial convective envelope, which is in thermal equilibrium (solid black line), and for a star with mass $M - \delta M$, also in thermal equilibrium (dot-dashed line). The solid red line shows the entropy distribution of the star of mass M after rapid moss loss by the amount δM.

former star will expand relative to its equilibrium radius as a result of rapid mass transfer, and so $\zeta_{\rm ad} < 0$ for such stars. This is in contrast to donor stars with a significant radiative core.

Figure 1.6 is similar to Figure 1.5 except that it shows the entropy profile of two stars of mass M (solid line) and $M - \delta M$ (dot-dashed line) which have substantial radiative cores. Again, both stars are in thermal equilibrium, and have entropy profiles given by $S_{\rm eq}(M_r)|_M$ and $S_{\rm eq}(M_r)|_{M-\delta M}$, respectively. From Figure 1.6 it can be seen that a star of mass M that rapidly loses mass δM, we have for the outer layers of the star

$$S_{\rm ad}(M_r \leq M - \delta M)|_M < S_{\rm eq}(M_r)|_{M-\delta M}. \tag{1.49}$$

In this case the outer layers of a radiative star rapidly losing mass is cooler than an isolated equivalent in thermal equilibrium. As a result predominantly radiative stars contract in response to rapid mass loss, and hence $\zeta_{\rm ad} > 0$.

The second factor which contributes to $\dot{R}_2/R_2$ is the thermal relaxation term, $(\dot{R}_2/R_2)_{\rm th}$,

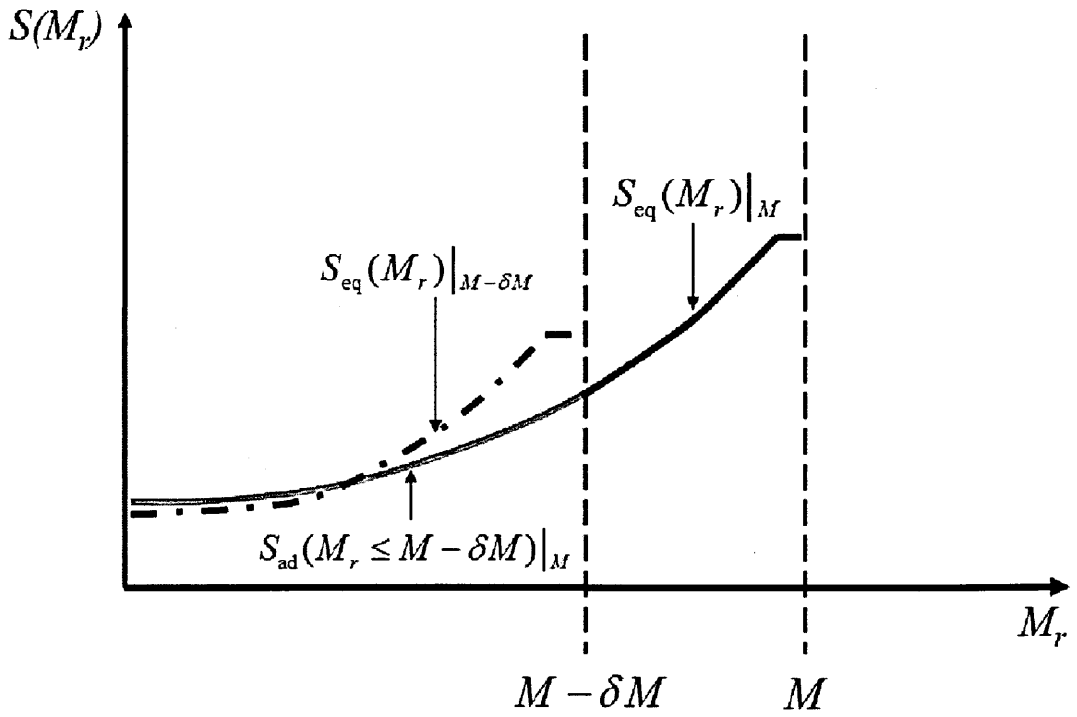

Figure 1.6: The same as Fig. 1.5 but this time showing the entropy distributions for radiative (with insubstantial convective envelopes) stars of mass M and $M - \delta M$, both in thermal equilibrium. The red line shows the entropy distribution of the star of mass M once it has rapidly lost mass by an amount δM.

which is the rate of change of the donor's radius as it re-establishes thermal equilibrium. Another example which highlights this is in the case where the donor's stellar and Roche lobe radius have made contact after the initial turn-on phase, and they now move in step. We can therefore assume stationary mass transfer, $\ddot{M}_2 = 0$. If the resulting mass loss timescale is sufficiently long such that $\tau_{\dot{M}} >> \tau_{\rm KH}$ then the donor star is able to re-establish thermal equilibrium by its Kelvin-Helmholtz time.

The total rate of change of the donor's radius is therefore the sum of the contributions due to the donor's adiabatic reaction to mass loss, and its subsequent return to thermal equilibrium. Hence,

$$\frac{\dot{R}_2}{R_2} = \left(\frac{\dot{R}_2}{R_2}\right)_{\rm ad} + \left(\frac{\dot{R}_2}{R_2}\right)_{\rm th} . \tag{1.50}$$

Depending on the mass loss timescale either the first or the second term on the right hand side of equation (1.50) will dominate. Indeed, during the turn-on of mass transfer we initially have $(\dot{R}_2/R_2)_{\rm th} = 0$. Using the definition of $\zeta_{\rm ad}$ from equation (1.22), equation (1.50) during

mass transfer turn-on can be re-written as

$$\begin{aligned}\frac{\dot{R}_2}{R_2} &= \left(\frac{\dot{R}_2}{R_2}\right)_{\rm ad} \\ &= \frac{1}{R_2}\left(\frac{{\rm d}R_2}{{\rm d}M_2}\right)_{\rm ad}\frac{{\rm d}M_2}{{\rm d}t} = \zeta_{\rm ad}\frac{\dot{M}_2}{M_2}.\end{aligned} \tag{1.51}$$

However, in general (especially in the case of CVs; see Chapter 2, Section 2.3.1), we have $\tau_{\dot{M}} \sim \tau_{\rm KH}$. Both terms in equation therefore play a role in the evolution of the donor's radius. The term $(\dot{R}_2/R_2)_{\rm ad}$ takes into account the previous adiabatic response history of the donor. On the other hand, after the donor's initial adiabatic reaction during turn-on of mass transfer, the donor will attempt to re-establish thermal equilibrium, i.e. $(\dot{R}_2/R_2)_{\rm th} \neq 0$, but not fully attain it.

We can re-express the total rate of change of the donors stellar radius in terms of the mass loss rate, and the 'effective' mass-radius exponent $\zeta \equiv {\rm d}\ln R_2/{\rm d}\ln M_2$, i.e.

$$\frac{\dot{R}_2}{R_2} = \zeta\frac{\dot{M}_2}{M_2}. \tag{1.52}$$

By combining equations (1.50) to (1.52) we can obtain an expression for the thermal relaxation term, given by

$$\left(\frac{\dot{R}_2}{R_2}\right)_{\rm th} = (\zeta - \zeta_{\rm ad})\frac{\dot{M}_2}{M_2}. \tag{1.53}$$

For the case of main sequence donor's that are slightly out of thermal equilibrium, then $\zeta \approx \zeta_{\rm th} \approx 1$. Equation (1.53) therefore shows that for predominantly convective donors ($\zeta_{\rm ad} < 0$), they will shrink back towards their equilibrium radii. On the other hand, for donors which are predominantly radiative ($\zeta_{\rm ad} > 0$), then equation (1.53) shows that such donors will expand towards their equilibrium radii.

Finally, we note that we could have supplemented equation (1.50) with a term which describes the evolution of the donor radius due to nuclear evolution, $(\dot{R}_2/R_2)_{\rm nuc}$. However, as discussed in Section 1.2 in the case of CV donors, this term can in general be neglected. [3]

By combining equations (1.15) (assuming stationary mass transfer), (1.44) and (1.51) gives an alternative expression for the mass transfer rate. This is given by

$$\frac{\dot{M}_2}{M_2} = \frac{2(\dot{J}/J)_{\rm sys} - (\dot{R}_2/R_2)_{\rm th}}{\zeta_{\rm ad} - \zeta_{\rm L}}, \tag{1.54}$$

[3] As discussed in Chapter 2, Section 2.4.2, CVs with orbital periods between about 4 and 5 hours are observed to be dominated by nuclear evolved donors.

[e.g. Ritter (1988)]. Recalling that $(\dot{J}/J)_{\rm sys} < 0$, then mass transfer will be dynamically stable as long as the denominator in equation (1.54) is positive, i.e. $\zeta_{\rm ad} > \zeta_{\rm L}$. The denominator in equation (1.54) is therefore analogous to the quantity $\mathcal{D}$; by decreasing the quantity $\zeta_{\rm ad} - \zeta_{\rm L}$, we are enhancing the mass transfer rate. This occurs by increasing the value of $\zeta_{\rm L}$, which in turn occurs as a result of consequential angular momentum losses.

In the next chapter, we apply the theoretical tools discussed in this chapter to describe in more detail our current understanding of CV evolution, in particular the mechanisms which contribute to systemic angular momentum loss. Indeed, the features seen in the orbital period distribution of the observed sample of CVs which indicate different phases of CV evolution, can be explained in the context of these angular momentum loss mechanisms.

2

The Evolution of Cataclysmic Variables

In this chapter we discuss our current understanding of CV evolution. We begin in Section 2.1 with an outline of the systemic angular momentum loss mechanisms which drive CV evolution, with particular focus on one such mechanism called magnetic braking. We then review in Section 2.2 how the angular momentum loss rate due to magnetic braking is typically calculated in CV evolutionary models. In Section 2.3, we discuss the orbital period distribution of the observed sample of CVs, and explain how these features arise in the context of these angular momentum loss mechanisms. Of particular interest for this thesis is the period gap – a dearth of observed CVs with orbital periods between approximately 2 and 3 hours – and the most widely cited explanation for it, called the disrupted magnetic braking hypothesis. This is discussed in Section 2.3.1. We critically examine the disrupted magnetic braking hypothesis as a likely reason for the period gap, and discuss the current observational and theoretical evidence for and against this hypothesis in Section 2.4. Finally, a simple and robust test to determine if the disruption of magnetic braking actually occurs in nature is described in Section 2.5.

2.1 Magnetic Braking

As discussed in Chapter 1, one of the driving mechanisms behind CV evolution are systemic angular momentum losses from the binary's orbit. One such sink of orbital angular momentum is gravitational wave radiation. These are ripples in space-time which are emitted from the binary due to the orbital motion of the stellar components (Landau & Lifshitz 1975). Orbital energy, and therefore orbital angular momentum, is removed from the binary causing the orbital separation to decrease. The angular momentum loss rate due to gravitational wave radiation, $(\dot{J}/J)_{\rm GR}$, is given by [e.g. Kolb & Stehle (1996)]

$$\left(\frac{\dot{J}}{J}\right)_{\rm GR} = -2.6 \times 10^{-12} \frac{M_1 M_2}{(M_1 + M_2)^{1/3}} \left(\frac{P_{\rm orb}}{\rm days}\right)^{-8/3} {\rm yr}^{-1}, \qquad (2.1)$$

where M_1 and M_2 are in solar masses. While it is accepted that gravitational wave radiation is one sink of angular momentum for CVs, it cannot explain the high observed mass transfer rates of $\sim 10^{-8}$ M$_\odot$ yr^{-1} in CVs with $P_{\rm orb} \gtrsim 3$ hours (Verbunt & Zwaan 1981).

Verbunt & Zwaan (1981) therefore suggested an extra sink of angular momentum in the form of a magnetically coupled stellar wind emitted from the donor star. Due to the plasma nature of the stellar wind, it is initially forced to flow along the donor's magnetic field lines.

A basic illustration of the magnetic field of a donor star, which spins with an angular frequency Ω, is shown in Figure 2.1, which depicts the two components of the magnetic field (Mestel & Spruit 1987). The first component, indicated by the solid black lines, comprises the set of closed loops in the magnetic field close to the donor's equator. This is called the 'dead zone' as the stellar wind is trapped within these closed field loops. Here, the thermal energy of the stellar wind, and the centrifugal forces due to the rotation of the donor, cannot overcome the magnetic pressure.

The second component, which is shown in Figure 2.1 as the dashed lines, consists of the open field lines, lying at higher latitudes, towards the poles of the donor. Close to the surface of the star, the pressure exerted onto the wind due to the donor's magnetic field, $P_{\rm B}$, is larger than the ram pressure exerted onto the magnetic field due to the motion of the stellar wind, $P_{\rm w}$. Thus, $P_{\rm w} << P_{\rm B}$, and the stellar wind is forced to flow along the magnetic field lines, and hence is forced to co-rotate with the same angular frequency as the donor star. Close to the surface of the star, the magnetic field lines therefore have an approximately dipolar configuration.

The magnetic field strength, B, for this dipolar configuration, however, will decrease with the distance, r, from the donor star according to $B \propto 1/r^3$, and hence $P_{\rm B}$ will decrease

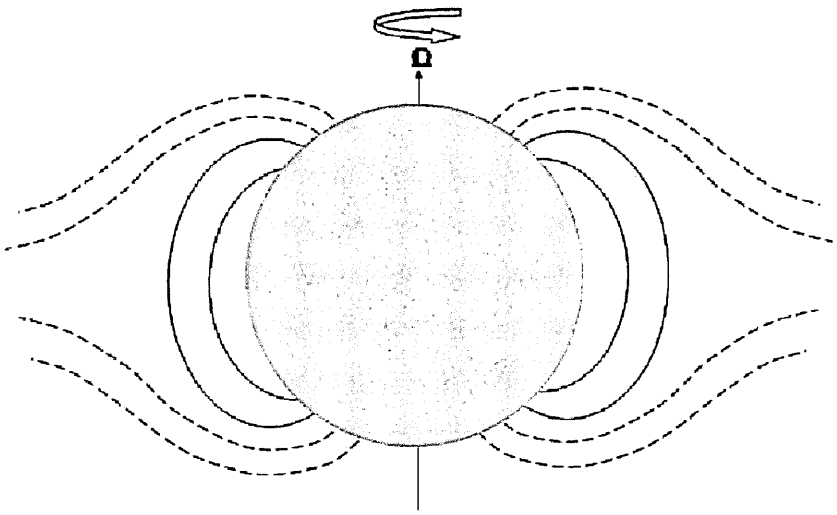

Figure 2.1: A graphical illustration of the magnetic field of a CV donor, rotating with angular frequency Ω. The magnetic fields shown as the dashed lines denote the wind zone, while the field lines in solid denote the dead zone.

with increasing r. As a result, the stellar wind will begin to distort the magnetic field into a more radial configuration, as shown by the dashed lines in Figure 2.1.

Eventually, a point will be reached where $P_{\rm w} \gtrsim P_{\rm B}$. This is achieved at the Alfvén radius, $R_{\rm A}$, away from the donor star. As a result, the stellar wind is no longer forced to co-rotate with the donor star beyond $R_{\rm A}$, and instead drags the open field lines along with it. Hence the wind removes specific angular momentum given by

$$j = \Omega R_{\rm A}^2, \tag{2.2}$$

where $R_{\rm A} \approx 100$ R$_\odot$, causing the star to spin down. Such a large value of $R_{\rm A}$ provides a long lever-arm for the stellar wind to provide the spin down torque onto the donor. Hence magnetic braking is highly efficient at removing the spin angular momentum from the star.

As a result of the spin-down of the donor star, tidal torques will act to spin the donor star back to synchronous rotation with the binary orbit. This results in the removal of angular momentum from the binary orbit, and therefore a decrease in the binary's orbital separation.

2.2 Parameterised Modelling of Magnetic Braking

In order to model the evolution of systems as a result of magnetic braking, we need to calculate the angular momentum loss rate from the binary orbit.

A clue as to how this could be achieved came from Skumanich (1972) who analysed the luminosity of calcium emission lines from G-type field stars. The luminosity of the calcium emission lines from stellar spectra can be used as a proxy to determine the magnetic field strength at the surface of the star [see, for example, Hartmann & Noyes (1987)]. Skumanich (1972) found that the equatorial velocity, v_e and calcium emission luminosity, L_{Ca}, followed $v_e \propto L_{Ca}$. This may be a result of dynamo action within the rotating star, which may be responsible for the generation of stellar magnetic fields.

Furthermore, Skumanich (1972) found that the equatorial velocity of the star, v_e, bore a relationship to the star's age since it landed on the ZAMS, t_{MS}, according to

$$v_e \propto L_{Ca} \propto {t_{MS}}^{-1/2}. \tag{2.3}$$

This spin down was interpreted as a result of magnetic braking; the spinning down of the star will result in a less efficient generation of the magnetic field, which consequently causes a weaker magnetic field strength at the stellar surface (and hence a lower value of L_{Ca}). This will in turn affect magnetic braking; a weaker magnetic field will cause R_A to move closer to the star and, from equation (2.2), the magnetic braking will be less efficient in spinning the star down.

From equation (2.3) the angular momentum loss rate due to magnetic braking, $\dot{J}_{MB}$, can be estimated. For a synchronously rotating CV donor star with mass M_2, radius R_2, spin frequency Ω and moment of inertia I, then $\dot{J}_{MB}$ is given by

$$\begin{aligned} \dot{J}_{MB} &= I\dot{\Omega} \\ &= k^2 M_2 R_2^2 \dot{\Omega}, \end{aligned} \tag{2.4}$$

where k^2 is the gyration radius of the donor star. Using $v_e = \Omega R_2$, and differentiating equation (2.3) with respect to time gives

$$\dot{\Omega} \propto -\frac{1}{2}\frac{t_{MS}^{-3/2}}{R_2}. \tag{2.5}$$

From equation (2.3),

$$t_{\rm MS}^{-3/2} \propto (\Omega R_2)^3. \tag{2.6}$$

Substituting equation (2.5) and (2.6) into equation (2.4) gives (Verbunt & Zwaan 1981)

$$\dot{J}_{\rm MB} \propto -k^2 M_2 R_2^4 \Omega^3. \tag{2.7}$$

Note that equation (2.3) was derived from the spin-down rate of G-type stars which typically have spin periods of between 1 and 30 days. The spin periods of CV donors however, as a consequence of tidal locking, are typically of a few hours. Thus, we are extrapolating equation (2.7) down to spin periods which are 1 to 2 orders of magnitude smaller than the spin periods of stars from which this relation was derived. It is therefore unclear whether equation (2.7) can be appropriately applied to M-dwarf CV donors.

In light of this, Rappaport et al. (1983) modified equation (2.7) into a parameterised form, where different dependencies of the angular momentum loss rate on the donor star's radius were considered. This is given by

$$\dot{J}_{\rm MB} = -3.8 \times 10^{-30} R_\odot^4 \,{\rm s\,cm^{-2}}\, M_2 \left(\frac{R_2}{R_\odot}\right)^\gamma \Omega^3, \tag{2.8}$$

where γ is a free parameter. By setting $\gamma = 4$, equation (2.8) reduces to the form of equation (2.7).

Yet another form of magnetic braking has been suggested by Hurley et al. (2002), which is described in terms of the mass of the donor's convective envelope, $M_{\rm env}$. While the magnetic braking prescriptions suggested by Verbunt & Zwaan (1981) and Rappaport et al. (1983) assume that the whole star is braked, Hurley et al. (2002) suggest that only the convective envelope of the donor is braked, i.e. there is no coupling between the spins of the donor's radiative core and convective envelope. Hurley et al. (2002) give an angular momentum loss rate of the form

$$\dot{J}_{\rm MB} = -5.83 \times 10^{-16} \,{\rm M_\odot\, R_\odot^{-1}\, yr^2}\, \frac{M_{\rm env}}{M_2} R_2^3 \Omega^3, \tag{2.9}$$

Thus, $\dot{J}_{\rm MB} \to 0$ when $M_{\rm env} \to 0$, which will occur for predominantly radiative stars. Hurley et al. (2000) calculate that the convective envelope vanishes for stars with masses greater than 1.25 $M_\odot$. However, as we shall discuss in the remainder of this chapter, the strength of magnetic braking as suggested by equations (2.8) and (2.9), has been thrown into some doubt by observational evidence. Alternative magnetic braking formulations are discussed in Section 2.4.1.

2.3 The Orbital Period Distribution of the Observed CV Population

A vital tool which facilitates our understanding of the secular evolution of CVs, and with which we can compare our theoretical models to, is the orbital period distribution of the observed CV population. As it is orbital angular momentum losses which drives the evolution of the binary separation (and therefore the orbital period), an orbital period distribution of the observed CVs will therefore provide clues into the mechanisms driving the evolution, and the associated angular momentum loss rates.

The left panel of Figure 2.2 shows the orbital period distribution of the current observed sample of CVs and related systems, from the Ritter & Kolb (2003) catalogue, Edition 7.9 (2008). Three features of this distribution have been highlighted: a sharp cut-off in the number of observed CVs at $P_{\rm orb} \approx 1.3$ hours, termed the period minimum. Secondly, the dearth of observed systems with orbital periods in the range $2 \lesssim P_{\rm orb}/{\rm hours} \lesssim 3$, coined the period gap, the location of which is indicated by the long-dashed lines. Finally, we have a long period cut-off in the CV population at $P_{\rm orb} \approx 12$ hours, which is termed the period maximum.

Also shown in the left panel of Figure 2.2 are systems which are closely related to the CV. The first type are AM CVn binaries, which contain a helium-rich, degenerate donor star, and an accreting white dwarf [e.g. Nelemans (2005)]. These have orbital periods typically of $P_{\rm orb} < 77$ minutes. Secondly, there are the GK Per binaries, where the donor star has significantly evolved away from the main sequence. The donor stars in these systems are filling their Roche lobes as a result of radial expansion due to nuclear evolution. These systems typically lie at orbital periods of $P_{\rm orb} > 12$ hours. We do not consider either the GK Per or AM CVn binaries any further. Instead we focus on CVs with main sequence secondaries, which inhabit the orbital period range $1.3 \lesssim P_{\rm orb}/{\rm hours} \lesssim 12$.

We will now discuss the features of the observed CV orbital period distribution in turn, beginning with the period gap.

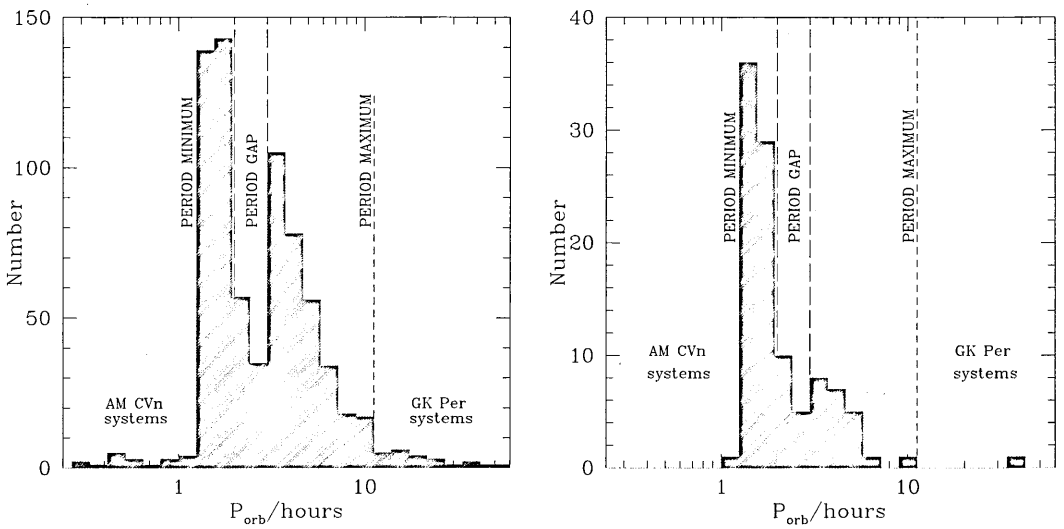

Figure 2.2: Left panel: The orbital period distribution of the observed CV population, obtained from the Ritter & Kolb (2003) catalogue, Edition 7.9 (2008). Right panel: the orbital period distribution of CVs detected from the Sloan Digital Sky Survey. In both panels, various features of the orbital period distributions are indicated: the location of the period gap is shown by the long-dashed lines, which lies between $2 \lesssim P_{\rm orb}/{\rm hours} \lesssim 3$. The location of the maximum orbital period for CVs with unevolved, main sequence donors, is indicated by the short-dashed line at $P_{\rm orb} \approx 12$ hours, while the minimum period cut-off is indicated at $P_{\rm orb} \approx 1.3$ hours. Also shown are the population of AM CVn systems with helium rich donors, at $P_{\rm orb} < 1.3$ hours, and the population of systems with evolved donors, at $P_{\rm orb} \gtrsim 12$ hours.

2.3.1 The Period Gap and the Disrupted Magnetic Braking Hypothesis

Any successful theory describing the evolution of CVs must explain the paucity of observed systems with orbital periods in the range $2 \lesssim P_{\rm orb}/{\rm hours} \lesssim 3$, coined the period gap. Theories attempting to explain the period gap suggest that CVs must somehow be rendered undetectable (i.e. their detection probability drastically decreases) as they enter the period gap. Alternative theories suggest that the reason only a few CVs are detected within the period gap is because the orbital evolution of the majority of systems never takes them there.

One model which fits into the former category of theories is the disrupted magnetic braking hypothesis, which suggests that CVs become undetectable as they enter the period gap. This model has become the most widely cited explanation for the period gap, as a

result of the fact that it can adequately reproduce the sharp upper and lower edges of the gap, as well as its observed width and location [see, for example, Kolb et al. (1998), Kolb (2002)]. This is in contrast to rival models for the period gap, which we briefly discuss in Section 2.4. In the remainder of section 2.3.1 we review the mechanism behind the disrupted magnetic braking hypothesis.

2.3.1.1 The Reaction of the Donor to Mass Loss

Not only does magnetic braking drive orbital evolution of the binary, but also mass transfer (see Section 1.2). If the angular momentum loss timescale due to magnetic braking is $\tau_{\rm MB} \equiv |(J/\dot{J})_{\rm MB}|$, and the resulting mass loss timescale is $\tau_{\dot{M}} \equiv |M_2/\dot{M}_2|$ then, from equation (1.37), we have

$$\tau_{\dot{M}} \propto \tau_{\rm MB}. \tag{2.10}$$

By comparing the value of $\tau_{\rm MB}$ to $\tau_{\rm KH}$ or $\tau_{\rm dyn}$, we can determine whether the donor star can maintain its thermal or dynamical equilibrium. As $\tau_{\rm MB} \approx 10^8$ years (King 1988), we can immediately conclude that the donor star will maintain hydrostatic equilibrium. Pertinent to our discussion is a comparison between the timescales $\tau_{\dot{M}}$ and $\tau_{\rm KH}$ as a result of mass transfer.

The mass-radius relation of low-mass main sequence stars is approximately given by $(R_2/{\rm R}_\odot) \sim (M_2/{\rm M}_\odot)$, while the donor's luminosity is given by $(L_2/{\rm L}_\odot) \sim (M_2/{\rm M}_\odot)^{7/2}$. Thus, from equation (1.19), the Kelvin-Helmholtz time for low-mass main sequence stars is

$$\tau_{\rm KH} \approx 3 \times 10^7 \left(\frac{M_2}{{\rm M}_\odot}\right)^{-5/2} \text{ years}. \tag{2.11}$$

Equation (2.11) therefore shows that as the mass of the donor decreases as a result of mass loss, its Kelvin-Helmholtz time increases. As a consequence of continuing mass loss, the donor star will therefore find it harder and harder to maintain thermal equilibrium. Indeed, using equation (2.11), donors with $M_2 \lesssim 0.6\ {\rm M}_\odot$ which are losing mass via magnetic braking will be driven out of thermal equilibrium.

While $\tau_{\dot{M}}$ is not sufficiently short for the donor star to react adiabatically, we can still apply the discussion in Section 1.2.2 to determine the consequence of a donor star being driven out of thermal equilibrium. Predominantly convective donor stars will expand as a result of being driven out of thermal equilibrium, while donors with substantial radiative cores will contract. Irrespective of the initial structure of the donor star at turn-on of mass transfer, continual mass loss will change its internal structure towards a fully convective

state. Hence, donor stars in CVs will in general be over-sized as a result of mass loss compared to isolated, main sequence stars of the same mass.

2.3.1.2 Turning off Mass Transfer

The conception behind the idea that magnetic braking is disrupted at an orbital period of approximately 3 hours was motivated by the fact that a fully convective main sequence star with a mass of ≈ 0.3 $M_{\odot}$ (which corresponds to the mass where the radiative core disappears) would fill its Roche lobe within the vicinity of the upper edge of the period gap (Robinson et al. 1981). This led Spruit & Ritter (1983) and Rappaport et al. (1983) to suggest that the transition of a star to a fully convective state as a consequence of continued mass loss may be responsible for the cessation of magnetic braking.

Indeed, Spruit & van Ballegooijen (1982) suggest that the boundary between the radiative core and the convective envelope (which is called the tachocline) plays a crucial role in the generation and the anchoring of the stellar magnetic field; an idea that has received observational support in recent times. For example, Schou et al. (1998) observed that there is a strong radial shear at the Solar tachocline. It is suggested that it is this strong radial shear that generates, and subsequently anchors, the poloidal component of the magnetic field [Tobias et al. (2001); Mason et al. (2002)].

Once the donor becomes fully convective, this boundary is therefore lost. The consequence of this is still uncertain. The loss of the tachocline may result in the severe weakening of the magnetic field (Spruit & Ritter 1983) or rearrangement of the magnetic field lines into a more complex topology (Taam & Spruit 1989). In either case, it is the abrupt decrease in the efficiency of magnetic braking, and hence a corresponding decrease in the angular momentum loss rate of the binary system, which is the crux of the disrupted magnetic braking hypothesis, and hence the appearance of the period gap.

The chain of events leading to the disruption of magnetic braking is illustrated in Figure 2.3, which shows the evolution of a donor's radius (red) and Roche lobe radius (blue) as a function of orbital period. The initial mass of the donor at the onset of mass transfer is 0.4 $M_{\odot}$, and the white dwarf mass is 0.6 $M_{\odot}$. The labels (1) to (4) indicate the various stages in the donor's evolution.

Initially, the CV evolution is driven by magnetic braking above orbital periods of approximately 3 hours (1). This causes a corresponding shrinking of the donor's Roche lobe radius, $R_{L,2}$, on a timescale $|R_{L,2}/\dot{R}_{L,2}|_{MB} \approx \tau_{MB}$. Once the donor star becomes fully convective

at approximately 3 hours (2), magnetic braking becomes less efficient, causing an instantaneous decrease in the angular momentum loss rate, leaving gravitational radiation as the only sink of orbital angular momentum (3a). The timescale for the shrinkage of the donor's Roche lobe due to gravitational radiation is $|R_{\rm L,2}/\dot{R}_{\rm L,2}|_{\rm GR} \approx \tau_{GR}$, where $\tau_{\rm GR} \equiv |J/\dot{J}|_{\rm GR}$ is the angular momentum loss timescale due to gravitational radiation, which is much longer than $\tau_{\rm MB}$. As a result the donor star can relax back towards its equilibrium radius (3b).

The combined effect of (3a) and (3b) is that the donor star detaches from its Roche lobe radius, and mass transfer shuts off at an orbital period of $\sim$ 3 hours. Thus, the system is rendered 'invisible' and is no longer observed as a CV. Gravitational radiation is now the sole driving mechanism of this 'detached CV' (dCV) driving it to shorter orbital periods, and hence the Roche lobe radius of the secondary to smaller values. There will therefore be a point when the Roche lobe radius will catch up with the secondary star and mass transfer resumes again at an orbital period of $\sim$ 2 hours (c). The disrupted magnetic braking therefore explains the lack of accreting CVs in the period gap by predicting the presence of detached white dwarf-main sequence systems crossing it.

Although a decline in stellar magnetic activity has been observed for stars with spectral types later than about M5 (which corresponds to fully convective stars) (Giampapa & Liebert 1986) this decline is not abrupt. Indeed, magnetic activity appears to persist for late type stars (Cram & Giampapa 1987). It therefore appears unlikely that a weakening of the donors magnetic field is responsible for a decrease in the magnetic braking efficiency, and the corresponding sharp decline in the angular momentum loss rate in CVs.

Taam & Spruit (1989) consider the possible consequences of the disappearance of the tachocline, and suggest that the magnetic field changes from an initial dipole field to a higher order multipole field once the donor becomes fully convective. In such cases, the fraction of open field that extend to the Alfvén radius decreases, meaning that the angular momentum loss mechanism is less efficient. While the Alfvén radius also decreases with increasing multipole orders, the role this plays in the decrease in the angular momentum loss rate is minor compared to the contribution due to the fraction of open field lines. Depending on the order considered, they find that the fraction of open field lines decreases by 2 to 200, corresponding in a reduction in the angular momentum loss rate at an orbital period of 3 hours by between 3 and 2000. For the donor star to be able to detach from its Roche lobe and re-establish thermal equilibrium before mass transfer resumes, the angular momentum loss rate must decrease by at least a factor of 3 (Spruit & Ritter 1983). This is

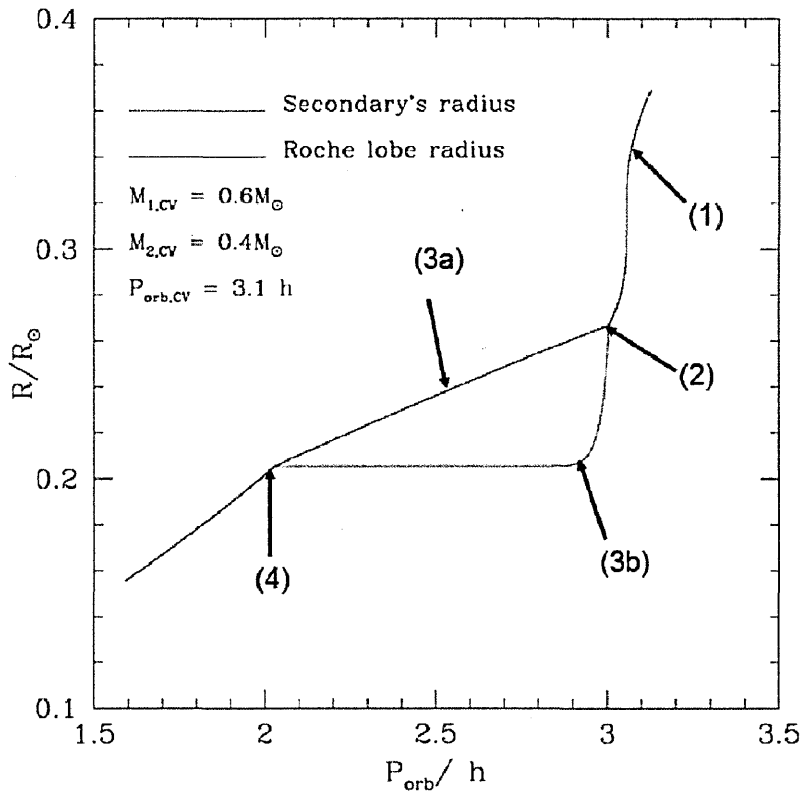

Figure 2.3: The plot shows the evolution of the radius of the donor (red) of initial mass of 0.4 $M_\odot$ and its Roche lobe radius (blue) as a function of orbital period. The model CV has a white dwarf of mass 0.6 $M_\odot$. (1): The evolution of the CV is initially driven by magnetic braking; (2): The donor star becomes fully convective and magnetic braking shuts off at $\approx$ 3 hours; (3a): as a result the orbital evolution is driven only by gravitational radiation, causing an instantaneous increase in the evolutionary timescale of the donor's Roche lobe radius; (3b) simultaneously, the donor star shrinks back to its equilibrium radius; (4): Shrinking of the Roche lobe radius eventually leads to the donor star re-establishing contact with its Roche lobe radius at $\approx$ 2 hours.

easily attainable by a re-arrangement of the donor's magnetic field.

2.3.2 The Period Maximum

The observed population of CVs begins to decline at $P_{\rm orb} \approx 12$ hours. This is a consequence of the requirement that mass transfer in CVs is thermally stable. We can find the critical mass ratio, $q_{\rm crit}$, at which mass transfer is just thermally stable, by requiring $\mathcal{D} > 0$ with $\zeta = \zeta_{\rm eq}$ in equation (1.38). Assuming conservative mass transfer as an approximation, then

equation (1.38) gives

$$q_{\rm crit} \approx \frac{5}{6} + \frac{\zeta_{\rm eq}}{2}, \tag{2.12}$$

[see also King (1988); Warner (1995)]. For main sequence stars in thermal equilibrium, we have $\zeta_{\rm eq} \approx 1$. Thus, for CVs to undergo thermally stable mass transfer, their mass ratio, q, must satisfy $q \lesssim q_{\rm crit} \approx 4/3$. Also, as the maximum white dwarf mass is given by the Chandrasekhar mass of 1.44 $M_\odot$, then the maximum secondary which can commence thermally stable Roche lobe overflow is $1.44 q_{\rm crit} \approx 1.9$ $M_\odot$. CVs with such systems will commence mass transfer at ≈ 13 hours, as observed.

2.3.3 The Period Minimum

As discussed in Section 2.3.1, the standard picture of CV evolution states that gravitational radiation is the only sink of angular momentum for orbital periods $P_{\rm orb} \lesssim 2$ hours [e.g. Kolb (1993)], further decreasing the mass of the donor. From equations (2.1) and (1.37), the evolution timescale due to gravitational radiation, and hence the mass transfer timescale, will decrease as the orbital period decreases.

As shown by equation (2.11), the Kelvin-Helmholtz time for the donor will decrease as it loses mass. It is the fact that $\tau_{\rm KH}$ eventually exceeds $\tau_{\dot{M}}$ which is responsible for the period minimum [Paczynski (1981); Rappaport et al. (1982)]. Indeed, at the observed minimum period cut-off of ≈ 77 minutes, $\tau_{\rm KH} \approx 4.5 \times 10^9$ years, while $\tau_{\dot{M}} \approx 1 \times 10^9$ years (King 1988), and hence the donor star cannot re-establish thermal equilibrium rapidly enough. As the donor star is fully convective, it reacts to the rapid mass loss by expanding. It is this increase in the donor star's radius which results in the CV evolving from a phase of decreasing orbital period ($\dot{P}_{\rm orb}/P_{\rm orb} < 0$) towards a phase of increasing orbital period ($\dot{P}_{\rm orb}/P_{\rm orb} > 0$).

In fact the orbital evolution of the CV can be expressed in terms of $\tau_{\dot{M}}$ and the effective mass radius exponent of the donor, ζ, according to

$$\frac{\dot{P}_{\rm orb}}{P_{\rm orb}} = \frac{1}{2\tau_{\dot{M}}}(3\zeta - 1). \tag{2.13}$$

(Kolb et al. 1998). Note that the CV will evolve towards shorter orbital periods as long as $\zeta > 1/3$ (Rappaport et al. 1982).

Continual removal of mass from the donor will eventually lead to the donor becoming a degenerate brown dwarf at $M_2 \approx 0.06$ $M_\odot$ (Chabrier et al. 2009) at which point nuclear

fusion within the donor star ceases. As a result, the donor star can never be in thermal equilibirium below the hydrogen burning limit, and hence cannot shrink rapidly enough to mass transfer. The mass-radius relation of such donors in the sub-stellar regime is $R_2 \sim {M_2}^{-1/3}$, and hence $\zeta = -1/3$ [e.g. Chabrier et al. (2009)]. From equation (2.13), we therefore see that once the donor star becomes degenerate, the CV will evolve towards long orbital periods.

Hence the minimum period cut-off marks the point at which CVs begin to 'bounce' towards longer orbital periods, $\dot{P}_{\rm orb}/P_{\rm orb} = 0$, as the donor star makes the transition from a low-mass main sequence star to a degenerate brown dwarf.

2.3.3.1 The Theoretically Predicted and Observed Location of the Period Minimum Cut-off

There has been a long-standing disparity between the theoretically predicted and observed location of the period minimum cut-off [e.g. Kolb et al. (2001)]. While observations indicate that the period minimum lies at approximately 77 minutes, theoretical models predict a location of approximately 67 minutes. In fact, recent observations from the Sloan Digital Sky Survey (SDSS) place the location of the period minimum at approximately 82 minutes Gänsicke et al. (2009), which is more incongruous with the predicted location of the period minimum.

As the calculated location of the period minimum depends on $\tau_{\rm KH}$ and $\tau_{\dot{M}}$, the discrepancy may be a result of either an inadequate description of the structure of the secondary, or of the systemic angular momentum losses driving CV evolution below $P_{\rm orb} \lesssim 2$ hours.

Despite the incorporation of improved physics describing brown dwarf stars into CV evolutionary calculations (Kolb & Baraffe 1999), this discrepancy remains. Testing the validity of the assumptions made for the Roche model, Rezzolla et al. (2001) and Renvoizé et al. (2002) find that the assumptions are valid, and do not sufficiently account for the disparity between the theoretically predicted and observed period minimum cut-off.

Alternatively, Kolb & Baraffe (1999) suggested that an angular momentum loss rate which is a factor of about 4 greater than that due to gravitational wave radiation can resolve the disparity. Taam & Spruit (2001) and Spruit & Taam (2001) suggest that a circumbinary disk may provide the extra sink of angular momentum, as a result of gravitational torques applied onto the stellar components by the circumbinary ring. Population

synthesis calculations performed by Willems et al. (2005) find that circumbinary disks can satisfactorily provide the necessary extra angular momentum loss rates, in contrast to that provided by consequential angular momentum losses (Barker & Kolb 2003), which is not sufficient to give a theoretical minimum period cut-off of 77 minutes.

2.3.3.2 The Period Spike and CVs with Brown Dwarf Donors

The consequences of a period bounce is two-fold. Firstly, there should be a large accumulation of CVs at the location of the period minimum, i.e. the point at which CVs begin to 'bounce' towards longer orbital periods. This is a result of the the low speed in period space with which CVs are evolving through the period minimum. The probability, $\mathcal{P}$, of detecting a CV within some range in orbital period is inversely proportional to the speed with which the CV is evolving through that region. Thus,

$$\mathcal{P}(\ln P_{\rm orb}) \propto \frac{1}{\dot{P}_{\rm orb}/P_{\rm orb}}, \tag{2.14}$$

(Kolb et al. 1998). As $\dot{P}_{\rm orb}/P_{\rm orb} = 0$ at the period minimum, we can expect high detection probabilities here. A second consequence of the period minimum is the existence of CVs with brown dwarf donors which are evolving back towards long orbital periods. Indeed, population synthesis calculations show that approximately 70 per cent of the total CV population should be such 'post-bounce' CVs [de Kool (1992), Kolb (1993), Politano (1996)]. However, until recently neither the period spike (see left panel of Figure 2.2, for example) or the population of CVs with brown dwarf donors have been detected.

This has been attributed to the fact [e.g. Kolb & Baraffe (1999)] that there is a selection bias against the detection of such systems, on account of the small accretion rates in these systems [$\approx 10^{-10}$ to $\approx 10^{-12}$ $M_\odot$ yr^{-1}, King (1988)], resulting in infrequent nova outbursts (Kolb & Baraffe 1999), and low effective temperatures of the accreting white dwarfs $\approx 10\,000$ K (Townsley & Bildsten 2003).

However, the advent of the SDSS has identified approximately 200 CVs (Gänsicke et al. 2009), 4 of which have been positively identified as CVs with brown dwarf donors [Southworth et al. (2006), Littlefair et al. (2006), Littlefair et al. (2008)]. While such systems may be possible period-bouncers, it should be borne in mind that the donor mass at the period minimum can be less than the hydrogen burning limit. Hence, CVs with brown dwarf donors does not necessarily imply post-bounce systems.

The orbital periods of approximately 100 of these CVs have been determined, the distribution of which is shown in the right panel of Figure 2.2, yielding the long-elusive period spike (Gänsicke et al. 2009). This is in contrast to Willems et al. (2005), who predicted that the presence of a circumbinary disk would smear out the presence of a period spike.

The radii of the brown dwarf donors in this sample of CVs are approximately 10 per cent larger than their isolated equivalents, prompting speculation that circumbinary disks as well as gravitational radiation are driving the donors further out of thermal equilibrium (Littlefair et al. 2008). While the inclusion of a circumbinary disk (or in fact any mechanism which gives an angular momentum loss rate of the right order) can account for the larger radii, the white dwarf temperatures of between 10 000 and 15 000 Kelvin are too cool, in contrast to the enhanced mass transfer rate which a circumbinary disk would create. Nonetheless, Littlefair et al. (2008) find that the discrepancy in the brown dwarf radii, and hence the location of the period minimum, can be resolved if at least 50 per cent star-spot coverage is included.

2.4 Caveats With the Standard Evolutionary Picture

2.4.1 The Strength of Magnetic Braking

The main problem with equations (2.8) to (2.9) is that they have been derived from spin down rates of G-type stars, and are being extrapolated to M-dwarf spectral types which have rapid spin periods of a few hours. Clearly, these magnetic braking prescriptions lack a formulation which calculate the spin down rates of stars with a variety of spectral types and spin periods [see, for example, Kolb (2002)].

From the Verbunt & Zwaan (1981) form of magnetic braking, the spin down rate of the star follows $\dot{\Omega} \propto -\Omega^3$, which shows that the timescale for spin-down of rapid rotators is much shorter than for a slow rotator. Such efficient braking appears to be in contradiction with observations. Indeed, observations of the Pleiades cluster, which has an age of 110 Myr [Jones et al. (1996); Sills et al. (2000)] indicate that rapidly rotating stars still persist.

It has been suggested that for such rapid rotators with rotational periods $\leq$ 2.5 to 5

days (Andronov et al. 2003), the magnetic braking prescriptions based on equation (2.3) overestimate the angular momentum loss rate. Indeed, the observational signatures that can be used as proxies for the magnetic field strength of star, for example Hα and CaII emission lines, saturate for fast rotators.

Saturation may occur if the stellar wind is accelerated outwards as a result of centrifugal forces (Mestel & Spruit 1987). This will increase the ram pressure of the outflowing stellar wind, meaning $R_{\rm A}$ will be brought closer to the surface of the star. This will cause a weaker dependence of the angular momentum loss rate on the angular frequency of the star. Alternatively, saturation may occur if the magnetic field increases in complexity. For increasing multipole orders larger than 2, the braking efficiency decreases with increasing angular frequency (Taam & Spruit 1989). Finally, a weaker dependence of the angular momentum loss rate on Ω may occur if the stellar dynamo saturates (Collier Cameron 2002).

The magnetic braking prescriptions given by equations (2.7) to (2.9) may therefore overestimate the angular momentum loss rate in CVs. Instead, MacGregor & Brenner (1991) suggest that the angular momentum loss rate for rapidly rotating young stars in open clusters must saturate to account for them. Sills et al. (2000) consider the angular momentum loss rate given by

$$\dot{J}_{\rm MB} \propto \begin{cases} \Omega^3 & \text{for } \Omega \leq \Omega_{\rm crit}, \\ \Omega\Omega_{\rm crit}^2 & \text{for } \Omega > \Omega_{\rm crit}, \end{cases} \tag{2.15}$$

where $\Omega_{\rm crit} \approx 10\Omega_{\odot}$ (Sills et al. 2000), and $\Omega_{\odot}$ is the spin frequency of the Sun.

Andronov et al. (2003) investigate the implications that such a saturated magnetic braking law prescription would have on the evolution of CVs. It was found that the angular momentum loss rate in this saturated regime is ≈ 100 times less than that for the Verbunt & Zwaan (1981) prescription. This certainly has implications for the period gap; the angular momentum loss rate timescale in the saturated regime is on the order of the Hubble time, which is significantly longer than the Kelvin-Helmholtz timescale of the donor star. Therefore, the donor star remains in thermal equilibrium and hence does not expand as a result of mass loss. If magnetic braking was to be disrupted when the donor star became fully convective, a period gap could not arise.

Such mass transfer rates predicted by the Sills et al. (2000) form of magnetic braking, however, contradict what is observed at the upper edge of the period gap. Firstly, high mass transfer rates are required to account for the presence of nova-like CVs above the period gap

(Warner 1995). Secondly, the high white dwarf temperatures suggest high accretion rates of $\approx 10^{-9}$ $M_\odot$ yr^{-1} (Townsley & Bildsten 2003), which is consistent with predictions from the Verbunt & Zwaan (1981) form of magnetic braking.

Nonetheless, it is a well observed fact that, for a given orbital period, there is a large spread in the observed mass transfer rate, which vary by a factor of ≈ 100 (Patterson 1984) between systems. Andronov et al. (2003) argue that the calculated mass transfer rates from a saturated magnetic braking law may not agree with the observed ones, on the basis of this short term behaviour of the mass transfer rate.

An alternative magnetic braking prescription was investigated by Ivanova & Taam (2003). In comparison to the Sills et al. (2000) form of magnetic braking, Ivanova & Taam (2003) also found that the angular momentum loss rate due to magnetic braking saturates beyond some critical angular frequency, $\Omega_{\rm crit}$. Their magnetic braking prescription was obtained by considering how the X-ray luminosity due to coronal gas trapped in the dead-zone depends on Ω . The angular momentum loss rate derived is

$$\dot{J}_{\rm MB} \propto \begin{cases} \Omega^3 & \text{for } \Omega \leq \Omega_{\rm crit}, \\ \Omega^{1.3}\Omega_{\rm crit}^{1.7} & \text{for } \Omega > \Omega_{\rm crit}, \end{cases} \tag{2.16}$$

where $\Omega_{\rm crit} \approx 10\Omega_\odot$. The saturation of $\dot{J}_{\rm MB}$ was found based on the saturation of the X-ray luminosity for rapid rotation, which Ivanova & Taam (2003) argues is not necessarily a result of a saturating magnetic field. Note that in the saturated regime, there is a larger dependence of the angular momentum loss rate on the spin frequency than in equation (2.15). As a result, evolutionary timescales are found to be only a factor of ≈ 5 shorter than those predicted from the standard magnetic braking laws. The predicted mass transfer rates above the period gap are found to be ≈ 2 to 3 times smaller than that required to produce a period gap of the observed width. Thus, this prescription would not drive the donor star sufficiently out of the thermal equilibrium to create a period gap with a width of one hour.

2.4.2 The Disruption of Magnetic Braking

Not only do the standard magnetic braking prescriptions based on $\dot{J}_{\rm MB} \propto \Omega^3$ overestimate the spin-down rates of single stars in young open clusters, there is also no observational evidence for any abrupt decline in the angular momentum loss rates between stars which still have radiative cores, and those which are fully convective [Jones et al. (1996); Sills et al.

(2000)]. Instead, Sills et al. (2000) find a gradual decline in the angular momentum loss rate for stars with masses $\lesssim 0.4$ $M_{\odot}$. One of the attractive features of the disrupted magnetic braking model is that it can reproduce the sharp upper and lowers edges of the period gap if the decline in the angular momentum loss rate is rapid enough (Spruit & Ritter 1983).

Nonetheless, there are two pieces of evidence that are in favour of the disruption of magnetic braking. Firstly, if magnetic braking does drive mass transfer solely above the period gap, then we can expect the effective temperatures of the white dwarfs in CVs above the period gap to be higher than those white dwarfs below the period gap. This is indeed confirmed by Townsley & Bildsten (2003), who find the average accretion rates above and below the gap are $\approx 10^{-9}$ $M_{\odot}$ yr^{-1} and $\approx 10^{-10}$ $M_{\odot}$ yr^{-1} respectively. Clearly, the inferred mass accretion rate above the period gap suggests an angular momentum loss mechanism which acts over much shorter timescales than the saturated magnetic braking prescription found by Andronov et al. (2003).

Secondly, the disrupted magnetic braking model predicts that the donor stars in CVs above the period gap should possess radii that are larger than the radii of isolated main sequence stars of the same mass, as a result of the donors being driven out of thermal equilibrium. Furthermore, the spectral types of such donors would appear to be later than their isolated main sequence equivalents if they filled their Roche lobes at the same orbital period. This was indeed found to be the case by Beuermann et al. (1998).

Such an effect, however, could also be attributed to the fact that the donor stars in CVs have evolved off the main sequence. Theoretical arguments by Baraffe & Kolb (2000) suggested that the late spectral types of CV donors with orbital periods below approximately 6 hours can be reproduced assuming mass transfer rates obtained using the standard magnetic braking prescriptions. CV donors with orbital periods larger than 6 hours, on the other hand, were argued to be significantly evolved off the main sequence.

Patterson et al. (2005) and Knigge (2006) also observe that the mass-radius relation of donor stars in CVs above orbital periods of ≈ 3 hours lie systematically above the mass-radius relation for isolated main sequence field stars. The mass-radius relation of observed CV donors, adapted from Knigge (2006), is shown in Figure 2.4. The black symbols denote super-humping CVs, while red symbols denote eclipsing systems. Pertinent to our discussion are those CV donors which lie above the period gap at ≈ 3 hours, shown by the circles. The black solid line indicates a best fit through the data, while the dashed line is a theoretical mass-radius relation of isolated, main sequence stars. The best fit indicates that, for a given

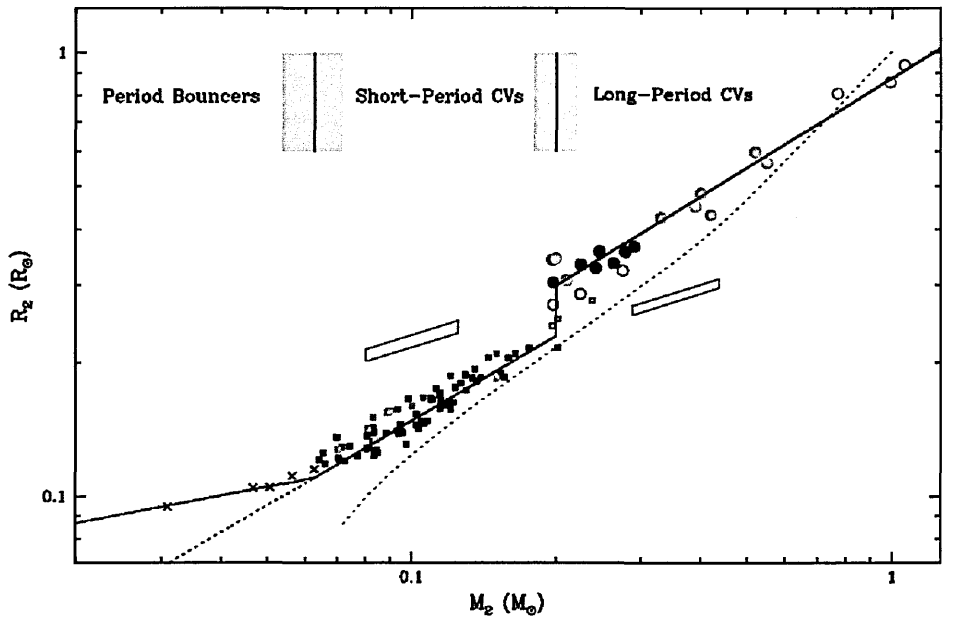

Figure 2.4: The mass-radius relation of the donor stars in the observed sample of CVs from the Ritter & Kolb (2003) catalogue, Edition 7.6 [diagram adapted from Knigge (2006)]. Black points indicate super-humping CVs, while red points are eclipsing systems. Circles: CVs which lie above the upper edge of the period gap at $\approx$ 3 hours; squares: CVs which lie below the lower edge of the period gap at $\approx$ 2 hours; crosses: post-bounce CVs; open circles: systems within the period gap, or systems which have evolved secondaries. The dotted line is a theoretical mass-radius relation for main sequence stars, while the black solid line indicates a best fit through the data.

mass, the donor stars are over-sized compared with their isolated main sequence equivalents.

Also of note is the fact that there is very little scatter in the observed mass-radius relation for the CV donors, suggesting that they evolve along a unique evolutionary track, as predicted by Stehle et al. (1996). This is in contrast to those CV donors that lie at orbital periods longer than about 6 hours (Beuermann et al. 1998). Baraffe & Kolb (2000) attributed the scatter in spectral types of the donor to the varying degrees of nuclear evolution of the donors stars from the main sequence.

Despite the sparse data, Figure 2.4 shows a tantalising hint of a discontinuity in the observed mass-radius relation at $M_2 \approx 0.2$ $M_\odot$; another feature which is predicted by the disrupted magnetic braking hypothesis.

2.4.3 An Alternative to the Disrupted Magnetic Braking Model?

A variation of the disrupted magnetic braking model has been proposed by Livio & Pringle (1994). They suggest that instead of mass loss being driven by magnetic braking which consequently drives the donor star out of thermal equilibrium, CV orbital evolution is driven by a combination of magnetic braking and consequential angular momentum losses. This is in the form of a wind emitted from the accretion disk. Livio & Pringle (1994) suggest that it is this wind that enhances the angular momentum loss rate from the CV and subsequently drives the donor out of thermal equilibrium. An increased star-spot coverage on the donor at $P_{\rm orb} \approx 3$ hours decreases the mass loss rate, decreasing the wind loss from the accretion disk, and in turn decreasing the angular momentum loss rate from the system. The reduced angular momentum loss timescale decreases sufficiently for the donor star to re-establish thermal equilibrium and shrink back to its equilibrium radius, shutting off mass transfer.

However, King & Kolb (1995) find that for this mechanism to reproduce the observed width of the period gap, mass loss at the upper edge of the period gap would be unstable to dynamical timescale mass transfer.

Alternatively, Clemens et al. (1998) suggest that it is the mass-radius exponent, ζ, for low-mass main sequence stars that plays a role in the detection probability of CVs within the period gap, compared to the detection probability on either side of it. They find that $\zeta = 1/3$ for main sequence stars with masses between approximately 0.2 and 0.3 $M_{\odot}$. CVs with such masses are undergoing mass transfer at orbital periods of ≈ 2 and 3 hours respectively; the approximate location of the period gap edges.

As shown by equations (2.13) and (2.14), by decreasing ζ from 1 to 1/3 at the edges of the period gap, the CV detection probability increases at these points. However, far from reproducing the period gap, Kolb et al. (1998) find that this prescription merely produces two spikes at about 2 and 3 hours, similar to the period spike which is proposed to lie at the period minimum. Furthermore, the predicted number of CVs lying in the range $2 \lesssim P_{\rm orb}/{\rm hours} \lesssim 3$ is approximately equal to that found on either side of this range. This is in contrast to the observed period gap, which shows a deficit of CVs compared to the population on either side of the period gap.

Rather than considering the occurrence of the period gap as a result of a decreased detection probability there, Willems et al. (2007) consider the evolution of CVs due to

circumbinary discs. They suggest that the angular momentum loss timescale due to circumbinary discs is sufficiently short to drive the donor star out of thermal equilibrium, causing them at orbital periods between 3 and 4 hours to evolve back towards longer orbital periods. This, Willems et al. (2007) suggest, may be responsible for the upper edge of the period gap.

However, Willems et al. (2005) were not able to satisfactorily reproduce the sharp, lower edge of the period gap. Indeed, as a result of systems bouncing at orbital periods above the upper edge of the period gap, few or no CVs would be able to evolve to shorter orbital periods below the period gap. Willems et al. (2005) had to artificially re-create the lower edge of the period gap by increasing the formation rate of CVs at this location by a factor of about 100.

2.5 Testing the Disruption of Magnetic Braking

As discussed above, there is intriguing evidence in favour of the disruption of magnetic braking. Yet it is an hypothesis that, despite its ubiquity in the literature as a likely cause for the period gap, has not been rigorously tested.

Recently Politano & Weiler (2006) calculated the secondary star mass distribution of the present day population of post-common envelope binaries (PCEBs, see Chapter 3) for a range of angular momentum loss prescriptions, including disrupted magnetic braking where equation (2.8) was used to calculate the angular momentum loss rate.

They found that the number of PCEBs per secondary mass interval decreases by 38 per cent once magnetic braking begins to drive their evolution for secondaries with radiative cores. They suggest that this decrease in the number of PCEBs with secondaries between ~ 0.25 and 0.5 $M_{\odot}$ provides an observable test for the disruption of magnetic braking.

However, we suggest an alternative, even more direct, test for the disruption of magnetic braking by investigating its explicit consequence: the existence of a population of white dwarf-main sequence star (WD+MS) binaries that were CVs in the past but became detached at $P_{\rm orb}/{\rm hours} \approx 3$ and are currently crossing the period gap, which we call dCVs

(for 'detached CVs'). However, the main challenge is to distinguish between the two varieties of WD+MS binaries. Our method for carrying out this test is described in Chapter 5.

Before we go on to describe the method we use to test the disruption of magnetic braking (see Chapters 4 and 5), we must first describe how CVs are formed, which exploits the concepts described in the present chapter.

3

The Common Envelope Phase

The existence of CVs presents a paradox; while the typical orbital separation of CVs is $a \lesssim R_{\odot}$, an orbital separation of between approximately 10 and 1000 $R_{\odot}$ was required to accommodate the progenitor giant of the white dwarf. Clearly, the white dwarf could not have formed within a system with orbital separations typical for those of CVs. Instead, some process must have occurred to drastically reduce the orbital separation of the progenitor binary system, containing the giant progenitor primary star.

A hint at the possible mechanism behind the process lies within systems such as V471 Tau; a WD+MS binary with an orbital separation of approximately 3 $R_{\odot}$ within a planetary nebulae, which may have formed from a progenitor binary with an orbital separation of approximately 600 $R_{\odot}$ [see, e.g. Webbink (2008)]. The existence of this system motivated Paczynski (1976) to suggest that large amounts of orbital energy, and therefore orbital angular momentum, are removed from the binary's orbit as a result of friction between the stellar components of the progenitor binary and material encompassing both of the stellar components. Such a process would leave behind a binary with a greatly reduced orbital separation and the planetary nebula. The process has been coined the common envelope (CE) phase, which we will now discuss in this chapter.

We begin in Section 3.1 by discussing how the CE forms, while in Section 3.2 we describe in detail the interaction between the binary and the CE and how this gives rise to the

eventual ejection of the CE from the system. In Section 3.3, we then discuss how the CE phase is modelled using parameterisations, usually in terms of the binary's orbital energy, or the binary's orbital angular momentum. Finally, in Section 3.4, we describe the pre-CV phase, which is the life of the CV progenitor between the point when it leaves the CE phase, and when the binary commences mass transfer as a CV.

3.1 Formation of the Common Envelope

As a CV contains a white dwarf primary and a main sequence secondary, then clearly the ZAMS primary star must have been more massive than the initial ZAMS secondary. This is illustrated in Figure 3.1(a). As a result, the main sequence primary would have evolved off the main sequence first and ascended the giant branch.

However, as discussed in Section 1.1, the presence of the secondary star will limit the extent to which the giant progenitor star can expand along the giant, or asymptotic giant, branch before the primary fills its Roche lobe and commences mass transfer to the companion secondary. This stage is shown in Figure 3.1(b). Indeed, the maximum orbital period a progenitor binary can have in order to commence mass transfer is calculated to be approximately 10^3 days [Willems & Kolb (2004); Politano & Weiler (2007)].

The consequences of this mass transfer are as follows. Assuming conservative mass transfer with $-\dot{M}_1 = \dot{M}_2$ and $\dot{J} = 0$, then we can use equation (1.29) to describe how the orbital separation evolves as a result of mass transfer from the primary giant to the main sequence companion. Thus, we have

$$\frac{\dot{a}}{a} = -\frac{2\dot{M}_1}{M_1}\left(1 - \frac{M_1}{M_2}\right). \tag{3.1}$$

As $M_1 > M_2$, then mass transfer from the giant to the secondary results in the orbital separation shrinking i.e. $\dot{a}/a < 0$. Hence, from equation (1.10) or (1.11) the Roche lobe radius of the primary giant will also shrink. The resulting mass transfer is stable only if the primary giant's radius can shrink more rapidly than the Roche lobe. However, giant and asymptotic giant branch stars possess deep convective envelopes and, in comparison to main sequence stars with substantial convective envelopes, expand adiabatically as a result of mass loss, i.e. $\zeta_{\rm ad} < 0$. Based on polytropic models, Hjellming & Webbink (1987) find that giant stars with core mass fractions $\lesssim 0.21$ will expand significantly as a result of

mass loss. More realistic stellar models by Hjellming (1989) find that a giant possessing a convective envelope which is $\gtrsim$ 50 per cent of the giant's total mass will also undergo dramatic expansion as a result of mass loss.

From equation (1.38), we can derive the critical mass ratio, $Q = M_1/M_2 = Q_{\rm crit}$, for which the resulting mass transfer is just dynamically stable. Replacing ζ in equation (1.38) with $\zeta_{\rm ad} = -1/3$, which is the typical value for giant stars (Hjellming & Webbink 1987), we find that $Q_{\rm crit} \approx 0.7$ [see also Iben & Livio (1993)]. As CV secondaries typically have $M_2 \lesssim 1$ M$_\odot$ [King (1988); Warner (1995)], and progenitor primaries with masses in the range $0.8 < M_1/{\rm M}_\odot \lesssim 7$ [e.g. Hurley et al. (2000)] are required to form a white dwarf, then we can see that the progenitors of CVs have $Q > Q_{\rm crit}$. Thus, the Roche lobe radius of the mass losing giant shrinks more rapidly than the giant's radius and the criterion for dynamically unstable mass transfer according to equation (1.24) is satisfied. Indeed, the combination of the expansion of the giant's radius due to mass loss, and the further decrease in its Roche lobe radius produces a run-away situation. This results in mass transfer rates of $-\dot{M}_1 \approx 1$ M$_\odot$ yr^{-1} [e.g. Ritter (2008)] and a correspondingly small mass transfer timescale, $\tau_{\dot{M}}$, of a few years.

Clearly, such large mass transfer rates have implications for the accreting main sequence companion. Firstly, the gravitational potential energy of the in-falling material will be converted into kinetic energy resulting in the deposition of hot layers of approximately 10^6 to 10^7 K (Meyer & Meyer-Hofmeister 1979) onto the surface of the secondary. Secondly, from equation (1.19), $\tau_{\rm KH} \gtrsim 10^7$ years for $M_2 \lesssim 1$ M$_\odot$. As a result these outer accreting layers have insufficient time to cool, and form a deep convective layer on top of the secondary star, similar to a convective envelope of a giant, or asymptotic giant, branch star. These layers will subsequently expand, causing the secondary to fill its own Roche lobe (Kippenhahn & Meyer-Hofmeister 1977), as shown in Figure 3.1(c).

As a result of both the secondary and the primary star having filled their Roche lobes, the binary resembles a contact binary akin to W Ursa Majoris systems. However, the continual mass transfer, and expansion of the secondary star will result in the accreting layers expanding beyond the critical Roche lobe of the secondary, and ultimately surrounding both the secondary star and the core of the giant star, as depicted in Figure 3.1(d). This material is the CE.

3.2 Common Envelope Evolution

3.2.1 Rapid In-Fall Phase

In contrast to the W Ursa Majoris systems, however, the CE surrounding both of the stellar components may not be necessarily co-rotating with the binary orbit. While tidal forces act to synchronise the rotation of the stellar components, the giant star can never be synchronised if the moment of inertia of its outer envelope, $I_{\rm env}$ is too large. Indeed, if $I_{\rm orb}$ is the moment of inertia of the binary's orbit, then the giant can never be synchronised to the orbital period if

$$I_{\rm env} > \frac{1}{3} I_{\rm orb}, \tag{3.2}$$

[e.g. Webbink (1985); Ritter (2008)]. This criterion is satisfied for those systems which have mass ratios $Q = M_1/M_2 \gtrsim 5 - 6$.

As a consequence of the mass transfer from the primary giant to the secondary, the binary orbit will shrink and the secondary will plunge into the envelope of the giant. If $\Omega_{\rm env}$ is the rotational frequency of the giant's envelope, then in general $\Omega > \Omega_{\rm env}$, and as such the orbit of the secondary companion will act to spin up the CE. If $\langle\rho\rangle$ is the average density of the CE in the vicinity of the secondary star and $v_{\rm rel}$ is the relative velocity between the secondary star and the CE, then the secondary will encounter a drag force, $F_{\rm drag}$, given by

$$F_{\rm drag} \approx \pi {R_{\rm acc}}^2 \langle\rho\rangle v_{\rm rel}^2, \tag{3.3}$$

(Taam & Spruit 1989) where $R_{\rm acc}$ is the Bondi-Hoyle accretion radius, given by

$$R_{\rm acc} = \frac{2GM_2}{v_{\rm rel}^2 + {c_{\rm s}}^2}, \tag{3.4}$$

where $c_{\rm s}$ is the local sound speed of the CE material. The origin of the drag is a result of the high density material in the secondary star's wake. The resulting rate at which energy is liberated, $L_{\rm drag}$, is therefore

$$\begin{aligned} L_{\rm drag} &= F_{\rm drag} v_{\rm rel} \\ &\approx \pi R_{\rm acc}^2 \langle\rho\rangle v_{\rm rel}^3. \end{aligned} \tag{3.5}$$

As a result of this frictional drag, orbital energy is lost and the orbital separation between the core of the giant (i.e the future white dwarf) and the secondary companion will decrease. The binary's orbital energy is transferred to the CE as kinetic energy (i.e. by spinning it up)

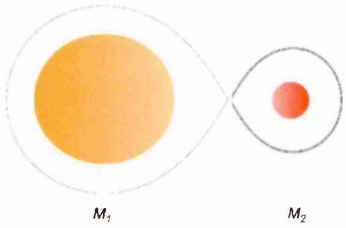

(a) A binary system initially consisting of a ZAMS primary and secondary star of mass M_1 and M_2 respectively. Note that the binary is detached.

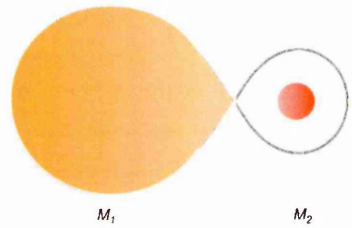

(b) Because $M_1 > M_2$, the primary evolves off the main sequence first. Depending on the orbital separation, the primary will fill its Roche lobe on either the giant or asymptotic giant branch for a CE to occur.

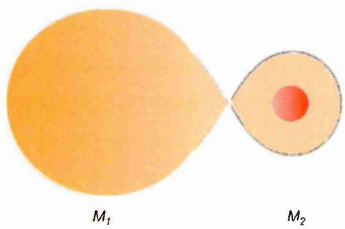

(c) Due to the dynamical timescale mass transfer, the accreting layers on the secondary do not have sufficient time to cool, and instead expand. The secondary subsequently fills its own Roche lobe.

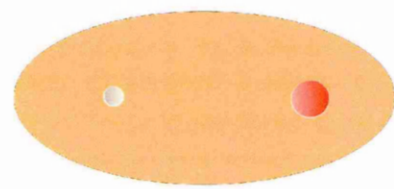

(d) The envelope of the giant primary surrounds both the secondary star and the core of the giant. Friction between the stellar components and the envelope provides a torque

(e) The torque removes angular momentum and energy from the orbit, greatly reducing the binary separation. If enough energy is imparted onto the CE it may be ejected from the system leaving a white dwarf-main sequence system.

Figure 3.1: Common Envelope evolution

and gravitational potential energy (in order to drive the CE out of the binary's gravitational potential well).

This orbital energy must be efficiently turned into mass motions within the CE before this energy can be transported to the surface of the CE and radiated away. In other words, the ejection process must be adiabatic. The duration of the CE phase, $\tau_{\rm CE}$, can be estimated from the time taken for the energy generated during the CE phase, $L_{\rm drag}$, to unbind the CE from the system, where the change in the binding energy is $\Delta E_{\rm bind}$. If $A_{\rm CE,i}$ and $A_{\rm CE,f}$ is the binary orbital separation immediately before and after the CE phase, and $A_{\rm CE,f} << A_{\rm CE,i}$, then the binding energy can be approximated from the amount of orbital energy released during the CE phase, $\Delta E_{\rm orb}$, given by

$$\begin{aligned} \Delta E_{\rm bind} &\approx \Delta E_{\rm orb} \\ &\approx \frac{GM_{\rm c}M_2}{2A_{\rm CE,f}}, \end{aligned} \tag{3.6}$$

where $M_{\rm c}$ is the mass of the giant's core (i.e. the white dwarf). During the initial spiral-in stage, $L_{\rm drag} \approx 10^6$ L$_\odot$ (Taam & Spruit 1989). Thus, $\tau_{\rm CE}$ is approximated by

$$\begin{aligned} \tau_{\rm CE} &\approx \frac{\Delta E_{\rm orb}}{L_{\rm drag}} \\ &\approx 200 \frac{M_{\rm c}}{\rm M_\odot} \frac{M_2}{\rm M_\odot} \frac{\rm R_\odot}{A_{\rm CE,f}} \text{ years}, \end{aligned} \tag{3.7}$$

[e.g. Iben & Livio (1993); Ritter (2008)], showing that the CE phase is clearly a rapid process.

This initial spiral-in of the secondary star into the CE, which lasts on a timescale of approximately 1 year (Sandquist et al. 1998), is responsible for a significant transfer of angular momentum and energy from the binary orbit to the CE. The ejection rate is typically about 0.3 M$_\odot$ yr^{-1} (Taam 2002). This mass ejection also carries away the binary's orbital angular momentum in the form of tightly wound spiral shocks (Sandquist et al. 1998), which expand away from the binary due to centrifugal forces. The result of this is that material is ejected from the system preferentially along the equatorial plane of the binary orbit [Sandquist et al. (1998); Sandquist et al. (2000)].

As a result of the material being ejected from the binary system, the location of the centre of mass between the stellar components will shift. As such the core of the giant is displaced from the centre of the CE (i.e. the giant's envelope) and will exhibit motion about the new location of the centre of mass [e.g. Rasio & Livio (1996)]. The motion of material between the core of the giant and the CE will also aid in the ejection process.

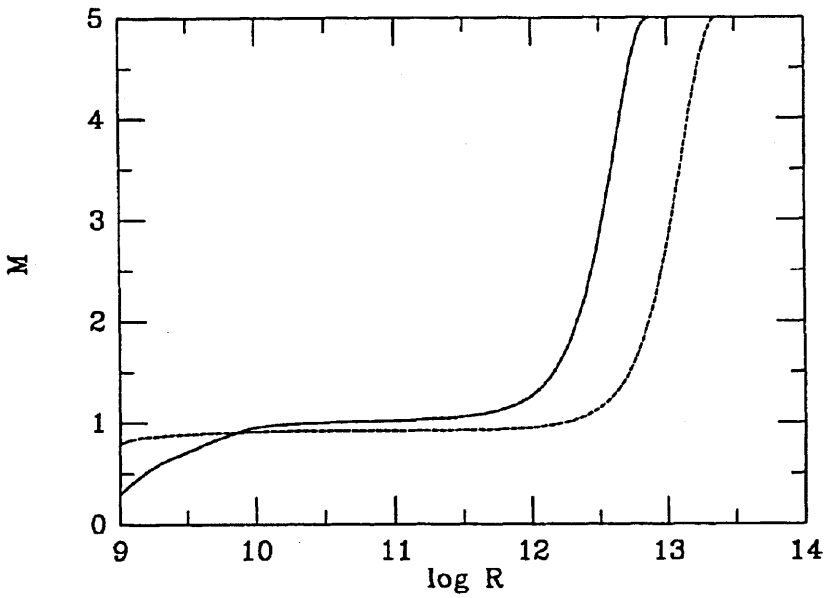

Figure 3.2: Mass-radius profile of a 5 $M_\odot$ giant star where the carbon-oxygen core is about to form (solid curve), and of the same giant but at a later phase in its evolution where it has a 0.8 $M_\odot$ carbon-oxygen core (dashed curve). The mass, M, contained within a radius R is in solar masses, while the radius, R, is in cm. Figure from Yorke et al. (1995).

3.2.2 Termination of the CE Phase

In order for the binary system to survive the CE phase, a sufficient amount of orbital energy must have been lost in order to unbind the CE from the system before the core of the giant and the secondary companion merge. That is to say, the timescale for CE ejection is shorter than the orbital decay timescale of the orbit.

A merger may be avoided if, as a result of the CE ejection process, the CE density in the locality of the stellar components has been reduced sufficiently. From equation (3.5) this has the effect of decreasing the energy dissipation rate from the orbit, thereby increasing the orbital decay timescale. For the case of CV progenitors undergoing a CE phase, the orbital decay timescale increases to approximately a few decades (Sandquist et al. 1998).

An increase in the orbital decay timescale may also be aided by the spinning up of the CE material in the vicinity of the two stellar components. This has the effect of decreasing $v_{\rm vel}$ between the stars, and hence decreasing $L_{\rm drag}$. However, it is uncertain how much of a role this plays in the survival of the binary as the CE was found to attain a angular frequency of between approximately 10 per cent (Sandquist et al. 2000) and 40 per cent (Terman et al.

1994) of the binary's angular frequency.

It has been argued that it is the structure of the giant's envelope which plays a major role in determining the outcome of the CE phase [e.g. Taam & Bodenheimer (1991)]. To illustrate this, Figure 3.2 shows the mass-radius profile of a 5 $M_\odot$ giant star at two different phases in its evolution (Yorke et al. 1995). The solid curve corresponds to a phase in the giant's evolution where a carbon-oxygen core is about to form, while the dashed curve corresponds to a later stage in the giant's evolution as it possesses a 0.8 $M_\odot$ carbon-oxygen core.

In both cases, the majority of the envelope mass is contained in the outer layers of the giant. At distances $\log_{10}(R/\text{ cm}) \lesssim 12$ (for the less evolved giant) and $\log_{10}(R/\text{ cm}) \lesssim 12.5$ (for the more evolved giant), the profile is approximately flat. Thus, the secondary companion reaching these locations would encounter little material, resulting in a decrease in the energy dissipation rate and an increase in the orbital decay timescale.

Indeed, Yorke et al. (1995) argue that a system is less likely to avoid a merger for more evolved giants because the location of where the constant mass-radius profile starts [1] lies at a greater distance from the core (as can be seen by comparing the solid and dashed curve in Figure 3.2). Furthermore, the constant mass-radius profile extends deeper into the interior of the more evolved giant. The envelopes of more evolved giants are also less tightly bound to the giant, hence further facilitating successful ejection of the CE before a merger occurs.

Therefore, once the secondary star reaches the point at which the mass-radius profile becomes flat, then the energy dissipation rate will significantly decrease. In turn, the orbital decay will dramatically decelerate. Furthermore, because the profile becomes flat at further distances from the giant's core for more evolved giant's, then the deceleration of secondary's orbital decay will begin at correspondingly further distances from the giant's core. The more extensive constant profile for more evolved giants will also facilitate the deceleration of the secondary's orbit for greater distances into the interior, further decreasing the chances of a merger. Indeed, as pointed out by Terman et al. (1995), the orbital decay does not cease immediately at the point the mass-radius profile becomes flat.

Taam & Bodenheimer (1991) and Sandquist et al. (2000) find that first giant branch stars with helium cores more massive than between approximately 0.25 and 0.35 $M_\odot$, and 5 $M_\odot$ asymptotic giant branch stars with carbon-oxygen cores more massive than about 1 $M_\odot$, possess such a constant mass-radius profile. Hence, systems possessing such giants are more

[1] As seen by the secondary companion as it plunges into the giant's envelope.

likely to avoid a merger compared to systems with giants having helium or carbon/ oxygen white dwarfs less massive than the corresponding limits given above. The implications of this, as noted by Terman et al. (1995), is that those systems which have more massive white dwarfs will emerge from the CE phase with longer orbital separations. As noted above, however, the point at which the binary orbit sufficiently decelerates does not exactly coincide with the location where the mass-radius profile of the giant becomes constant. Instead Terman et al. (1995) find that this point is a factor of 3 to 10 times smaller than where this constant profile appears. This last point is graphically illustrated in Figure 3.3 [from Terman et al. (1995)], which shows the predicted orbital separation of different systems immediately after the CE phase, for different core masses. Terman et al. (1995) assume that the orbital decay sufficiently decelerates at 1/6 of the distance from the core to where the mass-radius profile becomes flat.

However, it must be emphasised that the envelope must be unbound from the system by the time the secondary reaches the constant mass-radius profile. As pointed out by Sandquist et al. (1998), more massive giants will possess more massive envelopes, which must be ejected from deeper gravitational wells. Thus, from equations (3.4) and (3.5) if the secondary star is not massive enough, then insufficient energy dissipation will be generated to unbind the envelope.

3.3 Modelling of the Common Envelope Phase

Despite extensive three-dimensional hydrodynamical modelling of the CE phase [for a review see Taam (2002)], the underlying physics remains poorly understood [see e.g. Webbink (2008)]. This is mainly as a result of the wide range in length scales (from $\lesssim 1\ R_\odot$ to a few astronomical units) and timescales (few hours to several years) that need to be considered to adequately model the CE phase [e.g. Taam & Sandquist (2000)]. Therefore, any thorough modelling of the CE phase is too computationally intensive to incorporate into theoretical calculations describing the formation and evolution of CVs.

One common method used to model the CE phase considers the energy budget available

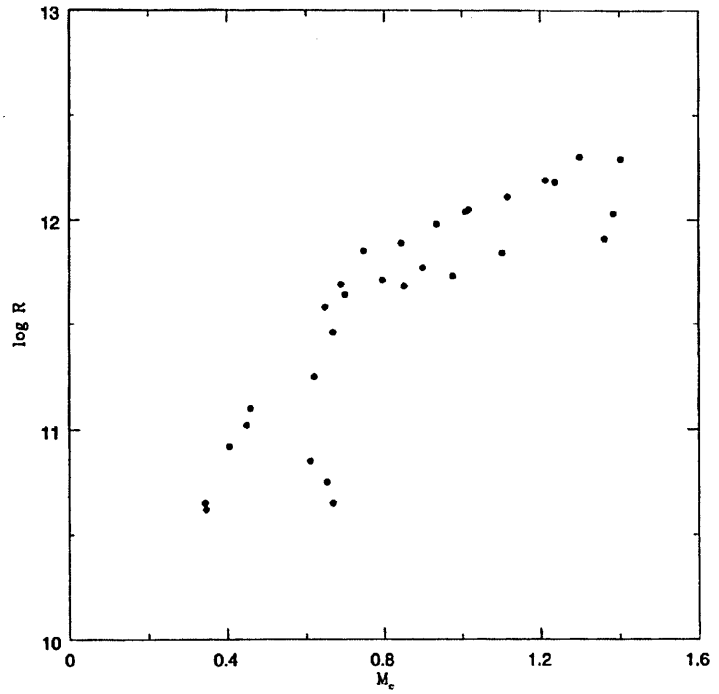

Figure 3.3: Core mass, M_c, (in solar masses) versus the orbital separation, R, (in cm) after the CE phase (Terman et al. 1995). The orbital separations have been calculated assuming that the orbital decay ceases at 1/6 of the distance from the core to where the mass-radius profile first becomes flat.

to the binary to unbind the envelope from the core of the primary. As stated in Section 3.2, the binary loses orbital energy as the stellar components spiral together. If sufficient orbital energy is imparted onto the envelope, then it may be unbound completely from the system [c.f. equation (3.6)].

If some fraction $\alpha_{\rm CE}$ of the orbital energy lost by the binary during the CE phase is used to unbind the envelope from the system, then from the first approximate form of equation (3.6), we get

$$\Delta E_{\rm bind} = \alpha_{\rm CE} \Delta E_{\rm orb}, \tag{3.8}$$

[e.g. (Livio & Soker 1988)], where $0 < \alpha_{\rm CE} \leq 1$.

The total orbital energy of the binary system is the sum of the kinetic energy of the stellar components as they orbit about the common centre of mass, and the gravitational potential energy of the binary. For a binary system which is just commencing the CE phase, with primary mass $M_1 = M_c + M_{\rm env}$ (where $M_{\rm env}$ is the mass of the giant's envelope), secondary

mass M_2 then the total orbital energy of the binary, $E_{\rm orb,i}$, is

$$E_{\rm orb,i} = -\frac{GM_1M_2}{2A_{\rm CE,i}}. \tag{3.9}$$

Once the CE is ejected, leaving the core of the giant (i.e. the future white dwarf) with the original secondary companion then the final orbital energy, $E_{\rm orb,f}$ is given by the second approximate expression in equation (3.6). The orbital energy lost by the binary during the CE phase is therefore given by

$$\Delta E_{\rm orb} = \frac{GM_{\rm c}M_2}{2A_{\rm CE,f}} - \frac{GM_1M_2}{2A_{\rm CE,i}}. \tag{3.10}$$

If $M_1(r)$ is the mass contained within the radius r of the primary giant star, then the gravitational binding energy, $E_{\rm bind}$, of the giant's envelope is given by

$$E_{\rm bind} = -\int_{M_{\rm c}}^{M_1} \frac{GM_1(r)}{r}{\rm d}m, \tag{3.11}$$

[e.g. Dewi & Tauris (2000)]. To evaluate equation (3.11) we require knowledge of the internal structure of the primary star in order to obtain $M_1(r)$. As this is not always possible in theoretical studies of CV formation, the binding energy can instead be expressed as

$$E_{\rm bind} = -\frac{GM_1M_{\rm env}}{\lambda_{\rm CE}R_1}, \tag{3.12}$$

[de Kool (1992); de Kool & Ritter (1993); Willems & Kolb (2004); Politano & Weiler (2007)] where $\lambda_{\rm CE}$ is the ratio of the approximate expression of the binding energy, $GM_1M_{\rm env}/R_1$, and the exact expression given by equation (3.11).

By combining equations (3.8), (3.10) and (3.12) we get

$$\frac{GM_1M_{\rm env}}{\lambda_{\rm CE}R_1} = \alpha_{\rm CE}\left(\frac{GM_2M_{\rm c}}{2A_{\rm CE,f}} - \frac{GM_2M_1}{2A_{\rm CE,i}}\right). \tag{3.13}$$

In computational models we will have knowledge of the initial binary parameters at the start of the CE phase. Hence, from equation (3.13) we can solve for $A_{\rm CE,f}$. Note also that the prescription according to equation (3.13) assumes that the mass of the secondary is constant throughout the CE phase. Hjellming & Taam (1991) have demonstrated that this is a good approximation, as the net change in the mass of a main sequence companion star during the CE phase is estimated to be $\lesssim 0.01$ M$_\odot$. Furthermore, because the secondary is being plunged into hydrogen rich material of the CE, Hjellming & Taam (1991) argue that there is little change in the surface composition of the secondary after the CE phase.

The greatest uncertainty in this parameterisation therefore lies within the product $\alpha_{\rm CE}\lambda_{\rm CE}$. As stated above, while $\lambda_{\rm CE}$ can usually be calculated from full stellar evolution models [e.g.

Dewi & Tauris (2000)], the physics pertaining to the CE ejection efficiency, and hence the value of $\alpha_{\rm CE}$, is far less certain. Indeed, the efficiency with which the envelope is ejected from the binary system requires knowledge of how efficiently the drag luminosity due to the orbital motion of the stellar components is transported to the surface of the CE, and subsequently radiated away. Furthermore, we also need to know if the orbital motion of the binary affects spin up of the CE locally, or over large portions of the envelope. Indeed, the former case tends to lower the ejection efficiency as small amounts of CE material is given a velocity greatly exceeding the escape speed (Livio & Soker 1988). Modelling of the CE phase estimates that $\alpha_{\rm CE} = 0.1$ to 0.6 (Iben & Livio 1993).

As a result of the ill-constrained values of $\alpha_{\rm CE}$, theoretical models of the CE phase based on equation (3.13) have had to resort to calculations which consider a wide range of constant, global values of $\alpha_{\rm CE}$ [e.g. de Kool (1992); de Kool & Ritter (1993); Willems & Kolb (2004); Willems et al. (2005); Willems et al. (2007) in the context of CVs and pre-CVs]. Such calculations also consider constant, global values of $\lambda_{\rm CE} = 0.5$. In other words, the same value of the product $\alpha_{\rm CE}\lambda_{\rm CE}$ is assumed to apply to all binary systems undergoing a CE phase, irrespective of the structure of the progenitor primary giant, and the mass of the immersed secondary star. This is in contrast to Yorke et al. (1995) who suggest $\alpha_{\rm CE}$ will vary from system to system, as the ejection process will depend on the location at which the mass-radius profile of the giant's envelope will be sufficiently flat.

Furthermore, as shown by equations (3.4) and (3.5), the energy dissipation rate decreases for decreasing secondary mass. This has prompted Politano & Weiler (2007) to suggest that $\alpha_{\rm CE}$ is a function of the secondary's mass. This suggestion was motivated by the fact that only about 3 per cent of the current observed population of CVs have brown dwarf secondaries with orbital periods below approximately 77 minutes. This is in stark contrast to Politano (2004) who predicted that such systems should make up approximately 15 per cent of the total zero-age CV population. Politano (2004) suggested that this discrepancy may be a result of the decreasing energy dissipation rate of orbital energy with the CE for decreasing secondary mass, and that below come cut-off mass, $M_{\rm cut}$, a CE merger would be unavoidable. As such they consider the function

$$\alpha_{\rm CE} = \begin{cases} 1 - \frac{M_{\rm cut}}{M_2} & M_2 > M_{\rm cut} \\ 0 & M_2 \leq M_{\rm cut} \end{cases} \tag{3.14}$$

Politano & Weiler (2007) consider a second functional form of $\alpha_{\rm CE}$, which is given by

$$\alpha_{\rm CE} = \left(\frac{M_2}{\rm M_\odot}\right)^p, \tag{3.15}$$

where p is a free parameter.

The standard theoretical description of the CE phase according to equation (3.13), however, has recently been challenged by the observed sample of post-CE binaries, particularly those systems which have two white dwarf components. In contrast to CVs, double white dwarf binaries form via two phases of mass transfer [e.g. Nelemans & Tout (2005)].

Nelemans et al. (2000) find that while equation (3.13) can adequately describe the second CE phase during the formation of the observed population of double white dwarf binaries, it nonetheless predicts a CE ejection efficiency of $\alpha_{\rm CE} > 1$ for this CE phase. This implies that gravitational potential energy of the binary orbit may not be the only source of energy being exploited during the ejection of the envelope. Instead, Han et al. (2002), Dewi & Tauris (2000) and Webbink (2008) suggest that this extra source of energy may exist as thermal energy, including the recombination energy of ionized material within the giant's envelope. If u is the thermal energy per unit mass of material in the CE, then we would have to add an extra term to equation (3.11) due to the thermal energy of the envelope, $E_{\rm th}$,

$$E_{\rm th} = \int_{M_{\rm c}}^{M_1} u \, {\rm d}m. \tag{3.16}$$

This would have the effect of increasing the value of $\lambda_{\rm CE}$ in equation (3.12). Indeed, Dewi & Tauris (2000) suggested that the constant values of $\lambda_{\rm CE} = 0.5$ typically used in CE modelling [e.g. Willems & Kolb (2004)], may overestimate the binding energy of the giant's envelope, and hence overestimate the amount of spiral-in (and therefore the orbital energy) of the binary required to eject the CE.

However, Sandquist et al. (2000) suggest that the ionization energy of the outer layers of the giant's envelope may contribute insignificantly to the ejection of the CE. While ionized hydrogen contributes significantly to the opacity at the base of the ionization zone in the giant's envelope, the fraction of recombined hydrogen increases towards the surface as the temperature decreases. This causes a correspondingly sharp drop in the opacity towards the surface of the giant (Harpaz 1998). Therefore, rather than the emitted radiation efficiently pushing against these layers to eject it, the radiation can just freely escape.

Taam & Spruit (1989) and Yorke et al. (1995) demonstrated that during the CE phase, a closed loop of CE material is circulated in the vicinity of the giant core. Taam & Spruit

(1989) suggested that if this hydrogen rich material is mixed within the helium burning shell, or carbon from the helium burning shell is mixed with the hydrogen burning shell, then this would enhance nuclear reaction rates, and the resulting energy released could aid the CE ejection process.

More problematic, equation (3.13) predicts values of $\alpha_{\rm CE}\lambda_{\rm CE} < 0$ for the first CE phase in the formation of double white dwarf binaries, which is clearly unphysical. In fact a value $\alpha_{\rm CE}\lambda_{\rm CE} < 0$ implies that instead of the binary losing orbital energy during the CE phase, the binary in fact gains orbital energy. Nelemans et al. (2000) suggested instead that the first phase of mass transfer was stable, rather than one leading to a CE phase. However, this predicts orbital periods which are too short compared to those of observed double white dwarf binaries.

The apparent shortcomings in the CE formalism given by equation (3.13) led Nelemans et al. (2000) to describe the CE phase in terms of the change in the binary's total angular momentum ΔJ during the CE phase, as opposed to the change in the binary's orbital energy $\Delta E_{\rm orb}$. Their prescription is based on equation (1.42). If J is the total angular momentum of the binary just at the onset of the CE phase, and $M_{\rm b}$ is the binary's mass at this point, and the binary loses mass ΔM during the CE phase, then from equation (1.42) we have

$$\Delta J = \gamma_{\rm CE}\frac{J\Delta M}{M_{\rm b}}, \tag{3.17}$$

where, $\Delta M = M_1 - M_{\rm c}$, i.e. the mass of the primary giant's convective envelope, $M_{\rm env}$, and $\gamma_{\rm CE}$ is the specific angular momentum of the ejected CE in units of the specific angular momentum of the binary system at the onset of the CE phase. Nelemans & Tout (2005) find that a value of $\gamma_{\rm CE} \approx 1.5$ could account for the observed sample of double white dwarf binaries and PCEBs. However, Nelemans & Tout (2005) do not offer a physical justification for either the value of $\gamma_{\rm CE} \approx 1.5$, or for the formalism according to equation (3.17).

As the accretion onto the companion star at the onset of the CE phase will clearly exceed the Eddington limit, King & Begelman (1999) suggest that a CE phase may be avoided if the accretion rate reaches the Eddington limit at a point within the accreting companion's Roche lobe. Instead the CE is ejected via radiation driven winds. If the Eddington limit is attained at a point outside the accretor's Roche lobe, then the CE phase is unavoidable. It is this wind loss from the accreting companion, which Beer et al. (2007) suggests as the physical justification for the prescription according to equation (3.17).

3.4 The Pre-CV Phase

If the binary system has survived the CE phase (i.e. the CE has been ejected from the system without the merging of the stellar components), then we are left with a WD+MS binary system with a greatly reduced orbital separation, as shown in Figure 3.1(e). We call such systems that have formed from a CE phase post-CE binaries (PCEBs). Such systems are detached, however, with orbital periods between approximately 1 hour to 1000 days, with the bulk of PCEBs lying at approximately 1 day [Willems & Kolb (2004); Politano & Weiler (2007)]. As such, the Roche lobe radius of the secondary star is larger than the secondary's stellar radius.

In order for the secondary to come into contact with its Roche lobe and commence mass transfer as a CV, the Roche lobe radius must shrink about the secondary star. For $\dot{M}_1 = \dot{M}_2 = 0$ in equations (1.29) and (1.31), then the evolution of the binary's orbital angular momentum can be related to the evolution of the secondary's Roche lobe radius according to

$$\frac{\dot{J}}{J} = \frac{1}{2}\frac{\dot{R}_{\mathrm{L},2}}{R_{\mathrm{L},2}}. \tag{3.18}$$

As we require the Roche lobe radius to shrink ($\dot{R}_{\mathrm{L},2}/R_{\mathrm{L},2} < 0$) then the binary orbit must lose orbital angular momentum. In comparison to CVs, this is in the form of systemic angular momentum losses, and so $\dot{J}/J = (\dot{J}/J)_{\mathrm{sys}}$. For WD+MS binaries which have secondaries which are not fully convective, i.e. $M_2 > M_{\mathrm{MS,conv}} = 0.35\ \mathrm{M}_{\odot}$ (Hurley et al. 2002), then, according to the standard disrupted magnetic braking prescription described in Section 2.3.1, WD+MS systems will be driven by a combination of magnetic braking and gravitational radiation. Conversely, for those WD+MS with secondaries which satisfy $M_2 \leq M_{\mathrm{MS,conv}}$, their orbital evolution will be driven purely by gravitational radiation.

While all PCEBs will become semi-detached given sufficient time, only those systems which will become semi-detached within the lifetime of the Galaxy, t_{gal}, (and only those systems which commence dynamically and thermally stable mass transfer), are representative progenitors of the CV population which we currently observe [e.g. Schreiber & Gänsicke (2003)]. We call these systems pre-CVs. This clearly imposes an upper limit on the post-CE orbital period which a PCEB can have if it is to become semi-detached within 10 Gyr. Now the evolution of a PCEB, as given by equation (3.18), can be re-written as

$$\left(\frac{\dot{J}}{J}\right)_{\mathrm{sys}} = \frac{1}{3}\frac{\dot{P}_{\mathrm{orb}}}{P_{\mathrm{orb}}}. \tag{3.19}$$

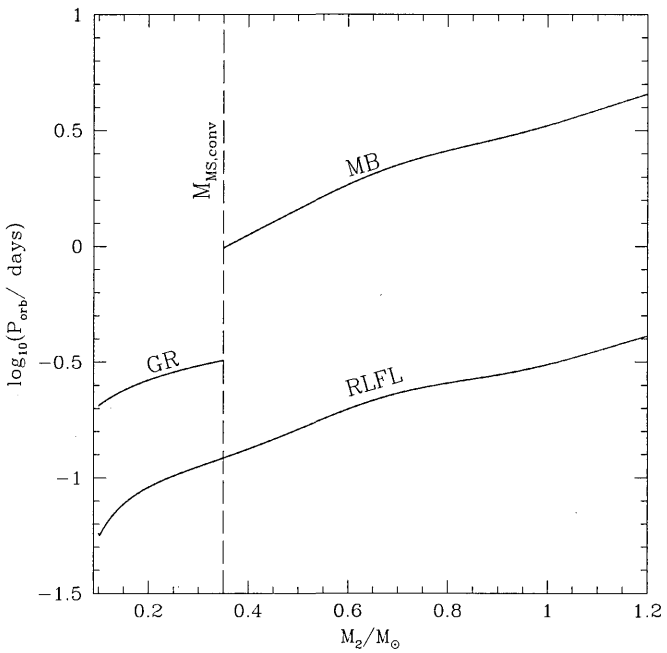

Figure 3.4: A plot showing the boundaries enclosing the population of pre-CVs as a function of M_2, i.e. PCEBs which will commence mass transfer within the lifetime of the Galaxy ($\approx$ 10 Gyr), assuming a typical white dwarf mass of 0.6 $M_\odot$. The lower boundary marked 'RLFL' (Roche lobe filling limit) marks the orbital period at which systems will become semi-detached. The vertical dashed line ($M_{\rm MS,conv}$) marks the mass at which isolated main sequence stars just become fully convective. The upper boundary marked 'GR' gives the maximum orbital period for PCEBs driven by gravitational radiation which will become semi-detached by 10 Gyr. The upper boundary marked 'MB' gives the maximum orbital period for PCEBs driven my magnetic braking [equation (2.8), $\gamma = 4$] which will become semi-detached by 10 Gyr.

The maximum upper period can be found by integrating equation (3.19) over the Galactic lifetime with $(\dot{J}/J)_{\rm sys} = (\dot{J}/J)_{\rm GR}$, [given by equation (2.1)] for those systems with $M_2 \leq M_{\rm MS,conv}$, or $(\dot{J}/J)_{\rm sys} = (\dot{J}/J)_{\rm MB}$[2] [given by equations (2.8) or (2.9)] for systems with $M_2 > M_{\rm MS,conv}$.

Figure 3.4 shows the boundaries in $\log_{10}P_{\rm orb} - M_2$ space enclosing the population of pre-CVs, assuming a typical white dwarf mass of 0.6 $M_\odot$. The lower boundary marked 'RLFL' (for Roche lobe filling limit) gives the orbital period at which these systems will become semi-detached, while the dashed vertical line marks the location of the fully convective limit

[2]Strictly, we should have for this case $(\dot{J}/J)_{\rm sys} = (\dot{J}/J)_{\rm MB} + (\dot{J}/J)_{\rm GR}$. However, as the angular momentum loss rate due to magnetic braking is typically a factor 100 greater than that due to gravitational radiation, this approximation is a good one [see also Schreiber & Gänsicke (2003)].

for isolated main sequence stars, $M_{\rm MS,conv}$. Thus the upper boundary to the left of this line (labelled 'GR') marks the maximum orbital period those PCEBs driven by gravitational radiation can have if they are to become semi-detached in the lifetime of the Galaxy. On the other hand, the upper boundary labelled 'MB' marks the maximum orbital period PCEBs driven by magnetic braking [according to equation (2.8), $\gamma = 4$] can have if they are to become semi-detached in the lifetime of the Galaxy.

3.4.1 Subdwarf-main sequence binaries

Closely related to the WD+MS binaries are the subdwarf-main sequence star (sd+MS) binaries. The primary is a core helium burning star with a very thin shell ($\lesssim 0.02$ $M_\odot$) of hydrogen rich material, and is a very blue object which is located on the extreme horizontal branch of the Hertzsprung-Russell diagram [for a review see e.g. Maxted (2004)]. A major formation channel for these systems is via the CE phase (Han et al. 2002). If the progenitor primary fills its Roche lobe near the tip of the first giant branch (i.e. just before the onset of the core helium flash), then after the ejection of the CE the helium core will ignite leaving a subdwarf star in a tight orbit around its secondary companion. Han et al. (2002) estimate the mass of a subdwarf star lies between approximately 0.32 and 0.48 $M_\odot$, with a mass on average of approximately 0.46 $M_\odot$, which is broadly in line with observation [e.g. Maxted (2004)]. Once the subdwarf star has exhausted its helium burning core after $\approx 10^8$ years, it will become a degenerate carbon-oxygen white dwarf (Dorman et al. 1993).

3.4.2 WD+MS Binaries via Stable Roche Lobe Overflow

It is important to also mention those WD+MS systems that form from mass transfer episodes which are dynamically stable. One circumstance by which this can occur is if the progenitor primary contracts in response to mass loss. This occurs if the progenitor has a radiative envelope as it is crossing the Hertzsprung Gap (Willems & Kolb 2004). Thus, such mass transfer constitutes case B mass transfer, as described in Section 1.1.2. Furthermore, if the mass ratio $Q \gtrsim 4/3$ [c.f. equation (2.12)], then mass transfer will ensue on the thermal

timescale of the primary donor star.

Once the secondary star has accreted sufficient material such that $Q < 1$, the orbital separation increases upon further mass transfer, and mass transfer becomes thermally stable. Any further mass transfer is driven due to the expansion of the primary star as it ascends the giant branch. Once the entire envelope of the primary has been accreted by the secondary, this leaves the exposed white dwarf with a typical mass of between about 0.25 and 0.35 $M_\odot$ orbiting a main sequence secondary with $M_2 < 5$ $M_\odot$ at an orbital period of between 1 and 100 days (Willems & Kolb 2004). For the purposes of this thesis we follow Willems & Kolb (2004) and designate this as formation channel 1.

On the other hand, for primary stars with initial masses $\gtrsim 2$ $M_\odot$, core helium burning may occur before the primary fills its Roche lobe. In contrast to channel 1 however, stellar winds and mass transfer may strip the envelope from the primary leaving an exposed naked helium star. Either by further mass loss from the helium star, or as a result of helium exhaustion in the core, will a white dwarf form, typically with a mass between 0.3 and 1.44 $M_\odot$, and an orbital period of between 10 and 1000 days (Willems & Kolb 2004). Willems & Kolb (2004) designate this as formation channel 2.

Alternatively, if the primary star has lost sufficient mass via winds such that the mass ratio becomes $Q \lesssim 0.8$ at the point of first contact with its Roche lobe (see Section 3.1) then mass transfer is dynamically stable even if the primary is ascending the asymptotic giant branch. Thus, mass transfer occurs as the giant star is expanding and hence constitutes as case C mass transfer. Wind losses and mass transfer from the envelope of the primary leaves the exposed high mass white dwarf typically with a mass of between 0.55 and 1.44 $M_\odot$ and a secondary main sequence star with $M_2 \approx 1$ to 7 $M_\odot$, and an orbital period between a few$\times$1000 to 20 000 days. Again, we adopt the nomenclature of Willems & Kolb (2004) for the purpose of this thesis and call this formation channel 3.

4

Population Synthesis

Any observation of an astronomical object, whether it is a Galaxy or a binary star, only represents a snap-shot of its evolution. From that snap-shot, particularly of single or binary stars, we cannot gain any knowledge regarding the initial conditions of that object, nor can we observe how it will subsequently evolve, as the timescales involved are so large. For the case of CVs, for example, their evolutionary timescales are on the order between 10^8 to 10^9 years (see Chapter 1). This, added to the intangibility of the astronomical subject, makes any hope of gaining insight into the physical principles underlying its evolution particularly challenging.

Nonetheless, the advent of large scale observational surveys (the SDSS in the case of WD+MS binaries, for example) provide us with the integrated characteristics of a given population of objects. A particularly pertinent example is the orbital period distribution in the observed population of CVs (see Chapter 2). As the population of CVs within such a distribution will invariably have different ages, the features in the distribution therefore provides an insight to how such binaries evolve.

It is this collective property of a given population of objects which we must exploit if we are to gain any physical understanding of their evolution, and indeed the initial conditions of the population needed to produce the current observed one. By modelling the formation and evolution of a large population of objects, governed by physical principles we believe to

be involved, we can therefore hope to reproduce the observed characteristics of our target population. This is the essence of population synthesis.

Of course, any theoretical description will be inherently incomplete, and will have unknown parameters as a result. One of the main goals of population synthesis is therefore to test or constrain the parameters used to describe the evolution of that population of interest. This is achieved by comparing the calculated characteristics of that population with the corresponding observed sample. If a model turns out to be in good agreement with observation, then we have provided a quantitative explanation for the observed characteristics of that population.

Population synthesis also allows us to predict the properties of populations which may not necessarily have been observed yet. Any uncertainties in such predictions are reflected by uncertainties in any input parameters. However, comparisons of such predictions with future observations will allow further opportunity to test and constrain the input parameters.

In the remainder of this chapter, we introduce our population synthesis code called BiSEPS (Binary System Evolution and Population Syntheis) used in this thesis, in Section 4.1. We then describe in Section 4.2 how BiSEPS calculates the formation rates, the present day numbers and the corresponding statistical characteristics of a certain target binary population.

4.1 Our Population Synthesis Code

In order to calculate the present day population of a particular variety of binary system (for example CVs), we need to evolve a large number of binary sequences, having initial stellar masses and orbital periods that cover a sufficiently wide range in parameter space. For the reasons stated above, it is necessary to repeat such calculations for different input parameters.

To calculate such a large number of evolutionary sequences, a rapid computational time is therefore highly desirable. Single star evolution (SSE) is typically carried out by solving the equations describing stellar structure and evolution, or by polytropic models. On current computer hardware, however, carrying out stellar evolution in this manner on such a large scale required for binary population synthesis is still not feasible [1].

[1] However, with the increasing trend in CPU speeds, population synthesis calculations based on full stellar

A more expedient manner of evolving a large number of stellar sequences in population synthesis is via the following. By calculating a library of evolutionary tracks of stars for a wide range of initial ZAMS masses and metallicities from full stellar evolution codes, the corresponding data can be stored either in the form of tables or analytical fit formulae. It is the latter approach which Hurley et al. (2000) have pursued, and forms the SSE component of BiSEPS [Willems & Kolb (2002); Willems & Kolb (2004)]. The resulting fit formulae describe the mass, radius and luminosity of the star as a function of its initial ZAMS mass and metallicity. These formulae are accurate to within 5 per cent, compared to full stellar evolution calculations.

As expounded by Eggleton (1996) and Hurley et al. (2000), the advantages of fit formulae are that they are more compact than tables, and more flexible, particularly when applied to binary star evolution. Furthermore, tables give a somewhat coarser level of coverage in parameter space.

In parallel to the evolutionary calculations of the stellar components, the binary evolution (BE) in BiSEPS is calculated based on the prescription given by Hurley et al. (2002). The parameterisations describing the physics of the pertinent phases of binary evolution have been described in Chapters 1 through 3. In the next Section, we describe how BiSEPS calculates the population of binaries, also based on the formulation given by Hurley et al. (2002).

4.2 Calculating the Population

BiSEPS first constructs a three dimensional, logarithmically spaced grid in primary mass $M_{1,\mathrm{i}}$, secondary mass $M_{2,\mathrm{i}}$ and orbital period $P_{\mathrm{orb,i}}$. We construct such a grid with 60 cells in $M_{1,\mathrm{i}}$ and $M_{2,\mathrm{i}}$, and 300 grid cells in $P_{\mathrm{orb,i}}$. We further consider initial masses in the range 0.1 to 20 $\mathrm{M}_{\odot}$, and initial orbital periods in the range 0.1 to 100 000 days. Each point within a grid cell represents an initial binary configuration (i.e. has a unique set of initial binary parameters $M_{1,\mathrm{i}}$, $M_{2,\mathrm{i}}$ and $P_{\mathrm{orb,i}}$) where both of the stellar components are on the zero-age main sequence (ZAMS). For the grid size we are using, we therefore have a total of 1.1×10^6 initial binary configurations. However, for grid cells a and b, two initial binary

evolution sequences may soon become feasible.

configurations are the same if $M_{1,i}(a) = M_{2,i}(b)$, and $M_{2,i}(a) = M_{1,i}(b)$. Therefore, as we want to consider only the one unique binary configuration once, we employ the convention that binaries with $M_{1,i} > M_{2,i}$ are evolved, and thereby following the convention that the initially more massive star is the primary, while the less massive companion is the secondary. We therefore evolve a total of approximately 5.4×10^5 binary configurations.

We assume that both stars enter the ZAMS at the same time. This is because the contraction phase onto the main sequence comprises a very small fraction of the total main sequence life of the star. To avoid artificial structure in the binary population as a result of the equidistant grid, each binary within the grid cell is displaced away from the centre, where the offset is random.

Each of these ZAMS binary configurations are evolved simultaneously using the aforementioned SSE and BE components for a maximum evolution time of the age of the Galactic disk. This age can be estimated from calculations of the cooling tracks of the oldest, and therefore the least luminous, white dwarfs in the Galactic disk (Schmidt 1959). However, the calculated disk ages depend on the assumed compositions of these white dwarfs, and the models describing the cooling of these white dwarfs as a result [e.g. Wood (1995), Hansen (1999)]. The age of the Galactic disk has been calculated to be between 6 and 14 Gyr (Hansen & Liebert 2003). We therefore adopt the commonly used average value for the Galactic disc age of 10 Gyr.

Furthermore, the stellar components are assumed to have Population I compositions, with a solar metallicity of $Z = 0.02$. However, this is a somewhat simplistic assumption. Each generation of stars born throughout the life of the Galaxy will enrich the next generation of stars with heavier elements due to nucleosynthesis (McWilliam 1997). Nonetheless, there is some debate as to whether the so-called 'age-metallicity relation' actually exists, as the observations of open clusters can attest [e.g. Friel & Janes (1993)]. In contrast a decreasing metallicity with increasing galactic age was argued for from the observations of field stars [e.g. Jonch-Sorensen (1995)].

Neither of these possibilities are conclusive as, for a given age of the stars, there is a large spread in the metallicity, which has been attributed to an inhomogeneous chemical evolution of the Galaxy [e.g. Pilyugin & Edmunds (1996*a*), Pilyugin & Edmunds (1996*b*)]. As this is not a trivial matter, we simply assume that $Z = 0.02$ for all our stars, irrespective of the time they were born.

If the binary configuration evolves into a particular target binary species that we are

intending to study, then the binary parameters at the point of birth of the target binary (the zero-age target parameters) are recorded, as well as the initial ZAMS parameters of that binary. We also record the evolutionary track of each target binary configuration from its formation until the point when it 'dies', i.e. becomes another variety of binary system.

4.2.1 Formation Rates

In order to calculate the formation rates of a given target binary population, we first need to calculate the formation probability of each of the ZAMS progenitors which subsequently evolve into the corresponding target binary system. The ZAMS binaries can be identified by their initial primary and secondary masses, $M_{1,\mathrm{i}}$ and $M_{2,\mathrm{i}}$, and the initial orbital period $P_{\mathrm{orb,i}}$, and so will occupy a point $(M_{1,\mathrm{i}}, M_{2,\mathrm{i}}, P_{\mathrm{orb,i}})$ in a three dimensional formation space.

Strictly speaking, we require the probability, $\mathcal{P}(V_\mathrm{i})$, that the ZAMS binary will form within some volume, V_i, of the formation parameter space. This probability is described by some probability density function, $\chi(M_{1,\mathrm{i}}, M_{2,\mathrm{i}}, P_{\mathrm{orb,i}})$ such that

$$\mathcal{P}(V_\mathrm{i}) = \int_{V_\mathrm{i}} \chi(M_{1,\mathrm{i}}, M_{2,\mathrm{i}}, P_{\mathrm{orb,i}}) \mathrm{d}V_\mathrm{i}, \tag{4.1}$$

where the integration is evaluated over the volume V_i, and $\mathrm{d}V_\mathrm{i} = \mathrm{d}M_{1,\mathrm{i}}\,\mathrm{d}M_{2,\mathrm{i}}\,P_{\mathrm{orb,i}}$ is just a volume increment of the formation space.

The function $\chi(M_{1,\mathrm{i}}, M_{2,\mathrm{i}}, P_{\mathrm{orb,i}})$, however, can be decomposed into the separate probability density functions describing the formation probabilities of the initial masses and the orbital period. The probability density function for the initial primary mass, $f(M_{1,\mathrm{i}})$, is given by the initial mass function (IMF), i.e.

$$f(M_{1,\mathrm{i}}) = \begin{cases} 0 & M_{1,\mathrm{i}}/\mathrm{M}_\odot < 0.1, \\ 0.29056 M_1^{-1.3} & 0.1 \leq M_{1,\mathrm{i}}/\mathrm{M}_\odot < 0.5, \\ 0.15571 M_1^{-2.2} & 0.5 \leq M_{1,\mathrm{i}}/\mathrm{M}_\odot < 1.0, \\ 0.15571 M_1^{-2.7} & 1.0 \leq M_{1,\mathrm{i}}/\mathrm{M}_\odot, \end{cases} \tag{4.2}$$

(Kroupa et al. 1993), while the initial orbital period distribution, $g(P_{\mathrm{orb,i}})$, can be found by using the initial orbital separation distribution, $h(a_\mathrm{i})$, according to

$$h(a_\mathrm{i}) = \begin{cases} 0 & a_\mathrm{i}/\mathrm{R}_\odot < 3 \text{ or } a_\mathrm{i}/\mathrm{R}_\odot > 10^6, \\ 0.078636 a_\mathrm{i}^{-1} & 3 \leq a_\mathrm{i}/\mathrm{R}_\odot \leq 10^6. \end{cases} \tag{4.3}$$

[Iben & Tutukov (1984), Hurley et al. (2002)] and where $P_{\rm orb,i}$ is converted into $a_{\rm i}$ using Kepler's Third Law. For the case of the initial secondary mass, however, there are uncertainties how the the formation of the primary star affects the formation of the secondary companion, and hence its mass function. In other words, is there a correlation between the masses of the primary and secondary stars? To investigate this, we consider an initial mass ratio distribution (IMRD) function according to

$$n(q_{\rm i}) = \begin{cases} \mu q_{\rm i}^{\nu} & 0 < q_{\rm i} \leq 1, \\ 0 & q_{\rm i} > 1, \end{cases} \tag{4.4}$$

[Hurley et al. (2002), Iben & Tutukov (1984)] where $q_{\rm i} = M_{2,\rm i}/M_{1,\rm i}$, μ is a normalization constant that depends on the value of the exponent ν. We explore three forms of equation (4.4): $\nu = -0.99$ [2] where extreme mass ratios are favoured; $\nu = 0$, which gives a flat distribution and so all mass ratios are equally favoured; $\nu = 1$ where, for a given primary mass, more massive secondaries are formed on average. Finally, we consider that the secondary star is formed independently of the primary star and is determined by equation (4.2), where $M_{1,\rm i}$ is replaced with $M_{2,\rm i}$.

In the case of BiSEPS, however, each ZAMS binary configuration lies within its own discrete grid cell with a volume

$$\Delta\log_{10}V_{\rm i} = \Delta\log_{10}M_{1,\rm i} \times \Delta\log_{10}M_{2,\rm i} \times \Delta\log_{10}P_{\rm orb,i}, \tag{4.5}$$

where $\Delta\log_{10}M_{1,\rm i}$, $\Delta\log_{10}M_{2,\rm i}$ and $\Delta\log_{10}P_{\rm orb,i}$ are the bin widths in initial primary mass, initial secondary mass and initial orbital period respectively. Their widths are determined by our choice of the number of bins for each parameter, as well as the range in their values we want to consider. If the kth ZAMS binary configuration is located at $(M_{1,{\rm i},k}, M_{2,{\rm i},k}, P_{\rm orb,i,k})$, then the kth. grid cell within which the ZAMS binary sits therefore carries a weighting, $\mathcal{P}_k$, according to

$$\mathcal{P}_k \approx \chi(M_{1,{\rm i},k}, M_{2,{\rm i},k}, P_{\rm orb,i,k})\Delta\log_{10}V_{\rm i}, \tag{4.6}$$

However, BiSEPS constructs an equidistant grid in log space, while each of the initial distribution functions above are defined in linear parameter space. For a variable, X, a linear spacing, ΔX, can be related to a logarithmic spacing $\Delta\log_{10}X$ by $\Delta X = X\ln 10 \times \Delta\log_{10}X$. Thus, from equations (4.2) to (4.4), equation (4.6) becomes

$$\mathcal{P}_k \approx (\ln 10)^3 \times M_{1,{\rm i},k}\, f(M_{1,{\rm i},k}) \times q_{{\rm i},k}\, n(q_{{\rm i},k}) \times P_{\rm orb,i,k}\, g(P_{\rm orb,i,k}) \times \Delta\log_{10}V_{\rm i}. \tag{4.7}$$

[2] We use $\nu = -0.99$ as opposed to $\nu = -1$ because the former can be normalised such that $\int n(q_{\rm i})\,{\rm d}q_{\rm i} = 1$.

Let the ZAMS binary with $(M_{1,\mathrm{i},k}, M_{2,\mathrm{i},k}, P_{\mathrm{orb,i},k})$ evolve into a target binary with primary mass, secondary mass and orbital period given by $M_{1,k}$, $M_{2,k}$ and $P_{\mathrm{orb},k}$ respectively, born at a time t since its progenitor binary landed on the ZAMS. Analogous to the ZAMS binary population, we can construct a grid in t, M_1, M_2 and P_{orb} space, where each grid cell volume is ΔV. Thus, this target binary will occupy a point given by $(t_k, M_{1,k}, M_{2,k}, P_{\mathrm{orb},k})$ in this 'birth' space. Clearly, the formation probability of this target binary is just $\mathcal{P}_k$, i.e. the formation probability of its ZAMS binary progenitor. However the weighting $\mathcal{P}_k$ is now applied to the grid cell in 'birth' space within which the target binary sits. Also, if different ZAMS progenitors evolve into zero-age target binaries with similar binary parameters, then that grid cell carries a probability weighting which is the sum of all the formation probabilities of the ZAMS binaries which form the target systems which lie within this grid cell.

Also analogous to the ZAMS binary population, we can now obtain how the primary masses, secondary masses and orbital separations are distributed in this target binary population, which is given by the probability density function $\phi(t_k, M_{1,k}, M_{2,k}, P_{\mathrm{orb},k})$. Thus for this particular binary

$$\phi(t_k, M_{1,k}, M_{2,k}, P_{\mathrm{orb},k}) = \frac{\mathcal{P}_k}{\Delta t \Delta M_1 \Delta M_2 \Delta P_{\mathrm{orb}}}, \tag{4.8}$$

where ΔM_1, ΔM_2 and ΔP_{orb} and Δt are the bin widths in primary mass, secondary mass orbital separation and time respectively in this target binary formation space. Therefore, by mapping the formation probability of each ZAMS binary progenitor onto the grid cell within which the associated target binary sits, we can build up a probability density function, $\phi(t, M_1, M_2, P_{\mathrm{orb}})$, which describes the distribution in primary mass, secondary mass, orbital separation and formation time of the target binary species.

Clearly the formation rate of target binaries within some grid cell is proportional to the corresponding formation probability of that grid cell. Furthermore, we need to have knowledge of the star formation rate (SFR) throughout the history of the Galaxy, $\mathcal{S}(T)$, where T is the time since the birth of the Galaxy.

As an example, consider the formation rate of a target binary population at the present day, $T = t_{\mathrm{gal}}$. If a target binary is formed at a time t_{f} since its progenitor binary landed on the ZAMS, and the ZAMS binary formed at a time t_{ZAMS} since the birth of the Galaxy, t_0 (see Figure 4.1), then for the target binary to form at the present moment we require

$$t_{\mathrm{ZAMS}} + t_{\mathrm{f}} = t_{\mathrm{gal}} \tag{4.9}$$

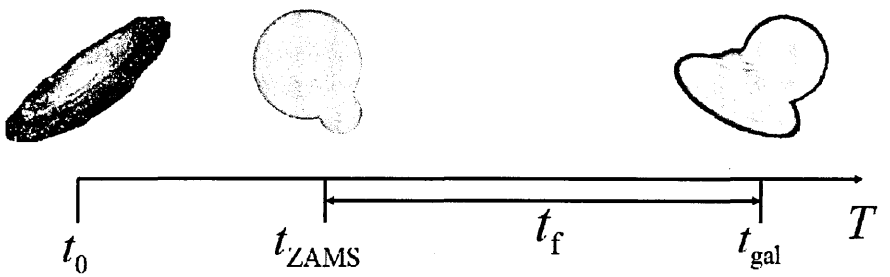

Figure 4.1: The Galaxy is born at t_0. After a time $t_{\rm ZAMS}$ a ZAMS binary system is formed, which evolves into a target binary system after a time $t_{\rm f}$. Note that in this example, the target binary is formed at the present day, $t_{\rm gal}$, because $t_{\rm ZAMS} + t_{\rm f} = t_{\rm gal}$.

While $\phi(t, M_1, M_2, P_{\rm orb})$ describes the distribution of the target zero-age population as a function of time since the birth of their progenitor binaries, the time at which the ZAMS binary progenitors were born can occur at any point throughout the history of the Galaxy. With this in mind, we can determine which target binaries will form at the present day, and hence their formation rates, by convolving the function $\phi(t_{\rm gal} - t_{\rm ZAMS}, M_1, M_2, P_{\rm orb})$ with $\mathcal{S}(t_{\rm ZAMS})$. Thus we associate the formation rate of the ZAMS progenitor with its corresponding zero-age target binary system. As $t_{\rm ZAMS}$ ranges from $t_0 = 0$ to $t_{\rm gal}$, then the formation rate per bin volume of the target binary population at the present day is given by

$$\mathcal{F}(M_1, M_2, P_{\rm orb}) = \int_0^{t_{\rm gal}} \mathcal{S}(t)\phi(t_{\rm gal} - t, M_1, M_2, P_{\rm orb}){\rm d}t. \tag{4.10}$$

However, we can obtain the formation rate of the target binary population at any moment in the Galaxy's history. Thus, we can generalise equation (4.10) to obtain the formation rate history of the target binary population, $\mathcal{F}(T, M_1, M_2, P_{\rm orb})$.

We calculate the SFR by assuming that one binary forms per year with $M_1 > 0.8$ M$_\odot$, which we also assume to be constant throughout the lifetime of the Galaxy. The lower limit of 0.8 M$_\odot$ is the smallest mass a primary star can have if it is to evolve into a white dwarf within the lifetime of the Galaxy. Combining this formation rate with the Galactic volume of 5×10^{11} pc^3 gives an average local birthrate for white dwarfs of 2×10^{-12} yr^{-1} pc^{-3}, which is consistent with observations (Weidemann 1990). To obtain the SFR we have

$$\mathcal{S} \int_{0.8}^{\infty} f(M_{1,{\rm i}})\, {\rm d}M_{1,{\rm i}} = 1\,{\rm yr}^{-1}, \tag{4.11}$$

which gives us $\mathcal{S} = 7.6$ yr^{-1}.

We note that the assumption of a constant SFR throughout the lifetime of the Galaxy is a simplifying one. Indeed, the SFR has a power law dependence on the density of gas

available for star formation (Schmidt 1959). The early history of galaxies is thought to be dominated by star-burst activity due to the large abundance of gas. After a period of 10^8 to 10^9 years (Kennicutt 1998) the SFR declines and is approximately constant thereafter for late spirals (Kennicutt et al. 1994). As such star-burst episodes last for a small fraction of the galaxy's life, and so a constant SFR throughout the Galaxy's life is a good one. Star-burst activity would only have a significant effect on the population of the oldest CV population, which would have evolved well beyond the minimum period, and would be too faint to detect.

4.2.2 The Present Day Population

In order to calculate the present day distribution and number of a target binary population, we need to have knowledge of how each target binary configuration evolves with time, as well as its formation rate history. As mentioned in the previous section, the ZAMS progenitor of a given target binary system can be born at any point in the lifetime of the Galaxy. In order for us to observe a given target binary system at the present day, it must still exist as such (i.e. does not change into another binary species). Thus, if $t_{\rm life}$ is the time that the binary system spends as a target of interest then it must satisfy

$$t_{\rm ZAMS} + t_{\rm f} + t_{\rm life} \geq t_{\rm gal}. \tag{4.12}$$

Therefore, the target binary will reach different points in its evolution at the present day, depending on when during the Galaxy's life the target binary was born. Thus, we must have knowledge of the point in evolution that each target binary has reached by the present day, for all possible formation times in the Galaxy's history.

To illustrate this, the left-hand set of axes in Figure 4.2 shows a set of evolutionary tracks (solid red curves), labelled (a) to (c), describing the evolution in orbital period with Galactic time, while the dashed boxes represent binnings in orbital period and time. Track (a) shows the orbital period evolution of one particular target binary species, while track (b) is for the same target binary but where the binary is formed later on in the Galaxy's life. Track (c) corresponds to the orbital evolution of a different target binary configuration. The orbital period bins which this one target binary system evolves through at the present day are shaded in grey. Note that the bins in orbital period that the binary passes through, as well as the time spent in those bins at the present day thus depends on the evolutionary

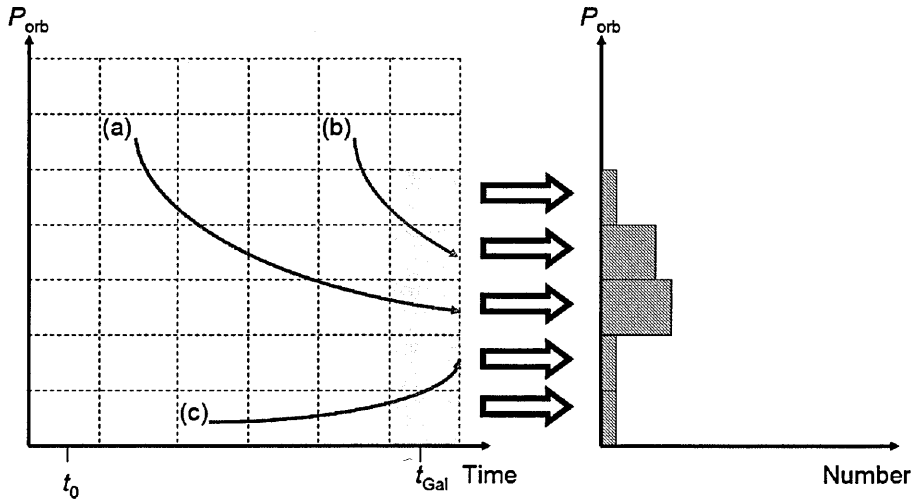

Figure 4.2: The left hand set of axes shows a grid in orbital period (y-axis) and Galactic time (x-axis), while the dashed boxes represent binnings in orbital period and time. The solid red curves labelled (a) to (c) are hypothetical evolutionary tracks in orbital period. Tracks (a) and (b) are for the same target binary system, but born at different times. Track (c) is an evolutionary track of a different binary system. The right set of axes shows the orbital period distribution of the target binaries, obtained by determining the amount of time that each track spends in each bin at a certain Galactic epoch (in this case the present) shown in grey.

stage that the binary has reached by the present time.

Recall that each grid cell in the 'birth' space of the target binary population represents a population of target binaries with similar binary parameters in M_1, M_2 and $P_{\rm orb}$, for which we have the formation rate (per bin volume) for. In our example as depicted in Figure 4.2, each dashed box represents a population of target binaries with similar values of $P_{\rm orb}$. The evolutionary tracks therefore represent the evolution of the population of target binaries within the bin that the track starts in.

We denote the amount of time which the systems spend in each of the grey bins as the dwell time, $t_{\rm D}$. Thus, the longer the systems spend in a given bin, the more systems will be found in that bin. For the case of track (a), if the formation rate (per bin width in $P_{\rm orb}$) of target binaries which this track corresponds to is $\mathcal{F}_{\rm (a)}$, and the systems spend a time $t_{\rm D,(a)}$ in the corresponding grey bin, then the present day number of such systems in this bin, $N_{\rm (a)}$ is

$$N_{\rm (a)} \propto \mathcal{F}_{\rm (a)} t_{\rm D,(a)}. \tag{4.13}$$

By considering the stage of evolution that each target binary configuration has reached by

the present day, for all possible formation times during the Galaxy's history, we can build up an orbital period distribution as depicted in the right set of axes in Figure 4.2. In the same manner outlined above, we can construct the present day distributions in primary and secondary mass of the target binary population.

PART II

Testing the Disruption of Magnetic Braking

5

Method

In this chapter, we describe our method in order to test the disrupted magnetic braking model. This test exploits the main consequence of disrupted magnetic braking: the existence of a population of WD+MS binaries that were CVs in the past but became detached at $P_{\rm orb}/{\rm hours} \approx 3$ and are currently crossing the period gap, (dCVs).

Using population synthesis techniques we calculate the present day population of these dCVs, as well as PCEBs. Specifically, we only consider PCEBs which will begin mass transfer within the period gap. For our stellar models and choice of gap boundaries (see Section 5.1.2), such systems have secondary masses in the range $0.17 \leq M_2/{\rm M}_\odot \leq 0.36$. This sub-set of PCEBs we henceforth designate as gPCEBs (for 'gap-PCEBs'). Note that gPCEBs have $P_{\rm orb}/{\rm hours} \geq 2$ but can also have $P_{\rm orb}/{\rm hours} > 3$.

In order to distinguish between the two varieties of WD+MS binary, we consider the orbital period distribution of the combined population of dCVs and gPCEBs, in order to determine if there is a clear feature within the period gap due to the presence of dCVs there, relative to the population of systems on either side of the period gap.

If such a dichotomy is observed in an observationally determined orbital period distribution of WD+MS systems at short orbital periods, then this would strongly corroborate the hypothesis that magnetic braking is disrupted.

The advent of the SDSS provides the ideal opportunity to carry out our test of the dis-

rupted magnetic braking model. Presently underway is a large-scale observational survey of WD+MS systems, approximately 1000 of which have already been identified [Schreiber et al. (2007), Silvestri et al. (2007)]. Attempts to establish the sub-sample of PCEBs among those systems, as well as their orbital periods and stellar properties is well underway [Rebassa-Mansergas et al. (2007), Rebassa-Mansergas et al. (2008)]. It is therefore feasible to subject the disrupted magnetic braking model to a stringent test by comparing the observed orbital period distribution to the predictions of our work here.

5.1 Modifications made to BiSEPS

The investigation into the population of dCVs has required significant modifications to the BiSEPS code. This has involved incorporating a new prescription which calculates the mass transfer rate in CVs in a more physically realistic manner (Section 5.1.1). We also needed to add a prescription which describes the reaction of the donor star's radius to rapid mass loss, and its subsequent return towards thermal equilibrium once it has detached from its Roche lobe due to the disruption of magnetic braking (Section 5.1.2). We describe these modifications below.

5.1.1 Mass Transfer in CVs

Originally, the mass transfer rate in CVs was calculated by using the prescription described in Hurley et al. (2002), according to

$$-\dot{M}_2 \propto \left[\ln\left(\frac{R_2}{R_{\mathrm{L},2}}\right)\right]^3, \tag{5.1}$$

where R_2 and $R_{\mathrm{L},2}$ is the donor's radius and Roche lobe radius respectively. Note that the mass transfer rate has a steep dependence on the amount that the donor star overfills its Roche lobe. The top panel of Figure 5.1 shows how the stellar radius (red) and Roche lobe radius (blue) of a donor star with an initial mass of 0.6 $\mathrm{M}_\odot$ evolves with orbital period, as calculated by equation (5.1). The donor is paired with a 0.8 $\mathrm{M}_\odot$ white dwarf, the mass of which is assumed to remain constant. The motivation behind equation (5.1) was to ensure that the donor star did not overfill its Roche lobe by an unrealistic amount, and instead

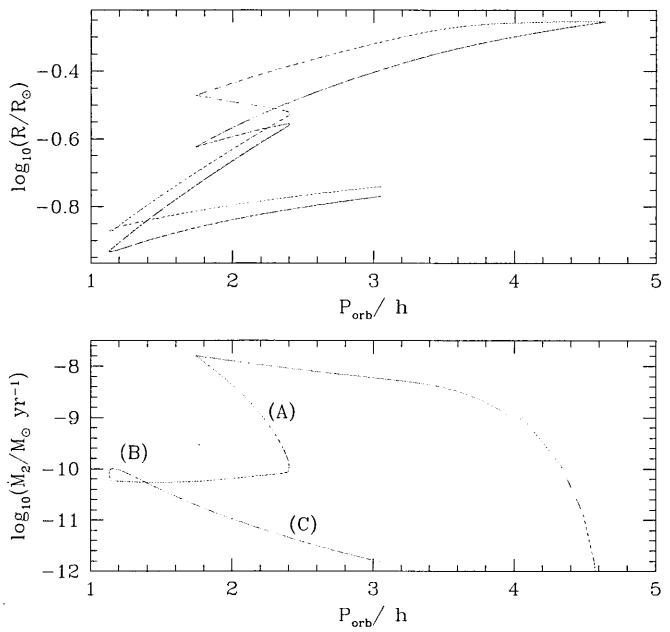

Figure 5.1: Top panel: The evolution of the Roche lobe (blue) and stellar radius (red) with orbital period of a CV donor with an initial mass of 0.6 $M_\odot$, calculated from eqn. (5.1). Bottom: the mass transfer rate with orbital period for the same CV donor, also calculated from eqn. (5.1). (A): Magnetic braking is disrupted once the donor becomes fully convective at 0.35 $M_\odot$; (B): period bounce; (C) unrealistic evolution to long orbital periods for CVs with sub-stellar donors.

maintain the relation $R_{\mathrm{L},2} \approx R_2$. It can be seen from the top panel of Figure 5.1, however, that this is not the case. Indeed the relative difference between the donor and Roche lobe radius is as great as 20 per cent.

This, however, is contrary to the theory of mass transfer in CVs, as discussed in Section 1.1.2, where stationary mass transfer implies that the donor's stellar and Roche lobe radius move in step (c.f. equation 1.17), with $R_2 \approx R_{\mathrm{L},2}$. Furthermore, from equation (1.14), we can see that as R_2/H_{p} is so large, then even if the donor star were to overfill its Roche lobe by a relative amount of approximately 10 per cent, then this would give an unphysically large value of $\dot{M}_2$.

The bottom panel shows the corresponding mass transfer rate for the same CV model, also calculated from equation (5.1). The features labelled (A) to (C) are unrealistic and unphysical. The feature (A) shows a sharp decline in the mass transfer rate, and a slight increase towards longer orbital periods. The former is a result of magnetic braking shutting off once the donor star becomes fully convective at 0.35 $M_\odot$ (see Section 2.3.1), while the

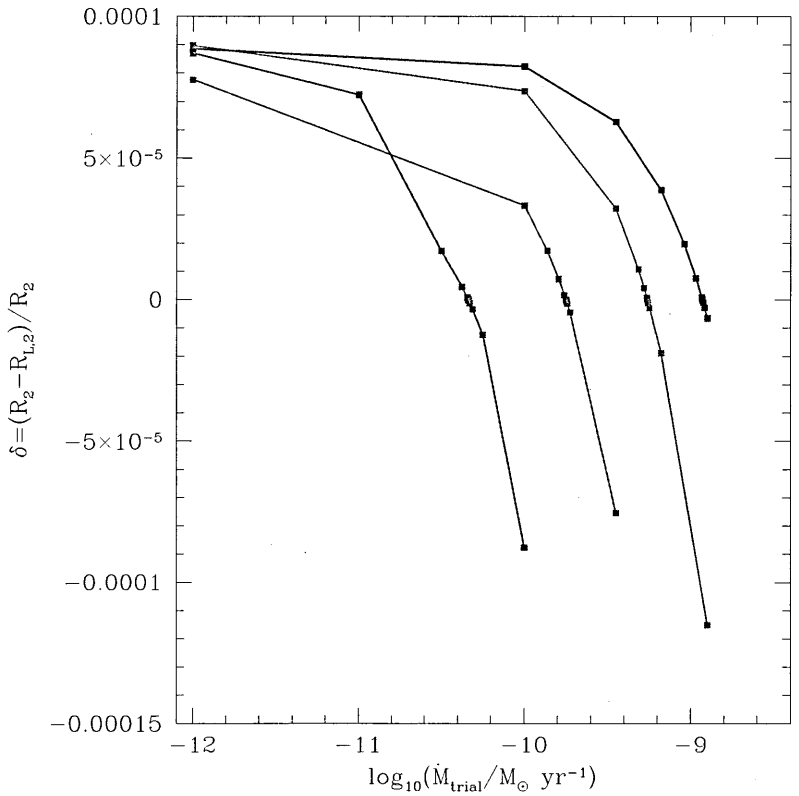

Figure 5.2: Example of the function $\delta(\dot{M}_{\rm trial})$ for the first time-step for CVs with different initial donor masses. Red: $M_2 = 0.1$ M$_\odot$; blue: 0.4 M$_\odot$; green: 0.7 M$_\odot$; magenta: 1.0 M$_\odot$.

latter is not a physical behaviour. In contrast to the standard theory of CV evolution, the mass transfer rate does not shut-off, and the donor star is still in contact with its Roche lobe.

The feature labelled (B) shows the point at which the CV begins to evolve towards longer orbital periods as a result of the donor becoming a degenerate brown dwarf, and therefore obeys a mass-radius relation of the form $R_2 \propto {M_2}^{-1/3}$. The 'loop' feature where the mass transfer rate slightly increases before the CV evolves towards longer orbital periods is, however, an artifact of the transition between the main sequence and brown dwarf stage as implemented by the code. Finally, (C) shows the CV evolving up to an orbital period of 3 hours after 10 Gyr. Throughout the post-bounce phase, it is assumed that the donor star still obeys the relation $R_2 \propto {M_2}^{-1/3}$. However, sub-stellar stars with masses between 0.01 and 0.07 M$_\odot$ follow the mass-radius relation according to $R_2 \propto {M_2}^{-1/8}$ (Chabrier & Baraffe 2000), and in fact the radius becomes independent of mass for $M_2 \lesssim 0.01$ M$_\odot$ (Chabrier et al. 2009).

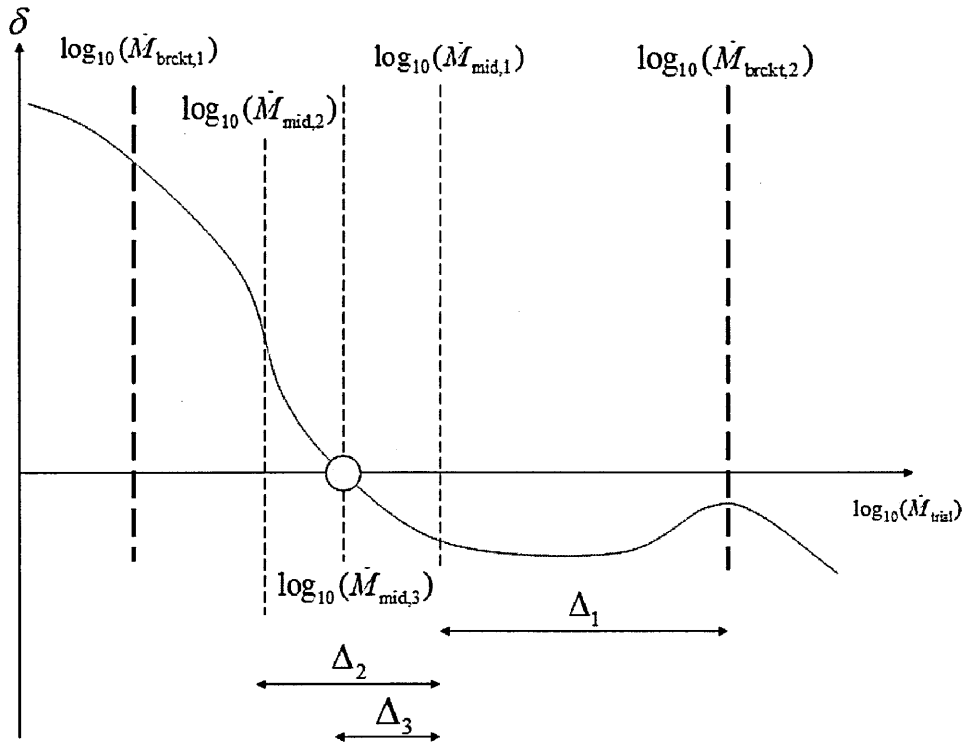

Figure 5.3: A schematic illustrating how the bisection locates the root of the function shown in red.

Our first aim was to incorporate a more physically realistic description of mass transfer of CVs into BiSEPS. For each CV model at every time-step, we calculated the relative difference between the donor's radius and its Roche lobe radius, $\delta \equiv (R_2 - R_{\mathrm{L},2})/R_2$, as a function of a range of trial values of the mass transfer rate, $\dot{M}_{\mathrm{trial}}$. An example of how δ varies with $\log_{10}\dot{M}_{\mathrm{trial}}$ for the first time step for CVs with different initial donor masses is shown in Figure 5.2. As we require $R_2 = R_{\mathrm{L},2}$, then we require the root of the function, $\delta(\log_{10}\dot{M}_{\mathrm{trial}}) = 0$. To find the root we employ a bisection algorithm, which is graphically illustrated in Figure 5.3, and which we describe below.

For the first time-step of mass transfer, we pick two values of the mass transfer rate, $\log_{10}\dot{M}_{\mathrm{brckt},1}$ and $\log_{10}\dot{M}_{\mathrm{brckt},2}$ (shown as the thick dashed lines in Figure 5.3), which have a sufficient width apart, Δ_0, to bracket the root of $\delta(\log_{10}\dot{M}_{\mathrm{trial}})$, which is shown as the blue circle, while $\delta(\log_{10}\dot{M}_{\mathrm{trial}})$ is represented by the red line. In order for the root to be bracketed, we require that $\delta(\log_{10}\dot{M}_{\mathrm{brckt},1}) \times \delta(\log_{10}\dot{M}_{\mathrm{brckt},2}) < 0$. In the case of the example shown in Figure 5.3, we have $\delta(\log_{10}\dot{M}_{\mathrm{brckt},1}) > 0$ and $\delta(\log_{10}\dot{M}_{\mathrm{brckt},2}) < 0$.

As the name suggests, we now bisect the width, $\Delta_0/2 = \Delta_1$. We then evaluate δ for the

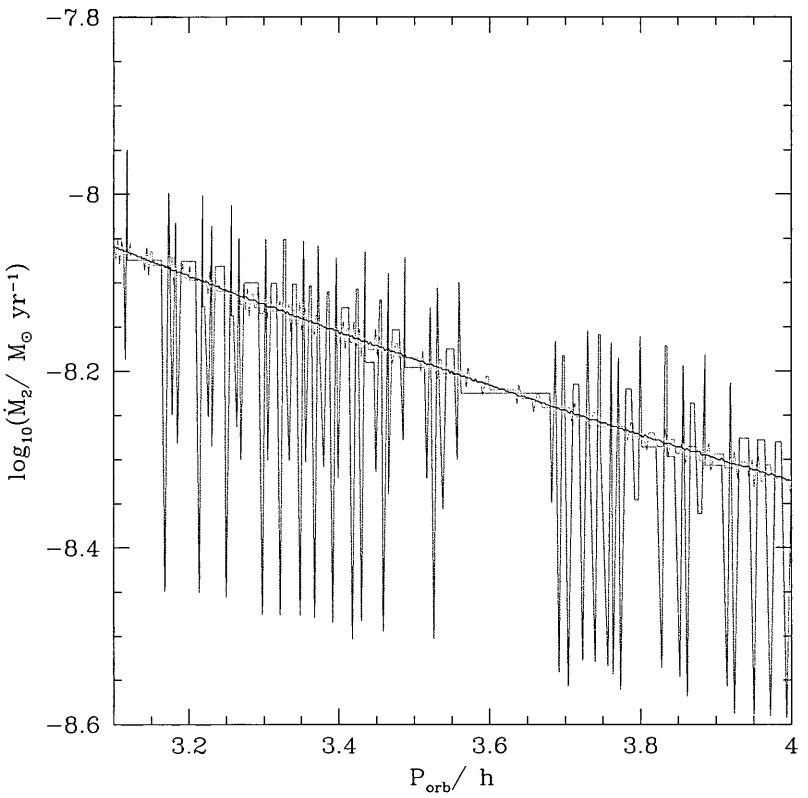

Figure 5.4: A close-up of the mass transfer rate evolution of a CV with a an initial donor mass of 0.6 $M_\odot$, for different values of δ_{tol}. $\delta_{tol} = 10^{-3}$ (red); 10^{-4} (green); 10^{-5} (black).

value of the trial mass transfer rate that lies between the two bracketing values, $\log_{10}\dot{M}_{mid,1}$ (represented by the thin dashed line in Figure 5.3). As we get $\delta(\log_{10}\dot{M}_{mid,1}) < 0$ then we find the mid point between $\log_{10}\dot{M}_{mid,1}$ and $\log_{10}\dot{M}_{brckt,1}$ i.e. $\Delta_2 = \Delta_1/2$. If, on the other hand, we had $\delta(\log_{10}\dot{M}_{mid,1}) > 0$, then we find the mid point between $\log_{10}\dot{M}_{mid,1}$ and $\log_{10}\dot{M}_{brckt,2}$ instead. The bisection procedure is repeated until the mid value of the trial mass transfer rate is within some tolerance of the root.

We establish that a tolerance of $\delta_{tol} = 10^{-5}$, i.e. $|\delta(\log_{10}\dot{M}_{trial})| \leq \delta_{tol}$, is a good compromise between accuracy and numerical stability. The value of $\log_{10}\dot{M}_{trial}$ which satisfies $\delta = 0$ within this tolerance is therefore the mass transfer rate we use for that time-step.

The reason we iterate to this value of δ_{tol} is to reduce the amount of noise in the calculated mass transfer rates. The calculated mass transfer rate, $\dot{M}_2$, for various values of δ_{tol} is shown in Figure 5.4. We note that our bisection procedure is similar to the one used by Kalogera et al. (2004), although we developed our method independently.

As the width of the bracketing values after i iterations is $\Delta_i = \Delta_0/2^i$, then the number

of iterations to locate the first root, $i_{\max}$, is therefore

$$i_{\max} = \log_2 \left[\frac{|\log_{10}(\dot{M}_{\rm brckt,1}) - \log_{10}(\dot{M}_{\rm brckt,2})|}{\delta_{\rm tol}} \right]. \tag{5.2}$$

We start off with $\dot{M}_{\rm brckt,1} = 10^{-12}$ M$_\odot$ yr^{-1} and $\dot{M}_{\rm brckt,2} = 10^{-7}$ M$_\odot$ yr^{-1}. We can therefore expect ~ 20 iterations to locate the root.

While the bisection method does not locate the root as rapidly as alternative algorithms (e.g. the Newton-Raphson method), it is more numerically stable and more straightforward to incorporate into the BE package of the BiSEPS code. Indeed, to implement the Newton-Raphson method, we would require a priori knowledge of the function $\delta(\log_{10}\dot{M}_{\rm trial})$ and the corresponding derivative for each time step of a given CV configuration, which is non-trivial.

There are two other adaptations of the bisection algorithm which we employ to keep the CPU time to a minimum. Firstly, for time-steps after the first one, we use the mass transfer rate calculated from the previous time-step as one of the bracketing values. This ensures that the bracketing values are in close proximity to the next possible root. From equation (5.2) we can therefore expect $i_{\max} < 20$. Secondly, if the bracketing values $\log_{10}\dot{M}_{\rm brckt,1}$ and $\log_{10}\dot{M}_{\rm brckt,2}$ for subsequent time-steps do not bracket the root, we employ a rapid searching routine. Figure 5.2 shows the shape of the function $\delta(\log_{10}\dot{M}_{\rm trial})$ for CV donors with different initial masses. In all cases $\delta(\log_{10}\dot{M}_{\rm trial})$ decreases for increasing values of $\log_{10}\dot{M}_{\rm trial}$. Thus, if we have the case where $\delta(\log_{10}\dot{M}_{\rm brckt,1}) > 0$ and $\delta(\log_{10}\dot{M}_{\rm brckt,2}) > 0$ then we increase the value of $\log_{10}\dot{M}_{\rm brckt,2}$ until we obtain a new bracketing value, $\log_{10}\dot{M}'_{\rm brckt,2}$, which gives us $\delta(\log_{10}\dot{M}'_{\rm brckt,2}) < 0$. We do this using

$$\log_{10}\dot{M}'_{\rm brckt,2} = \log_{10}\dot{M}_{\rm brckt,1} + k, \tag{5.3}$$

where k is the number of iterations. On the other hand, if we have $\log_{10}\delta(\dot{M}_{\rm brckt,1}) < 0$ and $\log_{10}\delta(\dot{M}_{\rm brckt,2}) < 0$, then we need to decrease $\dot{M}_{\rm brckt,2}$ until we find a new value $\log_{10}\dot{M}'_{\rm brckt,2}$, which gives us $\delta(\log_{10}\dot{M}'_{\rm brckt,2}) > 0$. We apply

$$\log_{10}\dot{M}'_{\rm brckt,2} = \log_{10}\dot{M}_{\rm brckt,1} - k. \tag{5.4}$$

The top panel of Figure 5.5 shows the evolution of R_2 (red) and $R_{\rm L,2}$ (blue) with orbital period for a donor star with an initial mass of 0.6 M$_\odot$, calculated using our bisection algorithm. The bottom panel shows the corresponding mass transfer rate with orbital period. This is clearly an improvement over the corresponding track shown in Figure 5.1, as the donor and Roche lobe radii are now nearly indistinguishable and move in step. The

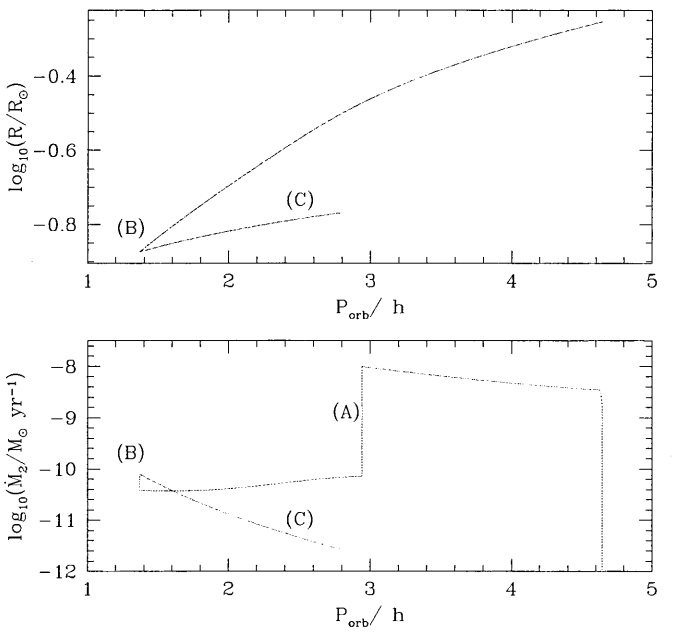

Figure 5.5: Similar to Figure 5.1, but this time the donor's stellar and Roche lobe radius (top panel) are calculated using our bisection algorithm. Note the two radii cannot be distinguished because they differ by less than 10^{-5} throughout. The corresponding mass transfer rate is shown in the bottom panel. (A): magnetic braking is disrupted once the donor star is fully convective at 0.35 $M_{\odot}$; (B): the period bounce; (C): unrealistic evolution to long orbital periods for CVs with substantial sub-stellar donors.

feature labelled (A) corresponds to where magnetic braking is shut off once the donor star becomes fully convective at 0.35 $M_{\odot}$. This gives an associated decrease in the mass transfer rate. The donor star is still filling its Roche lobe, however. As with Figure 5.1, the loop feature labelled (B) denotes the point at which the CV begins to evolve towards longer orbital periods, while (C) shows that for the CV to evolve to such long orbital periods with a substantially sub-stellar donor is unrealistic.

Our bisection algorithm, however, encounters numerical problems for those CVs which are close to dynamical or thermal instability, or where the CV donor has evolved significantly from the ZAMS. As a result we obtain unphysically high mass transfer rates at the onset of mass transfer. This is a result of our assumption, that the Roche lobe and donor radii move in step, breaking down.

5.1.2 The Period Gap and Period Gap Evolution

By looking at the evolution of the mass transfer rate for a donor star of initial mass 0.6 $M_\odot$ with orbital period, as shown in the bottom panel of Figure 5.5, we can see that there is no period gap between $2 \lesssim P_{\rm orb}/{\rm hr} \lesssim 3$. We now describe how we incorporate a period gap of the observed width and location into BiSEPS, as well as a physically realistic description of how the CV evolves across it.

5.1.2.1 The Width and Location of the Period Gap

In order to incorporate the period gap into CV evolution as calculated by BiSEPS, we first need to determine its width and location from the orbital period distribution of observed CVs.

Figure 5.6 shows the orbital period distribution of the $\sim$ 650 observed CVs from the Ritter & Kolb (2003) catalogue, Edition 7.7 (2006)[1], where we have zoomed in on the period gap, and where N is the number of systems. In order to objectively determine the edges of the period gap, we calculate the moving average of the cumulative distribution. This is shown as the red curve in Figure 5.6, with $N < P_{\rm orb}$ indicated on the right axis.

By visual inspection we perform linear fits on the cumulative distribution curve, within and on each side of the period gap. In order to consider the most pertinent portion of the cumulative distribution curve related to the period gap, we restrict our fits to the region $0.22 \leq \log_{10} P_{\rm orb}/{\rm hours} \leq 0.64$. The location of the edges of the period gap are therefore given where these linear fits intersect. We find that the orbital period of the upper edge of the gap is $P_{\rm u} = 3.0$ hours, and the lower edge of the gap is located at an orbital period of $P_\ell = 2.0$ hours, thus giving a width of 1 hour.

5.1.2.2 The Reaction of the Donor to Mass Loss

The period gap is a consequence of the donor star expanding due to mass loss, which we need to incorporate into BiSEPS first. We define the radius excess, f, as the factor by which the donor star has exceeded its equilibrium radius, $R_{2,\rm eq}$, due to mass loss. We parameterise the evolution of f according to a power law expression

$$f \equiv \frac{R_2}{R_{2,\rm eq}} = A M_2^{\beta}, \tag{5.5}$$

[1]The latest catalogue at the time of writing, Edition 7.9 (2008), gives similar results.

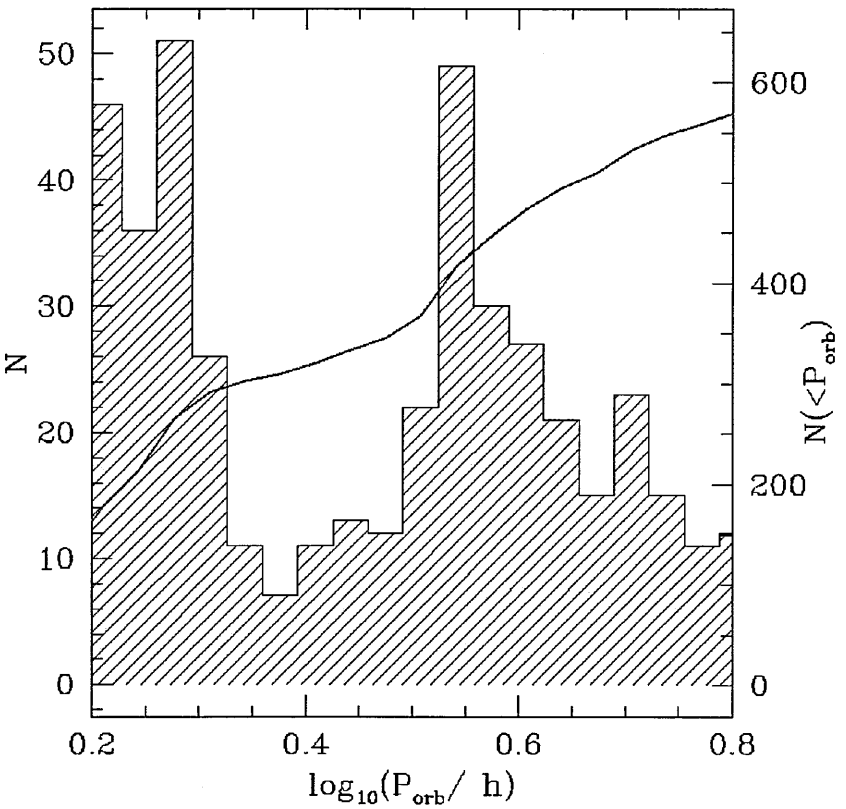

Figure 5.6: The orbital period distribution of the observed CV population, zoomed in on the period gap. The data was obtained from the RK Cat, Edition 7.7 (2006), Ritter & Kolb (2003). The red curve is the moving average of the cumulative distribution, $N(< P_{\rm orb})$, indicated on the right axis.

where A and β are constants.

As a consequence of the disrupted magnetic braking model, the width of the period gap is related to how much the donor star exceeds its equilibrium radius by the time it becomes fully convective at the upper edge of the period gap, $f = f_{\rm conv}$. We now calculate the value of $f_{\rm conv}$ appropriate for our determined period gap width of 1 hour.

By using equation (1.12), we can relate the radius of the secondary star at the upper and lower edge of the period gap, $R_{\rm L,u}$ and $R_{\rm L,\ell}$ respectively, to the orbital periods of the period gap edges by

$$\frac{P_{\rm u}}{P_\ell} = \left(\frac{R_{\rm L,u}}{R_{\rm L,\ell}}\right)^{3/2}. \tag{5.6}$$

Note that there is no term in M_2 because the mass of the secondary does not change across the period gap. Given that $P_{\rm u}/P_\ell = 3.0/2.0$, then

$$f_{\rm conv} \equiv \frac{R_{\rm L,u}}{R_{\rm L,\ell}} \approx 1.3. \tag{5.7}$$

At the point where mass transfer just commences at $M_2 = M_{2,0}$, we require that the donor star is in thermal equilibrium i.e. $f = f_0 = 1$. Combining this requirement with equation (5.5) gives

$$f_0 = AM_{2,0}^{\beta}. \tag{5.8}$$

Similarly, by requiring a radius excess of $f = f_{\rm conv}$ once the donor star becomes fully convective at $M_2 = M_{2,\rm conv}$, gives

$$f_{\rm conv} = AM_{2,\rm conv}^{\beta}. \tag{5.9}$$

Equations (5.8) and (5.9) allow us to solve for A and β. Combining (5.5), (5.8) and (5.9) yields

$$f = f_{\rm conv}\left(\frac{M_2}{M_{2,\rm conv}}\right)^{\beta}, \tag{5.10}$$

where

$$\beta = \frac{\ln(f_0/f_{\rm conv})}{\ln(M_{2,0}/M_{2,\rm conv})}. \tag{5.11}$$

The value of the donor's radius calculated by BiSEPS is then multiplied by f. We then assume that the donor's effective temperature, $T_{\rm eff}$, is the same as an isolated, main sequence star with the same mass as the donor under consideration (Stehle et al. 1996). The luminosity, L_2, of the donor star is calculated from the Stefan-Boltzmann Law

$$L_2 = 4\pi {R_2}^2 \sigma T_{\rm eff}^4. \tag{5.12}$$

where σ is Stefan-Boltzmann constant. Hence L_2 will be larger by a factor of f^2 compared to models without mass loss. The mass-radius relation of several CV evolutionary sequences calculated with this prescription is shown in Figure 5.7.

In order for the lower edge of the period gap to be in the correct location of $P_\ell = 2.0$ h, we disrupt magnetic braking when $M_2 = M_{2,\rm conv} = 0.17$ M$_\odot$.

Based on homology relations, Stehle et al. (1996) derived a first order differential equation that describes how the donor star's radius reacts to mass loss. This scheme shows that CVs with different initial system parameters at the onset of mass transfer quickly converge to a single, uniform evolutionary track, consistent with the well defined position of the period gap.

Our initial scheme to describe the reaction of the donor to mass loss in terms of the mass loss timescale $\tau_{\dot{M}_2}$ and its Kelvin-Helmholtz timescale $\tau_{\rm KH}$, was closely based on that of Stehle et al. (1996), according to

$$f = \kappa\frac{\tau_{\rm KH}}{\tau_{\dot{M}_2}} + 1, \tag{5.13}$$

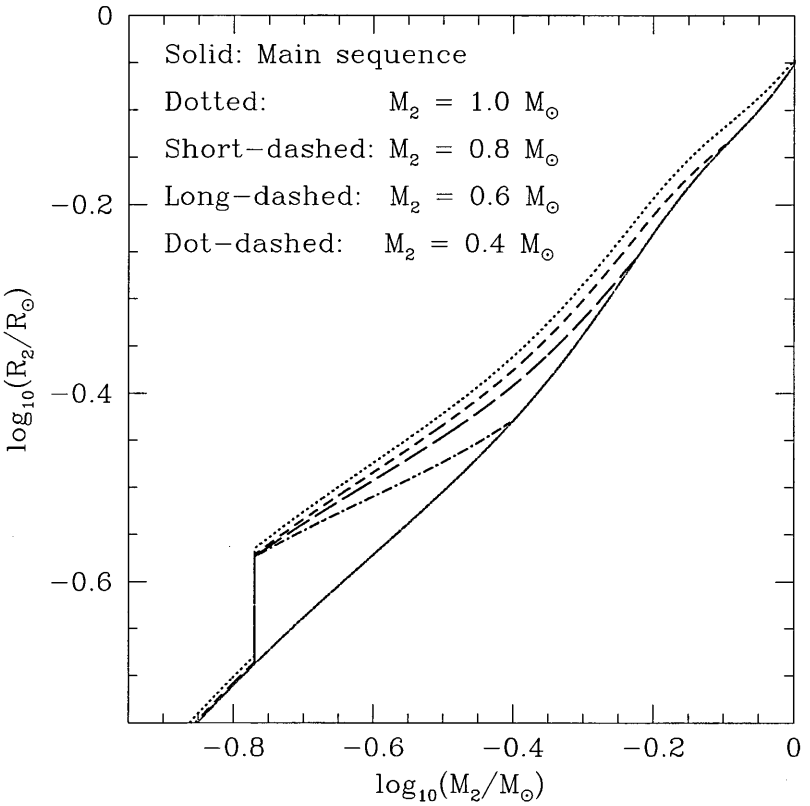

Figure 5.7: Mass-radius relations for CVs with different initial donor masses.

where the value of the constant κ can be determined by stipulating that $f = f_{\rm conv} = 1.3$ at the upper edge of the period gap. However, we encountered numerical instabilities due to feedback between the donor radius and the mass transfer rate. The scheme we use instead does not reproduce convergence of CV evolution onto a single track, but does ensure that the donors do exceed their equilibrium radius by the same amount by the time they become fully convective. As such, we ensure that we reproduce the observed width of the period gap with a well defined location. As we are interested in the evolution of systems across the period gap, rather than the detailed CV evolution above the gap, we believe the prescription we adopt is satisfactory.

5.1.2.3 Evolution of the Secondary Across the Period Gap

As discussed in Section 2.3.1.1, due to the high mass loss rate above the period gap, donor stars are driven out of thermal equilibrium and, as they possesses substantial convective envelopes, will expand. These donors will have radii which exceed their equilibrium radii

(c.f. Section 1.2.2), i.e. the radius the star would have, appropriate for its mass if it was isolated. Once mass transfer is shut off at the upper edge of the period gap, the donor star can now shrink back towards its equilibrium radius due to thermal relaxation as the detached system crosses the period gap, i.e. $\dot{R}_2/R_2 = (\dot{R}_2/R_2)_{\rm th}$.

We describe below how we calculate $(\dot{R}_2/R_2)_{\rm th}$, and the subsequent evolution of the donor's radius back towards thermal equilibrium by following the prescription of King & Kolb (1995).

The evolution of the radius excess with time, $f(t)$, as the donor star re-establishes thermal equilibrium is described by

$$f(t) = 1 - (1 - f_{\rm conv})e^{-t/\tau}, \tag{5.14}$$

where τ is the timescale for the donor star to contract back to its equilibrium radius. The time $t = 0$ corresponds to the donor detaching from its Roche lobe at the upper edge of the period gap.

Because we have $\tau_{\rm KH} \sim \tau_{\dot{M}}$ above the upper edge of the period gap, the mass loss timescale is not sufficiently short such that the donor star reacts adiabatically, while at the same time the mass loss timescale is short enough that the donor star cannot quite establish thermal equilibrium via thermal relaxation. The effective mass-radius exponent of the donor therefore lies within the range $\zeta_{\rm ad} < \zeta < \zeta_{\rm eq}$ for substantially convective donors. We therefore use the expression for $(\dot{R}_2/R_2)_{\rm th}$ as given by equation (1.53). The value of $(\dot{R}_2/R_2)_{\rm th}$ as the donor star re-establishes thermal equilibrium within the period gap is equal to $(\dot{R}_2/R_2)_{\rm th}$ just at the point that the donor loses contact with its Roche lobe at the upper edge of the period gap. Again, we do not consider the expansion of the donor due to nuclear evolution, $(\dot{R}_2/R_2)_{\rm nuc}$ as this is deemed to be negligible.

In order to calculate $(\dot{R}_2/R_2)_{\rm th}$ at the upper edge of the period gap, we first use equation (1.37) to replace the factor of $\dot{M}_2/M_2$ in (1.53). Thus we have

$$\left(\frac{\dot{R}_2}{R_2}\right)_{\rm th} = (\zeta - \zeta_{\rm ad})\frac{1}{\mathcal{D}}\left(\frac{\dot{J}}{J}\right)_{\rm sys} = -\frac{\zeta - \zeta_{\rm ad}}{\tau_J \mathcal{D}}, \tag{5.15}$$

where $\tau_J = -(J/\dot{J})_{\rm sys}$ is the angular momentum loss timescale due to gravitational radiation and magnetic braking, and $\mathcal{D}$ is given by equation (1.38), with $\nu_{\rm CAML}$ given by equation (1.41).

By differentiating equation (5.14) with respect to time and evaluating the result at $t = 0$, and recalling equation (5.7) for $f_{\rm conv}$, and the definition of f from equation (5.5), then we

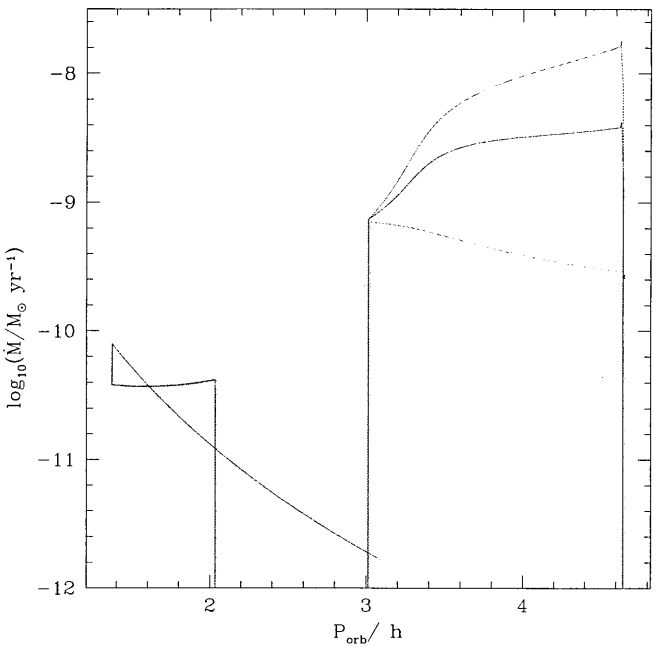

Figure 5.8: The variation of mass transfer rate with orbital period for a CV with donor star of initial mass 0.6 $M_\odot$, for different forms of the magnetic braking. Red: eqn. (5.18) with $\gamma = 4$; blue: eqn. (5.18) with $\gamma = 2$; green: eqn. (5.19).

obtain a second expression for $(\dot{R}_2/R_2)_{\rm th}$ which is given by

$$\left(\frac{\dot{R}_2}{R_2}\right)_{\rm th} = \frac{1}{R_{\rm L,u}} \frac{R_{\rm L,\ell} - R_{\rm L,u}}{\tau}. \tag{5.16}$$

Finally, after combining equations (5.16) to (5.15), and once again using equation (5.7), then

$$\tau = \left(1 - \frac{1}{f_{\rm conv}}\right) \frac{\mathcal{D}}{\zeta - \zeta_{\rm ad}} \tau_J. \tag{5.17}$$

where the constants $\mathcal{D}$, ζ, $\zeta_{\rm ad}$ and τ_J are evaluated just before the donor star detaches from its Roche lobe.

5.1.2.4 Calibrating the Angular momentum loss rate

We now need to calibrate the magnetic braking laws so that the mass transfer rate, and therefore the angular momentum loss rate, at the upper edge of the period gap is appropriate for the gap width we have determined.

We consider the magnetic braking prescriptions given by equation (2.8) and (2.9) (see Section 2.2), except we multiply these equations by some factor in order to give the appropriate angular momentum loss rate at the upper edge of the period gap. For the Rappaport

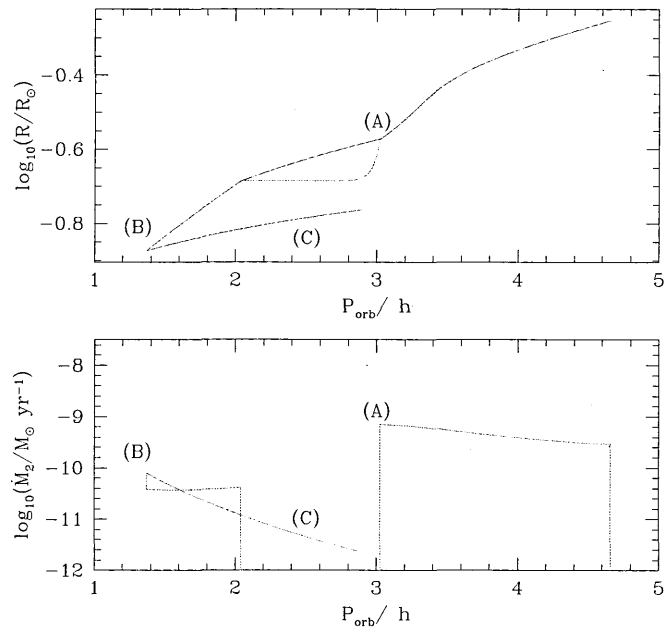

Figure 5.9: Similar to Figure 5.5 except period gap evolution is now incorporated into the BiSEPS code, and the angular momentum loss rate due to magnetic braking is calibrated to give the correct mass transfer rate at the top edge of the period gap, according to eqn. (5.19) with $\eta_{\rm h} = 0.19$. The bottom panel shows the corresponding mass transfer rate with orbital period. (A): magnetic braking, and hence mass transfer, is disrupted when the donor becomes fully convective at 0.17 $M_\odot$; (B): the period bounce; (C): unrealistic evolution to long orbital periods for substantially sub-stellar donors.

et al. (1983) prescription of magnetic braking, equation (2.8) is supplemented by an extra factor $\eta_{\rm rvj}^{[\gamma]}$, i.e.

$$\dot{J}_{\rm rvj} = -\eta_{\rm rvj}^{[\gamma]}\, 3.8 \times 10^{-30} R_\odot^4\, {\rm s\,cm^2}\, M_2 \left(\frac{R_2}{R_\odot}\right)^\gamma \Omega^3. \tag{5.18}$$

We consider values of γ of 2 and 4.

Similarly, the Hurley et al. (2002) magnetic braking prescription, as given by equation (2.9), is supplemented by a factor $\eta_{\rm h}$. Thus we have

$$\dot{J}_{\rm h} = -\eta_{\rm h}\, 5.83 \times 10^{-16}\, {\rm M_\odot\, R_\odot^{-1}\, yr^{-1}} \frac{M_{\rm env}}{M_2} R_2^3 \Omega^3. \tag{5.19}$$

We calibrate the parameters $\eta_{\rm rvj}^{[\gamma]}$ and $\eta_{\rm h}$ in order to give the correct mass transfer rate, and therefore the appropriate angular momentum loss rate, at the upper edge of the period gap. Spruit & Ritter (1983) find that in order to produce a period gap width of 1 hour, an angular momentum loss timescale of 2×10^8 years is required just before the point that mass transfer shuts off. This corresponds to a mass transfer rate of $\approx 10^{-9}$ $M_\odot$ yr^{-1}. By

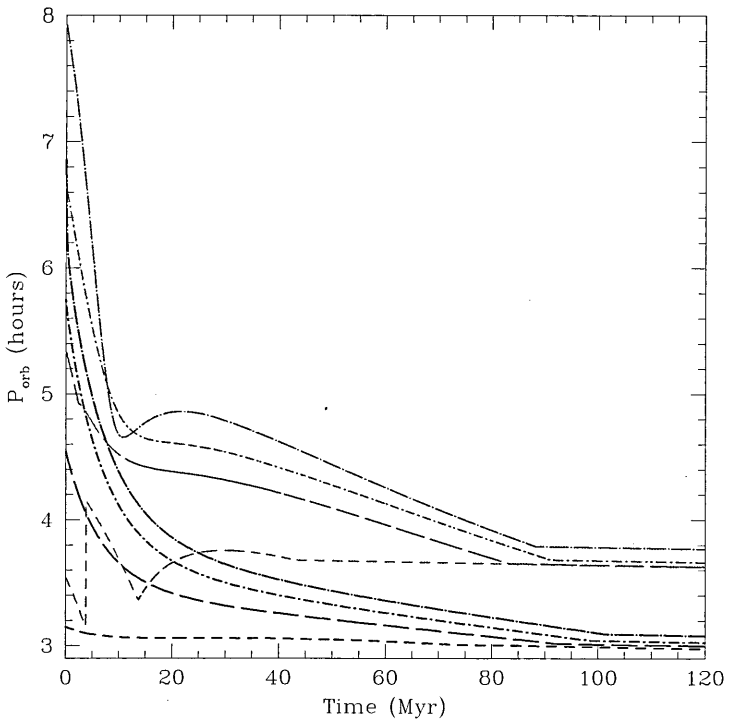

Figure 5.10: A plot showing the time it takes for CVs with a range of initial donor masses to reach the upper edge of the period gap, as calculated by BiSEPS according to equation (5.18), $\gamma = 4$ (black lines), and calculated by a full stellar evolution code (red lines). Short dashed: 0.4 $M_\odot$; long-dashed line: 0.6 $M_\odot$; short-dashed-dotted line: 0.8 $M_\odot$; long-dashed-dotted line; 1 $M_\odot$.

matching this value at the upper edge of the period gap, we obtain $\eta_{\rm h} = 0.19$, $\eta_{\rm rvj}^{[2]} = 0.28$ and $\eta_{\rm rvj}^{[4]} = 1.5$. Figure 5.8 shows the evolution of mass transfer rates with orbital periods for each of these forms of magnetic braking.

Table 5.1 summarizes our models where we use different forms of magnetic braking. The prefix 'h' denotes that the Hurley et al. (2002) prescription of magnetic braking is used according to equation (5.19). The labels 'rvj2' and rvj4' indicate that we use the Rappaport et al. (1983) form of magnetic braking according to equation (5.18) with $\gamma = 2$ and $\gamma = 4$ respectively.

The top panel of Figure 5.9 shows how the stellar (red) and Roche lobe radius (blue) of a donor with an initial mass of 0.6 $M_\odot$ evolves with orbital period, while the bottom panel shows the corresponding mass transfer rate. This has been calculated with all our modifications in place. The feature labelled (A) marks the point where the donor star detaches from its Roche lobe, and contracts back to its equilibrium radius. Point (A) in the

bottom panel corresponds to the upper edge of the period gap.

As for Figures 5.1 and 5.5, the feature marked (B) denotes the point where the CV begins to evolve towards longer orbital periods. Feature (C) indicates that the donor has become substantially sub-stellar at this point, and the evolution towards such long orbital periods is unrealistic. However, this has no impact on our test for the disruption of magnetic braking as we only consider the formation and evolution of CVs which lie above the upper edge of the period gap.

To check if our prescription to calculate the mass transfer rate and the bloating of the donor star realistically describes CV evolution above the period gap, we compare CV evolutionary tracks calculated by BiSEPS with those calculated from a full stellar evolution code. Figure 5.10 shows the time it takes for CVs with a range of initial donor masses to reach the upper edge of the period gap, as calculated by BiSEPS (black lines) and a full stellar evolution code (red lines; J. Barker, private communication) assuming a Verbunt & Zwaan (1981) form of magnetic braking.

As calculated by BiSEPS, it takes between approximately 95 to 100 Myr for a CV to reach the upper edge of the period gap. The full stellar evolution code predicts between approximately 80 and 90 Myr for CVs to reach the upper edge of the period gap. This corresponds to a relative error of between approximately 10 and 20 per cent. We note that the full stellar evolution code gives an upper edge of the period gap of approximately 3.6 hours. This is because the code predicts 0.35 $M_{\odot}$ as the point at which stars become fully convective, which is consistent with the opacities and treatment of convection used in the code. This may account for the slight differences in the calculated times found between the two codes. We also note, however, that the relative error found above is much less than the uncertainties related to the form of magnetic braking.

5.2 Treatment of the CE Phase

We model the CE phase using equation (3.13), which can be solved for the final orbital period that the PCEB will have upon leaving the CE phase. We therefore have

$$A_{\rm CE,f} = A_{\rm CE,i}\frac{M_{\rm c}}{M_1}\left[1+\left(\frac{2}{\lambda_{\rm CE}\alpha_{\rm CE}r_{\rm L,1}}\right)\left(\frac{M_{\rm env}}{M_2}\right)\right]^{-1}, \tag{5.20}$$

Table 5.1: Model assumptions for $\alpha_{\rm CE}$ and magnetic braking.

Model	$\alpha_{\rm CE}$	Magnetic braking law
hA	1.0	eqn. (2.9)
hCE01	0.1	eqn. (2.9)
hCE06	0.6	eqn. (2.9)
hCE3	3.0	eqn. (2.9)
hCE5	5.0	eqn. (2.9)
hPWR05	eqn.(3.15), $p = 0.5$	eqn. (2.9)
hPWR1	eqn.(3.15), $p = 1.0$	eqn. (2.9)
hPWR2	eqn.(3.15), $p = 2.0$	eqn. (2.9)
rvj2A	1.0	eqn. (2.8), $\gamma = 2$
rvj4A	1.0	eqn. (2.8), $\gamma = 4$

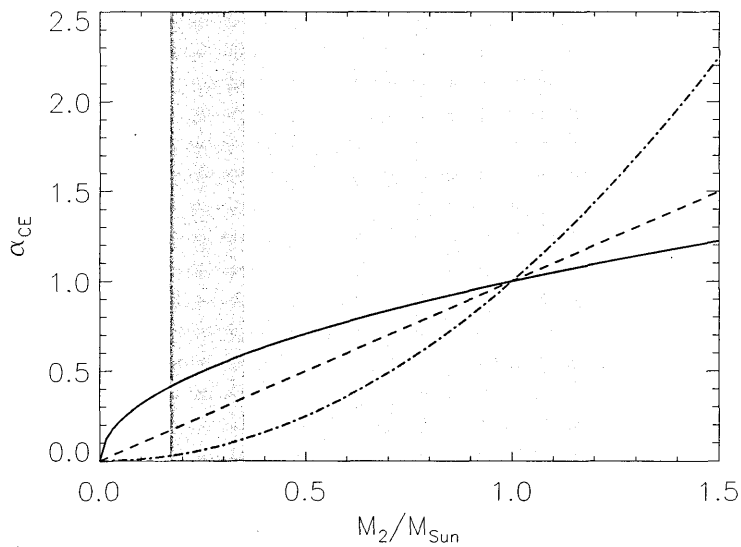

Figure 5.11: Variation of $\alpha_{\rm CE}$ with M_2 according to eqn. (3.15). Solid: $p = 0.5$; dashed: $p = 1.0$; dot-dashed: $p = 2.0$. Dark-grey shading indicates range of secondary masses in gPCEB systems; light-grey range of secondary masses for dCV progenitors.

where $r_{\rm L,1} \equiv R_{\rm L,1}/A_{\rm CE,i}$ is the radius of the Roche lobe filling primary in units of the orbital separation at the start of the CE phase, and the quantities on the right hand side of equation (5.20) are evaluated at the point that the CE phase is just commencing. Throughout this investigation we follow Willems & Kolb (2004) and use $\lambda_{\rm CE} = 0.5$.

In our calculations, we consider the impact of changing the common envelope ejection

efficiency $\alpha_{\rm CE}$. We consider constant, global values of $\alpha_{\rm CE} = 0.1$, 0.6, 1.0, 3.0 and 5.0. We use $\alpha_{\rm CE} = 1$ as our standard model 'A'. In addition, we follow Politano & Weiler (2007) and consider the possibility that $\alpha_{\rm CE}$ could be a function of the secondary mass. In this investigation we consider the functional form given by equation (3.15), with $p = 0.5$, 1 and 2. Figure 5.11 shows how $\alpha_{\rm CE}$ varies with M_2 for $p = 0.5$, 1.0 and 2.0. The dark-grey shading is the range of secondary masses of the gPCEB population, while the light-grey shading is the range of secondary masses found for dCV progenitors.

Table 5.1 summarises our population synthesis models for our different values of $\alpha_{\rm CE}$. The label 'CEx' denotes the value, x, of the constant, global value of $\alpha_{\rm CE}$. For example 'CE01' is $\alpha_{\rm CE} = 0.1$. Finally, the acronym 'PWRy' denotes the use of equation (3.15) with the value, y, of the parameter p, for example 'PWR05' is $p = 0.5$.

In the next chapter, we present the result of our population synthesis calculations.

6

Results and Analysis

We now present the results of our population synthesis calculations. As we shall describe in more detail, we find that there is a clear excess of dCVs over gPCEBs within the period gap. In an orbital period distribution of all WD+MS systems with short orbital periods, this excess manifests itself as a 'spike' in the distribution between orbital periods of 2 and 3 hours. This spike we henceforth coin the 'mirror gap'. A useful quantity which describes the height of this mirror gap is the ratio of the number of dCVs to the number of gPCEBs within the period gap, denoted by dCV:gPCEB.

It is therefore this mirror gap feature which we suggest as an observational test for the disruption of magnetic braking. If such a feature is detected in an orbital period distribution of the observed sample of all WD+MS systems with short orbital periods, then this would strongly corroborate the disrupted magnetic braking hypothesis.

We need to determine if it is actually feasible for the mirror gap to be detected (i.e. if the ratio dCV:gPCEB is significant). We therefore begin to describe how the present day population of dCVs and gPCEBs within the period gap changes for different constant, global values of the common envelope ejection efficiency, $\alpha_{\rm CE}$, and for different IMRDs. We will then discuss how this impacts overall on the ratio dCV:gPCEB, and hence the height of the mirror gap. This analysis is then repeated where $\alpha_{\rm CE}$ is assumed to be dependent of the secondary mass as described by Politano & Weiler (2007).

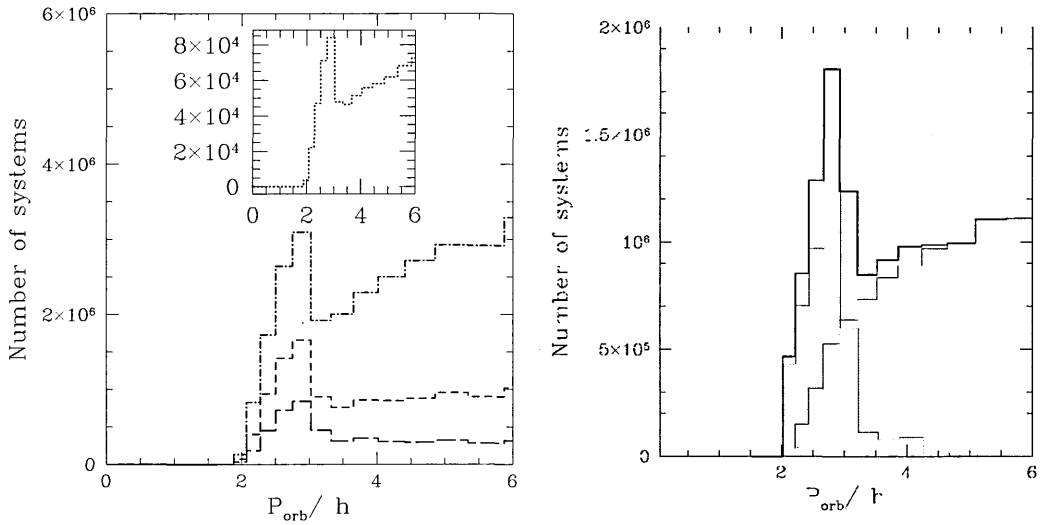

Figure 6.1: Left panel: orbital period distribution of dCVs and gPCEBs combined for our reference model hA, and for different initial mass ratio distributions. Long-dashed: $n(q_i) \propto q_i$; short-dashed: $n(q_i) = 1$ (our reference IMRD); dot-dashed: where M_2 is picked independently from the same IMF as M_1 according to equation (4.2); dotted: $n(q_i) \propto q_i^{-0.99}$ (inset). The peak apparent in all the distributions is due to the population of dCVs; the gPCEB orbital period distributions are increasing monotonically with P_{orb}. Right panel: orbital period distribution of dCVs (red), gPCEBs (blue) and the total population (black) for our reference model hA, and for $n(q_i) = 1$.

Due to the uncertainties in the form and the resulting angular momentum loss rate of magnetic braking, we briefly discuss how the populations of dCVs, gPCEBs and the ratio dCV:gPCEB changes for different forms of magnetic braking.

Finally, we discuss our results and consider the most likely values of α_{CE} and the most favoured form for the IMRD; we then predict the observed orbital period distribution of all WD+MS systems with short orbital periods. We then discuss the current observational WD+MS surveys underway, and the limitations of our calculations. Our results are then summarised in the Conclusions.

The results of our population synthesis calculations are summarised in Table 6.1, which lists the present day population of dCVs, gPCEBs and the ratio dCV:gPCEB in the period gap. For completeness we list the total present day formation rates of all PCEBs, and CVs above and below the period gap. For each of our models, we also show the results for the different forms of the IMRD, with $\nu = -0.99$, 0.0 or 1.0. We also determine the secondary mass from the same IMF as the primary star. Our reference IMRD is $n(q_i) = 1$.

The excess of dCVs over gPCEBs is illustrated in the left panel of Figure 6.1; a prominent

peak within the period gap in the orbital period distributions of the combined dCV and gPCEB populations. These have been calculated from our reference model hA, for different assumptions on the initial distribution of the secondary mass. The cut-off in the number of systems at 2.0 hours is because the smallest secondary mass considered in both the dCV and gPCEB systems is 0.17 $M_\odot$. Such systems become semi-detached at 2.0 hours. The right panel of Figure 6.1 shows the separate orbital period distributions of dCVs (red), gPCEBs (blue) and the combined distributions (black) for our reference model hA, and for $n(q_i) = 1$.

Note that the orbital period distribution of dCVs in the right panel of Figure 6.1 possesses a tail where the dCVs do not lie within the period gap. These are systems which have a secondary star that has significantly evolved away from the zero-age main sequence, typically where $M_2 \gtrsim 1$ $M_\odot$. As the secondary evolves away from the main sequence its radius increases, and so possesses a larger radius compared to a zero-age main sequence star of the same mass. A progenitor CV with such a nuclear evolved donor star will therefore cease mass transfer at a longer orbital period when the donor becomes fully convective, compared to a CV with a ZAMS secondary of the same mass.

Such systems, however, contribute only a small fraction of the total dCV population. For the case of our model hA, $n(q_i) = 1$, the population of such dCVs which lie outside the period gap is $\approx 3 \times 10^5$; approximately 10 per cent of the total dCV population.

6.1 Varying α_{CE}: Models hA to hCE5

We begin by examining how the present day populations of dCVs and gPCEBs within the period gap are affected by varying the value of the global parameter α_{CE} for $n(q_i) = 1$ (Figure 6.2). An understanding of these trends will yield an understanding of the overall trend of dCV:gPCEB with α_{CE}.

6.1.1 The gPCEB Population

The left panel of Figure 6.2 shows that increasing the value of α_{CE} from 0.1 to 1.0 increases the present day number of gPCEBs within the period gap (from 1.7×10^5 to 1.0×10^6 for our reference IMRD). This levels off (here to 1.1×10^6) for $\alpha_{CE} \gtrsim 1.0$.

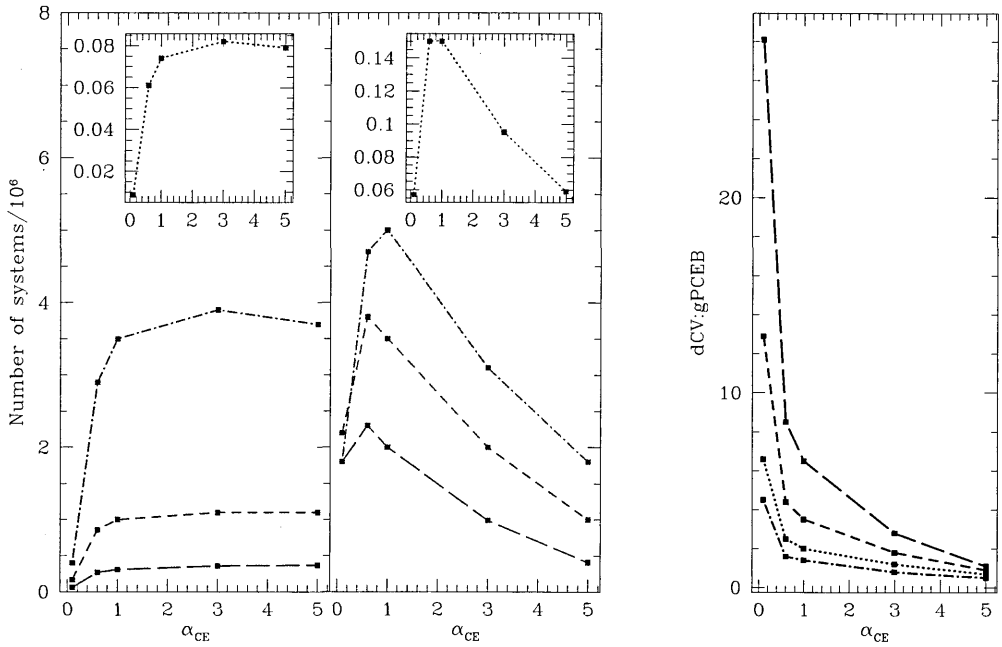

Figure 6.2: From left to right: the present day population of gPCEBs in the period gap (blue) and dCVs (red) as a function of $\alpha_{\rm CE}$, and the ratio dCV:gPCEB as a function of $\alpha_{\rm CE}$. Long-dashed: $n(q_{\rm i}) \propto q_{\rm i}$; short-dashed: $n(q_{\rm i}) = 1$ (our reference IMRD); dot-dashed: where M_2 is picked independently from the same IMF as M_1 according to equation (4.2); dotted: $n(q_{\rm i}) \propto q_{\rm i}^{-0.99}$ (insets).

To understand this consider Figure 6.3, where the dashed box $CDEF$ defined by $0.17 \leq M_2/{\rm M}_\odot \leq 0.36$ and $\log_{10}(P_\ell) \leq P_{\rm orb}/{\rm h} \leq \log_{10}(P_{\rm u})$ shows the location of gPCEBs in the period gap. We designate this region as $\Re$. Not only will $\Re$ consist of gPCEBs that formed there, but also of gPCEBs that evolve into $\Re$ from longer orbital periods.

Clearly, there is an upper limit in orbital period, $P_\Re^+$, from which gPCEBs can evolve into the period gap within the lifetime of the Galaxy of 10^{10} yr. To calculate $P_\Re^+$, we note that the evolution of the vast majority of gPCEBs will be driven by gravitational wave radiation. Using equation (2.1), their evolutionary timescale, $\tau_{\rm GR} \equiv -(J/\dot{J})_{\rm GR}$, is given by

$$\tau_{\rm GR} \equiv -\left(\frac{J}{\dot{J}}\right)_{\rm GR} = 3.8 \times 10^{11} \frac{(M_1+M_2)^{1/3}}{M_1 M_2} (P_{\rm orb}/{\rm days})^{8/3}\,{\rm yr}, \qquad (6.1)$$

where M_1 and M_2 are in solar masses. As the gPCEBs are detached, then their evolution in orbital period is described by equation (3.19), where we have $(\dot{J}/J)_{\rm sys} = (\dot{J}/J)_{\rm GR}$

By integrating equation (3.19) and using equation (6.1), the time, $t_{\rm u}$, it takes for a gPCEB born at an orbital period of $P_\Re^+$ to reach the upper edge of the period gap, $P_{\rm u}$, is

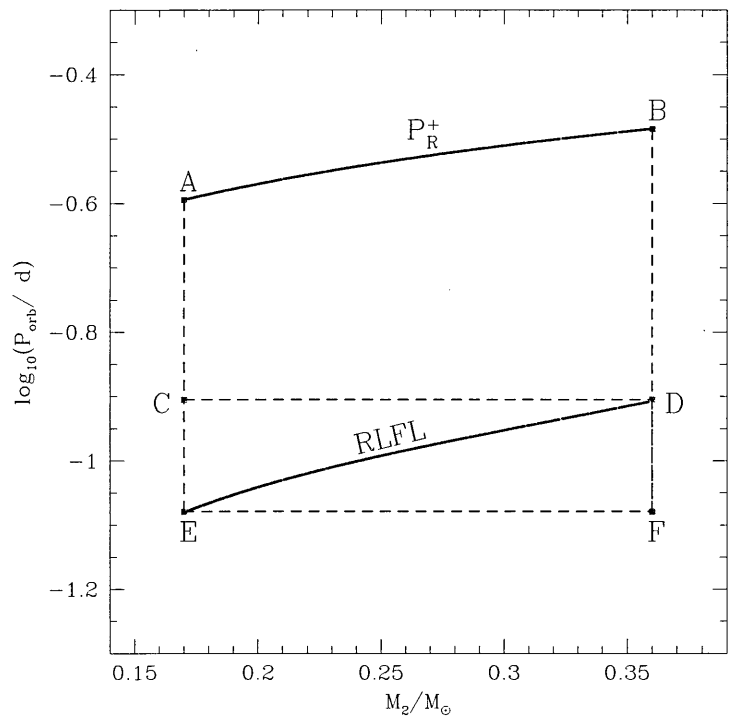

Figure 6.3: The dashed box, $CDEF$, shows the region $\Re$ defined by $0.17 \leq M_2/\mathrm{M}_\odot \leq 0.36$ and $\log_{10}(P_\ell) \leq \log_{10}(P_{\rm orb}/\mathrm{d}) \leq \log_{10}(P_{\rm u})$. The gPCEBs within $\Re$ will fill their Roche lobes within the period gap. The largest orbital period a gPCEB can have that will evolve into the period gap within the lifetime of the Galaxy is given by the boundary $P^+_{\Re}$. Thus the total area from which gPCEBs can flow into the period gap within the Galactic lifetime is the region $ABCD$.

given by

$$t_{\rm u} = \frac{\tau_{\rm GR}(P^+_{\Re}) - \tau_{\rm GR}(P_{\rm u})}{8}. \tag{6.2}$$

By stipulating that $t_{\rm u} = 10$ Gyr, we can therefore solve equation (6.2) for $P^+_{\Re}$.

The location of $P^+_{\Re}$ is shown in Figure 6.3. Therefore, the total area from which gPCEBs can evolve into $\Re$ within the Galactic lifetime is given by the region $ABCD$.

The whole population of gPCEBs is also bound within an upper limit, $P^+_{\rm PCEB}$ (shown in Figure 6.4), and the Roche lobe-filling limit (RLFL, also shown in Figure 6.3) which is the orbital period where systems become semi-detached. The upper boundary $P^+_{\rm PCEB}$ is a result of the progenitor giant primaries filling their Roche lobes at the longest orbital periods at the start of the CE phase. Due to the CE phase, the orbital periods of these progenitor systems are subsequently shifted to shorter post-CE orbital periods, giving the boundary $P^+_{\rm PCEB}$.

As the value of $\alpha_{\rm CE}$ is decreased the boundary $P^+_{\rm PCEB}$ and the population bound within

will shift to shorter orbital periods. This is graphically illustrated in Figure 6.4, which shows the location of $P^{+}_{\rm PCEB}$ for $\alpha_{\rm CE} = 1.0$ (left panel) and $\alpha_{\rm CE} = 0.1$ (right panel). For low ejection efficiencies, more orbital energy is required to eject the envelope from the system. The two stellar components will therefore need to spiral in further. The resulting PCEB (and therefore gPCEB) population will lie at shorter orbital periods.

We find that for all our models we consider, the flux of gPCEBs from $ABCD$ into $\Re$ is larger than the birthrate of gPCEBs within $\Re$ typically by a factor of ~ 7. If the typical lifetime of a gPCEB within $\Re$ is $\langle \tau_{\rm gPCEB} \rangle$ and the flux of gPCEBs from $ABCD$ into $\Re$ is $F_{\Re}$ then the present day number of gPCEBs within the period gap, $N_{\rm gPCEB}$, can be approximated as

$$N_{\rm gPCEB} \approx F_{\Re} \times \langle \tau_{\rm gPCEB} \rangle. \tag{6.3}$$

The typical value of $\langle \tau_{\rm gPCEB} \rangle \approx 380$ Myr. This was found by evolving a 0.27 $M_{\odot}$ (mean secondary mass in the range $0.17 \leq M_2/M_{\odot} \leq 0.36$) with a typical white dwarf mass of 0.6 $M_{\odot}$ using the BiSEPS code.

Clearly $F_{\Re}$ will depend on the formation rate of gPCEBs in $ABCD$. Figure 6.5 shows the formation rate of gPCEBs as a function of $\log_{10}(P_{\rm orb}/{\rm days})$ for $n(q_{\rm i}) = 1$, and for $\alpha_{\rm CE} = 0.1$ (red), 1.0 (black) and 5.0 (green). The distribution function is flat-topped and tails off towards longer orbital periods. As $\alpha_{\rm CE}$ increases and the whole population of gPCEBs shifts to longer orbital periods, the formation rate of the gPCEBs between $\log_{10}(P_{\rm u})$ and $P^{+}_{\Re}$ (inset)- and therefore in $ABCD$- changes as a consequence; at its smallest for $\alpha_{\rm CE} = 0.1$ but with little change for $\alpha_{\rm CE} \gtrsim 1.0$.

From equation (6.3) the trend in $N_{\rm gPCEB}$ with $\alpha_{\rm CE}$ will therefore mirror that of the birthrate of gPCEBs in $ABCD$. This is indeed the case as shown in the left panel of Figure 6.2.

6.1.2 The dCV Population

As with the present day population of gPCEBs, there is also an increase in the present day number of dCVs associated with an increase in $\alpha_{\rm CE}$ from 0.1 to 1.0, as shown in the middle panel of Figure 6.2. For our reference IMRD, the number of dCVs increases from 2.2×10^6 to 3.5×10^6. In contrast to the gPCEB population however, the number of dCVs decreases with a further increase in the value of $\alpha_{\rm CE}$.

Table 6.1: Present day population of dCVs, gPCEBs and the ratio dCV:gPCEB in the period gap for various values of $\alpha_{\rm CE}$ and various forms of magnetic braking. Also quoted is the present day formation rate of all PCEBs, and CVs above and below the upper edge of the period gap.

Model	Number of dCVs	Number of gPCEBs	Formation rate of PCEBs	Formation rate of CVs ≥ 3.0 h ($\rm yr^{-1}$)	Formation rate of CVs < 3.0 h ($\rm yr^{-1}$)	dCV:gPCEB
$n(q_{\rm i}) \propto q^{-0.99}$, $0 < q \leq 1$						
hCE01	5.7×10^4	8.7×10^3	2.1×10^{-4}	6.7×10^{-5}	3.7×10^{-5}	6.6
hCE06	1.5×10^5	6.1×10^4	1.5×10^{-3}	1.8×10^{-4}	2.3×10^{-4}	2.5
hA	1.5×10^5	7.4×10^4	2.0×10^{-3}	1.8×10^{-4}	2.7×10^{-4}	2.0
hCE3	9.5×10^4	8.2×10^4	3.1×10^{-3}	1.1×10^{-4}	2.4×10^{-4}	1.2
hCE5	5.9×10^4	7.9×10^4	3.5×10^{-3}	7.7×10^{-5}	2.0×10^{-4}	0.7
hPWR05	1.6×10^5	5.2×10^4	1.6×10^{-3}	1.8×10^{-4}	1.9×10^{-4}	3.1
hPWR1	1.4×10^5	2.5×10^4	1.3×10^{-3}	1.7×10^{-4}	1.0×10^{-4}	5.6
hPWR2	1.0×10^5	3.3×10^3	1.1×10^{-3}	1.4×10^{-4}	2.2×10^{-5}	30.3
rvj2A	2.2×10^5	7.4×10^4	2.0×10^{-3}	2.5×10^{-4}	2.8×10^{-4}	3.0
rvj4A	2.4×10^5	7.4×10^4	2.0×10^{-3}	3.2×10^{-4}	2.8×10^{-4}	3.2
$n(q_{\rm i}) = 1.0$, $0 < q \leq 1$ (our reference IMRD)						
hCE01	2.2×10^6	1.7×10^5	9.8×10^{-3}	3.1×10^{-3}	7.0×10^{-4}	12.9
hCE06	3.8×10^6	8.6×10^5	5.5×10^{-2}	5.6×10^{-3}	3.3×10^{-3}	4.4
hA	3.5×10^6	1.0×10^6	7.2×10^{-2}	5.0×10^{-3}	3.3×10^{-3}	3.5
hCE3	2.0×10^6	1.1×10^6	1.0×10^{-1}	2.7×10^{-3}	2.5×10^{-3}	1.8

Continued on next page

Table6.1 – continued from previous page

Model	Number of dCVs	Number of gPCEBs	Formation rate of PCEBs	Formation rate of CVs ≥ 3.0 h (yr^{-1})	Formation rate of CVs < 3.0 h (yr^{-1})	dCV:gPCEB
hCE5	1.0×10^6	1.1×10^6	1.2×10^{-1}	1.5×10^{-3}	1.9×10^{-3}	0.9
hPWR05	4.1×10^6	7.7×10^5	6.8×10^{-2}	5.2×10^{-3}	2.8×10^{-3}	5.3
hPWR1	3.9×10^6	4.4×10^5	6.5×10^{-2}	5.2×10^{-3}	1.9×10^{-3}	8.9
hPWR2	3.1×10^6	7.2×10^4	6.1×10^{-2}	4.8×10^{-3}	6.8×10^{-4}	43.1
rvj2A	5.5×10^6	1.0×10^6	7.2×10^{-2}	7.6×10^{-3}	3.6×10^{-3}	5.5
rvj4A	6.0×10^6	1.0×10^6	7.2×10^{-2}	1.0×10^{-2}	3.9×10^{-3}	6.0
$n(q_\mathrm{i}) \propto q_\mathrm{i}$, $0 < q \leq 1$						
hCE01	1.8×10^6	6.4×10^4	1.1×10^{-2}	3.2×10^{-3}	3.1×10^{-4}	28.1
hCE06	2.3×10^6	2.7×10^5	5.8×10^{-2}	4.2×10^{-3}	1.4×10^{-3}	8.5
hA	2.0×10^6	3.1×10^5	7.5×10^{-2}	3.6×10^{-3}	1.1×10^{-3}	6.5
hCE3	9.9×10^5	3.6×10^5	1.1×10^{-1}	1.7×10^{-3}	6.1×10^{-4}	2.8
hCE5	4.1×10^5	3.7×10^5	1.2×10^{-1}	7.0×10^{-4}	4.5×10^{-4}	1.1
hPWR05	2.3×10^6	2.5×10^5	7.7×10^{-2}	3.7×10^{-3}	1.1×10^{-3}	9.2
hPWR1	2.3×10^6	1.6×10^5	7.8×10^{-2}	3.7×10^{-3}	9.1×10^{-4}	14.4
hPWR2	2.0×10^6	3.2×10^4	7.8×10^{-2}	3.5×10^{-3}	5.3×10^{-4}	62.5
rvj2A	3.2×10^6	3.1×10^5	7.5×10^{-2}	5.7×10^{-3}	1.5×10^{-3}	10.3
rvj4A	3.6×10^6	3.1×10^5	7.5×10^{-2}	8.9×10^{-3}	1.9×10^{-3}	11.6

Continued on next page

Table6.1 – continued from previous page

Model	Number of dCVs	Number of gPCEBs	Formation rate of PCEBs	Formation rate of CVs ≥ 3.0 h (yr^{-1})	Formation rate of CVs < 3.0 h (yr^{-1})	dCV:gPCEB
			M_2 from IMF according to eqn. (4.2)			
hCE01	1.8×10^6	4.0×10^5	6.5×10^{-3}	1.9×10^{-3}	1.7×10^{-3}	4.5
hCE06	4.7×10^6	2.9×10^6	4.7×10^{-2}	4.8×10^{-3}	1.1×10^{-2}	1.6
hA	5.0×10^6	3.5×10^6	6.5×10^{-2}	4.8×10^{-3}	1.3×10^{-2}	1.4
hCE3	3.1×10^6	3.9×10^6	1.0×10^{-1}	3.1×10^{-3}	1.2×10^{-2}	0.8
hCE5	1.8×10^6	3.7×10^6	1.2×10^{-1}	2.1×10^{-3}	1.0×10^{-2}	0.5
hPWR05	5.2×10^6	2.4×10^6	4.4×10^{-2}	4.9×10^{-3}	9.0×10^{-3}	2.2
hPWR1	4.7×10^6	1.2×10^6	2.9×10^{-2}	4.6×10^{-3}	4.3×10^{-3}	3.9
hPWR2	3.1×10^6	1.4×10^5	1.7×10^{-2}	3.6×10^{-3}	8.2×10^{-4}	22.1
rvj2A	6.2×10^6	3.5×10^6	6.5×10^{-2}	6.3×10^{-3}	1.4×10^{-2}	1.8
rvj4A	6.8×10^6	3.5×10^6	6.5×10^{-2}	7.6×10^{-3}	1.4×10^{-2}	1.9

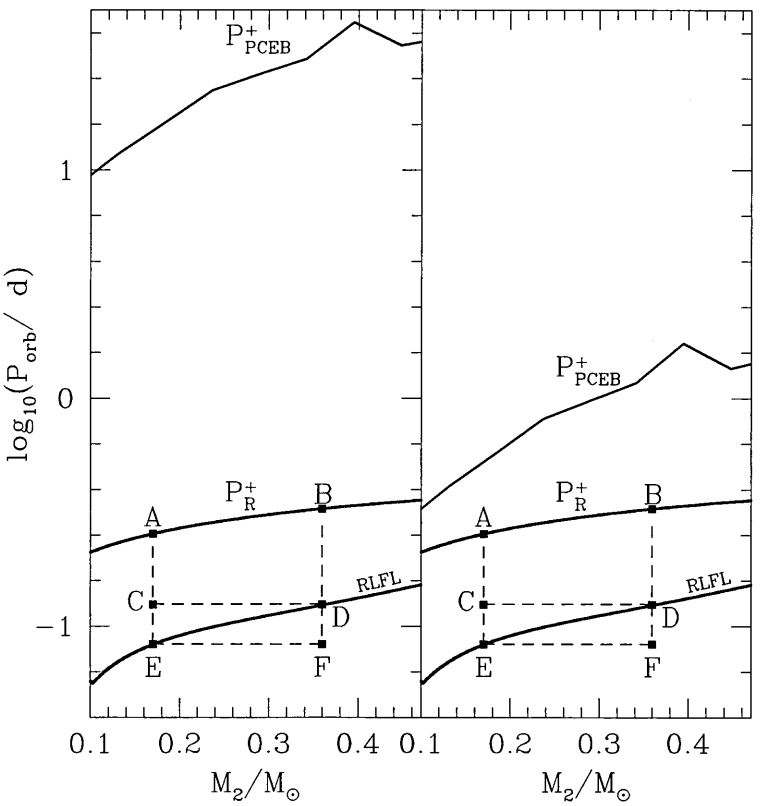

Figure 6.4: How the location of the upper boundary of the PCEB population, $P^{+}_{\rm PCEB}$, with low-mass secondaries changes for different values of $\alpha_{\rm CE}$. Left panel: $\alpha_{\rm CE} = 1.0$; right panel: $\alpha_{\rm CE} = 0.1$. Also shown on both panels is the region in $\log_{10}P_{\rm orb} - M_2$ space depicted in Figure 6.3.

If the formation rate of dCVs is $B_{\rm dCV}$ and their average lifetime is $\langle\tau_{\rm dCV}\rangle$, then the present-day population of dCVs can be approximated by

$$N_{\rm dCV} \approx B_{\rm dCV} \times \langle\tau_{\rm dCV}\rangle. \tag{6.4}$$

If we now assume that the populations above the period gap of pre-CVs (with $M_2 > M_{\rm MS,conv}$) and CVs are in a steady state, we then have for their respective formation rates $B_{\rm preCV}$ and $B_{\rm CV}$

$$B_{\rm PreCV} \approx B_{\rm CV} \approx B_{\rm dCV}. \tag{6.5}$$

The formation rate of dCVs is therefore linked to that of these pre-CVs above the period gap. Figure 6.6 shows how the formation rate of pre-CVs changes over the history of the Galaxy for our standard model hA, with $n(q_{\rm i}) = 1$. As can be seen, the formation rate levels off to $\approx 8.3 \times 10^{-3}$ yr^{-1} by the present epoch. Thus, the assumption of a steady-state pre-CV population is a good one.

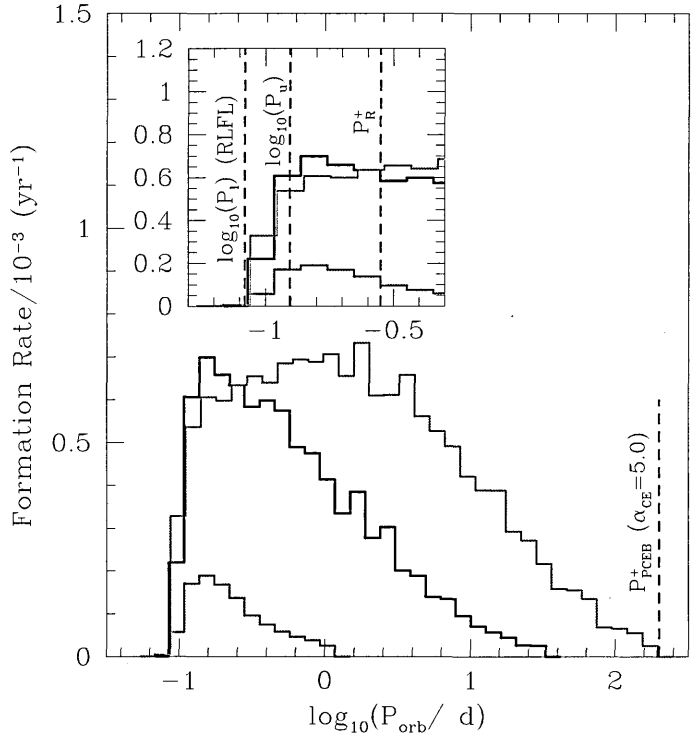

Figure 6.5: The formation rate of gPCEBs as a function of $\log_{10}(P_{\rm orb}/{\rm d})$ for $n(q_{\rm i}) = 1$ and for $\alpha_{\rm CE} = 0.1$ (red), 1.0 (black) and 5.0 (green). Shown in the inset are the period gap boundaries $\log_{10}P_\ell$ (which is also the RLFL for 0.17 $M_\odot$ secondaries) and $\log_{10}P_{\rm u}$, and $P^+_{\Re}$. The upper boundary $P^+_{\rm PCEB}$ for $\alpha_{\rm CE} = 5.0$ is shown in the main plot as the dashed line. Note that $P^+_{\rm PCEB}$, and in fact the whole distribution function, shifts to shorter periods as $\alpha_{\rm CE}$ decreases.

Figure 6.7 shows the present-day formation rate of pre-CVs for $n(q_{\rm i}) = 1$ on the $M_2 - \log_{10}(P_{\rm orb})$ plane, for $\alpha_{\rm CE} = 0.1$ (top panel), 1.0 (middle panel) and 5.0 (bottom panel), where the colour bar at the top indicates the formation rate in Myr^{-1} per bin area. The lower boundary in each of the populations is the RLFL, while the upper boundary is given by those PCEBs where the time taken for the primary progenitor to fill its Roche lobe plus the time taken for the secondary to subsequently come into contact with its Roche lobe is 10 Gyr (i.e. the Galactic lifetime). The shape of the upper boundary is determined by the angular momentum loss mechanism; gravitational radiation for systems with $M_2 \leq M_{\rm MS,conv}$ or a combination of magnetic braking and gravitational radiation for systems with $M_2 > M_{\rm MS,conv}$ (see Section 3.4).

Inspecting the upper and middle panels of Figure 6.7 shows that there is an increase in the formation rate of pre-CVs from $\alpha_{\rm CE} = 0.1$ to $\alpha_{\rm CE} = 1.0$. This is a consequence of the whole population of PCEBs being shifted to longer orbital periods for larger ejection

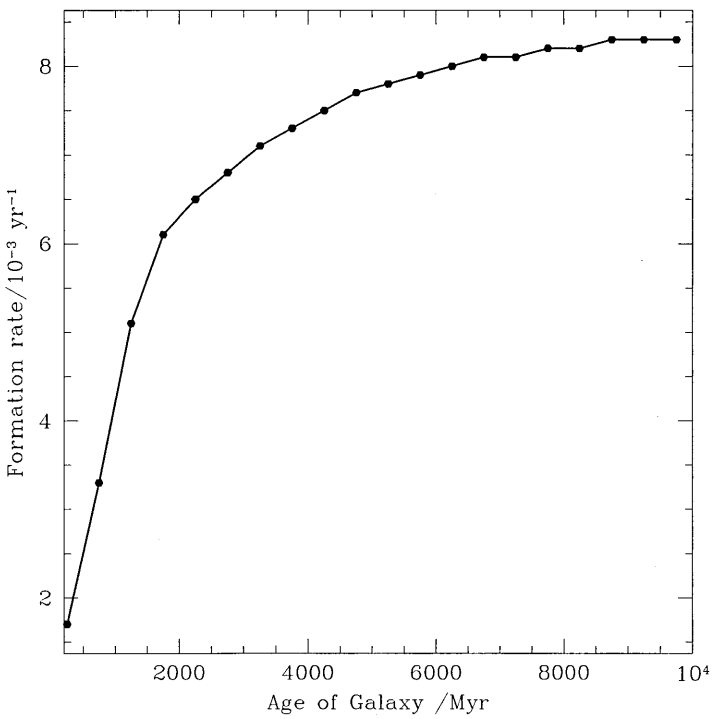

Figure 6.6: The formation rate of pre-CVs (in units of 10^{-3} yr^{-1}) versus the age of the Galaxy (Myr), for model hA and $n(q_i) = 1$. Note how the formation rate levels off by the present day, indicating a steady state population.

efficiencies, and hence more systems surviving the CE phase. For $\alpha_{\mathrm{CE}} = 5.0$ in the lower panel, however, there is an overall decrease in the formation rate of pre-CVs. Progenitor systems with even shorter initial orbital periods than those for models hCE01 or hA can now survive the CE phase. Such progenitors result in pre-CVs that formed through a case B CE phase with a naked helium star remnant. These systems lie below the solid line in the bottom panel of Figure 6.7, while those above the line are those pre-CVs that formed through a case C CE phase. The latter systems have ended up at much longer orbital periods than for models hCE01 and hA. The solid line represents those pre-CVs whose progenitor primaries just filled their Roche lobes on the base of the asymptotic giant branch. It is the disappearance of case C remnants and the appearance of the less abundant case B remnants that causes the decrease in the total pre-CV formation rate.

From equations (6.4) to (6.5) this trend in B_{PreCV} should be mirrored in the present day number of dCVs, which is the case as shown in the middle panel of Figure 6.2.

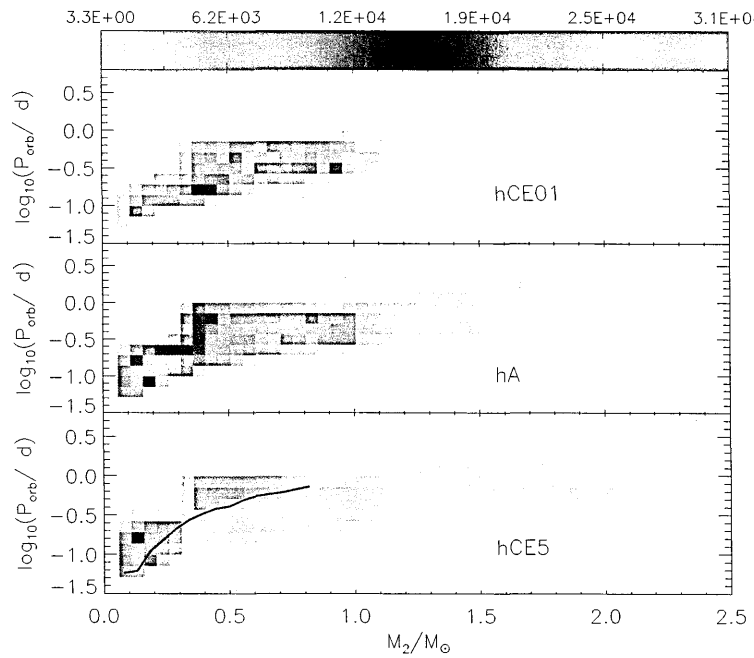

Figure 6.7: The formation rate of pre-CVs for $n(q_i) = 1$ on the $M_2 - \log_{10}(P_{orb})$ plane for $\alpha_{CE} = 0.1$ (top panel), 1.0 (middle panel) and 5.0 (bottom panel). Pre-CVs that lie above the solid line in the bottom panel formed through a case C CE phase, while those that lie below it formed through a case B CE phase with a naked helium star remnant. The colour bar at the top indicates the formation rate (Myr^{-1}) per bin area $\mathrm{d}M_2\,\mathrm{dlog}_{10}(P_{orb})$.

6.1.3 Overall Trends

These trends in the populations of gPCEBs and dCVs are the same for all forms of the IMRD function, and where the secondary mass is determined independently from the IMF according to (4.2). The largest population of gPCEBs and dCVs is obtained when the secondary mass is determined for this latter case. The smallest population numbers are found for $n(q_i) \propto q_i^{-0.99}$.

Combining the trends of dCVs and gPCEBs gives a decrease in the ratio of dCV:gPCEB with increasing α_{CE}, seen in the right-most panel of Figure 6.2. For our reference IMRD function, dCV:gPCEB decreases from 12.9 for $\alpha_{CE} = 0.1$ to 0.9 for $\alpha_{CE} = 5.0$. Again this trend is the same for all forms of the IMRD function. We note that the ratio dCV:gPCEB decreases with decreasing value of ν. To understand why, note that the dCVs will have formed from CVs filling their Roche lobes at long orbital periods above the period gap.

This is in contrast to gPCEBs in the period gap which have secondary masses in the range $0.17 \leq M_2/M_\odot \leq 0.36$. Thus, for a given primary mass, the dCV progenitor systems will have, on average, more massive secondaries than found in gPCEBs. The IMRD $n(q_i) \propto q_i$ will mostly favour the formation of systems with more massive secondaries, thus mostly favouring the formation of dCV progenitors over the gPCEB progenitors. Thus we obtain the largest values of dCV:gPCEB. This is in contrast with the IMRD of the form $n(q_i) \propto {q_i}^{-0.99}$ which most favour the formation of systems with less massive secondaries, thereby mostly favouring the formation of gPCEB progenitors over dCV progenitors. We therefore obtain the smallest values of dCV:gPCEB out of the three forms of the IMRD. The smallest values of dCV:gPCEB are obtained when the secondary mass is determined independently from the primary mass.

6.2 $\alpha_{\rm CE}$ as a function of Secondary Mass: models hPWR05 to hPWR2

In models where $\alpha_{\rm CE}$ is determined from equation (3.15) both the present day populations of gPCEBs and dCVs decrease as the power index p is increased. For our reference IMRD function, the left panel of Figure 6.8 shows that the number of gPCEBs decreases from 7.7×10^5 to 7.2×10^4. The middle panel shows that the number of dCVs decreases slightly from 4.1×10^6 to 3.1×10^6. As with the population of gPCEBs for models hA to hCE5, this trend depends on the flow rate of gPCEBs into the region $\Re$, and how this changes as the whole population of PCEBs is shifted with $\alpha_{\rm CE}$.

6.2.1 The gPCEB Population

The dark-grey area in Figure 5.11 indicates the range of secondary masses for the gPCEB systems. As p increases from 0.5 to 2, the average corresponding value of $\alpha_{\rm CE}$ for these systems decreases from ~ 0.5 to ~ 0.1. As a consequence the population of gPCEBs will shift to shorter orbital periods with increasing p. This in turn will change the formation rate of gPCEBs in the region $ABCD$ and hence the flux $F_{\Re}$.

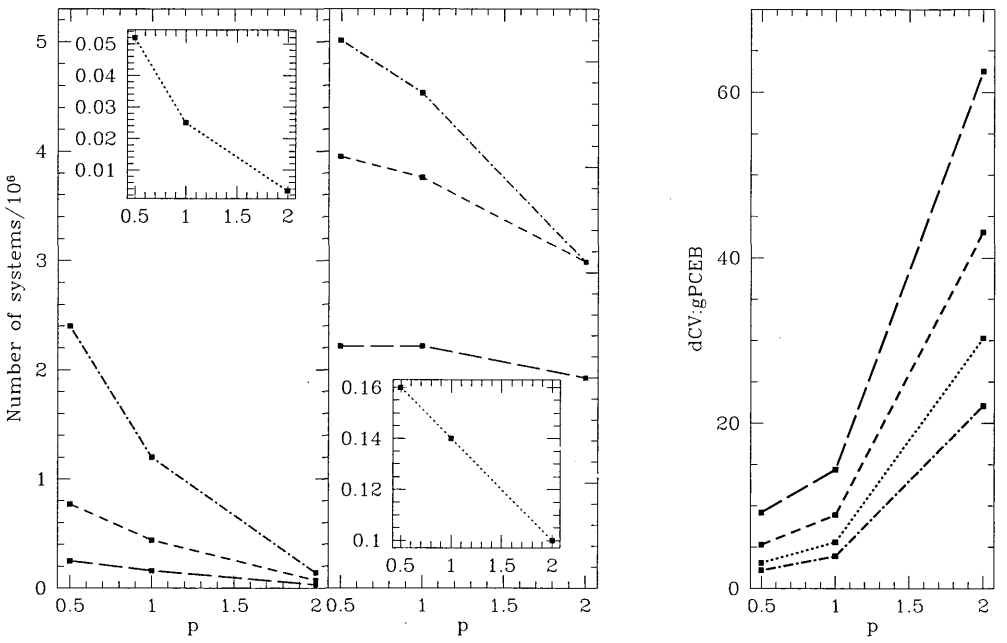

Figure 6.8: From left to right: the present day population of gPCEBs in the period gap (blue) and dCVs (red) as a function of the power index p, and the ratio dCV:gPCEB as a function of p. Long-dashed: $n(q_i) \propto q_i$; short-dashed: $n(q_i) = 1$; dot-dashed: where M_2 is picked independently from the same IMF as M_1 according to equation (4.2); dotted: $n(q_i) \propto q_i^{-0.99}$ (insets).

As can be seen in the left panel of Figure 6.2, a value of α_{CE} decreasing from ~ 0.5 to ~ 0.1 leads to the decrease in the present-day number of gPCEBs in the period gap. This corresponds to the decrease in the present-day number of gPCEBs with increasing p seen in the left panel of Figure 6.8.

6.2.2 The dCV Population

As with the dCVs for models hA to hCE5, the population of dCVs for hPL05 to hPL2 depends on the formation rate of pre-CVs with $M_2 > M_{MS,conv}$ above the period gap. The light-grey region in Figure 5.11 shows the range of secondary masses for dCV progenitor systems. For this range in secondary mass there is, on average, little change in α_{CE}. Indeed, the dominant secondary mass group for pre-CV progenitors is $M_2 \lesssim 0.6\ M_\odot$; here an increase in p from 0.5 to 2 corresponds to a decrease in α_{CE} from ~ 0.7 to ~ 0.3. Hence from the

middle panel of Figure 6.2 a slight decrease in $N_{\rm dCV}$ can be expected. This is indeed the case as shown in the middle panel of Figure 6.8.

6.2.3 Overall Trends

The trend in the present day populations of gPCEBs and dCVs with p is the same for all forms of the IMRD function, and where the secondary mass is determined from the same IMF as the primary mass. As before, the largest population of dCVs and gPCEBs occurs when the secondary mass is determined from the same IMF as the primary. The smallest populations occur when $n(q_{\rm i}) \propto {q_{\rm i}}^{-0.99}$.

As a consequence of the behaviour discussed in Sections 6.2.1 and 6.2.2, the ratio dCV:gPCEB increases as p increases. For our reference model, dCV:gPCEB increases from 5.3 for $p = 0.5$ to 43.1 for $p = 2$. The variation of dCV:gPCEB with p is shown in the most right hand panel in Figure 6.8.

Note that these ratios are very large for $p = 2$ as PCEBs with low-mass donors will encounter a merger. Hence the vast majority of all CVs will form above the period gap, with very few gPCEBs within the period gap. Politano & Weiler (2007) suggested that such a strong dependence of $\alpha_{\rm CE}$ on M_2 could explain the lack of CVs with sub-stellar secondaries. However, we note that a lack of calculated gPCEBs with low-mass secondaries appears to be inconsistent with observations [Ritter & Kolb 2003, catalogue Edition 7.7 (2006)], which show a modest number of PCEBs with $M_2 \approx 0.17$ M$_\odot$. We therefore believe that the $p = 2$ model is not a realistic one. As with models hA to hCE5, dCV:gPCEB decreases with decreasing values of ν. The reasons for this are the same as those described in Section 6.1. The smallest value of dCV:gPCEB occurs when the secondary mass is determined independently from the primary mass.

6.3 Alternative Magnetic Braking Laws: Models rvj2A and rvj4A

We now consider the impact of different forms of magnetic braking on gPCEBs and dCVs. Increasing γ from 2 to 4 increases the present day number of dCVs from 5.5×10^6 for $\gamma = 2$ to 6.0×10^6 for $\gamma = 4$, for our reference IMRD. The Rappaport et al. (1983) prescription of magnetic braking gives a larger present day population of dCVs than the Hurley et al. (2002) prescription, between any IMRD function; for our reference model hA, with $n(q_{\rm i}) = 1$, the present day number of dCVs is 3.5×10^6.

The pre-CV progenitor systems of CVs that form above the period gap will initially be driven by magnetic braking. Increasing the strength of magnetic braking will shift the upper limit in the pre-CV population, $P^{+}_{\rm preCV}$ (analogous to $P^{+}_{\rm PCEB}$), to longer orbital periods for systems with $M_2 > M_{\rm MS,conv}$. Thus more systems will become semi-detached within the lifetime of the Galaxy. From equations (6.4) to (6.5), this will result in an increase in the formation rate of pre-CVs above the period gap, and therefore increase the formation rate of dCVs. In turn, this will increase the present day population of dCVs.

Note that the number of present day gPCEBs does not change with magnetic braking law. In our model, the mass at which isolated stars become fully convective is 0.35 $M_\odot$ (Hurley et al. 2002). Thus, the evolution of gPCEBs with $M_2 \leq 0.35$ $M_\odot$ will be driven by gravitational radiation only. As we are only considering PCEBs with secondaries in the range $0.17 \leq M_2/M_\odot \leq 0.36$, only very few systems will evolve via magnetic braking while the large majority will be driven via gravitational radiation.

These trends in the population of dCVs and gPCEBs result in an increase in dCV:gPCEB with increasing magnetic braking strength. For our reference IMRD function, and where $\alpha_{\rm CE} = 1.0$, the ratio increases from 3.5 for the Hurley et al. (2002) form of magnetic braking, to 6.0 for the Rappaport et al. (1983) prescription, $\gamma = 4$. The largest values of dCV:gPCEB occur when the IMRD function is $n(q_{\rm i}) \propto q_{\rm i}$, while the smallest occur when $n(q_{\rm i}) \propto {q_{\rm i}}^{-0.99}$.

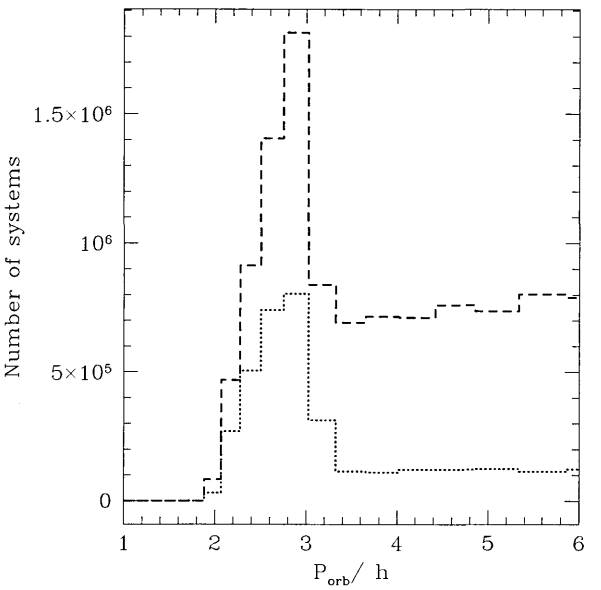

Figure 6.9: The orbital period distribution of the combined population of dCVs and gPCEBs for $n(q_i) = 1$, $\alpha_{CE} = 0.6$ (dashed line) and $\alpha_{CE} = 0.1$ (dotted line).

6.4 Discussion

6.4.1 Observational Predictions

In this section we consider the number of present day dCVs and gPCEBs, and hence the ratio dCV:gPCEB, given the commonly assumed form of the IMRD and values of α_{CE}. We can then gauge whether such an excess of dCVs over gPCEBs can be determined observationally.

Numerical calculations of the CE phase suggest that $\alpha_{CE} = 0.13$ to 0.6 (Iben & Livio 1993), while the IMRD seems to be flat in q_i, i.e. $n(q_i) = 1$ [Goldberg et al. (2003); Mazeh et al. (1992); Duquennoy & Mayor (1991)]. From Table 6.1 we can estimate that the number of dCVs currently occupying the Galaxy is $(2.2-3.8)\times10^6$, while the number of gPCEBs is in the range $(1.7-8.6)\times10^5$, giving a factor of ~ 4 to ~ 13 more dCVs than gPCEBs within the period gap. Hence we predict a prominent peak in the orbital period distribution of short orbital period WD+MS systems as shown in Figure 6.9. In determining these predictions, we have assumed that magnetic braking takes the form shown in equation (5.19).

Of course, the AM loss rate associated with magnetic braking is not very well constrained, and indeed it has been suggested that the magnetic braking strength is $\approx$ 100 weaker than the forms we have used in this investigation (see Section 2.4). However, we have not

considered the forms of magnetic braking that include a saturation point if the secondary star has a spin frequency larger than some critical value $\Omega_{\rm crit}$ [Sills et al. (2000); Ivanova & Taam (2003)]. This is because, in the case of the Sills et al. (2000) form of magnetic braking, the AM loss rate would be too small to sufficiently drive the donor star out of thermal equilibrium, and consequently produce a period gap. Furthermore, the Sills et al. (2000) form of magnetic braking predict mass transfer rates at the upper edge of the period gap that are too low compared to observations, and as such would not explain the presence of nova-like CVs above the period gap [e.g. Kolb (2002)]. The Ivanova & Taam (2003) form of magnetic braking on the other hand, which is $\sim$ 2 to 3 times weaker than the Verbunt & Zwaan (1982) form, would drive the donor star out of thermal equilibrium but not enough to explain the observed width of the period gap.

Such forms of magnetic braking are therefore inconsistent with the disrupted magnetic braking model. Instead, if they are a true representation of magnetic braking, alternative mechanisms must exist that combine in strength to reach the value that we consider at the upper edge of the period gap.

6.4.2 The Location of the Period Gap

We now discuss the impact the location of the period gap has on our results. We note that Knigge (2006), using a similar method to ours, determined that the period gap edges are 2.15 hours and 3.18 hours, which agrees with our determined period gap width of one hour. We attribute the slight difference between the two locations of the period gap to two things. The first is that Knigge (2006) used the Ritter & Kolb (2003) catalogue (Edition 7.6), while we use the later Edition 7.7, which was the most up-to-date edition at the time this investigation was completed. Secondly, Knigge (2006) constructed the CV orbital period distribution, and measured the corresponding location of the period gap edges, for a range of bin widths. In this investigation we only considered the one (as presented in Figure 5.6).

If the period gap was located according to Knigge (2006), this would have the effect of increasing the population of gPCEBs within the period gap, and consequently decrease the ratio dCV:gPCEB. The higher values of $P_{\rm u}$ and P_{ℓ} would shift the mass range of gPCEBs to $0.19 \leq M_2/{\rm M}_{\odot} \leq 0.40$, and therefore a larger fraction of gPCEBs would be driven by magnetic braking. In turn, the flow rate of gPCEBs from longer orbital periods into $\Re$ would

increase. However, as only gPCEBs within a narrow mass range of $0.35 \leq M_2/\mathrm{M}_\odot \leq 0.40$ will be driven by magnetic braking, the adoption of the period gap location according to Knigge (2006) would have only a very minor impact on our results. We also point out that a similar uncertainty is introduced with the value of $M_{\mathrm{MS,conv}}$, as this is not well constrained by stellar evolution models.

In their studies on circumbinary disk driven CVs Willems et al. (2005) considered the CV population below the gap, while Willems et al. (2007) studied the population above the gap. These authors never attempted to systematically model, or to achieve a best fit model for, the combined population. This is why their adopted period gap boundaries of 2.25 and 2.75 hours, respectively, result in an implausibly narrow gap when taken together.

Nonetheless we investigated how a narrower period gap would affect our results by calculating a further population model with the gap boundaries set to 2.25 and 2.75 hours. We considered $\alpha_{\mathrm{CE}} = 1.0$ with our standard IMRD, and re-calibrated equation (2.9) to give the AM loss rate appropriate for the narrower gap width. We find that dCV:gPCEB decreases to 2.1 compared to our model hA value of 3.5. Thus the prominence of the peak would decrease somewhat. This is because the time for a dCV to cross a narrower gap would decrease (we find $\langle \tau_{\mathrm{dCV}} \rangle \approx 438$ Myr), decreasing the present day population from 3.5×10^6 for model hA to 1.1×10^6. The number of gPCEBs in the period gap also decreases from 1.0×10^6 for model hA to 5.2×10^5 because the systems occupy a smaller area in period space.

We emphasise that a gap width of half an hour is a somewhat extreme assumption. Despite this we still obtain a clear excess of dCVs over gPCEBs in the period gap, and hence a prominent peak would still be detected. Indeed, a prominent peak would still be detected for any reasonable gap width.

6.4.3 An Extra Sink of Angular Momentum for Fully Convective Stars?

As discussed in Chapter 2, Section 2.3.3, a sink of orbital angular momentum other than gravitational radiation may drive the evolution of CVs with fully convective stars, below the upper edge of the period gap. Kolb & Baraffe (1999) suggest that the angular momentum loss rate due to this extra sink is approximately 4 times greater than that due to gravitational

radiation.

If such an extra sink of angular momentum exists, this will affect the time it takes for both dCVs and gPCEBs to cross the period gap, which in turn will affect the number of these systems existing within the period gap. This will consequently affect the prominence of the mirror gap. In this section, we will make a rough estimate as to how the numbers of dCVs and gPCEBs within the period gap are affected as a result of an extra sink of angular momentum. We will consider our standard model hA with $n(q_{\rm i}) = 1$.

We can use equations (6.3) and (6.4) to estimate the number of gPCEBs and dCVs within the period gap respectively. Now if the angular momentum loss rate is a factor of 4 greater than that due to gravitational radiation, then the values of $\langle \tau_{\rm gPCEB} \rangle$ and $\langle \tau_{\rm dCV} \rangle$ will be a 1/4 of the values appropriate for gravitational radiation only (which we calculated in Sections 6.1.1 and 6.1.2). We therefore have $\langle \tau_{\rm gPCEB} \rangle \approx 95$ Myr, and $\langle \tau_{\rm dCV} \rangle \approx 263$ Myr.

From table 6.1, the formation rate of CVs above the period gap for model hA, $n(q_{\rm i}) = 1$ is 5.0×10^{-3} yr^{-1}. Using the new value of $\langle \tau_{\rm dCV} \rangle$, we estimate the number of dCVs within the period gap with this extra sink of angular momentum is approximately 1.3×10^{6}.

For the case of gPCEBs, an extra sink of angular momentum will mean that gPCEBs from orbital periods longer than that depicted by $P_{\Re}^{+}$ in Figure 6.3 will be able to evolve into the period gap by the age of the Galaxy. This will increase the flux, $F_{\Re}$, in equation (6.3). However, we find that the location of $P_{\Re}^{+}$ increases by only about 1 day, meaning that the change in $F_{\Re}$ will be negligible.

Recalling from Section 6.1.1 that $F_{\Re}$ is about 7 times greater than the birth rate of gPCEBs within the period gap ($\approx 5 \times 10^{-4}$ yr^{-1} for our standard model), then the number of gPCEBs within the period gap with the extra sink of angular momentum is approximately 3.3×10^{5}.

Hence the ratio dCV:gPCEB with this extra sink of angular momentum becomes approximately 4. There is therefore no appreciable decrease in the prominence of the mirror gap. If an extra sink of angular momentum does drive the evolution of binaries with fully convective secondaries, we can still expect to detect a significant mirror gap.

6.4.4 Thermal Timescale Mass Transfer Systems

Observational investigations have shown that in many CVs above the period gap the donor is unlikely to be an unevolved main sequence donor [e.g. Beuermann et al. (1998)]. Instead, the spectral types of the donor are later than those of an isolated star of the same mass, while donors at orbital periods longer than 5 to 6 hours are nuclear evolved [Patterson et al. (2005); Knigge (2006)]. Theoretical calculations also predict this effect (Baraffe & Kolb 2000). It has been suggested that such systems had an initial thermal timescale mass transfer (TTMT) phase where the secondary star was much more massive than the white dwarf (Schenker et al. 2002). Kolb & Willems (2005) find that as much as 40 per cent of zero-age CVs form with a donor that has evolved more than half way through its main sequence lifetime. Gänsicke et al. (2003) have detected CNO abundance anomalies consistent with nuclear evolved donors among $\sim 10-15$ per cent CVs in a sample observed in the ultraviolet, corroborating the hypothesis that a significant fraction of the known CV population may be post-TTMT systems.

Such CVs, if they appear after their initial TTMT phase above the period gap, may contribute to the present day population of dCVs. Thus our values of dCV:gPCEB, which are calculated from the evolution of purely AM driven CVs, are lower limits. To calculate the contribution of post-TTMT CVs to the total dCV population would require a comprehensive treatment of the TTMT phase including the fate of the transferred material, which determines the point of re-appearance of the system as a 'normal' AM driven CV.

6.4.5 Magnetic CVs

We now consider how the contribution of magnetic CVs (mCVs) may affect the ratio dCV:gPCEB within the period gap. Intermediate polars (IPs) are thought to evolve as non-magnetic CVs and hence become detached at the upper edge of the period gap due to the disruption of magnetic braking. Their contribution to the population of dCVs is therefore already taken into account in our calculations, as are their progenitors to the gPCEB population.

Polars, on the other hand, may not become detached at the upper edge of the period gap, as it has been suggested that magnetic braking for these systems is estimated to be 1 to 2 orders of magnitude weaker than for non-magnetic CVs [Li et al. (1994*a*); Li et al. (1994*b*)].

This is supported observationally from their white dwarf temperatures: the accretion-heated white dwarfs in polars are consistently colder than those in non-magnetic CVs at similar orbital periods, implying lower accretion rates, and hence angular momentum loss rates (Araujo-Betancor et al. 2005). This difference is especially pronounced above the period gap, where magnetic braking is the dominant AM loss agent.

Furthermore, no progenitor WD+MS systems of mCVs with a magnetic white dwarf has as yet been detected (Liebert et al. 2005). It is possible that such progenitors evolve in the same way as progenitors of non-magnetic CVs. In such a case, the population of WD+MS progenitors of polars will already be taken into account in our calculations and are included in the number of gPCEBs we obtained.

The overall effect of the above on our results would be to reduce the number of dCVs and hence the ratio dCV:gPCEB by the fraction of polars among the total CV population. From the Ritter & Kolb (2003) catalogue, Edition 7.7 (2006), we find that polars contribute $\sim$ 13 per cent to the total CV population. However, this is likely to be larger than the true intrinsic fraction, due to selection effects and x-ray surveys that favour the detection of mCVs.

6.4.6 PCEB Candidates

Here we discuss the current situation regarding PCEB candidates and the surveys presently searching for them. Schreiber & Gänsicke (2003) studied 30 well observed PCEBs, which were chosen to be representative of PCEBs that will begin mass transfer within the Hubble time. These systems have orbital periods $\lesssim$2 days, have mass ratios less than 1, and do not include secondaries that are sub-giants. They found that the majority of systems contained young ($\lesssim 5 \times 10^8$ yrs), hot ($\approx$ 15 000-22 000 K) white dwarfs. This is a consequence of the fact that until recently PCEB candidates were almost exclusively identified in blue colour surveys such as the Palomar Green survey. Thus, systems containing cool white dwarfs and/or early type companion stars have been missed in most previous work, with the exception of a few systems identified as nearby large proper motion systems (e.g. RR Cae) or spectroscopic binaries (e.g. V471 Tau).

The potential of observational population studies of PCEBs has improved over the past few years dramatically through the SDSS. Because of the vast *ugriz* colour space probed by

SDSS, coupled with the availability of high-quality follow-up spectroscopy of a large number of objects with non-stellar colours, has already lead to the identification of more than 1000 WD+MS binaries (Silvestri et al. 2007), most of them being by-products of the search for quasars. A complementary program targeting specifically WD+MS binaries containing cool white dwarfs and/or early type companions is underway to compensate the bias against such systems in the previous surveys (Schreiber et al. 2007). For the first phase, the PCEBs among the full sample of WD+MS binaries have to be identified through radial velocity studies. A first effort along these lines has been carried out by Rebassa-Mansergas et al. (2007) who identified 18 PCEB candidates from multiple SDSS spectroscopy obtained for 101 WD+MS. Rebassa-Mansergas et al. (2008) confirmed through follow-up spectroscopy so far six of those candidates as PCEBs with orbital periods ranging from 164 min to 1048 min. Additional identification work of the PCEBs among the SDSS WD+MS is currently carried out at the Very Large Telescope (Schreiber et al. 2008) and the William Herschel Telescope (Pyrzas et al. 2009).

It is foreseeable that, sufficient observational effort being invested, it will be possible to build up an orbital period distribution of close WD+MS binaries comprising potentially a few hundred systems. While the SDSS PCEB sample will not be free of selection effects [see e.g. Rebassa-Mansergas et al. (2007); Pretorius et al. (2006)], those biases can be modelled to a large degree. It appears hence feasible to subject the disrupted magnetic braking model to a stringent test by comparing such an observed orbital period distribution to the predictions of our work here (Figure 6.9).

6.5 Conclusions

We have performed population synthesis calculations to obtain the present day population of two types of white dwarf-main sequence star systems within the 2 to 3 hour cataclysmic variable period gap. The first are post-CE binaries with secondaries that have masses $0.17 \leq M_2/\mathrm{M}_\odot \leq 0.36$, and so will commence mass transfer in the period gap (gPCEBs). The second type are systems that were CVs in the past, but detached at the upper edge of the period gap as a consequence of disrupted magnetic braking, and are crossing the period gap via gravitational radiation (dCVs).

Our calculations were repeated to consider constant, global values of the CE ejection efficiency, $\alpha_{\rm CE}$, and cases where $\alpha_{\rm CE}$ is a function of secondary mass according to equation (3.15). We considered various forms of magnetic braking according to equation (2.8) with $\gamma = 2$ and 4, and equation (2.9).

We find that there is a prominent peak in the orbital period distribution of the combined dCV and gPCEB population, due to the excess of dCVs over gPCEBs within the period gap. We find that the ratio dCV:gPCEB, which gives an indication of the peak's height, decreases with an increasing global value of $\alpha_{\rm CE}$, while increasing with increasing value of p. These trends are the same for all assumptions on the initial secondary mass distribution. The value of dCV:gPCEB ranges from 0.5 for model hCE5 where the secondary mass is determined independently from the primary mass using the same IMF, to 62.5 for model hPWR2 where $n(q_{\rm i}) \propto q_{\rm i}$.

We find further that dCV:gPCEB increases with increasing magnetic braking strength, although only slightly. For $n(q_{\rm i}) = 1$, dCV:gPCEB increases from 3.5 for model hA (the weakest) to 6.0 for rvj4A (the strongest).

For all our models we find that the values of dCV:gPCEB are largest when the IMRD function has the form $n(q_{\rm i}) \propto q_{\rm i}$ i.e. on average systems will have more massive secondary stars. The smallest values occur when the secondary mass is determined from the same IMF as the primary.

The most likely value of dCV:gPCEB is between ~ 4 to ~ 13, thus we can expect a significant peak as shown in Figure 6.9.We suggest that if such a feature is observed in the orbital period distribution of short orbital period WD+MS binaries, this would strongly corroborate the disruption of magnetic braking.

The remainder of this thesis is now dedicated to our population synthesis study of PCEBs, which uses the code BiSEPS as discussed in Chapter 4. The next chapter describes our motivation, and the new techniques developed and employed for this investigation.

PART III

A Comprehensive Population Synthesis Study of PCEBs

7

Method

In Chapter 3 we showed that our understanding of the CE phase is poorly understood, while the theoretical parameterisations which describe it are ill-constrained. We therefore calculate the present day population of PCEBs, as discussed in Section 7.1, for a range of theoretical treatments of the CE phase. The corresponding models are discussed in Section 7.2. In contrast to our treatment of the CE phase given in Chapter 5, we also consider the internal energy of the primary giant's envelope, and calculate the value of $\lambda_{\rm CE}$ appropriate for the structure of the progenitor primary (both with and without consideration of the envelope's internal energy; see Section 3.3). The CE phase in terms of the angular momentum budget of the binary is also considered in Section 7.3. The subsequent evolution of the PCEB due to magnetic braking is discussed in Section 7.4.

Our suite of population models represents a major advance over the work by Willems & Kolb (2004) who considered only the formation rate of PCEBs, and a simplified estimate of their present-day populations based on birth and death rates. Our models also cover a more comprehensive parameter space than those by Politano & Weiler (2007). Indeed, we carry out a comprehensive analysis between the distributions of the theoretical and observed PCEB populations in $(M_{\rm WD}, M_2, P_{\rm orb})$ space. To make this more convenient, we consider two dimensional distributions in $M_2 - \log_{10} P_{\rm orb}$ space for different intervals in white dwarf mass. The observed population is obtained from the Ritter & Kolb (2003) catalogue, Edition

7.9 (2008), and supplemented with new PCEB candidates described in Rebassa-Mansergas et al. (2007) and Rebassa-Mansergas et al. (2008). How we treat the related sd+MS systems (see Section 3.4.1) in our study is described in Section 7.5.

Finally, in light of the possible dependence of $\alpha_{\rm CE}$ on the secondary mass as suggested by Politano & Weiler (2007), we also calculate the possible values of $\alpha_{\rm CE}$ for the observed population of PCEBs. The investigation into the dependence of $\alpha_{\rm CE}$ on the secondary mass is investigated. Further noting the possible role that the structure of the giant's envelope may play in the CE ejection process (see Section 3.2.2), we also investigate if there is any dependence of $\alpha_{\rm CE}$ on $A_{\rm CE,f}$. The method to reconstruct the CE phase for the observed sample of PCEBs is described in Section 7.6.

7.1 The Initial Population

We employ the code BiSEPS as described in Chapter 4 to calculate the present day population of PCEBs. As further details can be found in this chapter, we present only a summary here.

We evolve a large number of binary systems, initially consisting of two ZAMS stellar components. We assume that the stars have population I chemical compositions with a solar metallicity of $Z = 0.02$, and that the binary orbits are circular at all times. The initial primary and secondary masses are in the range 0.1 to 20 $\rm M_{\odot}$, while the initial orbital periods lie in the range 0.1 to 100 000 days. There is one representative binary configuration per grid cell within a three dimensional grid consisting of 60 logarithmically spaced points in both primary and secondary mass, and 300 logarithmically spaced points in orbital period. For symmetry reasons only binaries with $M_1 > M_2$ are evolved. Hence we have approximately 5.4×10^5 binaries, which are evolved for a maximum evolution time of 10 Gyr, i.e. the Galactic lifetime.

If a binary configuration evolves into a PCEB (i.e. a WD+MS binary which has formed from a CE phase), then we record the binary parameters at the point the WD+MS binary immediately leaves the CE phase, as well as the initial ZAMS parameters of that binary. We also obtain the evolutionary tracks of each PCEB, which record the evolution of the binary parameters from the moment the PCEB is formed, to the moment it ceases to be such a

class of binary (for example, if the system becomes semi-detached, in which case it becomes a CV). Depending on the model calculation we are considering, the number of zero-age PCEBs we obtain (and hence the number of evolutionary tracks) is between approximately 30 000 and 100 000.

The probability of a zero-age PCEB forming with a given white dwarf mass $M_{\rm WD}$, a secondary mass M_2 and an orbital period $P_{\rm orb}$ is determined from the probability of the binary having initial primary mass $M_{1,\rm i}$, secondary mass $M_{2,\rm i}$ and orbital period $P_{\rm orb,i}$. We assume that the initial primary mass is distributed according to equation (4.2) (Kroupa et al. 1993), while the distribution in $M_{2,\rm i}$ is obtained from equation (4.4), or according to the same IMF as used for the initial primary mass [substituting $M_{1,\rm i}$ for $M_{2,\rm i}$ in equation (4.2)]. For brevity, we adopt the acronym 'IMFM2' for this latter case. For our standard model, we consider a flat initial mass ratio distribution, i.e. $n(q_{\rm i}) = 1$. Finally, we assume that the initial orbital separations are distributed according to equation (4.3) [Iben & Tutukov (1984); Hurley et al. (2002)].

We further assume that all stars are formed in binaries. The PCEB formation probabilities are convolved with a constant star formation rate which is normalised, according to equation (4.11), so that one binary with $M_{1,\rm i} > 0.8$ M$_\odot$ is formed each year (Weidemann 1990). This gives us a star formation rate of 7.6 yr^{-1}.

We then employ the code described in Willems et al. (2005) and Willems et al. (2007) (see Section 4.2.2) to calculate the present day distributions over $M_{\rm WD}$, M_2 and $P_{\rm orb}$ using the evolutionary tracks of each PCEB configuration. By doing this, we can determine the contribution of that PCEB configuration to the total population, determined by the aforementioned distribution functions and star formation rate, at each stage of its evolution.

7.2 Treatment of the CE Phase

Here we specify details of the different model prescriptions used for the CE phase. These are summarised in Table 7.1. In the energy budget approach, the CE phase is modelled according to equation (5.20), as described in Section 5.2. For our standard model we use $\lambda_{\rm CE} = 0.5$, again consistent with Willems & Kolb (2004).

We consider three, constant global values of $\alpha_{\rm CE}$. For our standard model A we use

Table 7.1: Different models on the treatment of the CE phase.

Model	α_{CE} or γ	λ
A	1.0	0.5
CE01	0.1	0.5
CE06	0.6	0.5
PL05	eqn. (3.15), $p = 0.5$,	0.5
PL1	eqn. (3.15), $p = 1$,	0.5
PL2	eqn. (3.15), $p = 2$,	0.5
CT0375	eqn. (3.14), $M_{cut}/M_\odot = 0.0375$	0.5
CT075	eqn. (3.14), $M_{cut}/M_\odot = 0.075$	0.5
CT15	eqn. (3.14), $M_{cut}/M_\odot = 0.15$	0.5
DTg	1.0	λ_g
DTb	1.0	λ_b
n15	1.5, eqn. (7.1)	-

$\alpha_{CE} = 1$. We also consider $\alpha_{CE} = 0.1$ and 0.6. We denote these models as CE01 and CE06 respectively, where the last two digits correspond to the value of α_{CE}.

Following Politano & Weiler (2007) we consider α_{CE} as a function of the secondary mass according to (3.14) and (3.15). For the case of equation (3.15) we consider $p = 0.5$, 1.0 and 2.0. These models are denoted as PL05, PL1 and PL2 respectively, where the last digits correspond to the value of p. For equation (3.14), we follow Politano & Weiler (2007) and consider $M_{cut} = 0.0375$, 0.075 and 0.15 $M_\odot$, which corresponds to $\times 1/2$, $\times 1$ and $\times 2$ of the sub-stellar mass respectively. These models are denoted CT0375, CT075 and CT15, where the digits correspond to the value of M_{cut}.

We also obtain population models with values of λ_{CE} calculated by Dewi & Tauris (2000), where just the gravitational binding energy of the envelope is considered ($\lambda_{CE} = \lambda_g$) and where both the gravitational binding energy and the thermal energy of the envelope are considered ($\lambda_{CE} = \lambda_b$). We denote these models as DTg and DTb respectively (and set $\alpha_{CE} = 1$ for these). For each of our binary configurations we calculate the value of λ_g or λ_b using linear interpolation of the values for M_1, R_1 and λ_g or λ_b tabulated by Dewi & Tauris (2000). As Dewi & Tauris (2000) only calculate λ_g and λ_b for primary masses $M_1 \geq 3$ $M_\odot$, we use the values of λ_g and λ_b calculated for $M_1 = 3$ $M_\odot$ for any $M_1 < 3$ $M_\odot$. Similarly,

Dewi & Tauris (2000) only calculate values of λ_g and λ_b for primary radii $R_1 \leq 600$ $R_\odot$. The primary progenitors can fill their Roche lobes at $\lesssim 1200$ $R_\odot$. For each of the masses Dewi & Tauris (2000) consider, we simply take the last tabulated value of λ_g and λ_b for any $R_1 > 600$ $R_\odot$.

If there is sufficient thermal energy within the giant's envelope such that its total binding energy becomes positive ($\lambda_b < 0$) the formalism described by equation (5.20) breaks down. We model this instead as an instantaneous ejection of the giant's envelope via a wind, which takes away the specific orbital angular momentum of the giant. What remains is a wide WD+MS binary. We do not consider these any further in our investigation.

7.3 The CE phase in terms of the binary's angular momentum

We follow Nelemans et al. (2000) and Nelemans & Tout (2005) by considering models where the CE phase is described in terms of the change of the binary's angular momentum, ΔJ, given by equation (3.17). If J and J_f are the total angular momentum of the binary immediately before and after the CE phase respectively, then equation (3.17) can be re-written as

$$J\left[1-\gamma_{CE}\left(\frac{M_1-M_c}{M_1+M_2}\right)\right]=J_f. \tag{7.1}$$

At the start of the CE phase, we not only consider the orbital angular momentum of the binary, $J_{orb,i}$, but also the spin angular momentum of the Roche lobe-filling giant star, $J_{spin,1}$, such that $J = J_{spin,1} + J_{orb,i}$. If the giant is rotating synchronously with the orbit with a spin angular speed of Ω_{orb}, then

$$J_{spin,1} = k^2 M_1 R_{L,1}^2 \Omega_{orb}, \tag{7.2}$$

where k^2 is the gyro-radius of the giant star. We use the values of k^2 tabulated by Dewi & Tauris (2000). Our procedure for calculating k^2 for each giant star configuration is the same as that used to calculate λ_g and λ_b. The initial orbital angular momentum of the binary, on the other hand is given by

$$J_{orb,i} = M_1 M_2 \left(\frac{G A_{CE,i}}{M_1+M_2}\right)^{1/2}. \tag{7.3}$$

Similarly the final orbital angular momentum of the binary after the CE phase, $J_{\rm orb,f}$, is given by

$$J_{\rm orb,f} = M_{\rm c} M_2 \left(\frac{G A_{\rm CE,f}}{M_{\rm c} + M_2} \right)^{1/2}. \tag{7.4}$$

Note that we do not consider the spin angular momentum of either of the stellar components after the CE phase as these are negligible compared to the orbital angular momentum of the binary. Thus, $J_{\rm f} = J_{\rm orb,f}$. By using equations (7.2) to (7.4) we can therefore solve for $A_{\rm CE,f}$ in equation (7.1).

For the large majority of the observed systems that Nelemans & Tout (2005) considered, they found that their CE phase could be reproduced with $\gamma_{\rm CE} \approx 1.5$. We therefore consider $\gamma_{\rm CE} = 1.5$ in equation (7.1). This is our model n15, which is summarised in Table 7.1.

7.4 Magnetic Braking

After the CE phase, the subsequent evolution of the PCEB will be driven by angular momentum losses from the orbit. For a fully convective secondary star with $M_2 \leq M_{\rm MS,conv} = 0.35$ $\rm M_\odot$ (where $M_{\rm MS,conv}$ is the maximum mass of a fully convective, isolated main sequence star), then gravitational radiation is the only sink of angular momentum as given by equation (2.1). For secondaries with $M_2 > M_{\rm MS,conv}$, then the evolution of the PCEB is driven by a combination of gravitational radiation and magnetic braking. For this investigation we consider the angular momentum loss rate due to magnetic braking according to Hurley et al. (2002), given by equation (5.19), as described in Chapter 5.

Once again we normalise equation (5.19) as described in Chapter 5 by applying a factor $\eta_{\rm h} = 0.19$ which gives the angular momentum loss rate appropriate for a period gap of the observed width of one hour. Magnetic braking also becomes ineffective for PCEBs with $M_2 \geq 1.25$ $\rm M_\odot$, which have very thin or no convective envelopes.

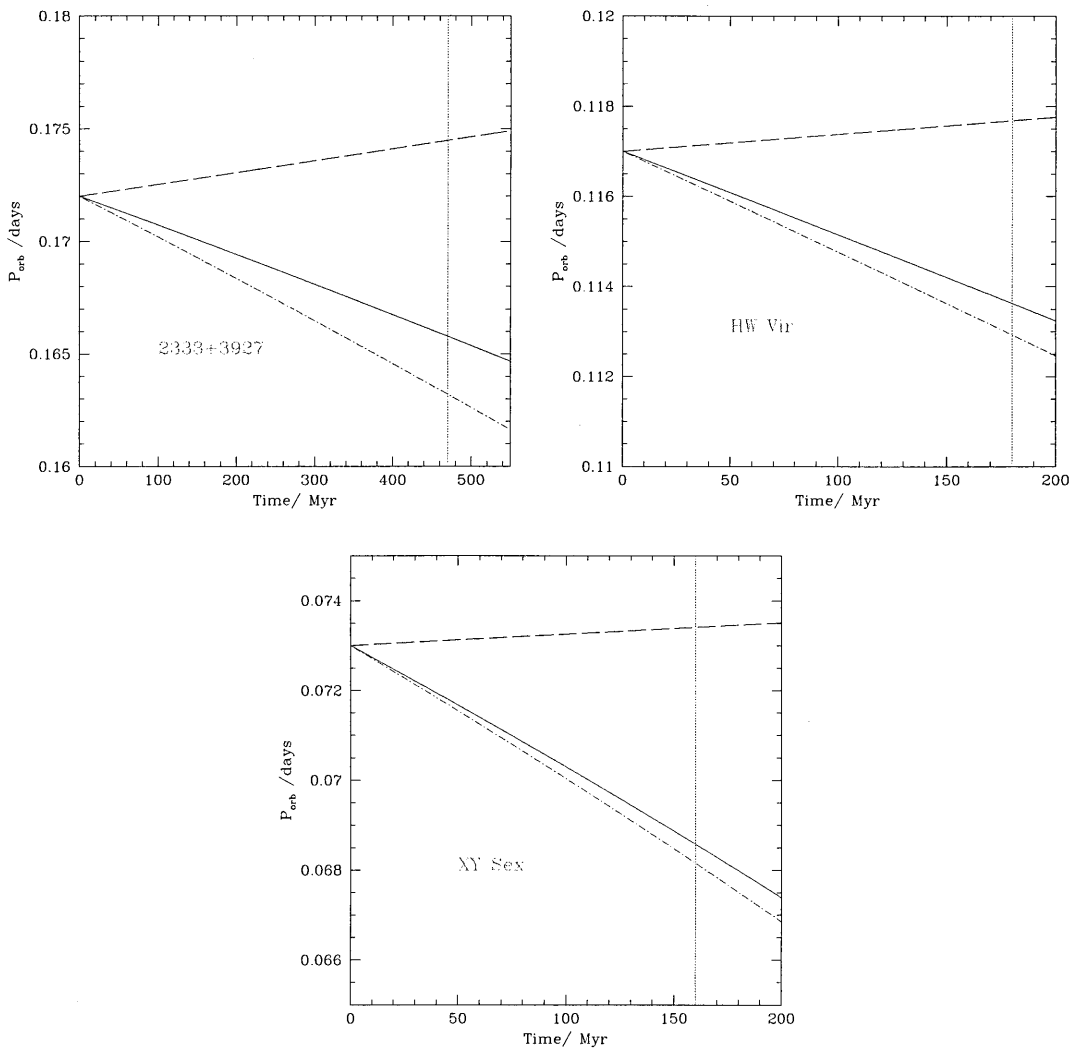

Figure 7.1: The evolution in orbital period of the sdB+MS binaries 2333+3927 (top left), HW Vir (top right) and XY Sex (bottom). The solid black line in each panel shows the evolution in orbital period with time as a result of both the wind losses from the subdwarf primary, and orbital angular momentum losses as a result of gravitational radiation. Also shown in each panel for comparison is the orbital period evolution purely due to wind losses (dashed line) and purely due to gravitational radiation (dot-dashed line). The vertical red line is the core helium burning lifetime of the primary, after which it becomes a white dwarf.

7.5 The Evolution of Subdwarf-Main Sequence Binaries

The SSE package of the BiSEPS code does not explicitly model the formation of subdwarf stars, but instead mimics the transition of stars from the giant branch across the horizontal

branch towards a white dwarf remnant as a result of significant mass loss from the giant star (Hurley et al. 2000). Indeed, a detailed treatment into the formation of subdwarf binaries requires various assumptions regarding the mass loss rate due to winds from the giant's envelope, the metallicity of the giant and detailed description of convective overshooting (Han et al. 2002). Therefore, such a detailed treatment of subdwarf binaries is beyond the scope of this study.

Due to the explicit modelling required, we suggest that the observed sample of sd+MS binaries can be plotted over our theoretical PCEB distributions which contain a white dwarf primary. We therefore assume that there is little evolution in the orbital periods of these systems by the time the subdwarf primary becomes a white dwarf.

To test this assumption, we first note that the orbital evolution of the sd+MS binary will not only be driven by systemic angular momentum losses from the binary orbit, but also due to wind losses from the hydrogen-rich envelope on the subdwarf primary. Vink (2004) and Unglaub (2008) estimate the mass loss rate from the primary due to winds to be $\dot{M}_{\rm sd} \approx 10^{-11}$ M$_{\odot}$.

Thus, we model the orbital evolution of the sd+MS binary with a subdwarf mass $M_{\rm sd}$, by combining equations (1.29), (1.33), (1.42) and (1.43), with $\dot{M}_{\rm sd} < 0$. Furthermore, we assume that all the material is lost from the system, i.e. $\alpha_{\rm CAML} = 1$ and $\dot{M}_2 = 0$. We therefore get

$$\left(\frac{\dot{J}}{J}\right)_{\rm sys} + \frac{M_2}{M_{\rm sd}}\frac{\dot{M}_{\rm sd}}{M_{\rm sd}+M_2} = \frac{\dot{M}_{\rm sd}}{M_{\rm sd}} + \frac{1}{2}\frac{\dot{a}}{a} - \frac{1}{2}\frac{\dot{M}_{\rm sd}}{M_{\rm sd}+M_2}. \tag{7.5}$$

We note that the current observed sample of sd+MS have secondaries with $M_2 \leq 0.35$ M$_{\odot}$ (Ritter & Kolb 2003). Hence we assume that gravitational radiation is the only sink of orbital angular momentum for these systems, and so $(\dot{J}/J)_{\rm sys} = (\dot{J}/J)_{\rm GR}$ in equation (7.5). Furthermore, we only maintain wind losses for as long as the subdwarf has a hydrogen-rich envelope.

By numerically integrating equation (7.5), we can obtain the evolution of the system's orbital period with time. We have done this for three observed sd+MS binaries: 2333+3927 which has $M_{\rm sd} = 0.38 \pm 0.09$ M$_{\odot}$, $M_2 = 0.28 \pm 0.04$ M$_{\odot}$ and $P_{\rm orb} = 0.172$ days (Heber et al. 2004); HW Vir which has $M_{\rm sd} = 0.48 \pm 0.09$, $M_2 = 0.14 \pm 0.02$ and $P_{\rm orb} = 0.117$ days (Wood & Saffer 1999); XY Sex which has $M_{\rm sd} = 0.50$ M$_{\odot}$, $M_2 = 0.078 \pm 0.006$ M$_{\odot}$ and $P_{\rm orb} = 0.073$ days (Maxted et al. 2002). In all cases we assume that the mass of the hydrogen envelope is 0.02 M$_{\odot}$.

The evolutionary tracks of these systems are shown as the solid black lines in their

respectively labelled panels in Figure 7.1. Also shown are the evolutionary tracks if orbital evolution is driven purely by gravitational radiation (dot-dashed line) and purely by wind losses (dashed line). The red vertical lines are the core helium burning times of the subdwarf primaries, which have been calculated from the SSE package of the BiSEPS code (Hurley et al. 2000). Therefore, beyond this point the subdwarfs become white dwarfs, and we are left with WD+MS binaries.

The relative change in the orbital period during the transition of the subdwarf to a white dwarf is approximately 3 per cent for both 2333+3927 and HW Vir, and approximately 7 per cent for XY Sex. Thus, our assumption that there is little orbital evolution of the sd+MS binaries towards its transition to a WD+MS binary is justified. Our theoretical PCEB population is also a good representation of those sd+MS binaries that have formed from a CE phase.

7.6 Reconstructing the CE Phase

We follow Nelemans et al. (2000) and Nelemans & Tout (2005) and reconstruct the CE phase for the observed sample of PCEBs in order to calculate the CE ejection efficiency, which we will now describe. For a given white dwarf mass within a PCEB, we can calculate all the possible giant star progenitors from which the white dwarf formed. When such giants fill their Roche lobes and the CE phase just commences, then the radius of the giant is $R_1 = R_{\rm L,1}$. As the radius of the Roche lobe filling giant will determine the orbital period at which the CE phase will commence [c.f. equation (1.12) for the case of a Roche lobe filling secondary], then we can calculate the possible orbital separations at the start of the CE phase given the mass of the secondary, and given the possible masses of the giant progenitors. We can further assume that the mass of the white dwarf is equal to the core mass of the giant at the start of the CE phase. This is because the duration of the CE phase [see equation (3.7)] is significantly shorter than the nuclear evolution time of the giant. Hence, the mass of the core will not increase appreciably during the CE phase.

We employ our BiSEPS code to reconstruct the CE phase by using the logarithmic grids for the initial orbital periods and primary masses described in Section 7.1.1. For the initial secondary mass we use the observed value of the PCEB system under consideration. Thus,

we evolve each initial binary system from the two-dimensional grid, for a given observed value of the secondary mass. If a binary system undergoes a CE phase, we calculate the core (the proto-white dwarf) mass of the Roche lobe-filling giant using the Hurley et al. (2000) SSE package of our code, as well as the initial orbital separation of the binary at the onset of the CE phase. If the core mass is equal to the observed white dwarf mass of the WD+MS under consideration (within the corresponding measured uncertainty of the white dwarf mass) then we can solve for $\alpha_{\rm CE}$ using equation (5.20), given the orbital period the PCEB had immediately after the CE phase, and the value of $\lambda_{\rm CE}$ for each of the possible progenitor giants. We currently just consider $\lambda_{\rm CE} = \lambda_{\rm g}$.

We now describe how we calculate the orbital period the observed PCEB had immediately after the CE phase. While Nelemans & Tout (2005) calculated $\alpha_{\rm CE}\lambda_{\rm CE}$ for PCEBs using their currently observed orbital period, $P_{\rm orb}$, we note that in reality such systems would have undergone orbital period evolution due to angular momentum losses via gravitational radiation and/or magnetic braking since emerging from the CE phase. We therefore follow Schreiber & Gänsicke (2003) to calculate the orbital period of our observed sample of PCEBs immediately after their emergence from the CE phase, $P_{\rm CE}$.

For observed PCEBs with $M_2 \leq M_{\rm MS,conv}$ such that their evolution is driven purely by gravitational radiation, then we insert equation (2.1) into equation (3.19), and integrate over the time since the PCEB emerged from the CE phase. This is just the age of the white dwarf, which can be calculated from its cooling age, $t_{\rm cool}$. Carrying out the integration and solving for $P_{\rm CE}$ gives

$$\left(\frac{P_{\rm CE}}{\rm days}\right)^{8/3} = 2.1 \times 10^{-11} \frac{M_{\rm WD} M_2}{(M_{\rm WD} + M_2)^{1/3}} t_{\rm cool} + \left(\frac{P_{\rm orb}}{\rm days}\right)^{8/3}, \qquad (7.6)$$

[e.g. Schreiber & Gänsicke (2003)] where masses are expressed in solar units and $t_{\rm cool}$ is in years.

For observed systems with $M_2 \geq M_{\rm MS,conv}$, which are driven by a combination of gravitational radiation and magnetic braking then, recalling that $(\dot{J}/J)_{\rm MB} >> (\dot{J}/J)_{\rm GR}$, we just substitute equations (5.19) and (1.28) into equation (3.19). Following the same integration procedure as described above gives

$$\left(\frac{P_{\rm CE}}{\rm years}\right)^{10/3} = \frac{(2\pi)^{10/3} \eta_{\rm h} t_{\rm cool} R_2^3 M_{\rm conv}}{1.72 \times 10^{15}\ G^{2/3}} \frac{(M_{\rm WD} + M_2)^{1/3}}{M_{\rm WD} M_2^2} + \left(\frac{P_{\rm orb}}{\rm years}\right)^{10/3}, \qquad (7.7)$$

for the Hurley et al. (2002) form of magnetic braking, where masses and radii are in solar units, and $t_{\rm cool}$ is in years. We estimate the convective envelope mass of the secondary star

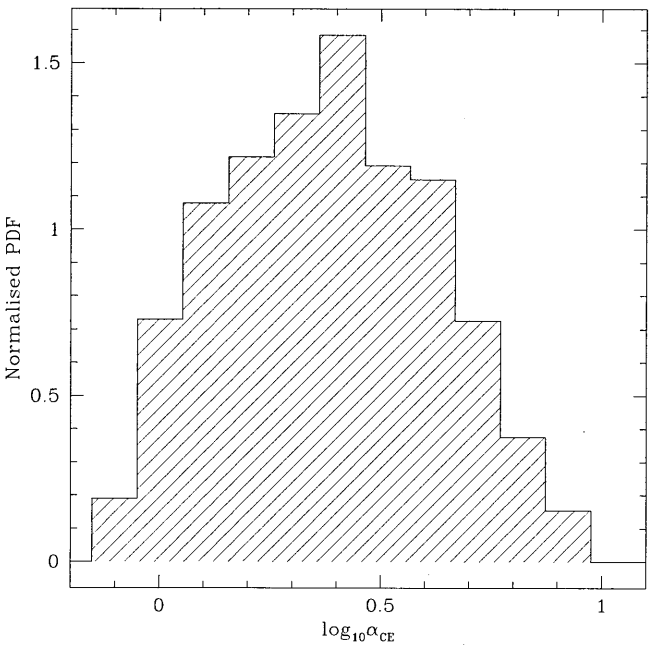

Figure 7.2: A normalised PDF of all the possible, reconstructed values of $\alpha_{\rm CE}$ for the observed WD+MS system 0137-3457.

using the formulae described in Hurley et al. (2000), given by

$$\frac{M_{\rm conv}}{\rm M_\odot} = \begin{cases} 0 & M_2 > 1.25\ \rm M_\odot \\ 0.35\left(\frac{1.25-M_2}{0.9}\right)^2 & 0.35 \leq M_2/\rm M_\odot \leq 1.25 \end{cases} \tag{7.8}$$

Note that equation (7.8) calculates the convective envelope mass for a star on the ZAMS. In reality, the mass of the convective envelope is a function of the fraction of the main sequence lifetime that the star has passed through (e.g. Hurley et al. 2000), thus making equation (7.8) time dependent and the solution to $P_{\rm CE}$ in equation (7.7) non-trivial. We therefore do not currently deal with the time dependence of the convective envelope mass in equation (7.7).

Using equation (5.20), we can therefore solve for $\alpha_{\rm CE}$ and calculate all the possible values of the CE ejection efficiency for a given observed PCEB, for each of its possible progenitor binary configurations at the start of the CE phase.

While there is a large possible range of values for $\alpha_{\rm CE}$ for a given PCEB, we can nonetheless determine the most likely value of $\alpha_{\rm CE}$ for that PCEB using BiSEPS. We calculate the formation probabilities of each of the possible ZAMS progenitors of that PCEB, and map this probability to the corresponding value of $\alpha_{\rm CE}$. We can therefore build up a probability distribution of the possible values of $\alpha_{\rm CE}$ for that system. An example of such a distribution

is shown in Figure 7.2, which shows a normalised PDF of the possible values of $\log_{10}\alpha_{\rm CE}$ for the system 0137-3457 (Maxted et al. 2006).

For each 'reconstructed' PCEB which has a normalised PDF in $\log_{10}\alpha_{\rm CE}$ given by F, then we calculate the most likely value of the CE ejection efficiency, $\log_{10}\overline{\alpha}_{\rm CE}$, using

$$\log_{10}\overline{\alpha}_{\rm CE} = \sum_{j=1}^{n} \log_{10}\alpha_{{\rm CE},j} \times F\Delta\log_{10}\alpha_{\rm CE}, \tag{7.9}$$

where the subscript j refers to the value of $\log_{10}\alpha_{\rm CE}$ in the jth bin, $\Delta\log_{10}\alpha_{\rm CE}$ is the bin width and n is the number of bins in the distribution. The standard deviation, σ, of the distribution is found from

$$\sigma^2 = \sum_{j=1}^{n} (\log_{10}\alpha_{{\rm CE},j} - \log_{10}\overline{\alpha}_{\rm CE})^2 \times F\Delta\log_{10}\alpha_{\rm CE}, \tag{7.10}$$

Thus, for the case of 0137-3457 in Figure 7.2, we find $\log_{10}\overline{\alpha}_{\rm CE} = 0.38 \pm 0.24$.

The results of population synthesis calculations are presented in the next chapter.

8

Results and Analysis

We begin by comparing our theoretical population of PCEBs from model A, $n(q_{\rm i}) = 1$, with observed WD+MS (Section 8.1) and sd+MS (Section 8.2) systems, obtained from Edition 7.10 (2008) of RKCat (Ritter & Kolb 2003). This sample is also supplemented with newly discovered PCEBs from SDSS (Rebassa-Mansergas et al. 2007; Rebassa-Mansergas et al. 2008). Observed WD+MS systems are tabulated in Table 8.1, while observed sd+MS systems are tabulated in Table 8.2. We then discuss the shape of the PCEB distributions on the $M_2 - P_{\rm orb}$ plane in Section 8.3. The present day number and local space densities of PCEBs are then presented in Section 8.4. Next, in Section 8.5, we compare each of the CE models in turn with the interesting PCEB called IK Pegasi, in the hope to shed light into the CE ejection mechanism. We then obtain the possible values of $\alpha_{\rm CE}$ for observed PCEB candidates in Section 8.6 by reconstructing its CE phase, and investigate any dependence of $\alpha_{\rm CE}$ on secondary mass and orbital separation of these PCEBs. Finally, the most likely IMRD is considered in Section 8.7. Our results are discussed in Section 8.8, and then summarised in Section 8.9.

8.1 White dwarf-main sequence systems

Figure 8.1 shows the theoretical present-day PCEB populations on the $M_2 - \log P_{\rm orb}$ plane for model A, assuming an IMRD of $n(q_{\rm i}) = 1$, along with the observed WD+MS systems.

Both the theoretical distributions and observed systems are divided into panels according to their white dwarf masses as indicated in each of the nine panels, labelled (a) to (i). The grey-scale bar at the top of the plot indicates the number of systems per bin area. We take into account the uncertainty of the white dwarf masses for each observed system by calculating the weighting of the system in each panel that overlaps with the white dwarf uncertainty interval. The panels in which these systems lie, and the associated weightings, are also shown in Table 8.1. The weightings are calculated from a Gaussian distribution with a mean white dwarf mass $\langle M_{\rm WD} \rangle$ and a standard deviation σ, which corresponds to the measured white dwarf mass and its uncertainty respectively. The colour bar on the right hand side of the plot indicates the weightings.

There is an acceptable overall agreement between the observed systems and the theoretical distributions, in the sense that all but two observed systems are in areas populated by the standard model. However, the model distributions extend to areas at orbital periods longer than about 1 d and donor masses larger than about 0.5 $\rm M_\odot$ with very few, if any, observed systems. The two outliers that cannot be accounted for by our standard model are V651 Mon (Mendez & Niemela 1981; Mendez et al. 1985; Kato, Nogami & Baba 2001) and IK Peg (Vennes, Christian & Thorstensen 1998). These are shown in Figure 8.2 as the blue and red diamonds respectively (these systems lie outside of the range displayed in Figure 8.1 and so are not shown there). We shall discuss these systems in turn to deduce whether they are in fact PCEBs.

IK Peg contains a 1.2 $\rm M_\odot$ white dwarf, and a 1.7 $\rm M_\odot$ secondary star with spectral type A8 (Landsman, Simon & Bergeron 1993; Smalley et al. 1996; Vennes, Christian & Thorstensen 1998). Smalley et al. (1996) found that the secondary star had an overabundance of iron, barium and strontium, which may be accounted for if IK Peg underwent mass transfer. Smalley et al. (1996) suggest that this was in the form of a CE phase. As the secondary plunged into the envelope of the giant it would be contaminated by s-processed material. As WD+MS systems can also form through a thermally unstable Roche lobe overflow (RLOF) phase (see Section 3.4.2), we calculated the present day population of WD+MS systems with $1.1 \leq M_{\rm WD}/\rm M_\odot \leq 1.44$ that form through such a case B thermal–timescale mass

Table 8.1: The orbital periods, white dwarf masses (M_{WD}), and secondary masses, M_2, of the observed sample of WD+MS systems. Also shown are the weightings of each system in the associated white dwarf mass range, corresponding to panels (a) to (i) (see Fig. 8.1).

Name	Alt. Name	P_{orb} /days	M_{WD} /$M_\odot$	M_2 /$M_\odot$	Panel	Weighting	Ref
V651 Mon	AGK3-0 965	15.991	0.40±0.05	1.80±0.3	a,b	50.0,48.0	1,2
SDSS J1529+0020		0.165	0.40±0.04	0.25±0.12	a,b	50.0,49.0	3
CC Cet	PG 0308+096	0.287	0.40±0.11	0.18±0.05	a,b,c	50.0,32.0,1.00	4
LM Com	CBS 60	0.259	0.35±0.03	0.17±0.02	a	95.0	5
HR Cam	WD 0710+741	0.103	0.41±0.01	0.096±0.004	a,b	16.0,84.0	6,7
0137-3457		0.080	0.39±0.035	0.053±0.006	a,b	61.0,39.0	8
SDSS J2339-0020		0.656	0.8±0.4	0.32±0.09	a,b,c,d	14.0,7.0,4.0,4.0	3
					e,f,g,h,i	5.0,5.0,10.0,27.0,17.0	
SDSS J1724+5620		0.333	0.42±0.01	0.25 - 0.38	b	98.0	3
RR Cae	LFT 349	0.303	0.44±0.023	0.18±0.01	b	95.0	9
MS Peg	GD 245	0.174	0.49±0.04	0.19±0.02	b,c	59.0,33.0	10
HZ 9		0.564	0.51±0.1	0.28±0.04	b,c,d,e	32.0,10.0,16.0,10.0	11,12,13
GK Vir	PG 1413+015	0.344	0.51±0.04	0.10	b,c	40.0,44.0	14,15
LTT 560		0.148	0.52±0.12	0.19±0.05	b,c,d,e	28.0,16.0,15.0,11.0	16
DE CVn	J1326+4532	0.364	0.54±0.04	0.41±0.06	c,d	44.0,33.0	17
2237+8154		0.124	0.57±0.1	0.30±0.1	b,c,d,e,f	20.0,18.0,20.0,17.0,12.0	18

Continued on next page

Table8.1 – continued from previous page

Name	Alt. Name	P_{orb} /days	M_{WD} /$M_\odot$	M_2 /$M_\odot$	Panel	Weight	Ref
SDSS J1151-0007		0.142	0.6±0.1	0.19±0.08	b,c,d,e,f	14.0,15.0,19.0,19.0,15.0	3
UZ Sex	1026+0014	0.597	0.68±0.23	0.22±0.05	b,c,d,e, f,g,h	11.0,6.90,7.80,8.40, 8.7,16.0,27.0	4
NN Ser	PG 1550+131	0.130	0.54±0.04	0.150±0.008	c,d	44.0,33.0	19
FS Cet	Feige 24	4.232	0.57±0.03	0.39±0.02	c,d	24.0,59.0	20,21
J2013+4002		0.706	0.56±0.03	0.23±0.01	c,d	35.0,54.0	21,22
J2130+4710		0.521	0.554±0.017	0.555±0.023	c,d	41.0,59.0	23
1042-6902		0.337	0.56±0.05	0.14±0.01	c,d,e	31.0,37.0,18.0	21
SDSS J0314-0111		0.263	0.65±0.1	0.32±0.09	c,d,e,f,g	9.0,15.0,19.0,19.0,24.0	3
IN CMa	J0720-3146	1.262	0.58±0.03	0.43±0.03	d,e	59.0,24.0	24
J1016-0520AB		0.789	0.61±0.06	0.15±0.02	d,e,f	28.0,31.0,19.0	24
EG UMa	Case 1	0.668	0.63±0.05	0.36±0.04	d,e,f	22.0,38.0,26.0	25
2009+6216		0.741	0.62±0.02	0.189±0.004	e	77.0	26
BE UMa	PG 1155+492	2.291	0.70±0.07	0.36±0.07	e,f,g	16.0,26.0,42.0	27,28
1857+5144		0.266	0.80±0.2	0.23±0.08	e,f,g,h	6.80,8.20,19.0,43.0	29
SDSS J0246+0041		0.726	0.9±0.2	0.38±0.07	f,g,h	5.0, 15.0,53.0	3
SDSS J0052-0053		0.114	1.2±0.4	0.32±0.09	g,h,i	5.0,24.0,32.0	3

Continued on next page

Table8.1 – continued from previous page

Name	Alt. Name	$P_{\rm orb}$ /days	$M_{\rm WD}$ /$M_\odot$	M_2 /$M_\odot$	Panel	Weight	Ref
BPM 71214		0.202	0.77±0.06	0.540:	g,h	57.0,31.0	30
QS Vir	1347-1258	0.151	0.78±0.04	0.43±0.04	g,h	67.0,31.0	31
V471 Tau	BD+16 516	0.521	0.84±0.05	0.93±0.07	g,h	21.0,79.0	32
IK Peg	BD+18 4794	21.72	1.19±0.05	1.7	i	96.0	33

References: (1) Mendez & Niemela (1981), (2) Mendez et al. (1985), (3) Rebassa-Mansergas et al. (2008), (4) Saffer et al. (1993), (5) Shimansky et al. (2003), (6) Marsh & Duck (1996), (7) Maxted et al. (1998), (8) Maxted et al. (2006), (9) Bragaglia et al. (1995), (10) Schmidt et al. (1995), (11) Stauffer (1987), (12) Lanning & Pesch (1981), (13) Guinan & Sion (1984), (14) Fulbright et al. (1993), (15) Green et al. (1978), (16) Tappert et al. (2007), (17) van den Besselaar et al. (2007), (18) Gänsicke et al. (2004), (19) Catalan et al. (1994), (20) Vennes & Thorstensen (1994), (21) Kawka et al. (2008), (22) Good et al. (2005), (23) Maxted et al. (2004), (24) Vennes et al. (1999), (25) Bleach et al. (2000), (26) Morales-Rueda et al. (2005), (27) Wood et al. (1995), (28) Ferguson et al. (1999), (29) Aungwerojwit et al. (2007), (30) Kawka et al. (2002), (31) O'Donoghue et al. (2003), (32) O'Brien et al. (2001), (33) Landsman et al. (1993)

transfer (TTMT) phase (channel 2 in Willems & Kolb 2004), which is shown in the right panel of Figure 8.3. The red diamond indicates the location of IK Peg. As the location of IK Peg cannot be accounted for by our theoretical population of case B TTMT systems, it is hence a likely PCEB candidate. We explore this possibility further in Section 8.5 where we consider more population synthesis models of the CE phase.

V651 Mon contains a 0.4 $M_\odot$ hot white dwarf primary with an A-type secondary star. This system lies within a planetary nebula, which could be the remnant of a CE phase. However, de Kool & Ritter (1993) suggest that the planetary nebula may have formed when the compact primary underwent a shell flash, and instead the binary formed via a thermally unstable RLOF phase. As for IK Peg, we calculate the present day population of WD+MS systems with $M_{\rm WD}/M_\odot \leq 0.4$ that formed through a thermally unstable RLOF phase (channel 1; Section 3.4.2), shown in the left panel of Figure 8.3. This is compared with the location of V651 Mon shown as the green diamond. From Figure 8.3 it appears hence feasible that V651 Mon formed from a case B RLOF phase.

To obtain the possible progenitor of V651 Mon, we first find the calculated WD+MS configuration which formed through the case B TTMT channel which is situated closest to the location of V651 Mon in $(M_{\rm WD}, M_2, P_{\rm orb})$ space. If $\delta M_{\rm WD}$, δM_2 and $\delta P_{\rm orb}$ is the difference between the observed white dwarf mass $M_{\rm WD,obs}$, secondary mass $M_{2,\rm obs}$ and orbital period $P_{\rm orb,obs}$ of V651 Mon and a calculated WD+MS binary configuration, then the normalised distance, Δ, in $(M_{\rm WD}, M_2, P_{\rm orb})$ space is given by

$$\Delta = \left(\left| \frac{\delta M_{\rm WD}}{M_{\rm WD,obs}} \right|^2 + \left| \frac{\delta M_2}{M_{2,\rm obs}} \right|^2 + \left| \frac{\delta P_{\rm orb}}{P_{\rm orb,obs}} \right|^2 \right)^{1/2} . \tag{8.1}$$

Thus we require the WD+MS binary configuration that gives the smallest value of Δ. We find that Δ is minimised for $M_{\rm WD} = 0.33$ $M_\odot$, $M_2 = 1.76$ $M_\odot$ and $P_{\rm orb} = 15.92$ d. This system has a ZAMS progenitor with $M_{1,\rm i} = 2.47$ $M_\odot$, $M_{2,\rm i} = 0.98$ $M_\odot$ and $P_{\rm orb,i} = 2.60$ d.

While the secondary mass of this WD+MS configuration is within the measured uncertainty of the secondary mass in V651 Mon, its white dwarf mass is not, and in fact underestimates the white dwarf mass of V651 Mon. Tout & Eggleton (1988*a*) and Tout & Eggleton (1988*b*) suggest that V651 Mon may have formed with enhanced mass loss from the primary star before it filled its Roche lobe. Thus, a more massive progenitor primary than the one found in our best-fit WD+MS configuration may have formed the white dwarf. If enough mass is lost from the primary due to enhanced wind losses before it fills its Roche lobe to sufficiently lower the mass ratio, M_1/M_2, then the resulting mass transfer will be

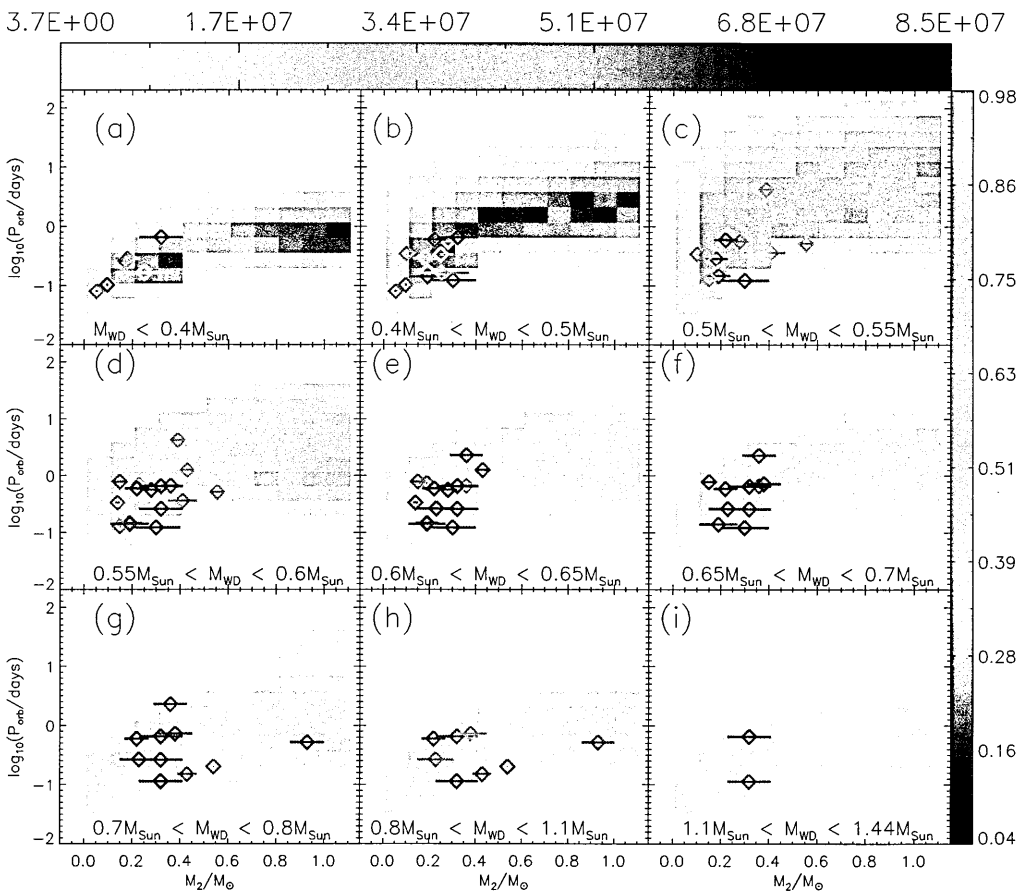

Figure 8.1: Calculated present-day PCEB populations, for model A and for $n(q_i) = 1$. The distributions over M_2 and $\log P_{\rm orb}$ are shown for nine different white dwarf mass intervals as indicated in each of the nine panels, labelled (a) to (i). The grey-scale bar at the top of the plot indicates the number of systems per bin area. Also shown are the known WD+MS systems obtained from Edition 7.10 (2008) of RKCat (Ritter & Kolb 2003). We take into account the uncertainties of the white dwarf mass for each system by calculating the weighting of each system within each panel. This is repeated for those systems whose error bars in white dwarf mass overlaps more than one panel. The weighting is indicated by the colour bar on the right hand side of the plot. The dotted line in panel (b) indicates that the secondary mass in SDSS J1724+5620 lies between 0.25 $M_\odot$ and 0.38 $M_\odot$.

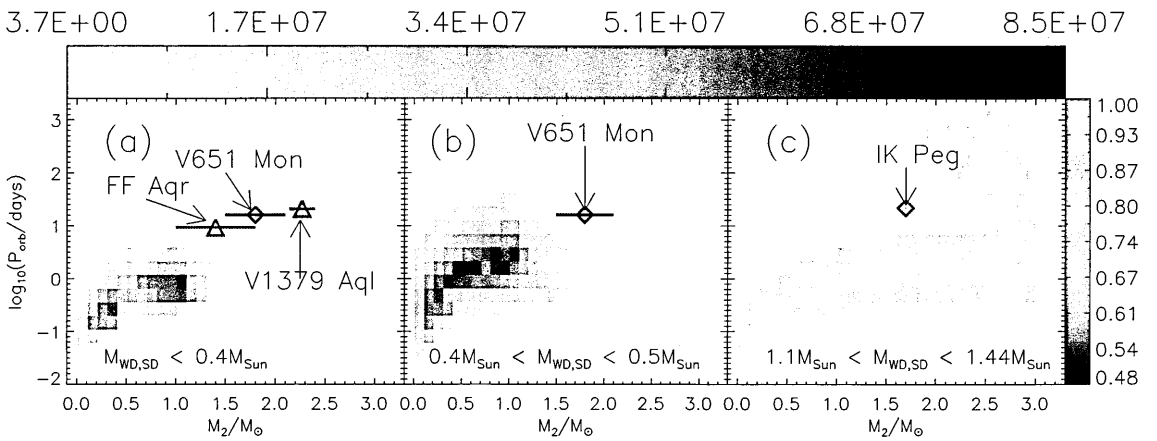

Figure 8.2: The theoretical present day PCEB population for model A, $n(q_i) = 1$, for a wider range in M_2 and P_{orb} than Fig. 8.1, for selected white dwarf mass intervals. Each panel labelled (a) to (c) represents the indicated range in white dwarf or sub-dwarf mass. Diamonds: WD+MS systems; triangles: sd+MS systems. The individual systems are V651 Mon (blue diamond, left and middle panels); IK Peg (red diamond, right panel); V1379 Aql (red triangle, left panel); FF Aqr (green triangle, left panel). The grey-scale on the top of the plot indicates the number of systems per bin area, while the bar on the right hand side indicates the weighting of the systems in their corresponding panels.

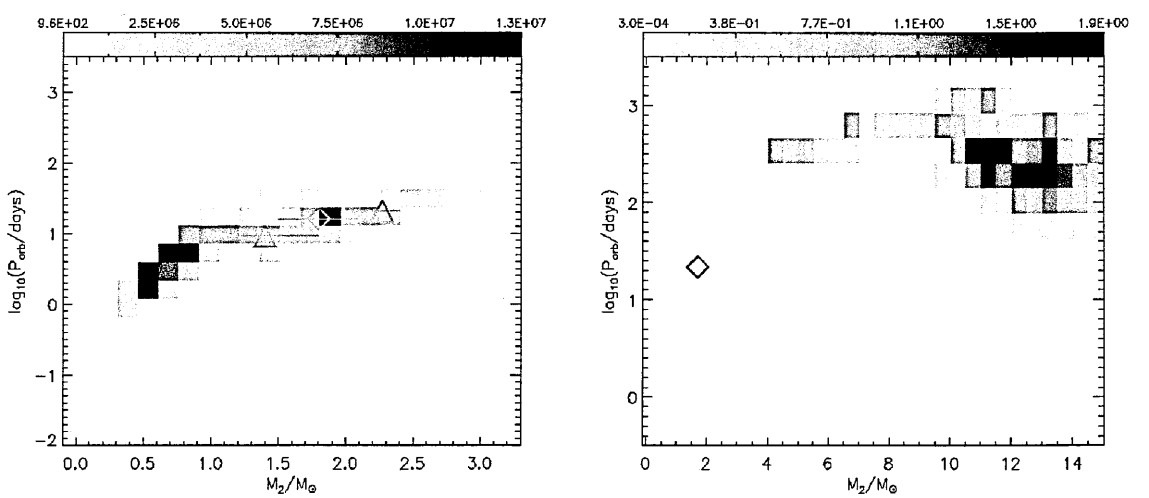

Figure 8.3: Left panel: The theoretical population of WD+MS systems with $M_{WD}/M_\odot \leq 0.4$ that formed through a channel 1 (see Section 3.4.2), thermally unstable RLOF phase, compared with the location of FF Aqr (brown triangle), V651 Mon (green diamond) and V1379 Aql (red triangle). Right panel: The theoretical population of WD+MS systems with $1.1 \leq M_{WD}/M_\odot \leq 1.44$ that formed through a channel 2, thermally unstable RLOF phase with a naked helium star remnant. This is compared with the location of IK Peg indicated by the red diamond.

dynamically stable.

8.2 Subdwarf-main sequence star binaries

Figure 8.4 shows that, as with the observed WD+MS systems, there are observed sd+MS systems that cannot be explained by our standard model. These are FF Aqr and V1379 Aql, which are shown in the left panel of Figure 8.2 as the green and red triangles respectively. We discuss these systems individually to determine whether they are in fact PCEBs.

V1379 Aql This system contains a K-giant secondary and an sdB primary, which may be a nascent helium white dwarf (Jeffery et al. 1992). Furthermore, Jeffery & Simon (1997) argue that V1379 Aql formed from a thermally unstable RLOF phase. As a consequence of the synchronous rotation of the secondary, the system exhibits RS CVn chromospheric activity due to the K-giant's enhanced magnetic activity. This is likely to occur if the system had a previous episode of RLOF, rather than if the system has emerged from a CE phase.

Tout & Eggleton (1988*b*) suggest that the progenitor binary of V1379 Aql had $M_{1,\mathrm{i}} = 2.0$ $\mathrm{M}_{\odot}$ and $M_{2,\mathrm{i}} = 1.6$ $\mathrm{M}_{\odot}$. The secondary star would have completed one half of its main sequence lifetime by the time the primary evolved to become a giant after $\sim 6 \times 10^8$ yr (Jeffery et al. 1992). If a CE phase did occur, then the secondary would still have been on the main sequence, and hence possess an insubstantial convective envelope. Consequently, magnetic braking would be ineffective in shrinking the orbital separation sufficiently for tidal interactions to enforce synchronous rotation of the secondary star.

Nelemans & Tout (2005), in reconstructing a possible CE phase for this system, could not find a solution for α_{CE}, and cited this as evidence for their alternative CE description in terms of the angular momentum balance. We suggest that no solution was found because of the possibility that V1379 Aql formed from a thermally unstable RLOF phase.

The left panel of Figure 8.3 compares the theoretical WD+MS systems with $M_{\mathrm{WD}}/\mathrm{M}_{\odot} \leq 0.4$ that formed through a thermally unstable RLOF phase (channel 1; Section 3.4.2) with the location of V1379 Aql shown as the red triangle. Hence it appears feasible that V1379 Aql formed through this evolutionary channel. As with V651 Mon, we apply equation (8.1) to find the WD+MS configuration which lies the closest to the location of V1379 Aql in $(M_{\mathrm{WD}}, M_2, P_{\mathrm{orb}})$. Doing this we find a WD+MS configuration with $M_{\mathrm{WD}} = 0.23$ $\mathrm{M}_{\odot}$,

Table 8.2: The orbital periods, sub-dwarf mass (M_{SD}), secondary mass, M_2, and spectral type, SpT, of the sub-dwarf for the observed sample of sd+MS systems. Also shown are the weightings of each system in the corresponding panels (a) to (f) (see Fig. 8.4), except for those systems where no uncertainty in the sub-dwarf mass is available. A colon denotes an uncertainty flag.

Name	Alt. Name	P_{orb} /days	M_{SD} /$M_\odot$	SpT 1	M_2 /$M_\odot$	Panel	Weighting	Ref
V1379 Aql	HD 185510	20.662	0.304±0.015	sdB	2.27±0.13	a	100.0	1
FF Aqr	BD -3 5357	9.208	0.35±0.06 :	sdOB	1.40±0.4 :	a,b	80.0,20.0	2,3
2333+3927		0.172	0.38±0.09	sdB	0.28±0.04	a,b	59.0,32.0	4
AA Dor	LB 3459	0.262	0.330±0.006	sdO	0.066±0.001	a	100.0	5
HW Vir	BD -7 3477	0.117	0.48±0.09	sdB	0.14±0.02	a,b,c,d	19.0,40.0,19.0,13.0	6
2231+2441		0.111	0.47 :	sdB	0.075	b	-	7
NY Vir	PG 1336-018	0.101	0.466±0.006	sdB	0.122±0.001	b	100.0	8
0705+6700		0.096	0.483	sdB	0.134	b	-	9,10
BUL-SC 16 335		0.125	0.5 :	sdB	0.16	b	-	11
J2020+0437		0.110	0.46	sdB	0.21	b	-	12
XY Sex	1017-0838	0.073	0.50	sdB	0.078±0.006	b	-	13
V664 Cas	HFG 1	0.582	0.57±0.03	sdB	1.09±0.07	c,d	24.0,59.0	14,15,16
UU Sge		0.465	0.63±0.06	sdO	0.29±0.04	d,e,f	22.0,32.0,25.0	17
KV Vel	LSS 2018	0.357	0.63±0.03	sdO	0.23±0.01	d,e,f	15.0,59.0,24.0	18

References: (1) Jeffery & Simon (1997), (2) Vaccaro & Wilson (2003), (3) Etzel et al. (1977), (4) Heber et al. (2004), (5) Rauch (2000), (6) Wood & Saffer (1999), (7) Østensen et al. (2007), (8) Kilkenny et al. (1998), (9) Drechsel et al. (2001), (10) Nemeth et al. (2005), (11) Polubek et al. (2007), (12) Wils et al. (2007), (13) Maxted et al. (2002), (14) Miller et al. (1976), (15) Pollacco & Bell (1993), (16) Bell et al. (1994), (17) Hilditch et al. (1996), (18) Shimanskii et al. (2004)

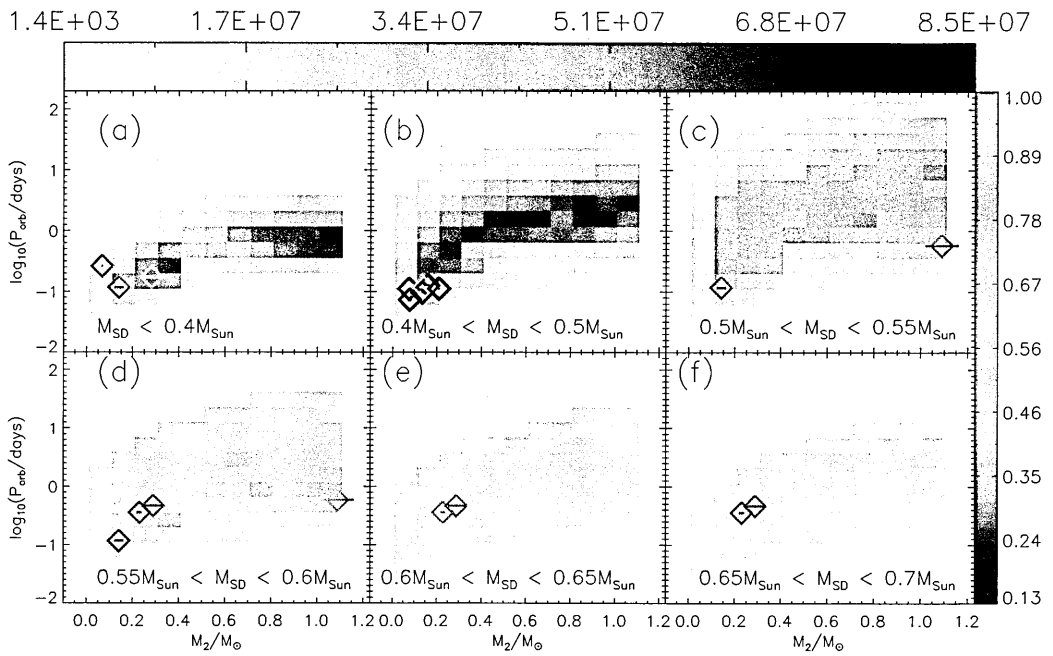

Figure 8.4: Same as Figure 8.1 but this time showing the observed sample of sub-dwarf+MS binaries. The black points represent those systems for which we have not calculated the weightings, as measured uncertainties for the sub-dwarf masses are not available.

M_2 = 2.31 $M_\odot$ and $P_{\rm orb}$ = 20.58 d. This system forms from a ZAMS progenitor with $M_{1,\rm i}$ = 1.79 $M_\odot$, $M_{2,\rm i}$ = 0.77 $M_\odot$ and $P_{\rm orb,i}$ = 1.41 d.

The mass of the white dwarf in our best-fit WD+MS configuration once again underestimates that of V1379 Aql. As for V651 Mon, Tout & Eggleton (1988*b*) suggest that the

primary star in V1379 Aql also underwent enhanced mass loss before it filled its Roche lobe. Thus, the mass ratio, M_1/M_2, was decreased sufficiently so that a dynamically unstable RLOF phase was avoided. The actual progenitor primary of V1379 Aql may therefore have been more massive than what we have predicted in our calculations. Note also that in our calculations, we do not treat the sdB phase of the white dwarf explicitly.

FF Aqr also displays RS CVn characteristics (Vaccaro & Wilson 2003), and hence we can apply the same argument used for V1379 Aql to FF Aqr; the secondary has a mass of $\sim$ 1.4 $M_\odot$ and so will have an insubstantial convective envelope. Indeed, de Kool & Ritter (1993) argue that FF Aqr formed from a thermally unstable RLOF phase, perhaps with enhanced wind losses (Tout & Eggleton 1988*b*).

The left panel of Figure 8.3, compares the theoretical WD+MS binary population with

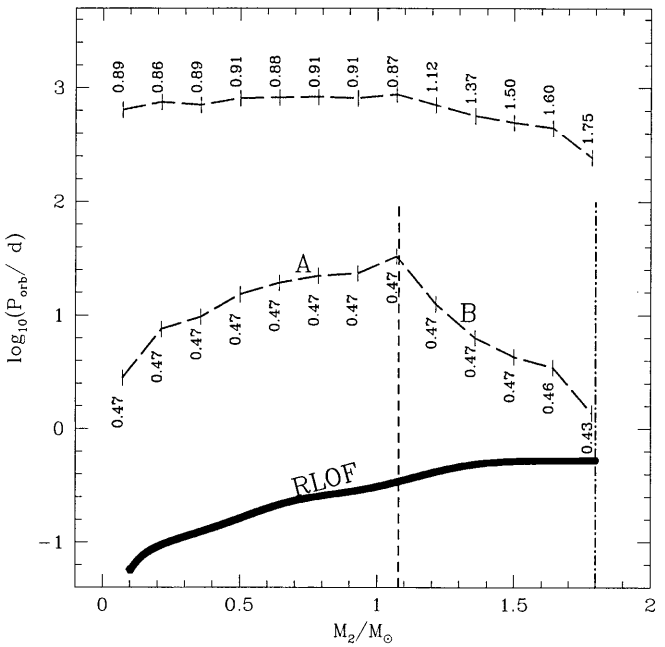

Figure 8.5: Critical boundaries in the $\log_{10}(P_{\rm orb}) - M_2$ plane. The red dashed line shows the upper boundary in the population of progenitor binaries at the start of the CE phase, which will form PCEBs with $0.4 < M_{\rm WD}/{\rm M}_\odot \leq 0.5$. The values along this line denote the mass of the Roche lobe-filling progenitor primary at the corresponding locations along the boundary. The blue dashed line is the upper boundary in the resulting population of PCEBs with $0.4 < M_{\rm WD} \leq 0.5$. The values along this line denote the white dwarf mass at the corresponding locations along the boundary. The label 'A' corresponds to the portion of the boundary at $M_2 \lesssim 1.1$ M$_\odot$ (short-dashed line), while 'B' denotes the portion of the boundary at $M_2 \gtrsim 1.1$ M$_\odot$. The thick black line is the Roche lobe-overflow (RLOF) limit, i.e. the point at which the PCEB will become semi-detached, and hence defines the lower limit in the distribution. Finally, the dot-dashed line corresponds to the cut-off in this PCEB population at $M_2 \approx 1.8$ M$_\odot$.

$M_{\rm WD}/{\rm M}_\odot \leq 0.4$, which formed through a channel 1 (see Section 3.4.2) RLOF phase, with the location of FF Aqr as the brown triangle. This supports the possibility that FF Aqr formed from a TTMT RLOF phase. While our best fit WD+MS configuration has $M_{\rm WD} = 0.30$ M$_\odot$, which is consistent with the observed value within the measured uncertainty, our best-fit configuration slightly underestimates the secondary mass with $M_2 = 1.22$ M$_\odot$.

8.3 The shape of the distributions

We will now discuss common features of the $M_2 - \log_{10} P_{\rm orb}$ PCEB distributions, using the middle panel of Figure 8.2 as a typical example. [1]

Figure 8.5 shows the upper boundary in the population of progenitor systems at the onset of the CE phase which will form PCEBs with $0.4 < M_{\rm WD}/{\rm M}_\odot \leq 0.5$ (red dashed line). The blue dashed line shows the corresponding upper boundary in the resulting population of PCEBs (this represents the upper boundary of the distribution shown in the middle panel of Figure 8.2), while the thick, black line shows the orbital period at which the secondary star will undergo Roche lobe overflow (RLOF), and hence the PCEB will become semi-detached.

The red dashed boundary in Figure 8.5 arises because for each mass M_2 there is an upper limit for the orbital period of the progenitor binary that will still form a white dwarf with a mass within the considered mass interval. Longer-period systems will either form a more massive white dwarf, or remain detached and not undergo a CE phase. More specifically, the upper boundary corresponds to the most massive white dwarfs in the panel. In the example shown this is 0.47 $\rm M_\odot$ (not 0.50 $\rm M_\odot$) because there is a gap in the white dwarf mass spectrum between the low-mass helium white dwarfs and the more massive carbon-oxygen white dwarfs. The SSE code (Hurley et al. 2000) places this gap in the range between $0.47 < M_{\rm WD}/{\rm M}_\odot < 0.6$.

This red dashed upper pre-CE boundary maps onto the blue dashed PCEB boundary, also shown in Figure 8.5. The masses of the progenitor primaries at the start of the CE phase are indicated along the red boundary, while the white dwarf masses are shown along the blue boundary of the PCEB population, at the corresponding point along the boundary.

Clearly, for a PCEB to form, the ZAMS progenitor primary must fill its Roche lobe and commence the CE phase before the secondary itself evolves off the main sequence. This point is of little consequence for $M_{2,\rm i} \lesssim 1$ $\rm M_\odot$ as the main sequence lifetime of such secondaries will be $\tau_{\rm MS,2} \gtrsim 10$ Gyr, which is on the order of the Galactic lifetime (and the maximum evolution time we consider). Thus, in such cases, the progenitor primary must ascend the giant branch and fill its Roche lobe within the lifetime of the Galaxy.

We find that the least massive ZAMS progenitor which will subsequently form a 0.47 $\rm M_\odot$ white dwarf within the lifetime of the Galaxy, is 1.1 $\rm M_\odot$. Hence, for the reasons stated above, $M_{2,\rm i} < 1.1$ $\rm M_\odot$, if the evolution of the secondary off the main sequence is to remain

[1] We note that the shapes of the distributions for model n15 are very different. We refer the reader to Nelemans & Tout (2005) for a detailed discussion.

unimportant. As indicated along the red boundary in Figure 8.5 for $M_2 < 1.1$ $M_\odot$(to the left of the dashed vertical line), the progenitor primaries, as a result of wind losses, commence the CE phase with masses of ≈ 0.9 $M_\odot$. Furthermore, as the red boundary for $M_2 < 1.1$ $M_\odot$ is approximately flat, the progenitor primaries along this boundary fill their Roche lobes at the same orbital period.

To see how this determines the shape of the resulting blue PCEB boundary for $M_2 < 1.1$ $M_\odot$ (labelled 'A' in Figure 8.5) we consider equation (5.20), which shows that for constant M_c (and hence the white dwarf mass), M_1 and $r_{L,1}$ (at the start of the CE phase), $A_{CE,f}$ decreases for decreasing M_2. Hence the orbital period of the blue boundary to the left of the dashed line in Figure 8.5 decreases for decreasing M_2.

On the other hand, for $M_{2,i} > 1.1$ $M_\odot$ (to the right of the dashed line in Figure 8.5), the main sequence lifetime of such stars is <10 Gyr, and so the progenitor primary must increasingly compete against the secondary to evolve off the main sequence first. As a result, the ZAMS progenitor primary star needs to be increasingly more massive for increasing secondary mass. This is reflected in the masses of the primaries at the start of the CE phase, as indicated along the red boundary in Figure 8.5 for $M_2 > 1.1$ $M_\odot$, which increase from ≈ 0.9 $M_\odot$ for $M_2 \approx 1.1$ $M_\odot$, to 1.8 $M_\odot$ for $M_2 \approx 1.8$ $M_\odot$.

For a primary star ascending the giant branch with luminosity L_1, its radius on the giant branch, R_{GB}, can be modeled as

$$R_{GB} \simeq \frac{1.1}{M_{1,i}^{0.3}} \left(L_1^{0.4} + 0.383 L_1^{0.76}\right), \tag{8.2}$$

(Hurley et al. 2000), where $L_1 \propto {M_c}^6$. Thus the radius of the star on the giant branch is a function of its core mass and (weakly) on its initial ZAMS mass. For a given core mass, in this case of $M_c = 0.47$ $M_\odot$, the corresponding value of R_{GB} will decrease for increasing mass of the ZAMS primary. For Roche lobe filling stars we have $P_{orb} \propto R^{3/2}/M^{1/2}$ so the orbital period at which the CE phase will occur will decrease with increasing M_2. This is shown as the slope in the red boundary in Figure 8.5 for $M_2 > 1.1$ $M_\odot$.

The shape of the blue boundary to the right of the dashed line in Figure 8.5 (labelled 'B') is a consequence of the shape of the corresponding portion of the red pre-CE boundary. Furthermore, for increasing M_2, while M_c remains constant, $M_{1,i}$ does increase, and so the mass of the primary giant's envelope will correspondingly increase. The result of this is that $A_{CE,f}$ will decrease for increasing M_2, as equation (5.20) shows. This explains why the blue PCEB boundary to the right of the dashed line Figure 8.5 decreases for increasing M_2.

Note that the cut-off in the population, as indicated by the vertical dot-dashed line (at $M_2 \approx 1.8$ M$_\odot$) in Figure 8.5, is a consequence of the fact that the most massive progenitor primary which will form a white dwarf in the range $0.4 < M_{\rm WD}/{\rm M}_\odot \leq 0.5$ is 1.8 M$_\odot$. For PCEB distributions with larger white dwarf masses, which will be formed from more massive primary progenitors, this cut-off will shift towards larger values of M_2.

8.4 The present day population and space densities of PCEBs

Table 8.3 summarises the formation rate, present day population and the local space density, ϱ, of PCEBs for each model describing the treatment of the CE phase, and for each population model we considered. We calculate the local space density of PCEBs by dividing the present day population by the Galactic volume of 5×10^{11} pc^3.

For a given initial secondary mass distribution, we see that the present day population of PCEBs increases with increasing values of $\alpha_{\rm CE}$. By increasing $\alpha_{\rm CE}$, less orbital energy is required to eject the CE and therefore the binary system will undergo less spiral in. Hence, less systems will merge during the CE phase. For a given IMRD, we find very little difference in the calculated formation rates, present day numbers and local space densities of PCEBs between models A and DTg. For model DTb, on the other hand, where we are now considering the internal energy of the giant's envelope, we obtain a modest increase in the present day population of PCEBs compared to model A.

The present day population of PCEBs decreases slightly with increasing values of p in equation (3.15). As shown in Figure 1 of Politano & Weiler (2007) the average value of $\alpha_{\rm CE}$ for a given range in M_2 decreases with increasing p. By increasing p more orbital energy is required to expel the envelope from the system, hence a larger spiral-in of the binary. This will in turn lead to more mergers.

On the other hand, the present day number (local space density) of PCEBs decreases from model CT0375 to model CT15. As we increase the value of $M_{\rm cut}$ the typical value of $\alpha_{\rm CE}$ for a given range of M_2 will decrease. Hence, less systems will survive the CE phase.

We notice that the model n15 which describes the CE phase in terms of the binary's

angular momentum gives the largest present day population of PCEBs. For $n(q_{\rm i}) = 1$, the present day number (local space density) of PCEBs is 6.1×10^8 (1.2×10^{-3} pc^{-3}).

Schreiber & Gänsicke (2003) estimated from the observed sample of PCEBs that $6 \times 10^{-6} \lesssim \varrho/{\rm pc}^{-3} \lesssim 3 \times 10^{-5}$. An IMRD of $n(q_{\rm i}) \propto {q_{\rm i}}^{-0.99}$ gives the best agreement with this observed estimate, where we obtain $6.0 \times 10^{-7} \leq \varrho/{\rm pc}^{-3} \leq 5.6 \times 10^{-5}$. However, we should mention the selection effects which greatly pervade the observed sample of PCEBs, i.e. the selection bias against cold white dwarfs, and PCEBs with secondaries with spectral types earlier than about M0. As such, the observed PCEB local space density may underestimate that of the intrinsic, Galactic PCEB population.

Our models with $\alpha_{\rm CE} = 0.1$ also provide small space densities ($6.0 \times 10^{-7} \leq \varrho/{\rm pc}^{-3} \leq 1.7 \times 10^{-5}$, depending on the IMRD), which are similar to the observed ones. However, we find that in these models no PCEBs with ${\rm M_{WD}/M_\odot} \leq 0.4$ form. Low mass helium white dwarfs form via a case B CE phase, when the primary fills its Roche lobe on the first giant branch, typically when $R_1 \approx 15$ to 100 $R_\odot$. This means that the orbital period at the onset of the CE phase is between ≈ 40 and 250 d. As a consequence of such a low ejection efficiency, the binary cannot spiral in sufficiently to eject the envelope before a merger occurs. The lack of PCEBs with low mass white dwarfs in models with $\alpha_{\rm CE} = 0.1$ is in conflict with observations; for example LM Com and 0137-3457 have 95 per cent and 61 per cent probabilities respectively of having $M_{\rm WD}/{\rm M_\odot} \leq 0.4$.

8.5 IK Peg: A Clue to the CE Mechanism?

As discussed above, the bulk of observed systems which have $M_2/{\rm M_\odot} \lesssim 1.0$ and $P_{\rm orb}/{\rm d} \lesssim 1$ are consistent with our reference model A. IK Peg, on the other hand, cannot be explained by models with $\alpha_{\rm CE} \leq 1.0$, for $\lambda_{\rm CE} = 0.5$. Figure 8.6 shows the theoretical PCEB population with $1.1 < M_{\rm WD}/{\rm M_\odot} \leq 1.44$ for a range of models, indicated in the bottom right hand corner of each panel. The location of IK Peg on the $M_2 - \log P_{\rm orb}$ plane is shown in each case.

In order to explain the location of IK Peg, we require $\alpha_{\rm CE} \gtrsim 3$, if $\lambda_{\rm CE} = 0.5$. Model PL2

achieves $\alpha_{\rm CE} \approx 2.9$ for this system and, as shown in the panel labelled 'PL2' in Figure 8.6 can account for the location of IK Peg. However, this model also generates a low-mass cut-off at $M_2 \approx 0.4$ M$_\odot$ in the PCEB population. This is a feature which is not consistent with observed systems, as highlighted in the top panel of Figure 8.7. LM Com and 0137-3457 have a 95 per cent and a 61 per cent probability of sitting in this panel. Thus it appears this model cannot adequately describe the CE phase in its present form.

Note that models CT0375 to CT15 cannot account for the location of IK Peg either. From equation (3.14) $\alpha_{\rm CE} \rightarrow 1$ as $M_2 \rightarrow \infty$. As with the model PL2, the cut-off (by design of the model) in the PCEB population at $M_2 = 0.15$ M$_\odot$ doesn't appear to be supported by the observed sample. The bottom panel of Figure 8.7 compares the theoretical PCEB population with $0.4 < M_{\rm WD}/{\rm M}_\odot \leq 0.5$, with the corresponding observed WD+MS systems. Indeed, model CT15 cannot account for the observed location of, for example, HR Cam or 0137-3457, which have a 84 and 61 per cent probability of occupying this panel.

Model DTb, where the thermal energy of the giant's envelope contributes to the ejection of the CE, can also account for the location of IK Peg, while DTg cannot (see panels labelled 'DTb' and DTg' in Figure 8.6). Model DTg shows a slight increase in the orbital period of the upper boundary in the theoretical PCEB population, compared to that shown in the panel labelled 'A', but this is not enough to account for IK Peg.

Recall that for giant radii which are larger than that calculated by Dewi & Tauris (2000) we simply use the last tabulated value of $\lambda_{\rm g}$ for each mass. Therefore, we may still underestimate the value of $\lambda_{\rm g}$, and hence the product $\alpha_{\rm CE}\lambda_{\rm g}$ (recalling that $\alpha_{\rm CE} = 1$ for this model). Hence, from equation (5.20), we will also underestimate the value of $A_{\rm CE,f}$. A possible primary progenitor of IK Peg would fill its Roche lobe with a mass of 6 M$_\odot$ and a radius of 725 R$_\odot$. For such a primary we find $\lambda_{\rm g} \approx 0.7$. To account for the location of IK Peg, we require $\lambda_{\rm g} \approx 2.2$ for our progenitor binary if $\alpha_{\rm CE} = 1$.

Instead of extending the last tabulated value of $\lambda_{\rm g}$ to $R_1 > 600$ R$_\odot$, we could alternately linearly extrapolate the data to larger radii. Using the values of $\lambda_{\rm g}$ tabulated by Dewi & Tauris (2000) for a 6 M$_\odot$ star calculated by Dewi & Tauris (2000) we find $\lambda_{\rm g} \approx 1.5$ at $R_1 = 725$ R$_\odot$. This is still too small to account for the location of IK Peg.

Finally, the location of IK Peg can be accounted for if we consider an angular momentum, rather than an energy, budget, as shown by the panel 'n15'. Of further interest is that, in contrast to the other models considered in Figure 8.15, model n15 predicts no PCEBs with $M_2 \lesssim 1.0$ M$_\odot$ at $P_{\rm orb} \lesssim 1$ d. Furthermore, while the PCEB population in models A to DTb

Table 8.3: The formation rates, present day numbers and local space densities of PCEBs for different treatments of the CE phase, and for different initial mass distributions of the secondary star. The space densities were calculated by dividing the present day numbers by the Galactic volume of 5×10^{11} pc^3.

Model	Formation rate /yr^{-1}	Number of systems	Local space density /pc^{-3}
$n(q_i) \propto q_i^{-0.99}$, $0 < q_i \leq 1$			
CE01	2.1×10^{-4}	3.0×10^{5}	6.0×10^{-7}
CE06	1.5×10^{-3}	4.4×10^{6}	8.8×10^{-6}
A	2.0×10^{-3}	7.3×10^{6}	1.5×10^{-5}
PL05	1.6×10^{-3}	4.8×10^{6}	9.6×10^{-6}
PL1	1.3×10^{-3}	3.6×10^{6}	7.2×10^{-6}
PL2	1.1×10^{-3}	2.7×10^{6}	5.4×10^{-6}
CT0375	1.8×10^{-3}	6.6×10^{6}	1.3×10^{-5}
CT075	1.7×10^{-3}	5.7×10^{6}	1.1×10^{-5}
CT15	1.3×10^{-3}	4.2×10^{6}	8.5×10^{-6}
DTg	1.9×10^{-3}	7.5×10^{6}	1.5×10^{-5}
DTb	2.5×10^{-3}	1.2×10^{7}	2.4×10^{-5}
n15	5.4×10^{-3}	2.8×10^{7}	5.6×10^{-5}
$n(q_i) = 1$, $0 < q_i \leq 1$ (our reference IMRD)			
CE01	9.8×10^{-3}	1.5×10^{7}	3.0×10^{-5}
CE06	5.5×10^{-2}	1.5×10^{8}	3.0×10^{-4}
A	7.2×10^{-2}	2.2×10^{8}	4.4×10^{-4}
PL05	6.8×10^{-2}	1.9×10^{8}	3.8×10^{-4}
PL1	6.5×10^{-2}	1.6×10^{8}	3.2×10^{-4}
PL2	6.1×10^{-2}	1.4×10^{8}	2.8×10^{-4}
CT0375	7.0×10^{-2}	2.1×10^{8}	4.3×10^{-4}
CT075	6.7×10^{-2}	2.0×10^{8}	4.0×10^{-4}
CT15	6.0×10^{-2}	1.7×10^{8}	3.5×10^{-4}
DTg	6.8×10^{-2}	2.2×10^{8}	4.4×10^{-4}
DTb	8.7×10^{-2}	3.1×10^{8}	6.2×10^{-4}
n15	3.6×10^{-1}	6.1×10^{8}	1.2×10^{-3}

Continued on next page

Table8.3 – continued from previous page

Model	Formation rate /yr^{-1}	Number of systems	Local space density /pc^{-3}
	$n(q_i) \propto q_i,\ 0 < q_i \leq 1$		
CE01	1.1×10^{-2}	1.9×10^{7}	3.8×10^{-5}
CE06	5.8×10^{-2}	1.4×10^{8}	2.8×10^{-4}
A	7.5×10^{-2}	2.0×10^{8}	4.0×10^{-4}
PL05	7.7×10^{-2}	1.8×10^{8}	3.6×10^{-4}
PL1	7.8×10^{-2}	1.8×10^{8}	3.6×10^{-4}
PL2	7.8×10^{-2}	1.6×10^{8}	3.2×10^{-4}
CT0375	7.3×10^{-2}	2.0×10^{8}	3.9×10^{-4}
CT075	7.2×10^{-2}	1.9×10^{8}	3.8×10^{-4}
CT15	6.8×10^{-2}	1.7×10^{8}	3.5×10^{-4}
DTg	7.1×10^{-2}	2.0×10^{8}	4.0×10^{-4}
DTb	9.0×10^{-2}	2.7×10^{8}	5.4×10^{-4}
n15	1.7×10^{-1}	4.9×10^{8}	9.8×10^{-4}
	IMFM2		
CE01	6.5×10^{-3}	8.3×10^{6}	1.7×10^{-5}
CE06	4.7×10^{-2}	1.5×10^{8}	3.0×10^{-4}
A	6.5×10^{-2}	2.5×10^{8}	5.0×10^{-4}
PL05	4.4×10^{-2}	1.4×10^{8}	2.8×10^{-4}
PL1	3.0×10^{-2}	8.3×10^{7}	1.7×10^{-4}
PL2	1.7×10^{-2}	4.7×10^{7}	9.4×10^{-5}
CT0375	5.8×10^{-2}	2.2×10^{8}	4.4×10^{-4}
CT075	4.9×10^{-2}	1.8×10^{8}	3.5×10^{-4}
CT15	3.3×10^{-2}	1.1×10^{8}	2.2×10^{-4}
DTg	6.2×10^{-2}	2.6×10^{8}	5.2×10^{-4}
DTb	8.5×10^{-2}	4.2×10^{8}	8.4×10^{-4}
n15	1.9×10^{-1}	1.1×10^{9}	2.2×10^{-3}

peaks at $P_{\rm orb} \approx 1$ to 10 d, the model n15 population peaks at $P_{\rm orb} \approx 1000$ d. This result is in comparison to Maxted et al. (2007), who also found an increasing number of PCEBs with increasing orbital period up to $\gtrsim 100$ days.

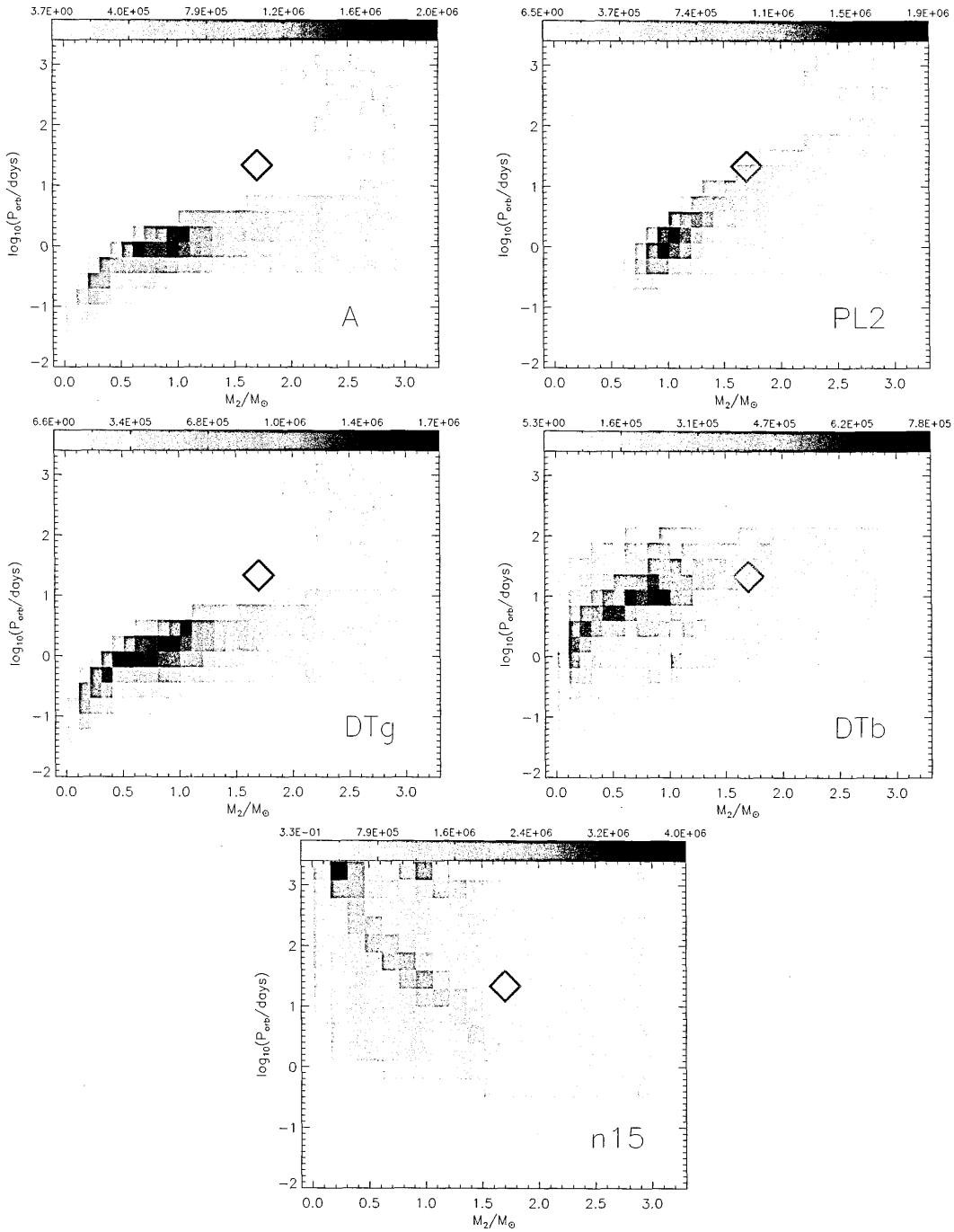

Figure 8.6: Calculated PCEB populations with $1.1 < M_{\rm WD}/{\rm M}_{\odot} \leq 1.44$ for a range of models indicated in the lower right hand corner of each plot. Here $n(q_{\rm i}) = 1$. The observed location of IK Peg is indicated by a red diamond. The grey-scale bars above each plot indicates the number of systems per bin area.

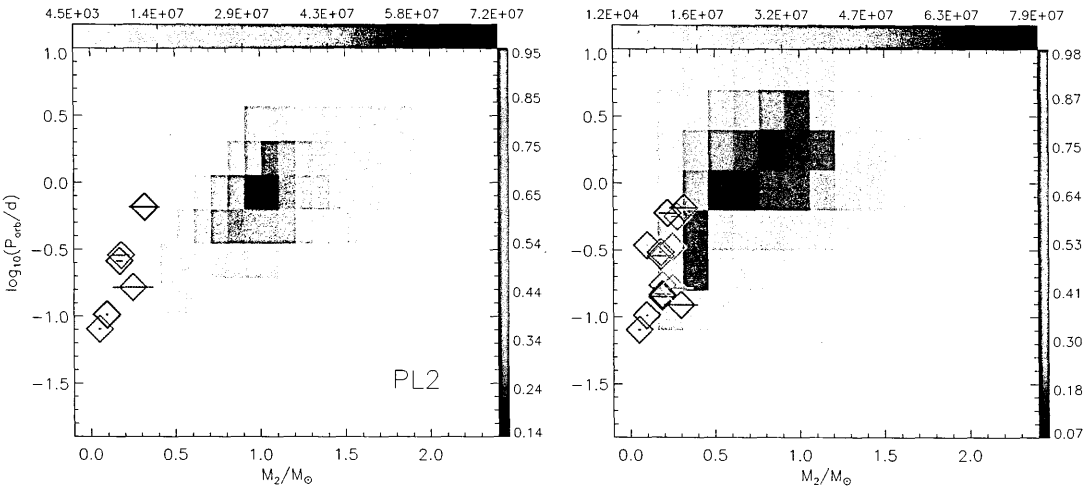

Figure 8.7: Same as for Fig. 8.1 but now showing the theoretical and observed PCEB population with $M_{\rm WD}/{\rm M}_{\odot} \leq 0.4$ for model PL2 (left panel) and $0.4 < M_{\rm WD}/{\rm M}_{\odot} \leq 0.5$ for model CT15 (right panel); in both cases $n(q_{\rm i}) = 1$. The grey-scale bar above the plots indicates the number of systems per bin area, while the bar on the right indicates the weightings of the observed systems.

8.6 Reconstruction of the CE phase for observed PCEBs

We now discuss the results of our CE reconstruction of the observed sample of PCEBs. The CE phase is only reconstructed for systems with white dwarf primaries. To briefly recap our method described in Section 7.6, the orbital period immediately after the CE phase, $P_{\rm CE}$, is calculated from the observed $P_{\rm orb}$ of each system by using the cooling age of the white dwarf, $t_{\rm cool}$, and the assumed angular momentum loss that the observed PCEB has been subject to since it emerged from the CE phase (see Section 3.4). We consider gravitational radiation only if $M_2 \leq M_{\rm MS,conv}$ M$_{\odot}$ and magnetic braking (according to equation 5.19) if $M_2 > M_{\rm MS,conv}$. The quantities $P_{\rm CE}$, $P_{\rm orb}$, $t_{\rm cool}$ and the effective temperature for the white dwarf, $T_{\rm eff,WD}$ for each WD+MS system we have reconstructed are summarised in Table 8.4.

As also described in Section 7.6, we have calculated the probability distribution of the possible values of $\alpha_{\rm CE}$ for each system. The values $\log_{10} \overline{\alpha}_{\rm CE}$ with the corresponding standard deviations for each reconstructed WD+MS binary are also summarised in Table 8.4.

8.6.1 The $M_2 - \log_{10}\alpha_{CE}$ plane

Note that the mass of the secondary stars in SDSSJ1529, SDSSJ0052, DE CVn and EG UMa lies just above $M_{MS,conv}$. Indeed, the measured uncertainties of the secondary masses in these systems carry the secondary masses below the fully convective limit. The evolution of these systems may therefore be driven purely by gravitational radiation or a combination of gravitational radiation and magnetic braking. We calculate P_{CE} for these systems for both scenarios. The first line in Table 8.4 for these systems gives the value of P_{CE} where we assume gravitational radiation only, while the second line gives P_{CE} where we assume both gravitational radiation and magnetic braking is operating. The theoretical value of $M_{MS,conv}$, however, is somewhat uncertain in itself.

Figure 8.8 shows the reconstructed values of α_{CE} versus M_2 for the observed WD+MS binaries we consider. The top panel is where we assume that the evolution of SDSSJ1529, SDSSJ0052, DE CVn and EG UMa is driven by magnetic braking according to equation (5.19) and gravitational radiation, while the bottom panel is where we assume that the evolution of these latter systems are driven purely by gravitational radiation.

Each coloured point corresponds to the value of $\overline{\alpha}_{CE}$ for each system, while the vertical, coloured error bars indicate the standard deviation. The full range of possible values of α_{CE} for each system is given by the black vertical lines. Red points indicate young systems where $P_{orb} = P_{CE}$, blue points indicate systems whose evolution is driven purely by gravitational radiation, while the green points indicate the evolution of systems are driven by gravitational radiation and magnetic braking according to equation (5.19).

Both panels in Figure 8.8 display substantial scatter in the values of $\overline{\alpha}_{CE}$, particularly in the range $0.1 \lesssim M_2/M_\odot \lesssim 0.4$. It is therefore unclear whether α_{CE} has a dependence on M_2. Figure 8.8 does, however, suggest that the value of α_{CE} does vary widely from system to system as suggested by Yorke et al. (1995) (see Section 3.3). This is in contrast to global, constant values of α_{CE} assumed in population synthesis calculations (see Section 3.3). Nonetheless, we attempt to fit a constant function to the data, which has the form

$$\log_{10}\alpha_{CE} = \epsilon_0, \tag{8.3}$$

where ϵ_0 is a constant. In order to estimate the mean value of ϵ_0 and the corresponding error, we apply the bootstrapping technique outlined in Press et al. (1992) (Chapter 14, pp. 529-532), to the data in Figure 8.8.

We point out, however, that the masses of the stellar components in LM Com are rather

Table 8.4: The values of $P_{\rm orb}$, $P_{\rm CE}$, the effective temperature of the white dwarf $T_{\rm eff,WD}$, $t_{\rm cool}$ (Myr)and the mean value of the ejection efficiency, $\log_{10}\overline{\alpha}_{\rm CE}$, for the observed sample of PCEBs for which we have reconstructed the CE phase for, as well as the calculated standard deviation. We consider both gravitational radiation only (first line), and a combination of magnetic braking and gravitational radiation (second line) for SDSSJ1529, SDSSJ0052, DE CVn and EG UMa. Unless otherwise stated, the cooling ages of the white dwarfs have been calculated by Schreiber & Gänsicke (2003). Systems have been grouped according to the assumed sink of angular momentum loss.

System	$P_{\rm orb}$ /days	$P_{\rm CE}$ /days	$T_{\rm eff,WD}/K$	$t_{\rm cool}$ /Myr	$\log_{10}\overline{\alpha}_{\rm CE}$
Gravitational radiation only (first line)					
Magnetic braking [eqn. (5.19)] (second line)					
SDSSJ1529	0.165	0.167	14 100±500 [a]	130 [a]	-0.11±0.26
		0.262			0.02±0.27
SDSSJ0052	0.114	0.147	16 100±4400 [a]	420 [a]	-0.36±0.11
		0.294			-0.16±0.11
DE CVn	0.364	0.372	8000±1000 [b]	800 [b]	-0.58±0.37
		0.486			-0.49±0.37
EG UMa	0.668	0.669	13 125±125 [c]	330	-0.08±0.26
		0.689			-0.06±0.25
Magnetic braking according to eqn. (5.19)					
J2130+4710	0.521	0.527	18 000±1000 [d]	71 [d]	-0.43±0.35
BPM 71214	0.202	0.298	17 200±1000 [e]	210	-0.43±0.10
QS Vir	0.151	0.315	14 220±300 [f]	370 [†]	-0.32±0.08
V471 Tau	0.521	0.521	34 500±1000 [g]	8.5	-0.45±0.08
FS Cet	4.232	4.232	57 000±2000 [h]	1.5 [†]	0.42±0.32
IN CMa	1.262	1.262	53 000±1100 [i]	1.3	-0.03±0.32
Gravitational radiation only					
HR Cam	0.103	0.104	19 000 [j]	45	0.01±0.22
0137-3447	0.080	0.084	16 500±500 [k]	250 [k]	0.38±0.24

Continued on next page

Table8.4 – continued from previous page

System	$P_{\rm orb}$ /days	$P_{\rm CE}$ /days	$T_{\rm eff,WD}$ /K	$t_{\rm cool}$ /Myr	$\log_{10}\overline{\alpha}_{\rm CE}$
RR Cae	0.303	0.309	7000[l]	1200	-0.09±0.26
LM Com	0.259	0.259	29 300±500[m]	12	0.51±0.25
					-0.28±0.30[%]
MS Peg	0.174	0.174	22 170[n]	28	-0.59±0.35
GK Vir	0.344	0.344	48 800±1200[o]	1.6	-0.09±0.36
NN Ser	0.130	0.130	55 000±8000[p]	1.3	-0.47±0.37
J2013+4002	0.706	0.706	49 000±700[i]	120	0.03±0.33
1042-6902	0.337	0.337	19 960±4000[h]	80[†]	-0.13±0.37
J1016-0520AB	0.789	0.789	55 000±1000[i]	1.5	0.33±0.28
2009+6216	0.741	0.741	25 870[q]	20[q]	0.29±0.22
IK Peg	21.72	21.72	35 500[r]	30[†]	0.59±0.13

[%]Value of $\log_{10}\overline{\alpha}_{\rm CE}$ where we consider the stellar masses determined by Orosz et al. (1999).

[†]Determined in this work using Fig. 4 of Schreiber & Gänsicke (2003).

References: [a]Rebassa-Mansergas et al. (2008); [b]van den Besselaar et al. (2007); [c]Bleach et al. (2000); [d]Maxted et al. (2004); [e]Kawka et al. (2002); [f]O'Donoghue et al. (2003); [g]O'Brien et al. (2001); [h]Kawka et al. (2008); [i]Vennes et al. (1999); [j]Maxted et al. (1998); [k]Maxted et al. (2006);[l]Bragaglia et al. (1995); [m]Shimansky et al. (2003); [n]Schmidt et al. (1995); [o]Fulbright et al. (1993); [p]Catalan et al. (1994); [q]Morales-Rueda et al. (2005); [q]Landsman et al. (1993)

uncertain (Shimansky et al. 2003). We therefore perform our bootstrapping analysis to the data in Figure 8.8 by considering two possible locations of LM Com in the $\alpha_{\rm CE} - M_2$ plane; where we have used the stellar masses found by Shimansky et al. (2003) (as labelled in both panels of Figure 8.8), and where we have used the stellar masses found by Orosz et al. (1999) (given by the data point with the magenta error bars), who find that $M_{\rm WD} = 0.45 \pm 0.05$ $\rm M_\odot$ and $M_2 = 0.28 \pm 0.05$ $\rm M_\odot$.

Our results from our bootstrapping analysis is graphically illustrated in Figure 8.9, and summarised in table 8.5.

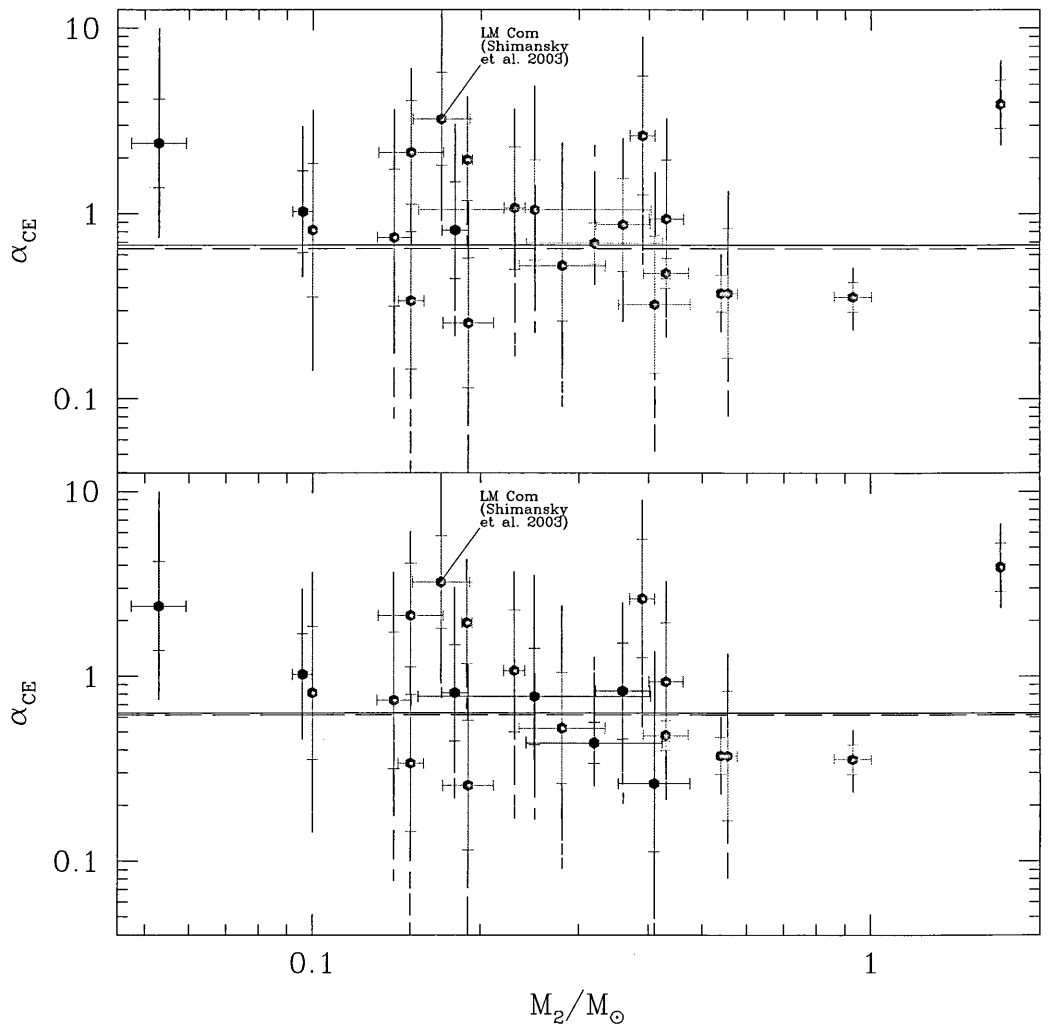

Figure 8.8: Reconstructed values of α_{CE} (represented by the black vertical lines) versus M_2. Each coloured point corresponds to the mean CE ejection efficiency, $\overline{\alpha}_{CE}$. Red: young PCEBs where $P_{orb} = P_{CE}$; blue: PCEBs with $M_2 \leq 0.35$ $M_\odot$, and hence their evolution is assumed to be driven purely by gravitational radiation; green: PCEBs with $M_2 > 0.35$ $M_\odot$, and hence their evolution is assumed to be driven by a combination of magnetic braking, according to eqn. (5.19), and gravitational radiation. The vertical black lines represent the full allowed range for α_{CE}, while the coloured vertical bars indicate the likely range. Top panel: SDSSJ1529, SDSSJ0052, DE CVn and EG Uma are assumed to be driven by magnetic braking; bottom panel: SDSSJ1529, SDSSJ0052, DE CVn and EG Uma are assumed to be driven by gravitational radiation only. Also shown are the lines of best fit, using a constant function in the form of eqn. (8.3). Solid line: fit performed where we assume stellar masses of LM Com found by Shimansky et al. (2003); long-dashed line: fit performed where the stellar masses of LM Com found by Orosz et al. (1999) are used.

Table 8.5: Results of our fits and bootstrap analysis to the data shown in Fig. 8.8, where we have considered a fit function of the form given by eqn. (8.3). We have carried out our fits where we have assumed SDSSJ1529, SDSSJ0052, DE CVn and EG UMa are driven by either gravitational radiation (GR) only or by magnetic braking (MB). We have also repeated our analysis using the stellar masses determined by Shimansky et al. (2003) and Orosz et al. (1999) (given in brackets). The table gives the values of ϵ_0 and the associated χ^2 values for the fits to the original data, and mean value of ϵ_0, $\langle\epsilon_0\rangle$ with errors, from the bootstrapped samples.

Quantity	SDSSJ1529, SDSSJ0052, DE CVn & EG UMa driven by GR	SDSSJ1529, SDSSJ0052, DE CVn & EG UMa driven by MB
Fits to the data in Fig. 8.8 using eqn. (8.3)		
ϵ_0	-0.20 (-0.21)	-0.17 (-0.19)
χ^2	88.13 (79.99)	85.79 (78.26)
Bootstrap analysis of data in Fig. 8.8 using eqn. (8.3)		
$\langle\epsilon_0\rangle$	-0.25 ± 0.07 (-0.27 ± 0.06)	-0.22 ± 0.08 (-0.24 ± 0.07)

As can be seen from table 8.5, our fits and bootstrapping results are rather insensitive to our assumptions regarding the evolutionary driving mechanisms for SDSSJ1529, SDSSJ0052, DE CVn and EG UMa, as well as the assumed stellar masses of LM Com. Indeed, our bootstrapping analysis shows that $\langle\epsilon_0\rangle$ lies between approximately -0.27 and -0.22. From equation (8.3), a value of $\alpha_{\rm CE}$ between approximately 0.54 and 0.60. The solid and dashed black lines in Figure 8.8 shows our fits according to equation (8.3), using LM Com's stellar masses as determined by Shimansky et al. (2003) and Orosz et al. (1999) respectively.

As shown by table 8.5, a constant fit to the original data gives a χ^2 of between approximately 78 and 88, which gives a goodness-of-fit probability of $Q \lesssim 10^{-8}$. While this clearly shows a that a constant fit to the data in Figure 8.8 is a poor one, it is appears somewhat unclear whether a higher order fit is required – or in fact necessary – to fit the data, due to the large amount of scatter exhibited.

8.6.2 The $A_{\rm CE,f} - \log_{10}\alpha_{\rm CE}$ plane

Figure 8.10 shows the reconstructed values of $\alpha_{\rm CE}$ versus orbital separation immediately after the CE phase, $A_{\rm CE,f}$ for the observed PCEBs, calculated from equation (7.7). The colours of the points are the same as for Figure (8.8). Also shown are the two possible locations of LM Com in the $A_{\rm CE,f} - \alpha_{\rm CE}$ plane, depending whether the stellar masses found

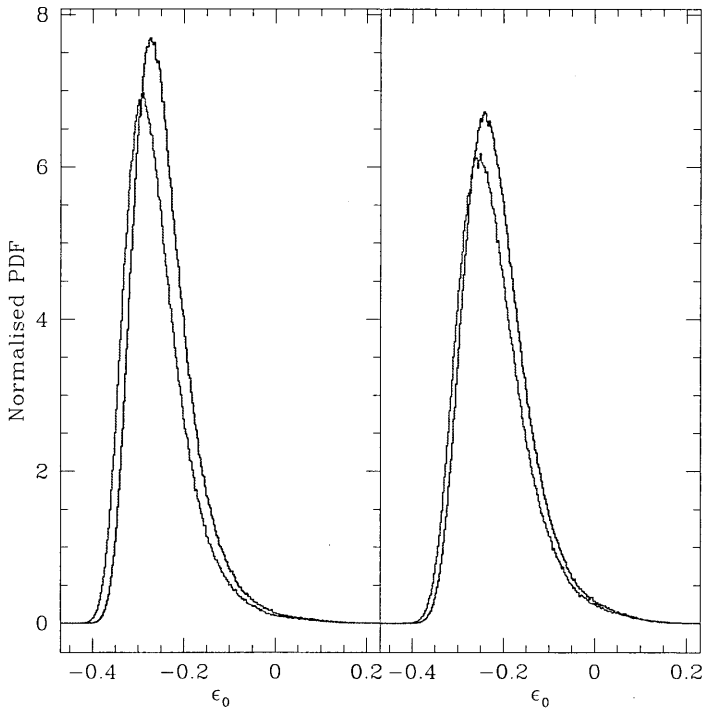

Figure 8.9: Results of our bootstrapping analysis of the data in Fig. (8.8). Left panel: where we have assumed SDSSJ1529, SDSSJ0052, DE CVn and EG UMa are driven by gravitational radiation only; right panel: where we have assumed the aforementioned systems are driven my magnetic braking. Green lines: LM Com stellar masses determined by Shimansky et al. (2003); red lines: LM Com stellar masses determined by Orosz et al. (1999).

by Shimansky et al. (2003) are used (as labelled in both panels of Figure 8.10) or those found by Orosz et al. (1999) (indicated by the data point with the magenta error bars).

We note that by fitting a function of the form given by equation (8.3), we will obtain the same parameters as shown in table 8.5, since $\alpha_{\rm CE}$ is independent of either M_2 or $A_{\rm f}$ in this case. This constant function, according to equation (8.3) using the parameters listed in table 8.5 is shown in Figure 8.10. However, while there is considerable scatter in both panels in Figure 8.10, there is a hint at a systematic behaviour with a shallow global minimum of $\alpha_{\rm CE}$ near post-common envelope separations of approximately 2 $\rm R_{\odot}$, with increasing values of $\alpha_{\rm CE}$ towards smaller and larger separations.

Indeed, we find that a fit to the data in Figure 8.10 with a cubic function of the form

$$\log_{10}\alpha_{\rm CE} = \epsilon_0 + \epsilon_1\left[\log_{10}\left(\frac{A_{\rm CE,f}}{\rm R_{\odot}}\right)\right] + \epsilon_2\left[\log_{10}\left(\frac{A_{\rm CE,f}}{\rm R_{\odot}}\right)\right]^2 + \epsilon_3\left[\log_{10}\left(\frac{A_{\rm CE,f}}{\rm R_{\odot}}\right)\right]^3, \quad (8.4)$$

(where ϵ_0 to ϵ_3 are constants), can adequately reproduce this systematic behaviour, and

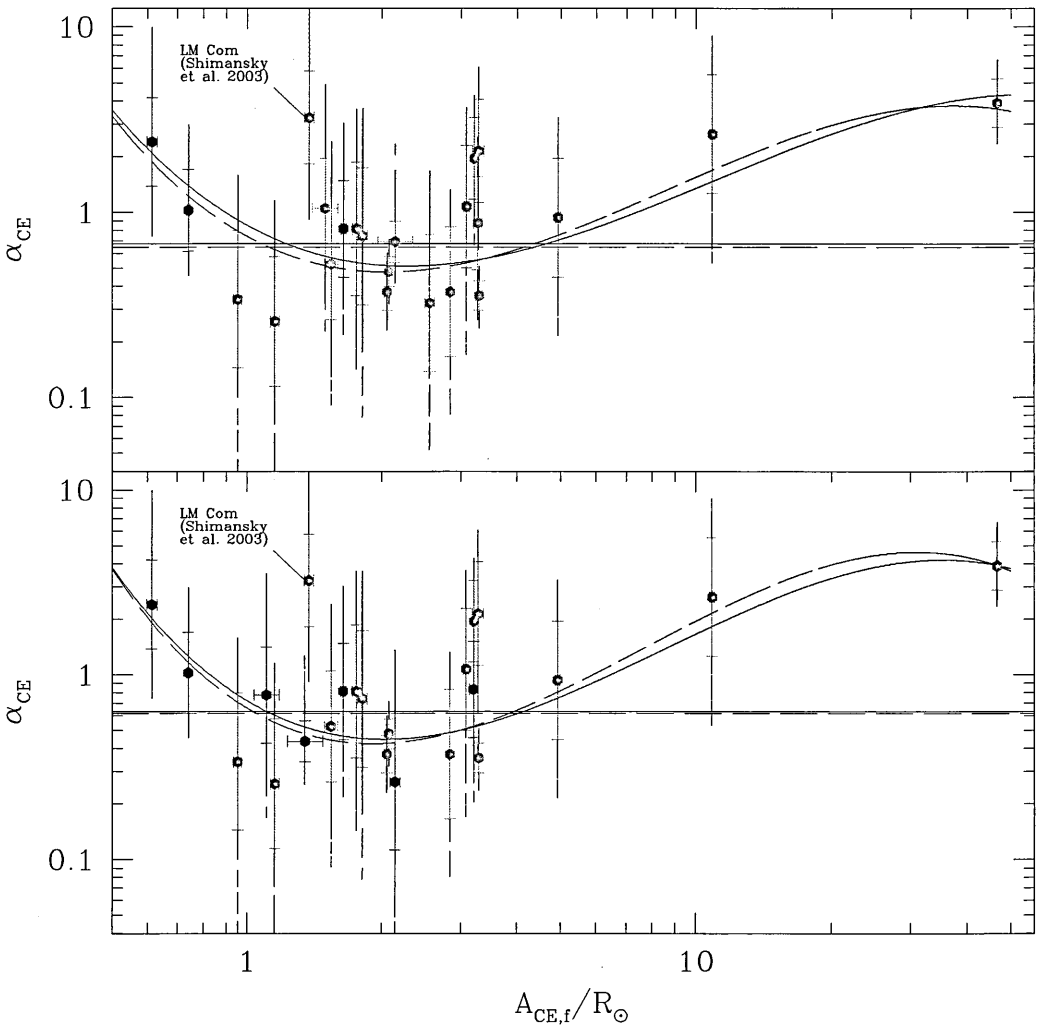

Figure 8.10: Similar to Fig. 8.8 but now showing reconstructed values of α_{CE} versus the orbital separation immediately after the CE phase, $A_{CE,f}$ (calculated from eqn 7.7). Also shown are the constant and cubic fits to the data according to eqns. (8.3) and (8.4) respectively. The meanings of the different line styles are the same as used in Fig. 8.8.

gives a better fit than that provided by equation (8.3). The results of our fit to the data in Figure 8.4 is summarised in table 8.6. As for the data in Figure 8.8, we again carry out a bootstrap analysis for the data in Figure 8.10. The results of this analysis is also summarised in table 8.6. These results are also graphically illustrated in Figures 8.11 and 8.12, which shows the distribution in the values of the coefficients ϵ_0 to ϵ_3, where we have assumed the evolution of SDSSJ1529, SDSSJ0052, DE CVn and BG UMa are driven purely by gravitational radiation in the former figure, and by magnetic braking in the latter figure.

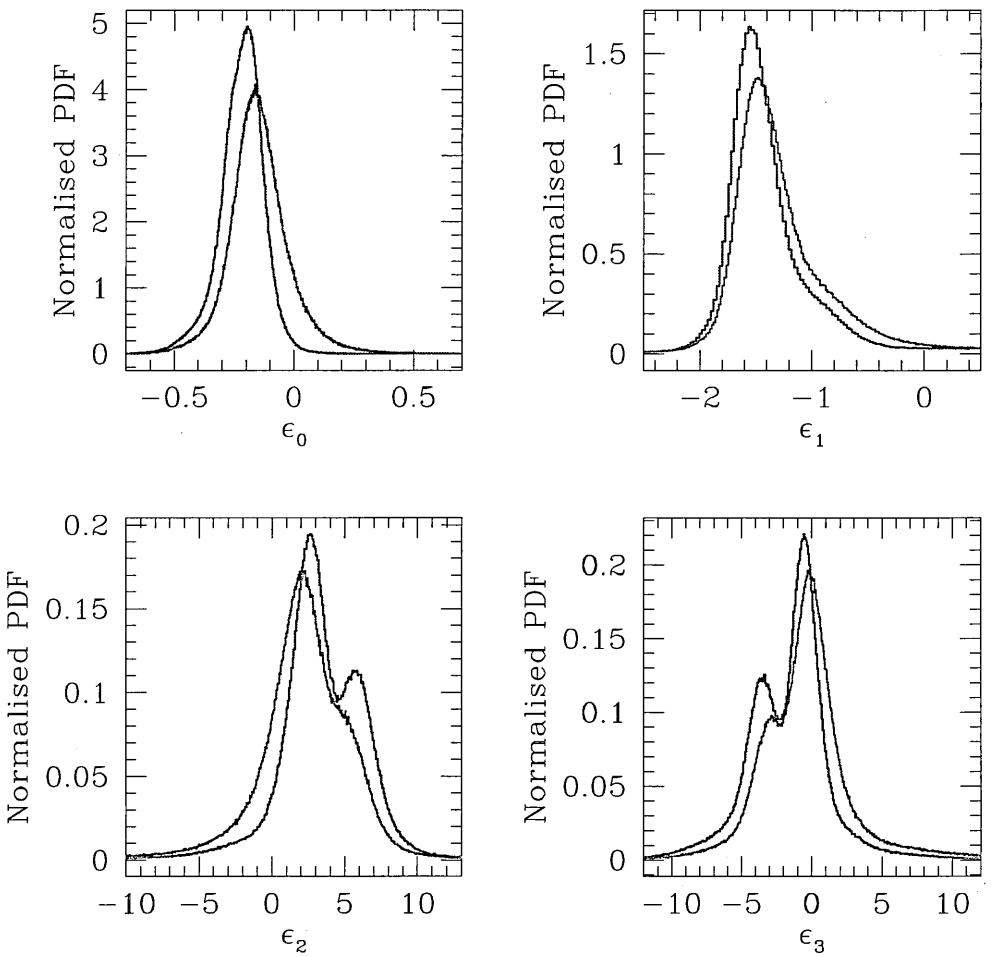

Figure 8.11: Results of our bootstrapping analysis of the data in Fig. (8.10) showing the values of ϵ_0 to ϵ_1, where we have assumed that the evolution of SDSSJ1529, SDSSJ0052, DE CVn and EG UMa are d aforementioned systems are driven by gravitational radiation. The meaning of the different coloured lines are the same as given in Fig. 8.9.

The fit parameters to the original data are somewhat insensitive to our assumption regarding the evolutionary driving mechanism of SDSSJ1529, SDSSJ0052, DE CVn and EG UMa, and whether we use LM Com's stellar masses found by Shimansky et al. (2003) or Orosz et al. (1999). Using the stellar masses for LM Com found by Orosz et al. (1999), however, gives a χ^2 of between approximately 24 and 27. This corresponds to a goodness-of-fit probability, $\mathcal{Q}$, of between approximately 0.0063 and 0.17, which is clearly an improvement over a constant fit of the form given by equation (8.3).

However, our bootstrap analysis suggests caution. The distributions in the values of the

cubic coefficient, ϵ_3, as shown in the bottom right hand panels of Figures 8.11 and 8.12 indicate that, irrespective of our assumption regarding the evolutionary driving mechanism of SDSSJ1529, SDSSJ0052, DE CVn and EG UMa, or of the stellar masses we use for LM Com, the mode value of ϵ_3 is close to zero. This suggests a very weak cubic term in equation (8.4). Furthermore, as shown in table 8.6, the standard deviation in the value ϵ_3 ranges from 4.12 to 6.23. On the other hand, the standard deviation for the value of ϵ_0 if we fit a constant function of the form given by equation 8.3 is between 0.06 and 0.07 (a scatter of approximately 30 per cent; see table 8.5).

An interesting feature in the distribution of ϵ_3 values occurs when we consider LM Com's stellar masses as determined by Orosz et al. (1999). The red curves in the lower, right hand panels of Figures 8.11 and 8.12 shows a secondary peak at $\epsilon_3 \approx -4$, which shows a possible fit through the data which has a significant cubic term. The appearance of this secondary peak, as well as the appearance of the peak at $\epsilon_3 \approx 0$ can be explained as follows.

Inspecting Figure 8.10, it can be seen that the bulk of the data can be found at orbital separations between approximately 1 and 3 $R_\odot$, which exhibits significant scatter. It is these data points which can be adequately fitted by a constant function, and which will show a weak or no cubic relationship. This gives rise to the major peak in the lower, right hand panels in Figures 8.11 and 8.12.

It is only by virtue of the few data points at orbital separations $A_{\rm CE,f} \lesssim 1$ $R_\odot$, and at $A_{\rm CE,f} \gtrsim 3$ $R_\odot$ that give rise to the significant cubic term in equation 8.4. This can be seen by looking at the cubic fits (using the parameters listed in table 8.6) to the original data in Figure 8.10. The long dashed line gives the fit where we have used the stellar masses for LM Com found by Orosz et al. (1999), while the solid line is where have used the stellar masses found by Shimansky et al. (2003). Hence, the secondary peak arises when these extreme-end data points are included in the bootstrapping analysis. Note that a secondary peak also appears in the distribution of ϵ_2 values (i.e. the lower left panels of Figures 8.11 and 8.12), again due to the same reasons given above.

This secondary peak is less prominent in the cases where we use LM Com's stellar masses as found by Shimansky et al. (2003). To see why, we again refer to the upper and lower panels of Figure 8.10. By comparing the location of LM Com (using the masses determined by Shimansky et al. (2003)) and the cubic function we have used to fit the data (again using the fit parameters listed in table 8.6). We can see that LM Com is a clear outlier from this best-fit curve. Therefore, the inclusion of this data point in bootstrapped samples will

Table 8.6: Similar to table 8.5, except we now show the results of our fits and bootstrap analysis to the data shown in Fig. 8.10, where we have considered a fit function of the form given by eqn. (8.4). The table gives the values of ϵ_0 to ϵ_3 and the associated χ^2 values for the fits to the original data, and mean value of $\epsilon_{0...3}$, $\langle\epsilon_{0...3}\rangle$ with errors, from the bootstrapped samples. The table also gives the F-values, F_0, for the original data as calculated using eqn. (8.5), and whether we can reject the null hypothesis, $\mathcal{H}_0$ that there is no cubic relationship between $A_{\rm CE,f}$ and $\alpha_{\rm CE}$. Finally, the probabilities that we will obtain an F-value $\gtrsim F_0$, assuming $\mathcal{H}_0$ is true, $\mathcal{P}(F \geq F_0)$ are also listed.

Quantity	SDSSJ1529, SDSSJ0052, DE CVn & EG UMa driven by GR	SDSSJ1529, SDSSJ0052, DE CVn & EG UMa driven by MB
	Fits to data in Fig. 8.10 using eqn. (8.4)	
ϵ_0	-0.14 (-0.18)	-0.07 (-0.13)
ϵ_1	-1.46 (-1.47)	-1.33 (-1.32)
ϵ_2	2.84 (3.11)	2.25 (2.54)
ϵ_3	-1.02 (-1.17)	-0.72 (-0.90)
χ^2	34.26 (23.60)	36.33 (27.34)
	Bootstrap analysis of data in Fig. 8.10 using eqn. (8.4)	
$\langle\epsilon_0\rangle$	-0.14 ± 0.15 (-0.22 ± 0.11)	-0.04 ± 0.28 (-0.17 ± 0.22)
$\langle\epsilon_1\rangle$	-1.18 ± 1.16 (-1.31 ± 0.92)	-1.03 ± 2.05 (-1.04 ± 1.74)
$\langle\epsilon_2\rangle$	2.04 ± 4.82 (3.40 ± 3.71)	0.59 ± 7.20 (2.40 ± 6.01)
$\langle\epsilon_3\rangle$	-0.12 ± 5.54 (-1.62 ± 4.12)	1.33 ± 7.83 (-0.95 ± 6.23)
	Permutation test results for the data in Fig. 8.10	
F_0	2.20 (2.91)	2.02 (2.45)
Reject $\mathcal{H}_0$?	yes (yes)	no (yes)
$\mathcal{P}(F \geq F_0)/\%$	1.82 (0.58)	3.09 (1.54)

'dilute' the cubic term in equation (8.4).

To see if a cubic fit to the data in Figure 8.10 is warranted we perform the F-test (Press et al. 1992). If the chi-squared value obtained from our constant fit to the original data is $\chi^2_{\rm const}$, and $\chi^2_{\rm cubic}$ is the chi-squared value we obtain from a cubic fit to the data in Figure 8.10, then the F-value is obtained from

$$F_0 = \frac{\chi^2_{\rm const}/\nu_{\rm const}}{\chi^2_{\rm cubic}/\nu_{\rm cubic}}, \tag{8.5}$$

where $\nu_{\rm const}$ and $\nu_{\rm cubic}$ are the corresponding number of degrees of freedom, and the subscript '0' denotes we are obtaining the F-value to the original data. If $N = 22$ is the number of

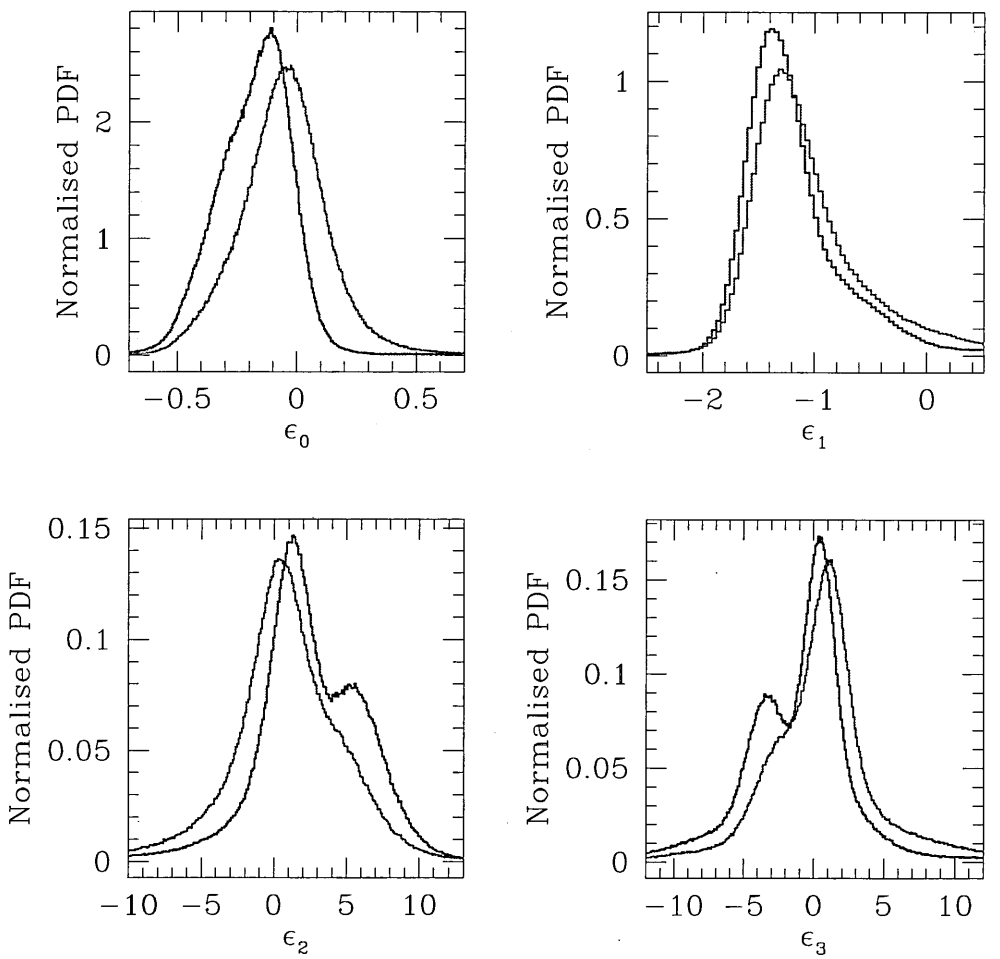

Figure 8.12: Similar to Fig. 8.11, except we now assume that the evolution of SDSSJ1529, SDSSJ0052, DE CVn and EG UMa are driven by magnetic braking. The meaning of the different coloured lines are the same as given in Fig. 8.9.

data points and M is the number of orders of the fit (for example $M = 4$ for a cubic fit), then the number of degrees of freedom is given by $N - M$. Hence, we have $\nu_{\rm const} = 21$ and $\nu_{\rm cubic} = 18$. The resulting values of F_0 are shown in table 8.6.

Our null hypothesis, $\mathcal{H}_0$, is that there is no cubic trend in the data displayed in Figure 8.10. If $\mathcal{H}_0$ is true, then the critical F-value, $F_{\rm crit}$, at the 5 per cent significance level for our values of $\nu_{\rm const}$ and $\nu_{\rm cubic}$ is $F_{\rm crit} = 2.18$. Hence, if we obtain $F_0 > F_{\rm crit}$, then we can reject $\mathcal{H}_0$. For the different values of F_0 listed in table 8.6, we have also indicated if we can reject $\mathcal{H}_0$, i.e. there is a cubic trend in the data of Figure 8.10.

In all but one of the cases listed, we can reject $\mathcal{H}_0$. This case is where we assume the

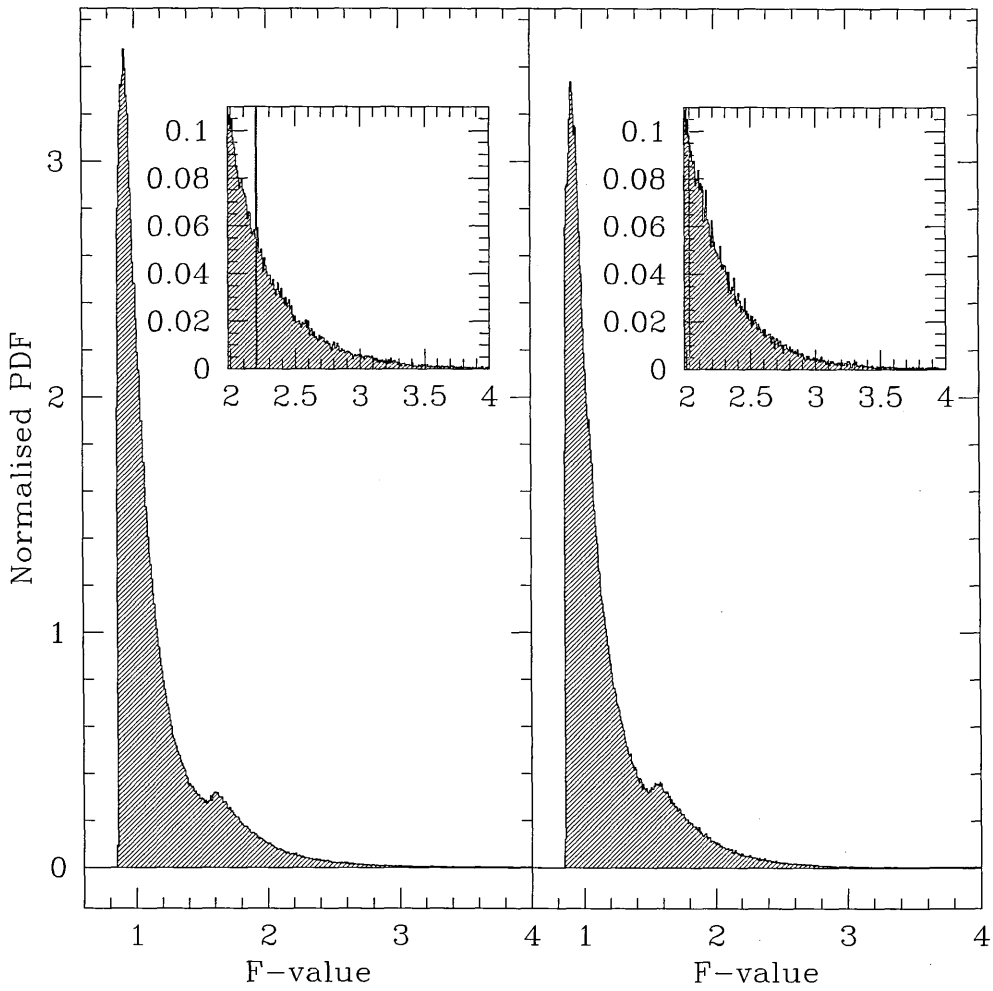

Figure 8.13: The distribution in F-values obtained from the data in Fig. 8.10, where we have used the stellar masses of LM Com determined by Shimansky et al. (2003). Left panel: where we have assumed SDSSJ1529, SDSSJ0052, DE CVn and EG UMa are driven by gravitational radiation only; right pane: where we have assumed the aforementioned systems are driven by magnetic braking.

evolution of SDSSJ1529, SDSSJ0052, EG UMa and DE CVn are driven by magnetic braking, and where we use stellar masses in LM Com as found by Shimansky et al. (2003). Note, though, that where we assume that the evolution of SDSSJ1529, SDSS0052, DE CVn and EG UMa are driven by magnetic braking, and use the stellar masses of Shimansky et al. (2003), we can only just reject $\mathcal{H}_0$. Hence, we have tentative evidence that a fit of order larger than 1 is required to adequately fit the data in Figure 8.10.

As a final test, we perform a permutation test on the data in Figure 8.10. In contrast to bootstrapping where we randomly pick with replacement a data point, for permutation

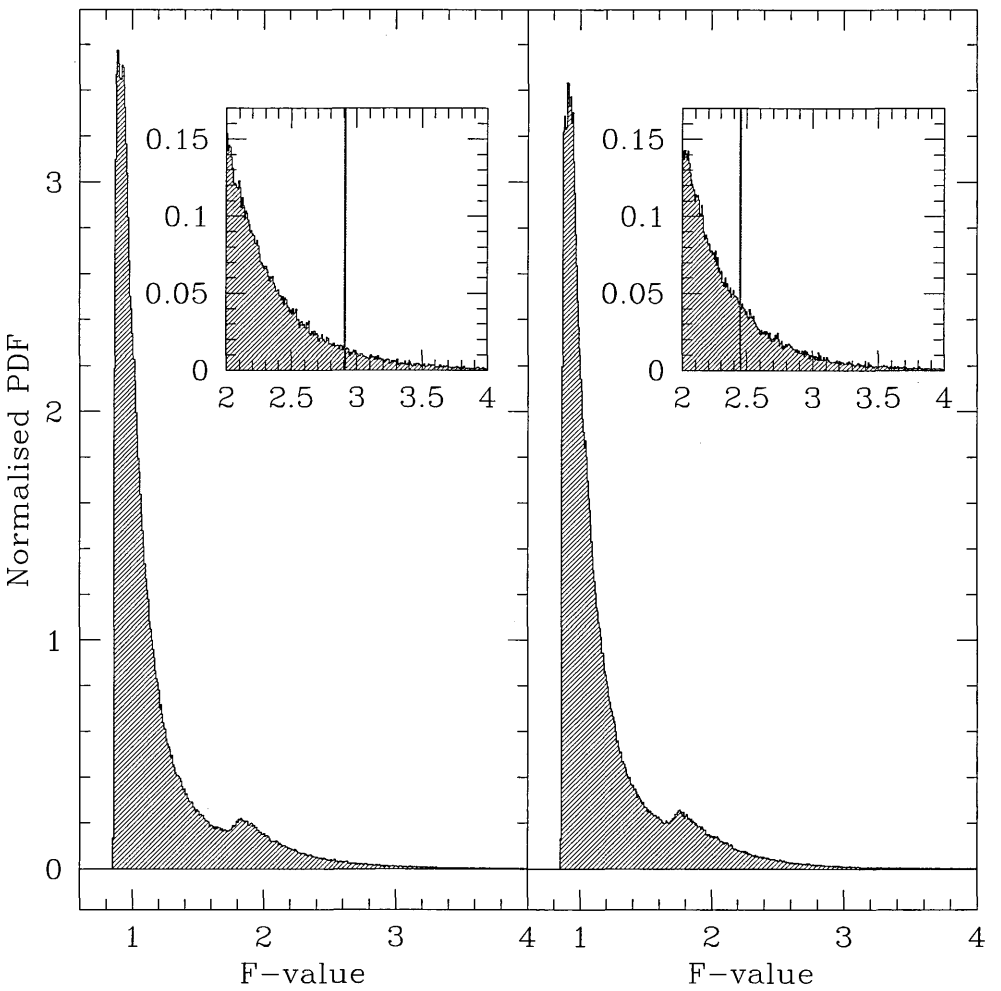

Figure 8.14: Similar to Fig. 8.14, except we now use the stellar masses in LM Com as found by Orosz et al. (1999). The meanings of the left and right panels are the same as that described in Fig. 8.13.

testing we randomly pick without replacement values of $\alpha_{\mathrm{CE,i}}$ for each $A_{\mathrm{CE,f}}$ of a given data point. By doing this we destroy any relationship which may exist between $A_{\mathrm{CE,f}}$ and α_{CE}. For each permuted sample, we fit a constant function of the form given by equation (8.3) and then with the cubic function given by equation (8.4). We then calculate the F-value for that sample using the resulting values of χ^2_{const} and χ^2_{cubic}, according to equation (8.5).

By repeating this procedure for a number of permuted samples (approximately 10^6 in our case), we therefore build up a distribution of F-values assuming that $\mathcal{H}_0$ is true, as shown by Figures 8.13 and 8.14. Figure 8.13 shows the distribution of F-values where we have used LM Com's stellar masses as determined by Shimansky et al. (2003), while Figure

8.14 uses the stellar masses of LM Com as found by Orosz et al. (1999). The left panels of theses figures corresponds to where we have assumed that the evolution of SDSSJ1529, SDSSJ0052, DE CVn and EG UMa are driven by gravitational radiation only, while the right panels corresponds to where we have assumed these systems are driven by magnetic braking.

Using Figures 8.13 and 8.14, and the corresponding values of F_0 listed in table 8.6, we can calculate the probability, assuming that $\mathcal{H}_0$ is true, that we will obtain an F-value equal to, or greater than, the F-value obtained from the original data, $\mathcal{P}(F \geq F_0)$. These probabilities are also listed in table 8.6. The values of F_0 are marked within the appropriate insets in Figures 8.13 and 8.14 with a vertical red line.

Thus, the smaller the value of $\mathcal{P}(F \geq F_0)$, the less likely the result, assuming $\mathcal{H}_0$ is true. Assuming a significance level of 5 per cent, we can therefore reject $\mathcal{H}_0$ in all cases listed in table 8.6. However, as discussed above, we cannot reject $\mathcal{H}_0$ based on the data where we have assumed the evolution SDSSJ152, SDSS0052, DE CVn and EG UMa are driven by magnetic braking, and where we have used LM Com's stellar masses as found by Shimansky et al. (2003), because $F_0 < F_{\rm crit}$. For the same case we find that $\mathcal{P}(F \gtrsim F_0) \approx 3.1$ per cent, which is close to our significance level.

The most convincing evidence for a cubic trend in the data in Figure 8.10 is where we have assumed the evolution of SDSSJ1529, SDSSJ0052, EG UMa and DE CVn are driven by gravitational radiation only, and using stellar masses of LM Com as found by Orosz et al. (1999). Here we find that $\mathcal{P}(F \geq F_0) \approx 0.6$ per cent. Not only can we reject $\mathcal{H}_0$ at the 5 per cent significance level, but also at the 1 per cent level.

While there is tantalising evidence for a high order (perhaps a cubic) dependence between $A_{\rm CE,f}$ and $\alpha_{\rm CE}$, we clearly need to acquire more data points at orbital separations longer than about 3 $R_\odot$ and less than about 1 $R_\odot$. Another obstacle is the angular momentum loss mechanism which drives the evolution of SDSSJ1529, SDSS0052, DE CVn and EG UMa. Furthermore, if the evolution of these systems are in fact driven by magnetic braking, there is the added problem that the angular momentum loss rate associated with magnetic braking is ill-constrained. Even if there is no strong relation between M_2 or $A_{\rm CE,f}$ with $\alpha_{\rm CE}$, Figures 8.8 and 8.8 show that the assumption of a constant, global value of $\alpha_{\rm CE}$ is not a realistic one. Nonetheless, we typically find that $\alpha_{\rm CE}$ lies between approximately 0.5 and 0.6 for the observed population of PCEBs.

8.7 The Initial Secondary mass Distribution

We now consider the impact of the initial mass ratio distribution on the theoretical PCEB populations. For our standard model A we calculated the PCEB population for each initial distribution of the secondary mass, which we compared to the observed WD+MS systems. Figure 8.15 illustrates the differences between the resulting PCEB populations in the range $0.4 < M_{\rm WD}/{\rm M}_{\odot} \leq 0.5$ as an example.

For the cases $n(q_{\rm i}) \propto qi^{-0.99}$ and IMFM2 the bulk of the PCEB population lies at $M_2 \lesssim 0.4$ M$_{\odot}$ and $P_{\rm orb} \lesssim 1$ d. This is consistent with the location of the observed WD+MS systems in Figure 8.15. The theoretical distribution with $n(q_{\rm i}) = 1$ suggests a peak at $M_2 \approx 1$ M$_{\odot}$ and $P_{\rm orb} \approx 1$ d, yet no systems are observed in this region of $M_2 - \log P_{\rm orb}$ space. However, this is likely to be a selection effect; PCEB candidates are selected according to their blue colour due to the optical emission from the white dwarf and/or high radial velocity variations. The flux from early-type secondaries will dominate over that of the white dwarf, and hence these systems go undetected. Schreiber & Gänsicke (2003) predicted that there is a large as yet undetected population of old PCEBs, with cool white dwarfs and long orbital period.

Rebassa-Mansergas et al. (2008) performed Monte-Carlo simulations to calculate the detection probability of PCEBs with $P_{\rm orb}/{\rm d} \lesssim 10$, based on the measurement accuracies of the Very Large Telescope (Schreiber et al. 2008), the SDSS, and for 1, 2 and 3σ significance of the radial velocity variations. They found that ~ 6 out of their sample of 9 PCEBs should have $P_{\rm orb} > 1$ d, yet this is not the case; all of their PCEBs have $P_{\rm orb} < 1$ d, in contrast with the predictions of Schreiber & Gänsicke (2003). Thus it is possible that the sharp decline in the population of PCEBs with $P_{\rm orb} > 1$ d is a characteristic of the intrinsic PCEB population, making the models with $n(q_{\rm i}) \propto {q_{\rm i}}^{-0.99}$ or IMFM2 more attractive. Note, however, that the local space density calculated for an IMRD of $n(q_{\rm i}) \propto {q_{\rm i}}^{-0.99}$ is in good agreement with the observationally determined one, while IMFM2 is not.

To determine if the intrinsic PCEB population does sharply decline for $P_{\rm orb} > 1$ d, we compared the orbital period distribution of our observed sample of PCEBs (containing 46 systems) with our calculated distribution, with $n(q_{\rm i}) = {q_{\rm i}}^{-0.99}$, model A. These distributions are shown as the hashed histogram and the red line in the top panel, left column of Figure

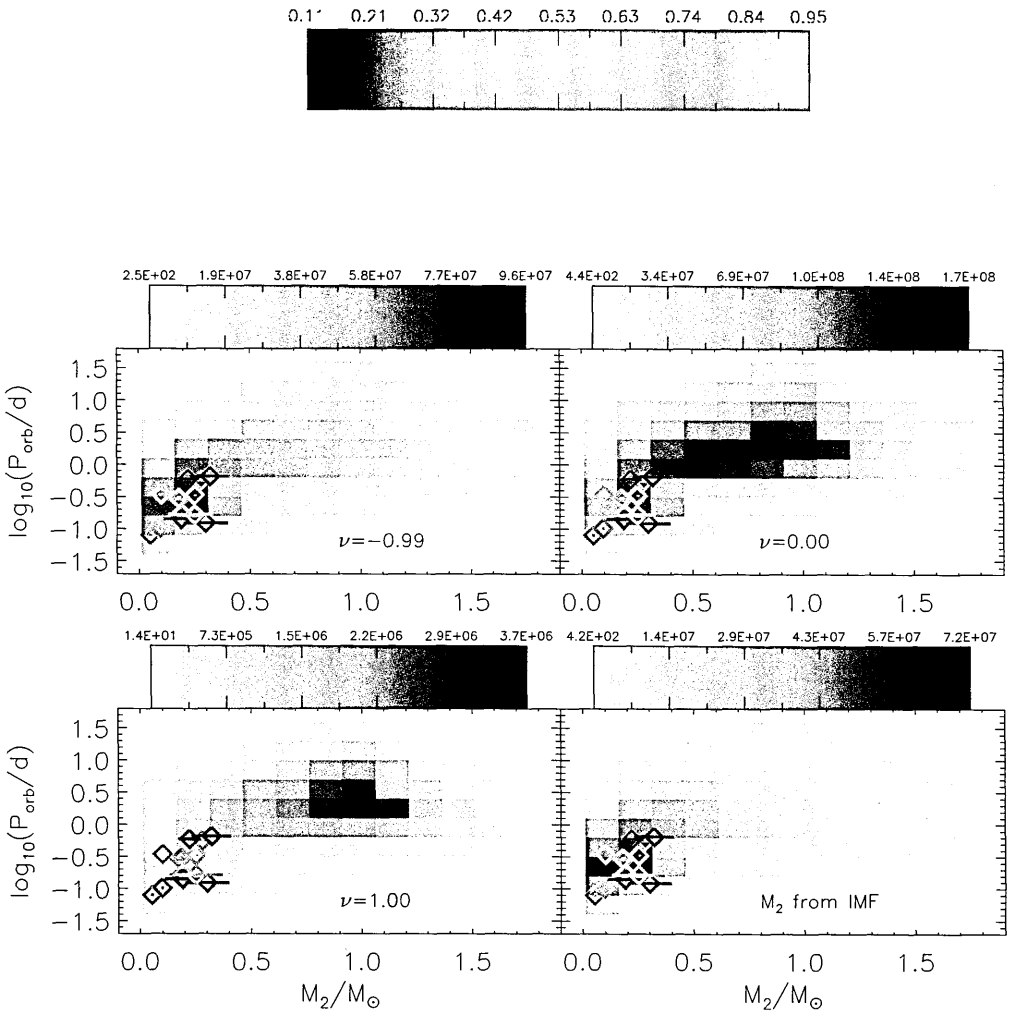

Figure 8.15: Same as Fig. 8.1, but showing the population of PCEBs with $0.4 < M_{\rm WD}/{\rm M}_{\odot} \leq 0.5$ for different initial secondary mass distributions, as indicated in each panel. The grey-scale bar above each panel gives the number of systems per bin area, while the colour bar at the top of the page gives the weighting of each system.

8.16. The corresponding normalised cumulative distribution functions (CDFs) are shown in the top panel, right column of Figure 8.16, with the scale indicated on the right axis. Note that, in contrast for the observed distribution, the number of PCEBs in the intrinsic population gradually declines for $P_{\rm orb} \gtrsim 1$ d, as opposed to a sharp decline.

We supplemented our calculated PCEB orbital period distribution with the detection probabilities calculated by Rebassa-Mansergas et al. (2008) (see their Figure 7). We considered the detection probabilities of WD+MS systems showing radial velocity variations in their spectra with a 3σ significance (the criterion used by Rebassa-Mansergas et al. (2007) and Rebassa-Mansergas et al. (2008) to identify PCEB candidates), as detected by the SDSS

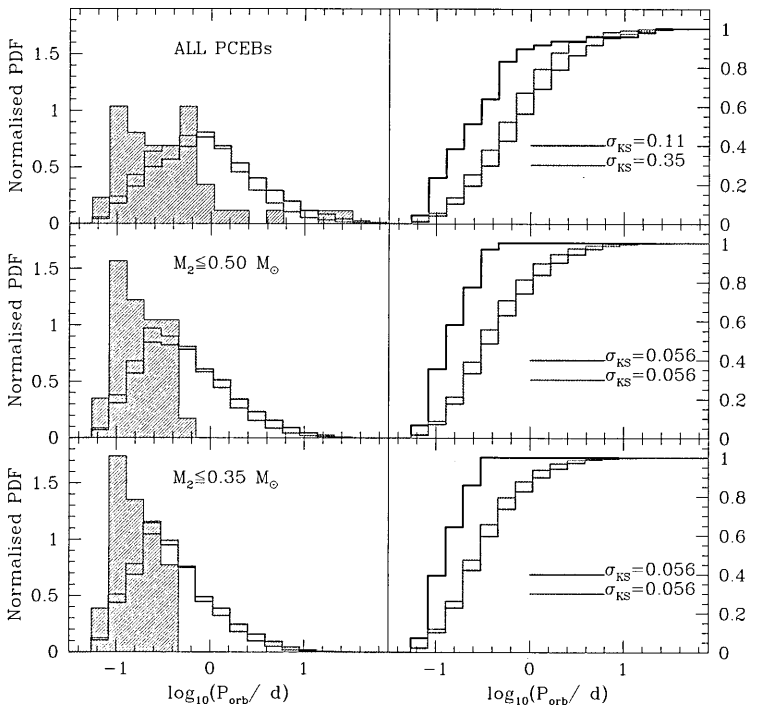

Figure 8.16: Left column: the normalised PDF of the orbital period distribution of the 46 observed sample of PCEBs (hashed histogram) compared with the calculated distribution of the intrinsic population for $n(q_i) = q_i^{-0.99}$ (red line), model A. The green line is similar to the red line, except here we also take into account the PCEB detection probability, as calculated by Rebassa-Mansergas et al. (2008), assuming a measurement accuracy of 15 km s^{-1} (appropriate for SDSS spectra), to detect 3σ radial velocity variations. Top: all PCEBs; middle: PCEBs with $M_2 \leq 0.5\ M_\odot$; bottom: PCEBs with $M_2 \leq 0.35\ M_\odot$. Right column: normalised CDFs of the corresponding orbital period distributions of the observed (solid black line), with the calculated distributions (red and green lines), with the scale indicated on the right axes. Also shown are the Kolmogorov-Smirnov significance levels, σ_{KS}, that the observed and calculated distributions are drawn from the same parent population.

(bottom curve of Fig. 7 in Rebassa-Mansergas et al. (2008)). As Rebassa-Mansergas et al. (2008) only calculate the detection probabilities, $\mathcal{P}$, for $P_{orb} \lesssim 10$ d, we extrapolated the curve up to $P_{orb} = 100$ d using the curve $\mathcal{P} = 0.43(P_{orb}/d)^{-0.35}$.

The corresponding orbital period distribution is shown as the green histogram in the top panels in the left and right columns of Figure 8.16. Note that the inclusion of the PCEB detection probabilities has a marginal effect. Indeed, we still predict a gradual decline in the number of PCEBs with $P_{orb} > 1$ d.

To determine the likelihood that the observed and calculated PCEB orbital period distri-

butions are drawn from the same parent distribution, we calculate the Kolmogorov-Smirnov statistic from the normalised CDF distributions, and therefore the corresponding significance level, $\sigma_{\rm KS}$. A very small value of $\sigma_{\rm KS}$ shows that the two distributions are significantly different, while $\sigma_{\rm KS} = 1$ shows that the two distributions are in good agreement. We find $\sigma_{\rm KS} = 0.11$ when comparing the observed and calculated intrinsic (red) orbital period distributions in the top panel, left column of Figure 8.16. On the other hand, we find $\sigma_{\rm KS} = 0.35$ between the observed and the calculated (green) orbital period distribution with the detection probabilities included.

We also consider the selection bias towards late-type secondaries by only considering the observed and theoretical orbital period distribution of PCEBs which have $M_2/{\rm M}_\odot \leq 0.5$ (middle panels of Fig. 8.16) and $M_2/{\rm M}_\odot \leq 0.35$ (bottom panels). There is a better agreement between the location of the peaks in the observed and theoretical PCEB orbital period distributions. However, the theoretical distributions (with and without the inclusion of PCEB detection probabilities), still predict a gradual decline in the number of PCEBs with $P_{\rm orb} \gtrsim 1$ d, while there is a sharp decline in the observed distribution. For the population of PCEBs with $M_2 \leq 0.5$ M$_\odot$ and M$_\odot \leq 0.35$, we find $\sigma_{\rm KS} = 5.6 \times 10^{-2}$ between the observed and calculated orbital period distributions, with and without the inclusion of PCEB detection probabilities.

Thus, we cannot reproduce the observed sharp decline in the number of PCEBs with $P_{\rm orb} \lesssim 1$ d, even if we take into account in our calculations the selection biases towards PCEBs with late-type secondaries, and the biases against the detection of PCEBs with long orbital periods. It is still unclear whether this sharp decline is indeed a characteristic of the intrinsic PCEB population, or if it is a result of further selection effects which have yet to be considered.

8.8 Discussion

8.8.1 Constraining the CE phase

We have shown that the majority of observed PCEBs (containing either a sub-dwarf or white dwarf primary) can be reproduced by canonical models with a constant, global value

of $\alpha_{\rm CE} > 0.1$ for the CE ejection efficiency. The systems V651 Mon, FF Aqr and V1379 Aql are likely to have formed from a thermally unstable RLOF phase. This is contrary to Nelemans & Tout (2005) who assumed them to be PCEBs, and attempted reconstruct their values of $\alpha_{\rm CE}$. For the case of V1379 Aql Nelemans & Tout (2005) could not find a solution for $\alpha_{\rm CE}$, and hence took this system as evidence for their 'γ-algorithm'. We have shown that this system could have formed from a thermally unstable RLOF phase.

There is only one system, IK Peg, that is both likely to be a PCEB and at the same time inconsistent with the standard energy budget CE model. Unlike the vast majority of the observed sample of PCEBs, this system contains an early-type secondary star, and this may provide a clue to the ejection mechanism during the CE phase.

Formally, the observed configuration of IK Peg requires $\alpha_{\rm CE} \gtrsim 3$. This means that a source of energy other than gravitational potential energy is exploited for the ejection of the CE. It has been suggested that this is the thermal and ionization energy of the giant's envelope (Han et al. 1995, Han et al. 1995, Dewi & Tauris 2000, Webbink 2007). We find that by considering this extra energy source in our models we can indeed account for the location of IK Peg. However, this is a concept which has been challenged by Harpaz (1998) and Soker & Harpaz (2003). Harpaz (1998) argue that, during the planetary nebula phase, the opacity of the giant's envelope decreases during recombination. Hence the envelope becomes transparent to its own radiation. The radiation will therefore freely escape rather than push against the material to eject it.

Previous population synthesis studies have considered constant, global values of $\lambda_{\rm CE} = 0.5$ (e.g. deKool 92, Willems & Kolb 2004). Dewi & Tauris (2000) suggested that this may lead to an overestimation of the binding energy of the giant's envelope, and hence underestimate the final PCEB orbital period. Dewi & Tauris (2000) calculated values of $\lambda_{\rm g}$ for range of masses and radii, which we incorporated into our population synthesis code. This, however, cannot account for IK Peg either. We note that Dewi & Tauris (2000) do not calculate values of $\lambda_{\rm g}$ for $R > 600$ R$_\odot$. We concede that we may still underestimate the value of $\lambda_{\rm g}$ for the case of IK Peg due to our adopted extrapolation to larger radii. If we do linearly extrapolate $\lambda_{\rm g}$ for a progenitor primary of IK Peg with $M_1 = 6$ M$_\odot$ and $R_1 = 725$ R$_\odot$ we find that $\lambda_{\rm g} \approx 1.5$, which is still not large enough to account for IK Peg. It would therefore be beneficial to calculate $\lambda_{\rm CE}$ in the mass and radius regime for PCEB progenitors.

Rather than consider the CE phase in terms of energy, Nelemans et al. (2000) and

Nelemans & Tout (2005) describe the CE phase in terms of the angular momentum of the binary. Indeed, this is also a prescription favoured by Soker (2004). Our model n15 can account for the location of IK Peg. However, Maxted et al. (2007) found that for the γ-prescription, the number of PCEBs increases with increasing orbital period up to $\gtrsim 100$ d. Indeed, we also find increasing number of PCEBs with high mass white dwarfs with increasing orbital period, with the bulk of the population lying at ≈ 1000 d. This is contrast with observations by Rebassa-Mansergas et al. (2008), who found a sharp decline in the number of PCEBs with increasing orbital period beyond 1 d.

8.8.2 Observing PCEBs

Even though we have critically examined a variety of treatments for the CE phase by comparing our models to the observed sample of PCEBs, we have been unable to significantly constrain the underlying physics. We believe this is mainly due to the selection effects still pervading the observed sample of PCEBs. The large majority of our observed PCEB sample contain late type secondaries, typically M3 to M5. This is a consequence of the fact that until recently PCEB candidates were identified in blue colour surveys, such as the Palomar Green survey. As a result systems containing secondaries with early spectral types will be missed, as their optical flux will dominate over that from the white dwarf. A few exceptions include systems identified by their large proper motions (e.g. RR Cae) or spectroscopic binaries (e.g. V471 Tau). IK Peg was detected due to the emission of soft X-rays from the young white dwarf, which has an effective temperature of 40 000 K.

The present sample of PCEBs is therefore covering an insufficient range in secondary masses. However, matters are improving with the advent of the SDSS, which probes a large *ugriz* colour space. This will allow an extra 30 PCEBs to be supplemented to the currently known 46 systems in the foreseeable future (Gänsicke 2008, private communication). A complementary program is currently underway to target those WD+MS systems with cool white dwarfs and/or early-type secondaries in order to compensate for the bias against such systems in the previous surveys (Schreiber et al. 2007). It is therefore feasible that we will be able to further constrain our models in the near future.

The observed sample of PCEBs also have $P_{\rm orb} \lesssim 1$ d, which can be argued to be a further selection effect; PCEBs are also detected due to radial velocity variations of their

spectra. However, Rebassa-Mansergas et al. (2008) found that this long-period cut-off may be a characteristic of the intrinsic PCEB population, rather than a selection effect. More precisely, we have shown in Section 8.7 that this may be a feature intrinsic to the population of PCEBs with late-type secondaries.

We also find that an IMRD distribution of $n(q_{\rm i}) \propto {q_{\rm i}}^{-0.99}$ can reproduce the local space density inferred from observed PCEBs by Schreiber & Gänsicke (2003), as well as accounting for the location of the currently known sample of PCEBs in $M_2 - \log P_{\rm orb}$ space. However, the more generally preferred binary star IMRD is $n(q_{\rm i}) = 1$ (e.g. Duquennoy & Mayor 1991, Mazeh et al. 1992, Goldberg, Mazeh & Latham 2003).

8.9 Conclusions

By applying population synthesis techniques we have calculated the present day population of post-common envelope binaries (PCEBs) for a range of models describing the common envelope (CE) phase and for different assumptions about the initial mass ratio distribution. We have then compared these models to the currently known sample of PCEBs in the three-dimensional configuration space made up of the two component masses and the orbital period.

We find that the canonical model of a constant, global value of $\alpha_{\rm CE} > 0.1$ can account for the observed PCEB systems with early-type secondaries. However, this cannot explain IK Peg, which has an early-type secondary star. Thus, we suggest that the detection of more PCEBs with early type secondaries may shed further light on the CE phase. IK Peg can be accounted for if we assume that the thermal and ionization energy of the giant primary's envelope, as well as the binary's orbital energy, can unbind the CE from the system. IK Peg can also be explained by describing the CE phase in terms of the binary's angular momentum, according to the γ-prescription proposed by Nelemans et al. (2000) and Nelemans & Tout (2005).

We find that the present day population (local space density) of PCEBs ranges from 3.0×10^5 (6.0×10^{-7} pc^{-3}) for model CE01, $n(q_{\rm i}) \propto {q_{\rm i}}^{-0.99}$, to 1.1×10^9 (2.2×10^{-3} pc^{-3}) for model n15 and for IMFM2.

We also find that an initial mass ratio distribution (IMRD) of $n(q_{\rm i}) \propto {q_{\rm i}}^{-0.99}$ gives local

space densities in the range $6.0 \times 10^{-7} \lesssim \varrho/\mathrm{pc}^{-3} \lesssim 5.6 \times 10^{-5}$, in good agreement with the observationally determined local space density of $6.0 \times 10^{-6} \lesssim \varrho/\mathrm{pc}^{-3} \lesssim 3.0 \times 10^{-5}$. This form of the IMRD also predicts a decline in the population of PCEBs with late-type ($M_2 \leq 0.35$ $\mathrm{M}_\odot$) secondaries, which is what is observed by Rebassa-Mansergas et al. (2008). However, while observations show a sharp decline in the number of PCEBs with orbital periods larger than 1 d, our theoretical calculations instead predict a gradual decline. We cannot reproduce this sharp decline even if we take into account observational biases towards PCEBs with late spectral-type secondaries, and the selection biases against PCEBs with orbital periods greater than 1 d.

We find that there is no clear evidence for a strong dependence between the reconstructed values of α_{CE} and M_2, or the final orbital separation of the PCEBs after the CE phase, $A_{\mathrm{CE,f}}$. However, as $A_{\mathrm{CE,f}}$ indicates the depth the secondary star has penetrated into the giant's envelope, we suggest that the possible $\alpha_{\mathrm{CE}} - A_{\mathrm{CE,f}}$ trend may shed light onto the role of the giant envelope structure into the CE ejection mechanism. We note, however, that the calculation of $A_{\mathrm{CE,f}}$ for those PCEBs which are driven by magnetic braking is uncertain.

Finally, selection biases need to be overcome, especially in the case towards detecting PCEBs with early-type secondaries and/or cool white dwarfs, which will help to further our understanding of the CE phase.

PART IV

Summary of Work and Future Directions

9

Conclusions

9.1 Summary of Main Findings

9.1.1 Testing the Disrupted Magnetic Braking Model

Part of this thesis has been dedicated to conceiving a test for the disrupted magnetic braking model in CV evolution by exploiting its main consequence: the existence of detached WD+MS binaries that underwent mass transfer at some point in their past but ceased mass transfer at $P_{\rm orb} \approx 3$ hours, and are crossing the period gap due to gravitational radiation (which we have called dCVs, for 'detached CVs').

Using our population synthesis code BiSEPS, we calculated the present day population of two varieties of WD+MS binaries. The first are those which have formed from a CE phase, specifically systems that will become semi-detached within the period gap (gPCEBs). The second variety are the aforementioned dCVs. These calculations were repeated for a range of theoretical models describing the CE phase, initial mass ratio distributions, and magnetic braking prescriptions.

We find that in general there is an excess of dCVs over gPCEBs within the period gap.

In an orbital period distribution of the combined dCV and gPCEB population, this excess manifests itself as a prominent peak which coincides with the location of the period gap due to the population of dCVs there. We have coined this feature the 'mirror gap'.

It is the detection of this mirror gap which we propose as a test for the disrupted magnetic braking hypothesis. If such a feature is detected in the orbital period distribution of all WD+MS systems with short orbital periods, then this would strongly corroborate the disrupted magnetic braking model.

Note that this test provides a simple and robust means of identifying the population of dCVs via the detection of the mirror gap. However, is the detection of the mirror gap feasible? For the most likely range of the CE ejection efficiency, $\alpha_{\rm CE} \approx 0.1$ to 0.6 (Iben & Livio 1993), and a flat initial mass ratio distribution, i.e. $n(q_{\rm i}) = 1$ (Goldberg et al. 2003), we find that dCVs outnumber gPCEBs within the period gap by a factor of between approximately 4 and 13. Thus, we can expect a significant mirror gap to be observed. Furthermore, the population of dCVs within the period gap is not too sensitive on the form of magnetic braking. Indeed, between the strongest and weakest magnetic braking prescriptions we considered [Rappaport et al. (1983), with $\gamma = 4$, and Hurley et al. (2002) respectively] the number of dCVs differs by only a factor of approximately 2.

However, in light of the fact that the angular momentum loss rate may not be as high as suggested by the $\dot{J}_{\rm MB} \propto \Omega^3$ prescription, we repeated our calculations for a period gap width of only half an hour. This may occur if the donor star is driven less out of thermal equilibrium as a result of a weaker form of magnetic braking, as suggested by Ivanova & Taam (2003). We find that dCVs outnumber gPCEBs by a factor of about 2. Thus, the detection of the mirror gap is still feasible even if magnetic braking in CV evolution is in fact much weaker.

If the mirror gap is detected, this has implications not only for CV evolution, but for the evolution of related systems as well, such as low-mass X-ray binaries. As these binary systems also have a main sequence donor star, their evolution is also expected to be driven by magnetic braking.

The detection of the mirror gap also has implications for the theory of magnetic field generation in stars; the detection of the mirror gap will confirm that the internal structure of the star plays a vital role in the structure and/or generation of the magnetic field.

9.1.2 The Population of PCEBs

Many theoretical descriptions have been suggested to describe the CE phase, in terms of either the binary's energy or angular momentum budget available to eject the CE from the system. However, none of these models have been adequately compared against the observed population of PCEBs.

Using BiSEPS we have calculated the theoretical present day population of PCEBs for a range of theoretical models describing the CE phase, both in terms of the energy budget (the '$\alpha_{\rm CE}$-prescription') and angular momentum budget (the '$\gamma_{\rm CE}$-algorithm') of the binary. For the former case, we have considered constant, global values of $\alpha_{\rm CE}$, as well as considering $\alpha_{\rm CE}$ as a function of the secondary mass. Specifically, we considered $\alpha_{\rm CE}$ having a power law dependence on the secondary mass, where p is some power, and also where $\alpha_{\rm CE}$ drops to zero below some cut-off mass, $M_{\rm cut}$. We also considered the internal energy of the giant primary's envelope, which may also be exploited during the ejection of the CE.

By comparing our theoretical PCEB populations with the observed one in the full three-dimensional ($M_{\rm WD}, M_2, P_{\rm orb}$) space, we can more reliably assess how well these theoretical models can account for the distribution of the observed PCEB population.

We find that a constant, global value of $\alpha_{\rm CE} = 1.0$ can adequately account for the distribution of the observed PCEB population, except in the interesting case of the system IK Pegasi, which we have determined to be a likely PCEB candidate. In order to explain its long orbital period of 21.72 days, we require $\alpha_{\rm CE} \approx 3$ (assuming $\lambda_{\rm CE} = 0.5$). This could be explained if an energy source other than gravitational potential energy is exploited during the CE phase. Indeed, we find that we can account for IK Peg if we include internal energy of the giants' envelope.

IK Peg can also be accounted for if we describe the CE phase in terms of the angular momentum of the binary, with $\gamma_{\rm CE} = 1.5$. However, one of the main predictions of this prescription is that the number of PCEBs increases with increasing orbital period, with the bulk of the population lying at approximately 1000 days. This is contrary to the observed sharp decline in the number of PCEBs with $P_{\rm orb} \gtrsim 1$ days, which is unlikely to be a result of selection effects, and hence may be a characteristic of the intrinsic population.

Indeed, we can best account for the location of the observed population of PCEBs, by assuming an IMRD of $n(q_{\rm i}) \propto q_{\rm i}^{-0.99}$ and applying the standard $\alpha_{\rm CE}$-prescription. Furthermore, we estimate a PCEB local space density of between 6×10^{-7} and 5.6×10^{-5} pc^{-3}, which is in good agreement with the observationally determined PCEB local space density

of between 6×10^{-6} and 3×10^{-5} pc^{-3}. The $\gamma_{\rm CE}$-algorithm, on the other hand, predicts local space densities typically 1 to 2 orders of magnitude greater than the observed estimate. It therefore appears unlikely that the CE phase can be adequately described in terms of the binary's angular momentum budget.

Recent observations have detected PCEBs with brown dwarf secondaries, a good example being the system 0137-3457. We require $\alpha_{\rm CE} > 0.1$ for these systems if they are to survive the CE phase. In the context of $\alpha_{\rm CE}$ as a function of the secondary mass, for systems with brown dwarf secondaries to survive, $\alpha_{\rm CE}$ cannot be too sensitive on the secondary mass, such that $p < 2$. For the case of $\alpha_{\rm CE}$ in terms of $M_{\rm cut}$, we require $M_{\rm cut} \lesssim 0.05$ M$_{\odot}$ if we are to explain the existence of 0137-3457.

In light of a possible dependence that $\alpha_{\rm CE}$ may have on the secondary mass, we reconstructed the CE phase for each of the observed PCEB systems using our BiSEPS code. We also investigated if $\alpha_{\rm CE}$ depended on the orbital separation of the PCEB immediately after the CE phase. By calculating the formation probabilities of each progenitor system for an observed PCEB, we can calculate the most likely value of $\alpha_{\rm CE}$ for that PCEB.

While we obtain substantial scatter, there is a hint at a possible dependence of $\alpha_{\rm CE}$ on the PCEB orbital separation immediately after the CE phase. Indeed, we find that there is global minimum of $\alpha_{\rm CE}$ near orbital separations of approximately 2 R$_{\odot}$, with increasing values of $\alpha_{\rm CE}$ towards shorter and longer orbital separations.

Such a dependence of $\alpha_{\rm CE}$ on the post-CE orbital separation may shed light onto the underlying physics of the CE phase. By calculating the post-CE orbital separations of PCEBs, we are determining the depth within the giant's envelope the secondary star has penetrated. This may therefore indicate the location within the giant's envelope where the mass-radius profile becomes flat (Terman et al. 1995).

As the post-CE orbital separation may indicate the evolutionary state of the progenitor primary at the onset of the CE phase, then an increase in $\alpha_{\rm CE}$ for orbital separations $\gtrsim 2$ R$_{\odot}$ may reflect the fact the CE is easier to eject from the system. This may be a result of the mass-radius profile becoming flat further away from the centre for more evolved giants. Hence, there will be less spiral-in of the binary during the CE phase. This increase in $\alpha_{\rm CE}$ may also be due to a combination of the envelope of more evolved primaries being less tightly bound, and the internal energy of the giant playing a role in the ejection of the CE.

As to why there is an increase in $\alpha_{\rm CE}$ for post-CE orbital separations less than 2 R$_{\odot}$ is somewhat more puzzling. Shorter post-CE orbital separations indicate less evolved giant

primaries, with more tightly bound envelopes, which would make their ejection harder.

A dependence of $\alpha_{\rm CE}$ on the secondary mass appears to be less compelling. However, fits to the data show a slight decline in $\alpha_{\rm CE}$ with increasing secondary mass for $M_2 \lesssim 1$ M$_\odot$. This may be opposite to what might be expected, as the energy dissipation rate within the CE decreases with decreasing secondary mass. Thus, CE ejection may be less efficient for less massive secondaries. However, it should be borne in mind that there is a lack of data points for systems with $M_2 \lesssim 0.1$ M$_\odot$, and with $M_2 \gtrsim 1$ M$_\odot$. We should also note that the angular momentum loss rate due to magnetic braking is ill-constrained, which makes determining the post-CE orbital separations highly uncertain.

9.2 Future Directions

9.2.1 The Evolution of CVs

With regards to our calculations of the present day dCV populations, it should be reiterated that these are lower limits. Angular momentum driven CVs can also form from systems which have undergone an initial TTMT phase (Schenker et al. 2002). If the mass ratio reaches $q \lesssim 1.3$ while the system is still above the period gap, then the 'normal' CV that will subsequently appear may contribute to the dCV population.

An investigation into the formation and evolution of such systems requires a comprehensive treatment of the TTMT phase, which depends on the extent of nuclear evolution of the donor, and the fraction of the transferred material accreted by the white dwarf (Schenker 2001). Thus, it would be interesting to determine how much such systems would contribute to the dCV population. It is also worth investigating if CVs which have formed from an initial TTMT phase would detach and re-attach at the observed location of the period gap.

The recent discovery of the period spike in the orbital period distribution of CVs detected by the SDSS provides us with an ideal opportunity to renew our efforts to probe the evolution of CVs with brown dwarf donors, and the angular momentum sinks which they are subject to, particularly with respect to the disparity between the theoretically predicted and the observed location of the minimum period cut-off.

Indeed, previous efforts to correct this disparity have involved supplementing gravita-

tional radiation with an extra sink of angular momentum, most recently by circumbinary disks [Willems et al. (2005); Willems et al. (2007)]. An alternative approach considers the 'bloating' of the donor star due to its intrinsic internal structure, as opposed to its thermal dis-equilibrium as a result of extra sinks of orbital angular momentum (Barker & Kolb 2003). A major challenge is to determine which of these effects are responsible for the disparity between the theoretically predicted, and observationally determined, location of the period minimum.

One possible sink of orbital angular momentum, besides gravitational radiation, is remnant magnetic braking. Indeed, observations suggest that rather than magnetic braking decreasing for later spectral type stars, the magnetic activity persists and may actually increase (Cram & Giampapa 1987). If this is the case, magnetic braking may still occur below the period gap albeit at a somewhat reduced strength owing to the distributed dynamo model for fully convective stars [e.g. Zangrilli et al. (1997)]. The major challenge, however, is to describe magnetic braking in a more physically realistic, self-consistent manner, rather than treating it in terms of simple parameterisations.

The location of the period minimum and the features exhibited by the period spike may provide clues regarding the hydrogen mass fraction of the donor star, and hence its evolutionary state at turn-on of mass transfer. As the location of the period minimum is a function of the hydrogen mass fraction of the donor, X, a population of donors with a spread of hydrogen abundances may impact on the width of the period spike.

Indeed, previous population synthesis calculations into the intrinsic CV orbital period distribution have assumed that all donors possess a solar chemical composition, i.e. $X = 0.7$, and $Z = 0.02$ [e.g. Kolb & Baraffe (1999)]. However, as pointed out by Baraffe & Kolb (2000), the spectral types of CV donor stars are significantly later than ZAMS main sequence stars with the same average density. The late-type spectral types of CV donors with $3 \lesssim P_{\rm orb}/{\rm hours} \lesssim 6$ is likely to be a result of significant nuclear evolution of the donors at turn-on of mass transfer, typically with central hydrogen abundance of $\lesssim 0.5$. The evolution of such systems below the period gap may therefore impact on the location and structure of the period minimum spike.

9.2.2 The PCEB Population

The comparison of our theoretical PCEB populations with the observed one has been hindered mainly due to the selection effects which plague the observed PCEB population. As a result, this makes it more difficult to determine which features in the observed population are a characteristic of the intrinsic, Galactic population. In turn, this makes any comparisons with theoretical models more difficult, and less reliable.

However, the advent of the SDSS is providing high quality observations of PCEBs, due to the extensive colour space which the SDSS probes. We will obtain a more representative sample of PCEBs than in previous large-scale surveys. Parallel to this, there is large-scale survey underway to detect PCEBs with cold ($\lesssim 20\,000$ K) white dwarfs and/or early spectral type secondaries (as early as M0), using SEGUE [Sloan Extension for Galactic Understanding and Exploration; see Schreiber et al. (2007)].

Nonetheless, it will be necessary to model the selection effects which occur. The most pertinent selection biases in the observed population of PCEBs result from the colour selection criteria used to detect them, and the Galactic latitudes which are probed. Furthermore, there will be a bias against the detection of PCEBs with long orbital periods. By incorporating a detailed model of the Galactic structure, we can calculate the observable PCEB population. Carrying out an investigation similar to that described in this thesis, but with the selection effects modelled and using PCEBs samples being observed by the SDSS, we can hope to better constrain the CE phase, and the angular momentum losses they are subsequently subjected to.

While we have solely focused on PCEBs containing white dwarf-main sequence components, we can clearly apply the population synthesis techniques presented in this thesis to extend our investigation to the precursors of low-mass x-ray binaries, and binaries containing double neutron star or black holes. Indeed, calculating the relative numbers and space densities of these systems, and reconstructing their CE phase, will provide further observational constraints on CE evolution, and shed new light onto the underlying physics of the CE phase, and the angular momentum losses they are subsequently subjected to. This will hopefully pave the way for a more universal theoretical description of the formation and evolution of all compact binaries.

REFERENCES

ANDRONOV, N., PINSONNEAULT, M. H., SILLS, A., 2003; *Cataclysmic Variables: An Empirical Angular Momentum Loss Prescription from Open Cluster Data.* ApJ, 582, 358

ARAUJO-BETANCOR, S., GÄNSICKE, B. T., LONG, K. S., BEUERMANN, K., DE MARTINO, D., SION, E. M., SZKODY, P., 2005; *Far-Ultraviolet Spectroscopy of Magnetic Cataclysmic Variables.* ApJ, 622, 589

AUNGWEROJWIT, A., GÄNSICKE, B. T., RODRÍGUEZ-GIL, P., HAGEN, H.-J., GIANNAKIS, O., PAPADIMITRIOU, C., ALLENDE PRIETO, C., ENGELS, D., 2007; *HS 1857+5144: a hot and young pre-cataclysmic variable.* A&A, 469, 297

BARAFFE, I., KOLB, U., 2000; *On the late spectral types of cataclysmic variable secondaries.* MNRAS, 318, 354

BARKER, J., KOLB, U., 2003; *The minimum period problem in cataclysmic variables.* MNRAS, 340, 623

BATE, M. R., BONNELL, I. A., BROMM, V., 2003; *The formation of a star cluster: predicting the properties of stars and brown dwarfs.* MNRAS, 339, 577

BEER, M. E., DRAY, L. M., KING, A. R., WYNN, G. A., 2007; *An alternative to common envelope evolution.* MNRAS, 375, 1000

BELL, S. A., POLLACCO, D. L., HILDITCH, R. W., 1994; *Direct Optical Observations of the Secondary Component of Uu-Sagittae.* MNRAS, 270, 449

BEUERMANN, K., BARAFFE, I., KOLB, U., WEICHHOLD, M., 1998; *Are the red dwarfs in cataclysmic variables main-sequence stars?.* A&A, 339, 518

BLEACH, J. N., WOOD, J. H., CATALÁN, M. S., WELSH, W. F., ROBINSON, E. L., SKIDMORE, W., 2000; *Observations of the post-common-envelope binaries EG UMa and PG 1026+002.* MNRAS, 312, 70

BRAGAGLIA, A., RENZINI, A., BERGERON, P., 1995; *Temperatures, gravities, and masses for a sample of bright DA white dwarfs and the initial-to-final mass relation.* ApJ, 443, 735

CATALAN, M. S., DAVEY, S. C., SARNA, M. J., CONNON-SMITH, R., WOOD, J. H., 1994; *A Spectroscopic and Evolutionary Study of the Pre-Cataclysmic Variable Nn-Serpentis.* MNRAS, 269, 879

CHABRIER, G., BARAFFE, I., 2000; *Theory of Low-Mass Stars and Substellar Objects.* ARA&A, 38, 337

CHABRIER, G., BARAFFE, I., LECONTE, J., GALLARDO, J., BARMAN, T., 2009; *The mass-radius relationship from solar-type stars to terrestrial planets: a review.* In American Institute of Physics Conference Series (E. Stempels, ed.). vol. 1094 of *American Institute of Physics Conference Series*, 102–111

CLEMENS, J. C., REID, I. N., GIZIS, J. E., O'BRIEN, M. S., 1998; *The Lower Main Sequence and the Orbital Period Distribution of Cataclysmic Variable Stars.* APJ, 496, 352

COLLIER CAMERON, A., 2002; *Magnetic Activity in low-mass stars: Do the brakes come off?.* ASP Conference Series, 261, 11

CRAM, L. E., GIAMPAPA, M. S., 1987; *Formation of chromospheric lines in cool dwarf stars.* ApJ, 323, 316

DAVIS, P. J., KOLB, U., WILLEMS, B., 2009; *A comprehensive population synthesis study of post-common envelope binaries.* MNRAS, in press

DAVIS, P. J., KOLB, U., WILLEMS, B., GÄNSICKE, B. T., 2008; *How many cataclysmic variables are crossing the period gap? A test for the disruption of magnetic braking.* MNRAS, 389, 1563

DE KOOL, M., 1992; *Statistics of cataclysmic variable formation.* A&A, 261, 188

DE KOOL, M., RITTER, H., 1993; *On the formation rate and space density of close white dwarf main sequence star binaries.* A&A, 267, 397

DEWI, J. D. M., TAURIS, T. M., 2000; *On the energy equation and efficiency parameter of the common envelope evolution.* AAP, 360, 1043

DORMAN, B., ROOD, R. T., O'CONNELL, R. W., 1993; *Ultraviolet Radiation from Evolved Stellar Populations. I. Models.* ApJ, 419, 596

DRECHSEL, H., HEBER, U., NAPIWOTZKI, R., ØSTENSEN, R., SOLHEIM, J.-E., JOHANNESSEN, F., SCHUH, S. L., DEETJEN, J., ZOLA, S., 2001; *HS 0705+6700: A new eclipsing sdB binary.* A&A, 379, 893

DUCHÊNE, G., 1999; *Binary fraction in low-mass star forming regions: a reexamination of the possible excesses and implications.* A&AB, 341, 547

DUQUENNOY, A., MAYOR, M., 1991; *Multiplicity among solar-type stars in the solar neighbourhood. II - Distribution of the orbital elements in an unbiased sample.* A&A, 248, 485

EGGLETON, P. P., 1983; *Approximations to the radii of Roche lobes.* Astrophysical Journal, 268, 368

EGGLETON, P. P., 1996; *Combining Stellar Evolution and Stellar Dynamics.* In Dynamical Evolution of Star Clusters: Confrontation of Theory and Observations (P. Hut, J. Makino, eds.). vol. 174 of *IAU Symposium*, 123–+

ETZEL, P. B., LANNING, H. H., PATENAUDE, D. J., DWORETSKY, M. M., 1977; *BD -3 5357: a newly discovered eclipsing binary with a hot subluminous component..* PASP, 89, 616

FERGUSON, D. H., LIEBERT, J., HAAS, S., NAPIWOTZKI, R., JAMES, T. A., 1999; *Masses and Other Parameters of the Post-Common Envelope Binary BE Ursae Majoris.* ApJ, 518, 866

FRANK, F., KING, A., RAINE, D., 2002; Accretion Power in Astrophysics (CUP), Third Edition edn.

FRIEL, E. D., JANES, K. A., 1993; *Metallicities and radial velocities of old open clusters.* A&A, 267, 75

FULBRIGHT, M. S., LIEBERT, J., BERGERON, P., GREEN, R., 1993; *Spectroscopic observations of the detached binary PG 1413 + 015.* ApJ, 406, 240

GÄNSICKE, B. T., ARAUJO-BETANCOR, S., HAGEN, H.-J., HARLAFTIS, E. T., KITSIONAS, S., DREIZLER, S., ENGELS, D., 2004; *HS 2237+8154: On the onset of mass transfer or entering the period gap?.* A&A, 418, 265

GÄNSICKE, B. T., DILLON, M., R., S. J., R., T. J., 2009; *SDSS unveils the predicted population of intrinically faint cataclysmic variables at the minimum orbital period.* MNRAS

GÄNSICKE, B. T., SZKODY, P., DE MARTINO, D., BEUERMANN, K., LONG, K. S., SION, E. M., KNIGGE, C., MARSH, T., HUBENY, I., 2003; *Anomalous Ultraviolet Line Flux Ratios in the Cataclysmic Variables 1RXS J232953.9+062814, CE 315, BZ Ursae Majoris, and EY Cygni, Observed with the Hubble Space Telescope Space Telescope Imaging Spectrograph.* ApJ, 594, 443

GIAMPAPA, M. S., LIEBERT, J., 1986; *High-resolution H-alpha observations of M dwarf stars Implications for stellar dynamo models and stellar kinematic properties at faint magnitudes.* ApJ, 305, 784

GOLDBERG, D., MAZEH, T., LATHAM, D. W., 2003; *On the Mass-Ratio Distribution of Spectroscopic Binaries.* ApJ, 591, 397

GOOD, S. A., BARSTOW, M. A., BURLEIGH, M. R., DOBBIE, P. D., HOLBERG, J. B., 2005; *A search for binarity using Far-Ultraviolet Spectroscopic Explorer observations of DAO white dwarfs.* MNRAS, 364, 1082

GREEN, R. F., RICHSTONE, D. O., SCHMIDT, M., 1978; *PG 1413+01 - A white dwarf-red dwarf eclipsing binary.* ApJ, 224, 892

GUINAN, E. F., SION, E. M., 1984; *IUE spectroscopy of the degenerate components in the Hyades close binaries V471 Tauri and HZ9.* AJ, 89, 1252

HAN, Z., PODSIADLOWSKI, P., MAXTED, P. F. L., MARSH, T. R., IVANOVA, N., 2002; *The origin of subdwarf B stars - I. The formation channels.* MNRAS, 336, 449

HANSEN, B. M. S., 1999; *Cooling Models for Old White Dwarfs.* ApJ, 520, 680

HANSEN, B. M. S., LIEBERT, J., 2003; *Cool White Dwarfs.* ARA&A, 41, 465

HARPAZ, A., 1998; *The Role of Ionization Energy during Planetary Nebula Ejection.* ApJ, 498, 293

HARTMANN, L. W., NOYES, R. W., 1987; *Rotation and Magnetic Activity in Main Sequence stars.* ARA&A, 25, 271

HEBER, U., DRECHSEL, H., ØSTENSEN, R., KARL, C., NAPIWOTZKI, R., ALTMANN, M., CORDES, O., SOLHEIM, J.-E., VOSS, B., KOESTER, D., FOLKES, S., 2004; *HS 2333+3927: A new sdB+dM binary with a large reflection effect.* A&A, 420, 251

HILDITCH, R. W., 2001; An Introduction to Close Binary Stars (An Introduction to Close Binary Stars, by R. W. Hilditch, pp. 392. ISBN 0521241065. Cambridge, UK: Cambridge University Press, March 2001.)

HILDITCH, R. W., HARRIES, T. J., HILL, G., 1996; *On the reflection effect in three sdOB binary stars.*. MNRAS, 279, 1380

HJELLMING, M. S., 1989; Rapid mass transfer in binary systems. Ph.D. thesis, AA(Illinois Univ. at Urbana-Champaign, Savoy.)

HJELLMING, M. S., TAAM, R. E., 1991; *The response of main-sequence stars within a common envelope.* ApJ, 370, 709

HJELLMING, M. S., WEBBINK, R. F., 1987; *Thresholds for rapid mass transfer in binary systems. I - Polytropic models.* ApJ, 318, 794

HURLEY, J. R., POLS, O. R., TOUT, C. A., 2000; *Comprehensive analytic formulae for stellar evolution as a function of mass and metallicity.* MNRAS, 315, 543

HURLEY, J. R., TOUT, C. A., POLS, O. R., 2002; *Evolution of binary stars and the effect of tides on binary populations.* MNRAS, 329, 897

IBEN, JR., I., TUTUKOV, A. V., 1984; *The evolution of low-mass close binaries influenced by the radiation of gravitational waves and by a magnetic stellar wind.* ApJ, 284, 719

IBEN, I. J., LIVIO, M., 1993; *Common envelopes in binary star evolution.* PASP, 105, 1373

IVANOVA, N., TAAM, R. E., 2003; *Magnetic Braking Revisited.* ApJ, 599, 516

JEFFERY, C. S., SIMON, T., 1997; *Timing the eclipse of HD185510.* MNRAS, 286, 487

JEFFERY, C. S., SIMON, T., EVANS, T. L., 1992; *The hot subdwarf in the eclipsing binary HD 185510.* MNRAS, 258, 64

JONCH-SORENSEN, H., 1995; *CCD uvbyβ photometry of faint stars. III. Metallicities and ages of F-stars in the Galactic disk..* A&A, 298, 799

JONES, B. F., FISCHER, D. A., STAUFFER, J. R., 1996; *Keck Rotational Velocities of the Faintest Pleiades and Hyades Members.* ApJ, 112, 1562

KALOGERA, V., HENNINGER, M., IVANOVA, N., KING, A. R., 2004; *An Observational Diagnostic for Ultraluminous X-Ray Sources.* ApJ, 603, L41

KAWKA, A., VENNES, S., DUPUIS, J., CHAYER, P., LANZ, T., 2008; *Orbital Parameters and Chemical Composition of Four White Dwarfs in Post-Common-Envelope Binaries.* ApJ, 675, 1518

KAWKA, A., VENNES, S., KOCH, R., WILLIAMS, A., 2002; *Optical Observations and Orbital Parameters of the Close DA plus dMe Binaries BPM 71214, EUVE J0720-31.7, BPM 6502, and EC 13471-1258.* AJ, 124, 2853

KENNICUTT, JR., R. C., 1998; *Star Formation in Galaxies Along the Hubble Sequence.* ARA&A, 36, 189

KENNICUTT, JR., R. C., TAMBLYN, P., CONGDON, C. E., 1994; *Past and future star formation in disk galaxies.* ApJ, 435, 22

KILKENNY, D., O'DONOGHUE, D., KOEN, C., LYNAS-GRAY, A. E., VAN WYK, F., 1998; *The EC 14026 stars - VIII. PG 1336-018: a pulsating sdB star in an HWVir-type eclipsing binary.* MNRAS, 296, 329

KING, A. R., 1988; *The evolution of compact binaries.* QJRAS, 29, 1

KING, A. R., BEGELMAN, M. C., 1999; *Radiatively Driven Outflows and Avoidance of Common-Envelope Evolution in Close Binaries.* ApJL, 519, L169

KING, A. R., FRANK, J., RITTER, H., 1996; *Global analysis of mass transfer cycles in cataclysmic variables.* ApJ, 467, 761

KING, A. R., KOLB, U., 1995; *Consequential angular momentum loss and the period gap of cataclysmic variables.* ApJ, 439, 330

KIPPENHAHN, R., MEYER-HOFMEISTER, E., 1977; *On the radii of accreting main sequence stars.* A&A, 54, 539

KNIGGE, C., 2006; *The donor stars of cataclysmic variables.* MNRAS, 373, 484

KOLB, U., 1993; *A model for the intrinsic population of cataclysmic variables.* AAP, 271, 149

KOLB, U., 2002; *Braking and bouncing.* In The Physics of Cataclysmic Variables and Related Objects (B. T. Gänsicke, K. Beuermann, K. Reinsch, eds.). vol. 261 of *Astronomical Society of the Pacific Conference Series*, 180–190

KOLB, U., BARAFFE, I., 1999; *Brown dwarfs and the cataclysmic variable period minimum.* MNRAS, 309, 1034

KOLB, U., KING, A. R., RITTER, H., 1998; *The cataclysmic variable period gap: still there.* MNRAS, 298, L29+

KOLB, U., RAPPAPORT, S., SCHENKER, K., HOWELL, S., 2001; *Nova-induced Mass Transfer Variations.* ApJ, 563, 958

KOLB, U., STEHLE, R., 1996; *The age of cataclysmic variables.* MNRAS, 282, 1454

KOLB, U., WILLEMS, B., 2005; *Thermal-timescale mass transfer and evolved donor stars in CVs.* In ASP Conf. Ser. 330: The Astrophysics of Cataclysmic Variables and Related Objects. 17–+

KROUPA, P., TOUT, C. A., GILMORE, G., 1993; *The distribution of low-mass stars in the Galactic disc.* MNRAS, 262, 545

LANDAU, L. D., LIFSHITZ, E. M., 1975; The classical theory of fields (Course of theoretical physics - Pergamon International Library of Science, Technology, Engineering and Social Studies, Oxford: Pergamon Press, 1975, 4th rev.engl.ed.)

LANDSMAN, W., SIMON, T., BERGERON, P., 1993; *The hot white-dwarf companions of HR 1608, HR 8210, and HD 15638.* PASP, 105, 841

LANNING, H. H., PESCH, P., 1981; *HZ 9 - A white-dwarf-red-dwarf spectroscopic binary in the Hyades.* ApJ, 244, 280

LI, J. K., WU, K. W., WICKRAMASINGHE, D. T., 1994*a*; *On the Rate of Orbital Angular Momentum Loss of Synchronously Rotating Magnetic Cataclysmic Variables.* MNRAS, 270, 769

LI, J. K., WU, K. W., WICKRAMASINGHE, D. T., 1994*b*; *Reduced Magnetic Braking in Synchronously Rotating Magnetic Cataclysmic Variables.* MNRAS, 268, 61

LIEBERT, J., WICKRAMSINGHE, D. T., SCHMIDT, G. D., SILVESTRI, N. M., HAWLEY, S. L., SZKODY, P., FERRARIO, L., WEBBINK, R. F., OSWALT, T. D., SMITH, J. A., LEMAGIE, M. P., 2005; *Where Are the Magnetic White Dwarfs with Detached, Nondegenerate Companions?.* ApJ, 129, 2376

LITTLEFAIR, S. P., DHILLON, V. S., MARSH, T. R., GÄNSICKE, B. T., SOUTHWORTH, J., BARAFFE, I., WATSON, C. A., COPPERWHEAT, C., 2008; *On the evolutionary status of short-period cataclysmic variables.* MNRAS, 388, 1582

LITTLEFAIR, S. P., DHILLON, V. S., MARSH, T. R., GÄNSICKE, B. T., SOUTHWORTH, J., WATSON, C. A., 2006; *A Brown Dwarf Mass Donor in an Accreting Binary.* Science, 314, 1578

LIVIO, M., PRINGLE, J. E., 1994; *Star spots and the period gap in cataclysmic variables.* ApJ, 427, 956

LIVIO, M., SOKER, N., 1988; *The common envelope phase in the evolution of binary stars.* ApJ, 329, 764

MACGREGOR, K. B., BRENNER, M., 1991; *Rotational evolution of solar-type stars. I - Main-sequence evolution.* ApJ, 376, 204

MARSH, T. R., DUCK, S. R., 1996; *A detached white dwarf/M dwarf binary with an orbital period of 2.47h.* MNRAS, 278, 565

MASON, J., HUGHES, D. W., TOBIAS, S. M., 2002; *The Competition in the Solar Dynamo between Surface and Deep-seated α-Effects.* ApJL, 580, L89

MAXTED, P. F. L., 2004; *Hot subdwarfs.* In Spectroscopically and Spatially Resolving the Components of the Close Binary Stars (R. W. Hilditch, H. Hensberge, K. Pavlovski, eds.). vol. 318 of *Astronomical Society of the Pacific Conference Series*, 387–395

MAXTED, P. F. L., MARSH, T. R., HEBER, U., MORALES-RUEDA, L., NORTH, R. C., LAWSON, W. A., 2002; *Photometry of four binary subdwarf B stars and the nature of their unseen companion stars.* MNRAS, 333, 231

MAXTED, P. F. L., MARSH, T. R., MORALES-RUEDA, L., BARSTOW, M. A., DOBBIE, P. D., SCHREIBER, M. R., DHILLON, V. S., BRINKWORTH, C. S., 2004; *RXJ2130.6+4710 - an eclipsing white dwarf-M-dwarf binary star.* MNRAS, 355, 1143

MAXTED, P. F. L., MARSH, T. R., MORAN, C., DHILLON, V. S., HILDITCH, R. W., 1998; *The mass and radius of the M dwarf companion to GD448.* MNRAS, 300, 1225

MAXTED, P. F. L., NAPIWOTZKI, R., DOBBIE, P. D., BURLEIGH, M. R., 2006; *Survival of a brown dwarf after engulfment by a red giant star.* Nature, 442, 543

MAXTED, P. F. L., NAPIWOTZKI, R., MARSH, T. R., BURLEIGH, M. R., DOBBIE, P. D., HOGAN, E., NELEMANS, G., 2007; *Follow-up Observations of SPY White Dwarf + M-Dwarf Binaries.* In 15th European Workshop on White Dwarfs (R. Napiwotzki, M. R. Burleigh, eds.). vol. 372 of *Astronomical Society of the Pacific Conference Series*, 471–+

MAZEH, T., GOLDBERG, D., DUQUENNOY, A., MAYOR, M., 1992; *On the mass-ratio distribution of spectroscopic binaries with solar-type primaries.* ApJ, 401, 265

MCWILLIAM, A., 1997; *Abundance Ratios and Galactic Chemical Evolution.* ARA&A, 35, 503

MENDEZ, R. H., MARINO, R. F., CLARIA, J. J., VAN DRIEL, W., 1985; *The progressive occultation of the binary central star of NGC 2346 by a dense dust cloud.* Rev. Mex. Astron. Astrofis., 10, 187

MENDEZ, R. H., NIEMELA, V. S., 1981; *The binary central star of NGC 2346 and the extinction puzzle.* ApJ, 250, 240

MESTEL, L., SPRUIT, H. C., 1987; *On magnetic braking of late-type stars.* MNRAS, 226, 57

MEYER, F., MEYER-HOFMEISTER, E., 1979; *Formation of cataclysmic binaries through common envelope evolution.* A&A, 78, 167

MILLER, J. S., KRZEMINSKI, W., PRIEDHORSKY, W., 1976; *UU Sagittae..* IAU Circ., 2974, 1

MORALES-RUEDA, L., MARSH, T. R., MAXTED, P. F. L., NELEMANS, G., KARL, C., NAPIWOTZKI, R., MORAN, C. K. J., 2005; *Six detached white-dwarf close binaries.* MNRAS, 359, 648

NELEMANS, G., 2005; *AM CVn stars.* In The Astrophysics of Cataclysmic Variables and Related Objects (J.-M. Hameury, J.-P. Lasota, eds.). vol. 330 of *Astronomical Society of the Pacific Conference Series*, 27–+

NELEMANS, G., TOUT, C. A., 2005; *Reconstructing the evolution of white dwarf binaries: further evidence for an alternative algorithm for the outcome of the common-envelope phase in close binaries.* MNRAS, 356, 753

NELEMANS, G., VERBUNT, F., YUNGELSON, L. R., PORTEGIES ZWART, S. F., 2000; *Reconstructing the evolution of double helium white dwarfs: envelope loss without spiral-in.* A&A, 360, 1011

NEMETH, P., KISS, L. L., SARNECZKY, K., 2005; *Observations of Variables.* Information Bulletin on Variable Stars, 5599

O'BRIEN, M. S., BOND, H. E., SION, E. M., 2001; *Hubble Space Telescope Spectroscopy of V471 Tauri: Oversized K Star, Paradoxical White Dwarf.* ApJ, 563, 971

O'DONOGHUE, D., KOEN, C., KILKENNY, D., STOBIE, R. S., KOESTER, D., BESSELL, M. S., HAMBLY, N., MACGILLIVRAY, H., 2003; *The DA+dMe eclipsing binary EC13471-1258: its cup runneth over ... just.* MNRAS, 345, 506

OROSZ, J. A., WADE, R. A., HARLOW, J. J. B., THORSTENSEN, J. R., TAYLOR, C. J., ERACLEOUS, M., 1999; *The Post-Common Envelope and Pre-Cataclysmic Binary PG 1224+309.* AJ, 117, 1598

ØSTENSEN, R., OREIRO, R., DRECHSEL, H., HEBER, U., BARAN, A., PIGULSKI, A., 2007; *HS 2231+2441: A New Eclipsing sdB Binary of the HW Vir Type.* In 15th European Workshop on White Dwarfs (R. Napiwotzki, M. R. Burleigh, eds.). vol. 372 of *Astronomical Society of the Pacific Conference Series*, 483–+

PACZYŃSKI, B., 1971; *Evolutionary Processes in Close Binary Systems.* Annual Review of Astronomy and Astrophysics, 9, 183

PACZYNSKI, B., 1976; *Common Envelope Binaries.* In IAU Symp. 73: Structure and Evolution of Close Binary Systems. 75–+

PACZYNSKI, B., 1981; *Evolution of cataclysmic binaries.* Acta Astronomica, 31, 1

PACZYŃSKI, B., ZIÓŁKOWSKI, J., 1967; *Evolution of Close Binaries. III..* Acta Astronomica, 17, 7

PATTERSON, J., 1984; *The evolution of cataclysmic and low-mass X-ray binaries.* ApJS, 54, 443

PATTERSON, J., KEMP, J., HARVEY, D. A., FRIED, R. E., REA, R., MONARD, B., COOK, L. M., SKILLMAN, D. R., VANMUNSTER, T., BOLT, G., ARMSTRONG, E., MCCORMICK, J., KRAJCI, T., JENSEN, L., GUNN, J., BUTTERWORTH, N., FOOTE, J.,

BOS, M., MASI, G., WARHURST, P., 2005; *Superhumps in Cataclysmic Binaries. XXV. q_{crit}, $\epsilon(q)$, and Mass-Radius.* PASP, 117, 1204

PILYUGIN, L. S., EDMUNDS, M. G., 1996*a*; *Chemical evolution of the Milky Way Galaxy. I. On the infall model of galactic chemical evolution..* A&A, 313, 783

PILYUGIN, L. S., EDMUNDS, M. G., 1996*b*; *Chemical evolution of the Milky Way Galaxy. II. On the origin of scatter in the age-metallicity relation..* A&A, 313, 792

POLITANO, M., 1996; *Theoretical Statistics of Zero-Age Cataclysmic Variables.* ApJ, 465, 338

POLITANO, M., 2004; *The Formation of Cataclysmic Variables with Brown Dwarf Secondaries.* ApJ, 604, 817

POLITANO, M., WEILER, K. P., 2006; *The Distribution of Secondary Masses in Post-Common-Envelope Binaries: A Potential Test of Disrupted Magnetic Braking.* ApJL, 641, L137

POLITANO, M., WEILER, K. P., 2007; *Population Synthesis Studies of Close Binary Systems Using a Variable Common Envelope Efficiency Parameter. I. Dependence on Secondary Mass.* ApJ, 665, 663

POLLACCO, D. L., BELL, S. A., 1993; *New light on UU Sagittae.* MNRAS, 262, 377

POLUBEK, G., PIGULSKI, A., BARAN, A., UDALSKI, A., 2007; *BUL-SC16 335: A New Eclipsing Pre-Cataclysmic Binary with a Very Short Orbital Period.* In 15th European Workshop on White Dwarfs (R. Napiwotzki, M. R. Burleigh, eds.). vol. 372 of *Astronomical Society of the Pacific Conference Series*, 487–+

PRESS, W. H., TEUKOLSKY, S. A., VETTERLING, W. T., FLANNERY, B. P., 1992; Numerical Recipes in FORTRAN. The art of scientific computing (Cambridge: University Press, —c1992, 2nd ed.)

PRETORIUS, M., KNIGGE, C., KOLB, U., 2006; *The influence on selection effects on the observed cataclysmic variable population: modelling and application to the Palomar-Green sample.* MNRAS

PRINGLE, J. E., WADE, R. A., 1985; Interacting binary stars (Interacting Binary Stars)

PYRZAS, S., GÄNSICKE, B. T., MARSH, T. R., AUNGWEROJWIT, A., REBASSA-MANSERGAS, A., RODRÍGUEZ-GIL, P., SOUTHWORTH, J., SCHREIBER, M. R., NEBOT GOMEZ-MORAN, A., KOESTER, D., 2009; *Post-common-envelope binaries from SDSS - V. Four eclipsing white dwarf main-sequence binaries.* MNRAS, 394, 978

RAPPAPORT, S., JOSS, P. C., WEBBINK, R. F., 1982; *The evolution of highly compact binary stellar systems.* ApJ, 254, 616

RAPPAPORT, S., VERBUNT, F., JOSS, P. C., 1983; *A new technique for calculations of binary stellar evolution, with application to magnetic braking.* ApJ, 275, 713

RASIO, F. A., LIVIO, M., 1996; *On the Formation and Evolution of Common Envelope Systems.* ApJ, 471, 366

RAUCH, T., 2000; *NLTE spectral analysis of the sdOB primary of the eclipsing binary system LB 3459 (AA Dor).* A&A, 356, 665

REBASSA-MANSERGAS, A., GÄNSICKE, B. T., RODRÍGUEZ-GIL, P., SCHREIBER, M. R., KOESTER, D., 2007; *Post-common-envelope binaries from SDSS - I. 101 white dwarf main-sequence binaries with multiple Sloan Digital Sky Survey spectroscopy.* MNRAS, 382, 1377

REBASSA-MANSERGAS, A., GÄNSICKE, B. T., SCHREIBER, M. R., SOUTHWORTH, J., SCHWOPE, A. D., GOMEZ-MORAN, A. N., AUNGWEROJWIT, A., RODRÍGUEZ-GIL, P., KARAMANAVIS, V., KRUMPE, M., TREMOU, E., SCHWARZ, R., STAUDE, A., VOGEL, J., 2008; *Post-common envelope binaries from SDSS - III. Seven new orbital periods.* MNRAS, 1112–+

RENVOIZÉ, V., BARAFFE, I., KOLB, U., RITTER, H., 2002; *Distortion of secondaries in semi-detached binaries and the cataclysmic variable period minimum.* A&A, 389, 485

REZZOLLA, L., URYŪ, K. Ō., YOSHIDA, S., 2001; *Gravitational wave emission by cataclysmic variables: numerical models of semi-detached binaries.* MNRAS, 327, 888

RITTER, H., 1988; *Turning on and off mass transfer in cataclysmic binaries.* AAP, 202, 93

RITTER, H., 1996; *Principles of Semi-Detached Binary Evolution.* In NATO ASIC Proc. 477: Evolutionary Processes in Binary Stars (R. A. M. J. Wijers, M. B. Davies, C. A. Tout, eds.). 223–+

RITTER, H., 2008; *Formation and Evolution of Cataclysmic Variables.* ArXiv e-prints

RITTER, H., KOLB, U., 2003; *Catalogue of cataclysmic binaries, low-mass X-ray binaries and related objects (Seventh edition).* A&A, 404, 301

ROBINSON, E. L., BARKER, E. S., COCHRAN, A. L., COCHRAN, W. D., NATHER, R. E., 1981; *MV Lyrae - Spectrophotometric properties of minimum light; or on MV Lyrae off.* ApJ, 251, 611

SAFFER, R. A., WADE, R. A., LIEBERT, J., GREEN, R. F., SION, E. M., BECHTOLD, J., FOSS, D., KIDDER, K., 1993; *PG 0308 + 096 and PG 1026 + 002 - Two new short period binary stars resulting from common-envelope evolution.* ApJ, 105, 1945

SANDQUIST, E. L., TAAM, R. E., BURKERT, A., 2000; *On the Formation of Helium Double Degenerate Stars and Pre-Cataclysmic Variables.* ApJ, 533, 984

SANDQUIST, E. L., TAAM, R. E., CHEN, X., BODENHEIMER, P., BURKERT, A., 1998; *Double Core Evolution. X. Through the Envelope Ejection Phase.* ApJ, 500, 909

SCHENKER, K., 2001; *Thermal-Timescale Mass Transfer and CV Evolution.* In Evolution of Binary and Multiple Star Systems (P. Podsiadlowski, S. Rappaport, A. R. King, F. D'Antona, L. Burderi, eds.). vol. 229 of *Astronomical Society of the Pacific Conference Series*, 321–+

SCHENKER, K., KING, A. R., KOLB, U., WYNN, G. A. ZHANG, Z., 2002; *AE Aquarii: how cataclysmic variables descend from supersoft binaries.* MNRAS, 337, 1105

SCHMIDT, G. D., SMITH, P. S., HARVEY, D. A., GRAUER, A. D., 1995; *The Precataclysmic Variable GD 245.* AJ, 110, 398

SCHMIDT, M., 1959; *The Rate of Star Formation..* ApJ, 129, 243

SCHOU, J., ANTIA, H. M., BASU, S., BOGART, R. S., BUSH, R. I., CHITRE, S. M., CHRISTENSEN-DALSGAARD, J., DI MAURO, M. P., DZIEMBOWSKI, W. A., EFF-DARWICH, A., GOUGH, D. O., HABER, D. A., HOEKSEMA, J. T., HOWE, R., KORZENNIK, S. G., KOSOVICHEV, A. G., LARSEN, R. M., PIJPERS, F. P., SCHERRER, P. H., SEKII, T., TARBELL, T. D., TITLE, A. M., THOMPSON, M. J., TOOMRE, J., 1998; *Helioseismic Studies of Differential Rotation in the Solar Envelope by the Solar Oscillations Investigation Using the Michelson Doppler Imager.* ApJ, 505, 390

SCHREIBER, M. R., GÄNSICKE, B. T., 2003; *The age, life expectancy, and space density of Post Common Envelope Binaries.* A&A, 406, 305

SCHREIBER, M. R., GÄNSICKE, B. T., SOUTHWORTH, J., SCHWOPE, A. D., KOESTER, D., 2008; *Post common envelope binaries from SDSS. II: Identification of 9 close binaries with VLT/FORS2.* A&A, 484, 441

SCHREIBER, M. R., NEBOT GOMEZ-MORAN, A., SCHWOPE, A. D., 2007; *Understanding White Dwarf Binary Evolution with White Dwarf/Main Sequence Binaries: First Results from SEGUE.* In Astronomical Society of the Pacific Conference Series (A. Napiwotzki, M. R. Burleigh, eds.). vol. 372 of *Astronomical Society of the Pacific Conference Series*, 459–+

SHIMANSKII, V. V., BORISOV, N. V., SAKHIBULLIN, N. A., SURKOV, A. E., 2004; *The Nature of the Unique Precataclysmic Variable V664 Cas with Two-Peaked Balmer Lines in Its Spectrum.* Astronomy Reports, 48, 563

SHIMANSKY, V. V., BORISOV, N. V., SHIMANSKAYA, N. N., 2003; *The Impact of Reflection Effects on the Parameters of the Old Pre-Cataclysmic Variables MS Peg and LM Com.* Astronomy Reports, 47, 763

SILLS, A., PINSONNEAULT, M. H., M., T. D., 2000; *The Angular Momentum Evolution of Very Low Mass Stars.* ApJ, 534, 335

SILVESTRI, N. M., LEMAGIE, M. P., HAWLEY, S. L., WEST, A. A., SCHMIDT, G. D., LIEBERT, J., SZKODY, P., MANNIKKO, L., WOLFE, M. A., BARENTINE, J. C., BREWINGTON, H. J., HARVANEK, M., KRZESINSKI, J., LONG, D., SCHNEIDER, D. P., SNEDDEN, S. A., 2007; *New Close Binary Systems from the SDSS-I (Data Release Five) and the Search for Magnetic White Dwarfs in Cataclysmic Variable Progenitor Systems.* AJ, 134, 741

SKUMANICH, A., 1972; *Time Scales for CA II Emission Decay, Rotational Braking, and Lithium Depletion.* APJ, 171, 565

SMALLEY, B., SMITH, K. C., WONNACOTT, D., ALLEN, C. S., 1996; *The chemical composition of IK Pegasi.* MNRAS, 278, 688

SOKER, N., 2004; *Energy and Angular Momentum Deposition During Common Envelope Evolution.* In Revista Mexicana de Astronomia y Astrofisica Conference Series (G. Tov-

massian, E. Sion, eds.). vol. 20 of *Revista Mexicana de Astronomia y Astrofisica, vol. 27*, 30–32

SOKER, N., HARPAZ, A., 2003; *Criticism of recent calculations of common envelope ejection.* MNRAS, 343, 456

SOUTHWORTH, J., GÄNSICKE, B., MARSH, T. R., DE MARTINO, D., HAKALA, P., LITTLEFAIR, P., RODRIGUEZ-GIL, P., SZODY, P., 2006; *VLT/FORS spectroscopy of faint cataclysmic variables discovered by the Sloan Digital Sky Survey.* MNRAS, 373, 687

SPRUIT, H. C., RITTER, H., 1983; *Stellar activity and the period gap in cataclysmic variables.* Astronomy and Astrophysics, 124, 267

SPRUIT, H. C., TAAM, R. E., 2001; *Circumbinary Disks and Cataclysmic Variable Evolution.* ApJ, 548, 900

SPRUIT, H. C., VAN BALLEGOOIJEN, A. A., 1982; *Stability of toroidal flux tubes in stars.* A&, 106, 58

STAUFFER, J. R., 1987; *Dynamical mass determinations for the white dwarf components of HZ 9 and Case 1.* AJ, 94, 996

STEHLE, R., RITTER, H., KOLB, U., 1996; *An analytic approach to the secular evolution of cataclysmic variables.* MNRAS, 279, 581

TAAM, R. E., 2002; *Hydrodynamical Investigations of Common Envelope Evolution.* In Stellar Collisions, Mergers and their Consequences (M. M. Shara, ed.). vol. 263 of *Astronomical Society of the Pacific Conference Series*, 81–+

TAAM, R. E., BODENHEIMER, P., 1991; *Double core evolution. IV - The late stages of evolution of a 2-solar mass red giant with a 1-solar mass companion.* ApJ, 373, 246

TAAM, R. E., SANDQUIST, E. L., 2000; *Common Envelope Evolution of Massive Binary Stars.* ARA&A, 38, 113

TAAM, R. E., SPRUIT, H. C., 1989; *The disrupted magnetic braking hypothesis and the period gap of cataclysmic variables.* ApJ, 345, 972

TAAM, R. E., SPRUIT, H. C., 2001; *The Evolution of Cataclysmic Variable Binary Systems with Circumbinary Disks.* ApJ, 561, 329

TAPPERT, C., GÄNSICKE, B. T., SCHMIDTOBREICK, L., AUNGWEROJWIT, A., MENNICKENT, R. E., KOESTER, D., 2007; *The pre-cataclysmic variable, LTT 560.* A&A, 474, 205

TERMAN, J. L., TAAM, R. E., HERNQUIST, L., 1994; *Double-core evolution. 5: Three-dimensional effects in the merger of a red giant with a dwarf companion.* ApJ, 422, 729

TERMAN, J. L., TAAM, R. E., HERNQUIST, L., 1995; *Double core evolution. 7: The infall of a neutron star through the envelope of its massive star companion.* ApJ, 445, 367

TOBIAS, S. M., BRUMMELL, N. H., CLUNE, T. L., TOOMRE, J., 2001; *Transport and Storage of Magnetic Field by Overshooting Turbulent Compressible Convection.* ApJ, 549, 1183

TOUT, C. A., EGGLETON, P. P., 1988*a*; *The formation of ALGOLS without catastrophes.* ApJ, 334, 357

TOUT, C. A., EGGLETON, P. P., 1988*b*; *Tidal enhancement by a binary companion of stellar winds from cool giants.* MNRAS, 231, 823

TOUT, C. A., HALL, D. S., 1991; *Wind driven mass transfer in interacting binary systems.* MNRAS, 253, 9

TOWNSLEY, B., BILDSTEN, L., 2003; *Measuring white dwarf accretion rates via their effective temperature.* ApJ, 596, L227

UNGLAUB, K., 2008; *Mass-loss and diffusion in subdwarf B stars and hot white dwarfs: do weak winds exist?.* A&A, 486, 923

VACCARO, T. R., WILSON, R. E., 2003; *Fluorescence in ultraviolet active binaries: the case of FF Aquarii.* MNRAS, 342, 564

VAN DEN BESSELAAR, E. J. M., GREIMEL, R., MORALES-RUEDA, L., NELEMANS, G., THORSTENSEN, J. R., MARSH, T. R., DHILLON, V. S., ROBB, R. M., BALAM, D. D., GUENTHER, E. W., KEMP, J., AUGUSTEIJN, T., GROOT, P. J., 2007; *DE Canum Venaticorum: a bright, eclipsing red dwarf-white dwarf binary.* A&A, 466, 1031

VENNES, S., THORSTENSEN, J. R., 1994; *Spectroscopic, orbital, and physical properties of the binary Feige 24 and detection of transient He II absorption in the system.* AJ, 108, 1881

VENNES, S., THORSTENSEN, J. R., POLOMSKI, E. F., 1999; *Stellar Masses, Kinematics, and White Dwarf Composition for Three Close DA+DME Binaries.* ApJ, 523, 386

VERBUNT, F., ZWAAN, C., 1981; *Magnetic braking in low-mass X-ray binaries.* A&A, 100, L7

VINK, J. S., 2004; *Mass-loss predictions for Subdwarf B stars.* Ap&SS, 291, 239

WARNER, B., 1995; Cataclysmic variable stars (Cambridge Astrophysics Series, Cambridge, New York: Cambridge University Press, —c1995)

WEBBINK, R. F., 1985; Stellar evolution and binaries (Interacting Binary Stars), 39–+

WEBBINK, R. F., 2008; *Common Envelope Evolution Redux.* Short-Period Binary Stars: Observations, Analyses, and Results, 233–+

WEIDEMANN, V., 1990; *Masses and evolutionary status of white dwarfs and their progenitors.* ARA&A, 28, 103

WILLEMS, B., KOLB, U., 2002; *Population synthesis of wide binary millisecond pulsars.* MNRAS, 337, 1004

WILLEMS, B., KOLB, U., 2004; *Detached white dwarf main-sequence star binaries.* AAP, 419, 1057

WILLEMS, B., KOLB, U., SANDQUIST, E. L., TAAM, R. E., DUBUS, G., 2005; *Angular Momentum Losses and the Orbital Period Distribution of Cataclysmic Variables below the Period Gap: Effects of Circumbinary Disks.* ApJ, 635, 1263

WILLEMS, B., TAAM, R. E., KOLB, U., DUBUS, G., SANDQUIST, E. L., 2007; *Theoretical Orbital Period Distributions of Cataclysmic Variables above the Period Gap: Effects of Circumbinary Disks.* ApJ, 657, 465

WILS, P., DI SCALA, G., OTERO, S. A., 2007; *NSVS 14256825: A New HW Vir Type System.* Information Bulletin on Variable Stars, 5800, 1

WOOD, J. H., ROBINSON, E. L., ZHANG, E.-H., 1995; *Observations of the eclipse in the close binary star BE UMa.* MNRAS, 277, 87

WOOD, J. H., SAFFER, R., 1999; *Spectroscopy of the post-common envelope binary HW Virginis.* MNRAS, 305, 820

WOOD, M. A., 1995; *Theoretical White Dwarf Luminosity Functions: DA Models.* In White Dwarfs, Proceedings of the 9th European Workshop on White Dwarfs Held at Kiel, Germany, 29 August - 1 September 1994. Lecture Notes in Physics, Vol. 443, edited by Detlev Koester and Klaus Werner. Springer-Verlag, Berlin Heidelberg New York, 1995., p.41 (D. Koester, K. Werner, eds.). 41–+

YORKE, H. W., BODENHEIMER, P., TAAM, R. E., 1995; *Double Core Evolution. VIII. The Spiral-in of a Main-Sequence Star through the Envelope of an Asymptotic Giant Branch Companion.* ApJ, 451, 308

ZAHN, J.-P., 1966; *Les marées dans une étoile double serrée (suite).* Annales d'Astrophysique, 29, 489

ZAHN, J.-P., 1977; *Tidal friction in close binary stars.* A&A, 57, 383

ZANGRILLI, L., TOUT, C. A., BIANCHINI, A., 1997; *How two Cohabiting Magnetic Dynamos explain the Secular Evolution of Cataclysmic Variables.* MNRAS, 289, 59